

# Multi-wavelength surveys: object detectability and NIR luminosity function of galaxies

Mauro Stefanon  
Ph.D. Thesis

Valencia - 2011

---



**Dr. Alberto Fernández Soto,**

Científico Titular CSIC en el Instituto de Física de Cantabria

y

**Dr. Danilo Marchesini**

Assistant Professor in Astrophysics en Tufts University (EE.UU.)

### CERTIFICAN

Que la presente memoria, “Multi-wavelength surveys: object detectability and NIR luminosity function of galaxies”, ha sido realizada bajo su dirección por Mauro Stefanon, y que constituye su tesis doctoral para optar al grado de Doctor en Física.

Y para que quede constancia y tenga los efectos oportunos, firmo el presente documento en Paterna, a 16 de Septiembre de 2011.

Firmado: Alberto Fernández Soto

Firmado: Danilo Marchesini



*ai miei genitori*



# Contents

<b>1</b>	<b>Introduction</b>	<b>1</b>
1.1	The Cosmological framework . . . . .	1
1.2	The $\Lambda$ CDM model . . . . .	4
1.2.1	The observational picture . . . . .	5
1.2.2	Modelling . . . . .	8
1.3	Detection limits . . . . .	10
1.3.1	Why a detection limit exists . . . . .	10
1.4	Observational selection effects . . . . .	12
1.4.1	Flux selection . . . . .	12
1.4.2	Spatial selection . . . . .	15
1.4.3	False detections . . . . .	16
1.5	Multi-wavelength surveys . . . . .	16
1.5.1	Cosmological Photometric surveys . . . . .	17
1.6	Aim of this thesis . . . . .	26
1.6.1	Existing methods for the detection completeness measurement	29
<b>2</b>	<b>Absolute Magnitudes Measurement</b>	<b>39</b>
2.1	Introduction . . . . .	39
2.2	Absolute magnitudes and K-correction . . . . .	40
2.2.1	K-correction with SED . . . . .	46
2.2.2	Linear combination of a base filter set . . . . .	49
2.2.3	Discussion . . . . .	59
2.3	Luminosity Function . . . . .	63
2.3.1	$1/V_{max}$ . . . . .	64
2.3.2	Step-Wise Maximum Likelihood . . . . .	65
2.3.3	The STY maximum likelihood method . . . . .	68
2.3.4	Comparison among the three methods . . . . .	69
2.3.5	Normalization of the LF . . . . .	70
<b>3</b>	<b>Determination of Detection Completeness</b>	<b>75</b>
3.1	Introduction . . . . .	75
3.2	Description of the methods . . . . .	77
3.2.1	Determination of the weights . . . . .	81

## CONTENTS

---

3.2.2	The analytic method . . . . .	81
3.2.3	Monte Carlo simulation . . . . .	87
3.2.4	Detection completeness on the 20 filters . . . . .	91
3.2.5	Detection completeness on the <i>deep</i> image . . . . .	93
3.2.6	Point-source completeness . . . . .	94
3.2.7	Results . . . . .	97
3.3	Conclusions . . . . .	98
<b>4</b>	<b>ALHAMBRA field galaxy Luminosity Function - Preliminary results</b>	<b>107</b>
4.1	Introduction . . . . .	107
4.2	Star-galaxy separation . . . . .	108
4.3	Absolute magnitudes . . . . .	111
4.4	Detection completeness . . . . .	113
4.5	Color-Magnitude diagram . . . . .	114
4.6	Luminosity Functions . . . . .	117
4.7	Conclusions . . . . .	124
<b>5</b>	<b>The evolution of the rest-frame J and H luminosity function from <math>z=1.5</math> to <math>z=3.5</math></b>	<b>129</b>
5.1	Introduction . . . . .	129
5.2	Description of the sample . . . . .	131
5.2.1	MUSYC . . . . .	132
5.2.2	FIRES . . . . .	133
5.2.3	FIREWORKS . . . . .	133
5.2.4	Sample selection . . . . .	135
5.2.5	Photometric redshift and star/galaxy separation . . . . .	136
5.3	Methodology . . . . .	141
5.3.1	Cosmic variance and photometric redshift uncertainties . . . . .	142
5.4	J and H Luminosity Functions . . . . .	146
5.4.1	Discussion . . . . .	147
5.4.2	Luminosity densities . . . . .	154
5.4.3	Star Formation Rate . . . . .	157
5.5	Conclusions . . . . .	158
<b>6</b>	<b>Spectrophotometric redshifts: a new approach to the reduction of noisy spectra and its application to GRB090423</b>	<b>165</b>
6.1	Introduction . . . . .	165
6.2	Gamma-Ray Bursts . . . . .	167
6.3	Description of the data . . . . .	170
6.3.1	GRB090423 afterglow data . . . . .	170
6.4	Description of the method . . . . .	172
6.4.1	Model spectra . . . . .	172
6.4.2	CCD and instrumental characteristics . . . . .	175

---

6.4.3	Application of the method . . . . .	180
6.5	Results . . . . .	184
6.6	Conclusions . . . . .	186
<b>7</b>	<b>Conclusions</b>	<b>191</b>
<b>A</b>	<b>Resumen del trabajo de tesis</b>	<b>195</b>
A.1	[Cap. 1] Introducción . . . . .	195
A.1.1	Límites de detección . . . . .	195
A.1.2	Efectos observacionales de selección . . . . .	196
A.1.3	Cartografiados multi-banda . . . . .	196
A.1.4	Finalidades de esta tesis . . . . .	196
A.2	[Cap. 2] Medida de magnitudes absolutas . . . . .	197
A.2.1	Magnitudes absolutas y correcciones K . . . . .	197
A.2.2	Cálculo de la función de luminosidad . . . . .	199
A.3	[Cap. 3] Determinación de la completitud en la detección de objetos	200
A.3.1	Introducción . . . . .	200
A.3.2	Descripción de los métodos . . . . .	200
A.3.3	Conclusiones . . . . .	202
A.4	[Cap. 4] Función de luminosidad con datos ALHAMBRA . . . . .	203
A.4.1	Introducción . . . . .	203
A.4.2	Separación estrellas-galaxias . . . . .	203
A.4.3	Magnitudes absolutas . . . . .	203
A.4.4	Completitud en detección . . . . .	204
A.4.5	Diagrama color-magnitud . . . . .	204
A.4.6	Funciones de luminosidad . . . . .	204
A.5	[Cap. 5] Evolución de la FL en bandas J y H desde $z = 1.5$ hasta $z = 3.5$ . . . . .	205
A.5.1	Introducción . . . . .	205
A.5.2	Descripción de los datos . . . . .	205
A.5.3	Métodología . . . . .	207
A.5.4	Funciones de luminosidad en J y H . . . . .	207
A.5.5	Conclusiones . . . . .	208
A.6	[Cap. 6] Redshift espectrofotométricos: un nuevo enfoque para la reducción de espectros a bajo RSN y su aplicación a GRB090423 . . . . .	208
A.6.1	Introducción . . . . .	208
A.6.2	Estallidos de rayos gamma . . . . .	209
A.6.3	Descripción de los datos . . . . .	210
A.6.4	Descripción del método . . . . .	210
A.6.5	Resultados y conclusiones . . . . .	211
A.7	[Cap. 7] Conclusiones . . . . .	212

---



# 1

## Introduction

### 1.1 The Cosmological framework

---

The modern developments on the knowledge of the Universe are based on one single assumption, i. e. that the Universe is, on a sufficiently large scale, isotropic and homogeneous. This assumption has also been confirmed by a number of observations.

The standard model of cosmology directly comes from the application of general relativity to the matter (and energy) content of the Universe. The corresponding Einstein field equation then allows to describe the dynamical state of the Universe as a whole:

$$R_{\mu\nu} - \frac{1}{2}g_{\mu\nu}R - g_{\mu\nu}\Lambda = \frac{8\pi G}{c^4}T_{\mu\nu} \quad (1.1)$$

with  $R_{\mu\nu}$  the *Ricci tensor*, describing the local curvature of the space-time,  $g_{\mu\nu}$  the metric,  $R$  the curvature scalar,  $\Lambda$  the cosmological constant and  $T_{\mu\nu}$  the energy-momentum tensor (see e.g. Mo, van den Bosch, & White 2010).

In the case of a homogeneous and isotropic universe, the metric assumes a simple form, known also as the Friedmann-Lemaitre-Robertson-Walker metric, and which can be regarded as the generalization of spherical coordinates  $(r, \theta, \phi)$  embedded in a 4 dimensional space:

$$ds^2 = c^2 dt^2 - a^2(t) \left[ \frac{dr^2}{1 - Kr^2} + r^2(d\theta^2 + \sin^2\theta d\phi^2) \right] \quad (1.2)$$

The above equation allows to express the proper distance element  $ds$  in terms of comoving coordinates  $(r, \theta, \phi)$ , of the curvature  $K$ , of time  $t$  and of the scale factor  $a(t)$ .

Together with the above metric, the field equation, for the case of an isotropic and homogenous universe, leads to the Friedmann equation:

$$H^2(t) \equiv \left(\frac{\dot{a}}{a}\right)^2 = \frac{8\pi G}{2}\rho - \frac{Kc^2}{a^2} + \frac{\Lambda c^2}{3} \quad (1.3)$$

where  $\rho$  is the energy density in units of  $c^2$ .

Under the hypothesis that the Universe is an adiabatic ideal gas, it is also straightforward to obtain an expression for the evolution of any given equation of state  $P = P(\rho)$  :

$$\frac{d\rho}{da} + 3\left(\frac{\rho + P/c^2}{a}\right) = 0 \quad (1.4)$$

with  $P$  the pressure.

The two relations Eq. 1.3 and Eq. 1.4 allow then to determine the evolution with time of the fundamental parameters  $a$ ,  $\rho$  and  $P$ , once a set of initial conditions is established.

Although Eq. 1.2 contains all the ingredients to compute the proper distance  $ds$ , it is of limited utility when coming to the observational side as the quantity it defines is not directly measurable. From the analogy to the everyday experience that an object (e.g. a candle) appears smaller and fainter when located at a given distance from us than is it at a shorter distance, astronomers have introduced two distinct ways of expressing the distance of cosmological objects: the angular distance  $d_A$  and the luminosity distance  $d_L$ . If  $D$  is the transversal proper size of an object and  $\theta$  is its apparent angular size, the angular distance  $d_A$  is the term allowing to satisfy the relation:

$$\theta = \frac{D}{d_A} \quad (1.5)$$

Analogously, the luminosity distance  $d_L$  is defined by the relation between the

intrinsic luminosity  $L$  and the flux  $F$  measured on the Earth:

$$F = \frac{L}{4\pi d_L^2} \quad (1.6)$$

The  $d_A$  and  $d_L$  in the above two relations Eq. 1.5 and Eq. 1.6 can be expressed in terms of observable quantities. We first introduce the dimensionless density parameters  $\Omega = \rho/\rho_{crit}$ :

$$\Omega_m \equiv \frac{8\pi G}{3H_0^2} \rho_0 \quad (1.7)$$

$$\Omega_\Lambda \equiv \frac{\Lambda c^2}{3H_0^2} \quad (1.8)$$

$$\Omega_K = 1 - \Omega_m - \Omega_\Lambda \quad (1.9)$$

where  $H_0$ , the Hubble constant, corresponds to  $H(t = t_0)$ , with  $t_0$  indicating the present time. We can then define the quantity  $E(z)$  as:

$$E(z) = \sqrt{\Omega_m(1+z)^3 + \Omega_K(1+z)^2 + \Omega_\Lambda} \quad (1.10)$$

Here  $z$  denotes the redshift:

$$1+z \equiv \frac{a(t_0)}{a(t)} = \frac{\lambda_0}{\lambda_e} \quad (1.11)$$

The last equality allows to directly compute the redshift of a source from the measure of the rest-frame (or laboratory) wavelength value  $\lambda_e$  of some selected spectral line and its measure as from the Earth  $\lambda_0$ .

Using the above relations, the angular size distance  $d_A$  and luminosity distance  $d_L$  can finally be computed, for a  $\Omega_K = 0$  Universe, as:

$$d_A = (1+z)^{-1} \frac{c}{H_0} \int_0^z \frac{dz'}{E(z')} \quad (1.12)$$

$$d_L = (1+z)^2 d_A \quad (1.13)$$

For the present work, we adopted a concordance cosmology with parameters  $\Omega_K = 0$ ,  $\Omega_\Lambda = 0.7$ ,  $\Omega_m = 0.3$  and  $H_0 = 70\text{Km/s/Mpc}$ .

## 1.2 The $\Lambda$ CDM model

---

The fundamental assumption of a homogenous Universe in the Friedmann-Lemaitre-Robertson-Walker (FLRW) model has a natural antagonist: on smaller scales the Universe is evidently highly non-homogenous, manifesting this phenomenon in a beautiful variety of structures, ranging from large clusters of galaxies many Mpc wide to stars, planets and life. This requires that small perturbations in the density of matter were already present since the very first instants after the Big-Bang, perturbations which have then grown with time. The collisionless (*cold*) purely gravitational growth of these instabilities in the density field of a kind of matter still undetected by our instruments (hence *dark*) gave rise to large haloes which governed the assembly of ordinary (*baryonic*) matter in the formation of stars and galaxies - the so called Cold Dark Matter (CDM) model (Peebles, 1982; Blumenthal et al., 1984; Davis et al., 1985).

This model has its most convincing support from the Cosmic Microwave Background radiation (CMB). The distribution of the hot and cold *spots*, initially measured by COBE (Smoot et al., 1992) and more recently by WMAP (Bennett et al., 2003), can be related to the anisotropies in the distribution of matter when the Universe was only a few hundred thousand years old. Additional support to the CDM model has been brought by the analysis of the large scale structure in the local Universe using the two widest optical surveys available to date, i.e. the 2 Degree Field Galaxy Redshift Survey (2dF GRS Colless et al. 2001) and the Sloan Digital Sky Survey (SDSS - York et al. 2000). The wealth of information on the local Universe from the two surveys has allowed the most accurate measurement of the power spectrum of galaxy clustering, revealing also the acoustic oscillations on the baryonic matter power spectrum (BAOs) (Cole et al., 2005; Eisenstein et al., 2005).

The baryonic matter accumulates in the dark matter haloes, forming a corresponding halo of gas. Under the gravitational potential, the halo contracts and heats. However, while compressing, the gas can also cool through Compton scattering, excitation of rotational and vibrational energy levels through collisions and emission of photons from transitions between energy levels. When a critical density is reached, the nuclear reactions can start, originating a new star.

There is another fundamental, yet still not understood, ingredient in the current *concordance cosmology*: the dark energy. Observations of distant ( $z \approx 1$ ) supernovae, used as standard candles, have revealed that the expansion rate of the Universe is increasing with cosmic time (Riess et al., 1998; Perlmutter et al., 1999). In order to effectively take into account this effect, the cosmological constant ( $\Lambda$  - see Eq. 1.3) was re-introduced in the FRW model, leading to the definition of the  $\Lambda$ CDM framework currently adopted as the standard cosmological model. The values of parameters characterizing the model are known today with a precision of  $\approx 5\%$ , thanks to the combination of results from a number of different projects, like the measurement of the Hubble constant (Freedman et al., 2001), clustering measurements on nearby galaxies (Verde, Haiman, & Spergel, 2002) and WMAP CMB anisotropies (Spergel et al., 2003; Spergel, 2005; Komatsu et al., 2009).

### 1.2.1 The observational picture

One of the most remarkable aspects of the galaxy population is that galaxies can be classified into a small number of sequences. The first classification, purely based on morphological characteristics, was already proposed by Hubble (1926) and it is still in use today. Simply put, there are two broad classes of galaxies: ellipticals, systems with a rounded shape in the three axes, and spirals, showing a disk-like structure.

The analysis of data on the local universe, like the SDSS and 2dFGRS surveys, has confirmed and in some cases shown for the first time, that this dichotomy extends to a number of fundamental characteristics of galaxies.

The color-magnitude diagram (CMD) shows two well separated groups of galaxies, a red cloud and a blue sequence, with elliptical galaxies populating the red region, while spiral galaxies reside in the blue part (Strateva et al., 2001; Blanton et al., 2003). This characteristic is directly linked to another important difference between the two classes. In fact, bluer spectra are the footprint of an ongoing star formation, while redder spectra reflect an older stellar population, which is passively evolving (Kauffmann et al., 2003; Wyder et al., 2007). Moreover, the objects of each class are characterized by different masses: red/elliptical galaxies are massive systems, while blue/spiral galaxies have lower masses, with a quite clear boundary between the two classes falling at  $3 \times 10^{10} M_{\odot}$  (Kauffmann

et al., 2004; Blanton et al., 2005).

This bi-modality in the galaxy distribution is observed also at higher redshift (see for instance Bell et al. 2004; Brammer et al. 2009). Several studies using deep surveys have shown that the stellar mass of red galaxies has grown by a factor of 2 since  $z \simeq 2$ . On the contrary, the mass distribution of blue galaxies has remained almost constant, suggesting a possible transition from the blue sequence to the red cloud with cosmic time (Bell et al., 2004; Faber et al., 2007). In this scenario, elliptical galaxies are the result of early mass assembly and star formation, which would cause the galaxy to initially move along the blue cloud of the CMD, followed by quenching, moving the galaxy to the red sequence, and later by dry merging, with the result of displacing the galaxy along the red sequence towards higher masses/luminosities, with the details of these processes still not completely known. In particular, as pointed out in Renzini (2006), the most recent measurements of the merging rates still suffer from large uncertainties: on one side estimates show that 35% of early type galaxies showing a major merging event since  $z=0.1$  (van Dokkum, 2005), while on the other side there is less than 1% probability of a dry merger per Gyr since  $z=0.36$  (Masjedi et al., 2006).

To further complicate the framework, high redshift galaxies can appear red not only because they are the result of old and passively evolving stars. It has been shown, in fact, that the dust in star-forming galaxies can absorb the ultra-violet (UV) light of the young stars and re-emit it to longer wavelengths, typically in the infra-red region (IR) (Stiavelli et al., 2001; Franx et al., 2003). This class of objects, named Distant Red Galaxies - DRGs - would then escape from the classical dropout selection of Lyman Break Galaxies - LBG (Steidel et al., 1996, 1998). Furthermore, the DRGs revealed to be more massive, older and dustier than the LBG (van Dokkum et al., 2004; Labbé et al., 2005), providing evidence for the existence of a number of massive and evolved galaxies when the universe was still as young as 2-3Gyr.

It is a well known fact that galaxies do not reside in isolated environments, but that their locations constitute what is called the large scale structure of the Universe (see e.g. Springel, Frenk, & White 2006). When considering galaxies in their *environment*, there exists another important correlation between the intrinsic properties of the galaxy population, which is the so called morphology-density

relation. The pioneering works by Oemler (1974) and Dressler (1980) showed that star-forming galaxies preferentially reside in low-density environments, while inactive elliptical galaxies are found in higher density regions. The physical origin of this segregation is still unclear; in particular it is still unknown if the morphology-density relation generates at the time of formation of the galaxy (the so-called *nature* hypothesis) or if it is the result of an evolution driven by the density field (the *nurture* hypothesis). There are three main processes identified for the raise of this relation (Kauffmann et al., 2004). First, mergers or tidal interactions can destroy galactic disks, thus converting spiral star forming galaxies into bulge-dominated quiescent elliptical galaxies. A second factor is the interaction of galaxies with the dense intra-cluster gas, which can remove the interstellar medium of the galaxy, reducing thus the star formation. Finally, gas cooling processes strongly depend on the environment (White & Frenk, 1991; Birnboim & Dekel, 2003).

Recently Peng et al. (2010) have shown that the red sequence in the CMD could be the result of two independent quenching mechanisms, one dependent on the mass and the other on the environment, at least up to  $z \simeq 1$ . While the effect of the environment would be to act only once, mass quenching would rather be a continuous mechanism. The observed shape of the Schechter mass function then would imply a proportionality between the star formation rate (SFR) and the quenching rate of star-forming galaxies. This, in turn, would explain the double Schechter shape in the mass function of early type galaxies; in particular the mass quenching mechanism would be the responsible for the exponential cut-off at high mass, while the environment would be responsible for the lower mass component. This mechanism could be active since earlier times, as other determinations of the mass functions for  $z \lesssim 4$  show that it can be well described by the Schechter form (Fontana et al., 2006; Marchesini et al., 2009).

The stellar mass function (SMF) and its proxy, the luminosity function (LF), together with the star formation rate (SFR) as a function of mass, are a primer test bench for the current knowledge on galaxy formation. The availability of wide area surveys of the local universe and of deep surveys have allowed to draw the star formation history (SFH) up to  $z \simeq 7$  (Madau et al., 1996; Hopkins, 2004; Hopkins & Beacom, 2006), showing that the SFR is characterized by an increase

to  $z = 1$ , followed by a stationary period extending to  $z = 3$  and a subsequent rapid decrease to  $z = 7$ .

Direct SFR measurements are quite challenging at high redshift, particularly at the faint end of the galaxy luminosity function (Wang et al., 2009). On the other hand, individual stellar cataclysms as those seen in long-duration gamma-ray bursts (GRBs) triggered by the death of massive stars (Hjorth et al., 2003; Stanek et al., 2003), provide a complementary technique for measuring the SFR. The high intrinsic luminosities of GRBs (Ciardi & Loeb, 2000; Lamb & Reichart, 2000; Bromm & Loeb, 2002; Gou et al., 2004) make them good candidates as high-redshift universe probes (the farthest GRB to date is GRB 090429B at  $z = 9.4$  Cucchiara et al. 2011), in particular for the SFH (Totani, 1997; Wijers et al., 1998), potentially to higher redshifts than allowed by galaxies alone. Furthermore, GRBs are starting to become a tool to study the metallicity and dust content of normal galaxies at high- $z$  (Campana et al., 2007), and to probe the small-scale power spectrum of density fluctuations (Mesinger, Perna, & Haiman, 2005).

### 1.2.2 Modelling

An orthogonal approach for the understanding of the mechanisms of galaxy formation and evolution are the results from the *Semi-Analytic Models* (SAMS - see Baugh 2006 for a review). This approach consists in using the results from the well known N-body simulations of structure formation in dark matter halos - driven only by the gravitational potential and combining them with observational (analytic) relations describing the physical processes which govern the baryonic matter, attempting to reproduce the evolution of the statistical properties of the galaxy population with cosmic time by refining the values for a minimal set of fundamental parameters. As such, it can probably not be considered as a pure theoretical framework, but rather a tool allowing to fine tune the assumptions on the set of processes involved (Croton et al., 2006; Somerville et al., 2008). However, SAMs allow to describe (and *predict*) the complete star formation history of a galaxy, taking into account all mergers between the progenitors of the galaxy, star formation in bursts triggered by mergers and quiescent star formation in galactic disk. The star formation history of each galaxy is then supplemented by stellar population synthesis models, allowing to generate the stellar population

for the whole galaxy and, finally its spectral energy distribution (Bruzual A. & Charlot, 1993; Bruzual & Charlot, 2003; Fioc & Rocca-Volmerange, 1999).

Currently the semi-analytic models can reproduce quite well the faint-end slope of the SMF and LF in the optical bands with inclusion of feedback mechanisms like supernova winds and the photo-ionizing background (Somerville & Primack, 1999; Croton et al., 2006). Today the problem has shifted to the reproduction of the break and the bright-end of the SMF and LF.

Additionally, there is still a number of open questions. The prediction of the number of satellite of galaxies like the Milky Way is still one order of magnitude higher than what observed (Power et al., 2003; Moore et al., 1999). The zero point of the Tully-Fisher relation (i.e. the correlation between the rotational speed and the luminosity of spiral galaxies) has still not been reproduced, as the simulated galaxies are probably either too compact or contain too much mass. Analogously, although SAMs can reproduce the local fundamental plane of elliptical galaxies (Almeida, Baugh, & Lacey, 2007), these models are not able to reproduce the evolution of the zero-point of this plane. Although the abundances of the  $\alpha$ -elements (O, Mg, Si, S, Ca and Ti) are reproduced, the trend of  $\alpha$ /Fe ratio as a function of the velocity dispersion for elliptical galaxies suffers from an incorrect slope sign respect to the measured quantity (Nagashima et al., 2005). The availability of high- $z$  data allows now the models to compare their predictions over a wide range of redshift. While on one side models show that they can reproduce the number counts of galaxies (including massive ones) at high redshift, it is not clear if the same models are able to reproduce the local LF and SMF (Baugh, 2006; Granato et al., 2004; Trenti et al., 2010).

The study of the properties of the Universe as a whole requires observations of a significant part of the sky, which generally goes under the term *survey*. The data acquisition phase is only the beginning. Extracting as much information as possible, and in the most reliable way, from the images is the following necessary step. In the following sections we will briefly describe the issues involved in the detection of objects in astronomical surveys.

## 1.3 Detection limits

---

When analyzing any astronomical image, we are faced with the fact that the signal-to-noise ratio (SNR) of the objects does depend on the total flux we can recover from it: bright sources will generally have a high SNR, while the fainter the sources the lower the SNR will be. This leads to the identification of a *detection limit* which depends on the flux. However, we might be tempted to think that this limit is a pure matter of exposure time. If we had increased by a factor of e. g. 10 or 100 the exposure time, under that nice photometric sky we had during our last observing run, we could have ended up with much fainter objects in our images. Unfortunately, this is not exactly the case: for each telescope and instrument combination there exists a threshold for the exposure time above which it becomes unsuitable from the time budget point of view to extend the exposure time, as the SNR will only show very little increase. This threshold can not univocally be defined once for all, as it depends on several factors. In the next section we will try to show why such a detection limit exists.

### 1.3.1 Why a detection limit exists

A convenient parameter useful to express how well a given source has been observed is the signal-to-noise ratio (SNR).

The generalized expression to estimate the SNR as a function of the flux collected at the telescope, in the case of a point-like source, can be written as:

$$SNR = \frac{R_{obj} \cdot t}{\sqrt{R_{obj} \cdot t + readnoise^2 + P_{dark} \cdot t + P_{sky} \cdot t + P_{back} \cdot t}} \quad (1.14)$$

where  $R_{obj}$  is the object count rate,  $readnoise$  is the read-out noise associated to the electronics of the CCD,  $P_{dark}$  is the dark current rate,  $P_{sky}$  is the sky count rate,  $P_{back}$  is the count rate of any other source which may lay in the background and  $t$  is the time.

For our purposes, we will neglect  $readnoise$ ,  $P_{dark}$  and  $P_{back}$ . Equation 3.4

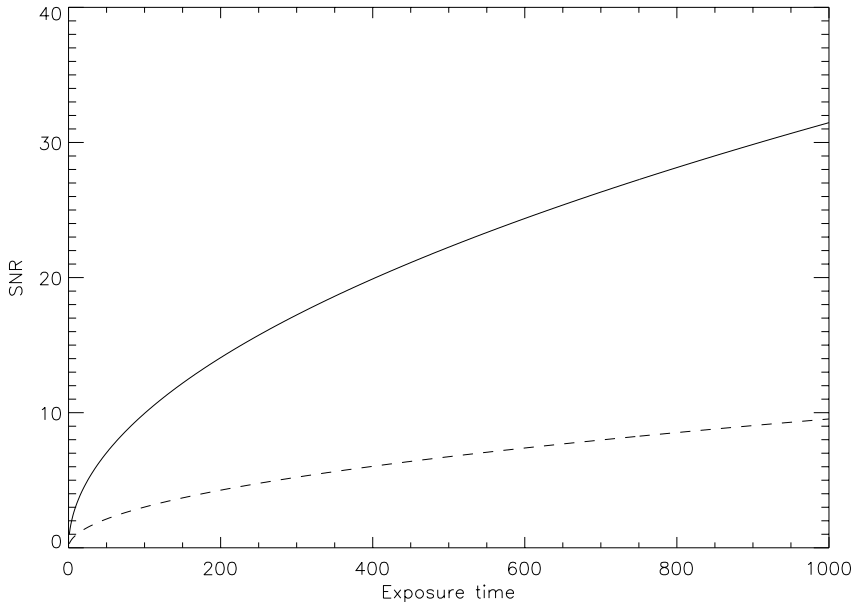


**Figure 1.1:** Signal-to-noise ratio for the background limited regime (dashed line) and for the photon limited regime (solid line).

then becomes:

$$SNR = \frac{\sqrt{R_{obj} \cdot t}}{\sqrt{1 + \frac{P_{sky}}{R_{obj}}}} \quad (1.15)$$

We can identify two distinct regimes, depending on the ratio between  $R_{obj}$  and  $P_{sky}$ . For  $R_{obj} \gg P_{sky}$  we are in the *photon limited* regime: the SNR in Eq. 1.15 can be approximated to  $SNR \simeq \sqrt{R_{obj} \cdot t}$ , i.e. it only depends on the photons from the source, other than on the exposure time.

For  $R_{obj} \ll P_{sky}$ , instead, we are in the so-called *background-limited* case, where the total signal is dominated by the background. Equation 1.15 then becomes  $SNR \simeq R_{obj} \cdot \sqrt{t/P_{sky}}$ : in this case the SNR no more depends only on the signal from the source, but there is also an inverse dependency on the background value, damping the effective SNR.

The two regimes are graphically presented in Figure 1.1. The two curves were

obtained for a source with the same  $R_{obj}$ , but with  $P_{sky}$  differing by 4 orders of magnitude, equivalent then to 10 mag. This is similar to the difference between observations in the optical region, where the sky brightness is  $\approx 25$  mag, and observations in the near infra-red (NIR), where the sky is much brighter, being  $\approx 15$  mag. In particular this means that, while in the optical the observations exit from the background limited region quite soon, all NIR observations (with the exception of the very brightest objects) are always done in the background limited regime. In order to improve the detection limits in NIR observations, astronomers have developed a different observing technique, presented in Sect. 6.4.2.

## 1.4 Observational selection effects

---

A deep look into the universe, as can be a cosmological survey, can lead to discordant results on the nature of the galaxy population and its evolution with cosmic time when selection effects presented in this section have not properly been taken into account.

### 1.4.1 Flux selection

The relationship between apparent magnitude and absolute magnitude can be written as:

$$M = m - 25 - 5 \log D_L(z) - 2.5 \log k(z) \quad (1.16)$$

where  $M$  is the absolute magnitude,  $m$  is the apparent magnitude,  $D_L(z)$  is the luminosity distance expressed in Mpc and  $k(z)$  is the K-correction. Equation 1.16 is only correct in the limit where the apparent magnitude,  $m$ , is an accurate measure of the total flux, regardless of redshift or morphological type. More typically, however, the apparent magnitude that is used is either an isophotal magnitude (see, e.g. Lilly et al. 1995; Ellis et al. 1996; Lin et al. 1996), a total magnitude measured within some multiple of the isophotal area (Small, Sargent, & Hamilton, 1997), a modified Kron (1980) magnitude measured within an aperture whose size is determined by the first moment radius of the light visible above some limiting isophote (Yee, Ellingson, & Carlberg, 1996; Lin et al., 1997) or, more rarely, an aperture magnitude (Gardner et al., 1996; Glazebrook et al., 1994).

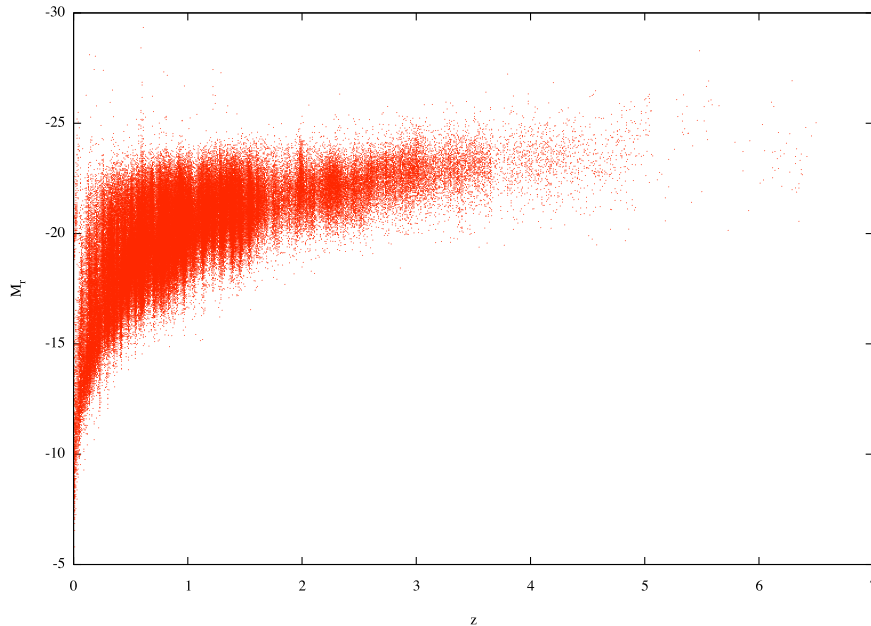


**Figure 1.2:** Selection effect in a flux-limited sample: this plot shows the absolute magnitude in the Sloan  $r'$  filter from ALHAMBRA preliminary data as a function of redshift. The faintest absolute magnitude at a given redshift grows with redshift.

The detection algorithm in galaxy surveys is usually based on a threshold of surface brightness  $S_L$  in conjunction with a minimum object area  $A_{min}$ . A galaxy is then detected when the total area of connected image pixels that lie above  $S_L$  is greater than  $A_{min}$ , and integration of surface brightness over the image area defines its apparent isophotal magnitude.

There is however a mismatch between how the data is taken and the underlying theoretical framework, mismatch becoming progressively more serious as one goes to fainter magnitudes. In order to maintain an internal consistency between observations and theory, it is then necessary to evaluate and apply some kind of correction. However, since these corrections depend on the cosmology, it needs a recursive procedure to determine the cosmological parameters from the corrected data.

The detection and selection effects inherent to faint observations are properly formulated as a function of three major factors:

1. observational conditions;
2. intrinsic properties of the objects;
3. cosmological parameters

For an isophotal magnitude measured within a limiting isophote,  $m_{lim}$ , some fraction of the light is lost outside the outer isophote. The fraction of detected light,  $f(z)$ , depends upon both intrinsic properties of the galaxy (such as the intrinsic central surface brightness,  $\mu_0$ , the true absolute magnitude,  $M$ , and the two-dimensional shape of the galaxy in the absence of seeing [i.e., its light profile]), as well as observational parameters of the survey, such as the limiting isophote,  $m_{lim}$ , and the point-spread function. The fraction of detected light also depends upon the redshift of the observed galaxy. As a galaxy moves to higher redshifts, it suffers two effects that rapidly decrease the fraction of light detected within a fixed isophotal limit. First, at large enough redshifts, it may happen that the galaxy appears small compared to the point-spread function (PSF) and begins to lose light beyond the limiting isophote due to the rapid falloff in the PSF with radius. Second, the apparent surface brightness drops off as  $(1+z)^4$  because of the difference in the redshift dependences of the angular diameter and luminosity distances. As the drop in apparent surface brightness becomes significant (a factor of 2 at  $z=0.2$ ), a larger fraction of the light from the galaxy falls below the limiting isophote, again increasing the fraction of lost light. The direction of both of these effects is for the apparent magnitude to drop off more quickly with distance than predicted by equation 1.16 (Yoshii, 1993).

We can then identify two major consequences from surface brightness selection effects (see for instance Lilly et al. 1995):

1. Reduce the fraction of light inside an isophote;
2. Reduce the overall number of galaxies detected in the field.

The first effect is crucial not only because it leads to underestimate the total light emitted by the source, with consequent underestimate of the physical observable associated to it, as can be the total mass of the galaxy or the luminosity function of the sample. The dependence of the isophotal boundary on the

wavelength, and hence of the recovered magnitude, has effects at the time of computing photometric redshifts, as these technique is based on the template fitting on a series of colors deduced from the photometry.

Additionally, this effect causes diameter- or magnitude-limited catalogs to mainly contain galaxies with a narrow range in central surface brightnesses. In other words, they will be biased and incomplete for galaxies with central surface brightnesses other than the optimum value.

An historical example may be taken from Freeman (1970) who noted that 28 galaxies out of his sample of 36 had disks with central surface brightnesses in the range  $\mu_B = 21.65 \pm 0.3 \text{ mag arcsec}^{-2}$ . Taken at face-value, this result had important implications for theories of galaxy structure and evolution. Freeman's law requires that either all galaxies have identical mass surface densities coupled with just a small spread in their mass- to-light ratios or that star formation history, age, angular momentum and mass all conspire to produce a constant central surface brightness.

Disney (1976) showed that selection effects could cause Freeman's law and suggested that there might be many galaxies of both high and low surface brightness hidden in the night sky.

### 1.4.2 Spatial selection

So far we have considered issues regarding limits in flux. However, it may be also important to characterize the completeness of the sources as a function of position on the detector. We will only mention it here, for completeness sake.

Two are the main effects which can prevent from detecting objects whose flux would otherwise be above the threshold of detectability. On one hand, bright and/or extended objects (as can be the wing of the light profile of a very bright star) may hide other more compact sources. On the other hand, physical defects on the CCD sensor can preclude some regions of the observed area from being properly imaged.

For spectroscopic observations the main cause of incompleteness arises as consequence either of the limited number of slits which can be created on the mask or by *collisions* between the optical fibers when too close to each other. However, in the recent years, spectrographs capable of recording the spectra of light falling on each single pixel (*integral field units*) are being built.

This kind of selection is especially important for analysis of e.g. the cosmological large scale structure, where the two-point correlation function relies on the fact that the sample used is spatially (other than photometrically) complete.

### 1.4.3 False detections

One effect that goes in the opposite direction from the photometric and spatial selection is the one generated by false detections. As the name suggests, this effect consists in the creation of sources in a photometric catalogue which do not have a physical counterpart. The probability of generating false sources grows as we approach the detection limit. In fact, in this case, some of the oscillations which are produced by the gaussian noise can be interpreted by the software as genuine sources. The choice of the parameters involved in the object detection phase of the catalogue generation is then of critical importance in order to minimize such effects.

Nonetheless, this effect is equally important at the time of estimating the completeness of the generated catalogues both in space and in flux.

The measurement and correction of such an effect is generally done on a statistical basis. If deeper data covering at least a section of the whole observed field exist, these are used to directly compare each object detected in the two catalogs and identify those sources which appear unphysical. Instead, when no such data is available, Monte Carlo methods are used.

## 1.5 Multi-wavelength surveys

---

The developments in computer science during the last 30 years have put in the hands of astronomers powerful tools for the analysis of astrophysical and cosmological processes. The introduction of CCD devices has allowed not only to observe fainter objects, but, thanks to the linear response, to do in a more reliable way and for a high number of objects simultaneously. On the other side, the possibility to handle the collected data in a digital manner has enormously simplified some common tasks, like the creation of object catalogues. For example, it has become easy and fast to match the same object on different frames.

The above framework is well represented by astronomical multi-wavelength

surveys, which consist in imaging a wide region of sky (although *wide* takes different values depending on the final main scientific aim of the survey and on the practical limits involved) using a set of photometric filters. The extension of the observed region is chosen in order to minimize the effects of variance of the distinct classes of observed objects in the final sample. The choice of the filter set is generally the result of a trade-off between the accuracy desired to recover the spectral energy distribution of the sources, or other fundamental parameter, and the total exposure time required to reach the needed limiting magnitude.

### 1.5.1 Cosmological Photometric surveys

In cosmology, the development of photometric redshift techniques has increased the power and, consequently, the diffusion, of the multi-wavelength surveys, as they allow to recover the redshift and the spectral energy distribution of objects which would otherwise be inaccessible through standard spectroscopic surveys, due to the shallower limiting magnitude available with this kind of instrument and to the fact that it is generally not possible to obtain the spectra of all the objects in a given field of view.

In Figure 1.3 we show a comparison between the area and the depth of some cosmological surveys.

In the following section we will review the some among the most important cosmological photometric surveys.

#### Hubble Deep Field and EGS

The Hubble Deep Field<sup>1</sup> (Williams et al., 1996; Ferguson, Dickinson, & Williams, 2000) is the result of imaging an undistinguished (i.e. avoiding known bright sources from the X-rays to the radio bands) field at high Galactic latitude ( $E(B - V) < 0.01$ ) in the northern sky, in four bands (F300W, F450W, F606W and F814W, corresponding approximately to the U, B, R and I filters), using the Wide Field Planetary Camera 2 onboard the Hubble Space Telescope and covering a region of about  $2.5 \times 2.5$  arcmin<sup>2</sup>. The  $10\sigma$  AB limiting magnitude in the original catalogue reached 26.98, 27.86, 28.21 and 27.60 respectively in the four bands, providing photometric data on about 3000 galaxies. The HDF data

---

<sup>1</sup><http://www.stsci.edu/ftp/science/hdf/hdf.html>

	Survey Name	AB Mag limit	Area (deg <sup>2</sup> )	Spectral Range	Resolution
Wide Band Photometric	2MASS	K 16.1	41252	JHK	4
	SDSS	21.3	8000	ugriz	6
	UKIDSS (LAS)	K 20.2	4000	JHK	4
	CFHTLS (wide shallow)	23.0	1300	gri	6
	CFHTLS (wide synoptic)	24.5	172	ugriz	6
	CFHT12K/ESO (VIRMOS)	25.0	16	UBVR <sub>1</sub> I <sub>1</sub> K <sup>1</sup>	5
	CFHTLS (deep synoptic)	26.5	4	ugriz	6
	LCIRS	H 21.9	1.1	BVR <sub>1</sub> I <sub>1</sub> Z <sup>1</sup> JHK	5
	MUNICS	23.0	0.6	BVR <sub>1</sub> I <sub>1</sub> K	5
	EIS Deep	26.0	0.06	UBVR <sub>1</sub> I <sub>1</sub> JHK	5
Medium Band Photometric	ALHAMBRA	25.0	4	3500-22000	25
	COMBO-17	24.0	1	3650-9140	25 (uneven)
	CADIS	23.0	0.20	4000-22000	25 (uneven)
	SDSS	17.4	8000	3800-9200	1800
Spectroscopic	2dFGRS	18.5	2000	3700-8000	950
	VVDS	22.5	16	3800-9000	250
	DEEP2	23.1	3.5	6000-9500	4000

Table 1.1: Main parameters for some of the main cosmological surveys and plotted in Figure 1.3

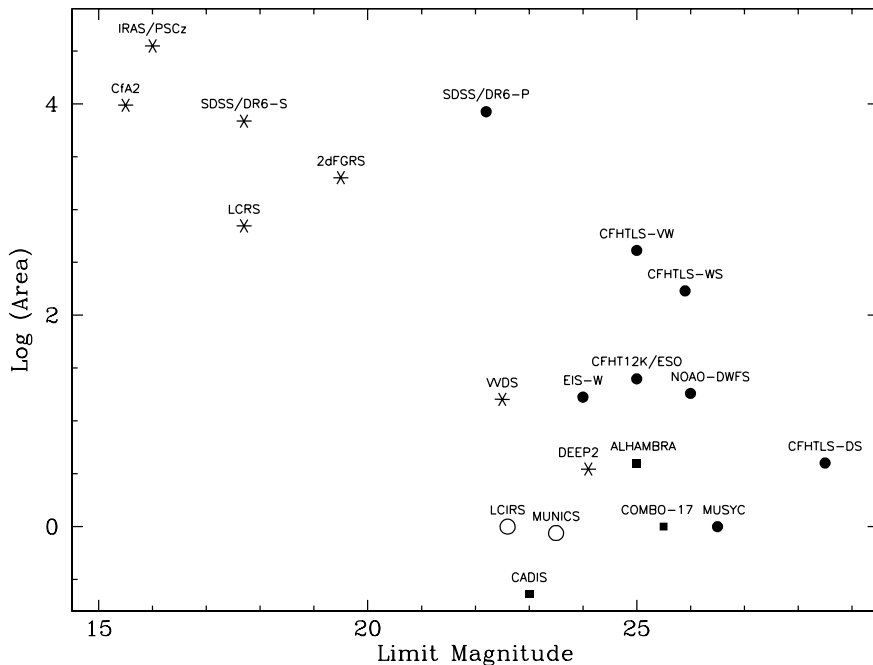


**Figure 1.3:** Covered area vs. depth for cosmological surveys. Asterisks indicate spectroscopic surveys, circles photometric and squares medium-narrow-band-like surveys (Moles et al., 2008).

avored the development of photometric redshift techniques, which until then had been used only occasionally.

Three adjacent fields, located in the southern hemisphere, were observed in 1998 as part of the Hubble Deep Field South. This time, the set of optical filters was accompanied by deep near-infrared images taken with the NICMOS instrument and by spectroscopic observations with the Space Telescope Imaging Spectrograph (STIS).

The HDF-S field was later observed with the Chandra X-ray telescope. After these observations, this field, named Chandra Deep Field South (CDF-S)<sup>2</sup>

<sup>2</sup>[http://www.eso.org/~vmainier/cdfs\\_pub/](http://www.eso.org/~vmainier/cdfs_pub/)

has become the center of one the most comprehensive multi-wavelength campaign ever carried out with ground-based and space observatories.

The Great Observatories Origins Deep Survey (GOODS)<sup>3</sup> is a project developed upon existing or ongoing surveys from space and ground based facilities, including NASAs Great Observatories (HST, Chandra and Spitzer). The program targets two fields, each  $10' \times 16'$ , around the Hubble Deep Field North (HDFN) and the Chandra Deep Field South (CDFS).

An evolution of the Hubble Deep Fields is the Extended Groth Strip (EGS)<sup>4</sup> program, covering an area of  $70 \times 10$  arcmin<sup>2</sup> and with a depth similar to the HDF, although in a single HST band. This was possible thanks to the increased sensitivity of the new HST-ACS camera. This region of sky was then observed in the framework of an international effort with a number of instruments covering a large region of the electromagnetic spectrum. These instruments include Chandra, GALEX, Hubble, Keck, CFHT, MMT, Subaru, Palomar, Spitzer and VLA. Figure 1.4 shows the coverage of the EGS by the programs from the major telescopes.

### **Combo-17**

The COMBO-17 survey<sup>5</sup> (Wolf et al., 2001, 2003) has imaged one square degree of sky, including the Chandra Deep Field South (CDFS), in 17 optical filters using the Wide Field Imager at the MPG/ESO 2.2-m telescope at La Silla, Chile. The filter set contains five broad-band filters (UBVRI) and 12 medium-band filters ranging from 400 to 930 nm in wavelength coverage.

The produced catalogue contains  $\approx 200000$  objects down to  $R \approx 25$ mag at a  $5\sigma$  limit, with  $\approx 25000$  galaxies and  $\approx 300$  QSOs with redshift errors of  $\Delta z/(1+z) \approx 0.02$ .

Figure 1.5 shows the efficiencies of the 17 filters adopted for by the Combo-17 survey.

---

<sup>3</sup><http://www.stsci.edu/science/goods/>

<sup>4</sup><http://aegis.ucolick.org/>

<sup>5</sup>[http://www.mpia.de/COMBO/combo\\_index.html](http://www.mpia.de/COMBO/combo_index.html)

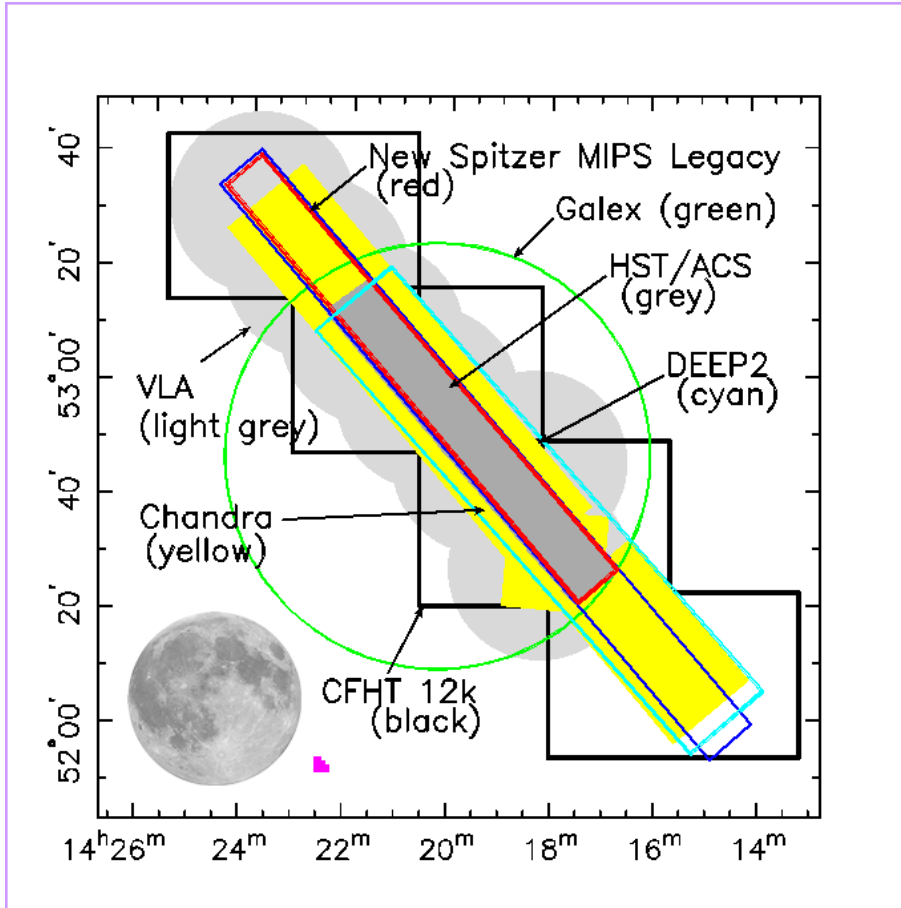


**Figure 1.4:** Coverage of the Extended Groth Strip (EGS) at various wavelengths. On the lower-left corner the size of the moon and of the original HDF (magenta shape) are shown for comparison (image credits: All-wavelength Extended Groth strip International Survey (AEGIS) team).

## SDSS

The Sloan Digital Sky Survey<sup>6</sup> (SDSS - York et al. 2000; Abazajian et al. 2003 and references therein) is a photometric and spectroscopic survey, using a dedicated 2.5 m telescope at Apache Point Observatory in New Mexico, covering more than a quarter of the sky at high Galactic latitude. The telescope uses two instruments.

<sup>6</sup><http://www.sdss.org/>

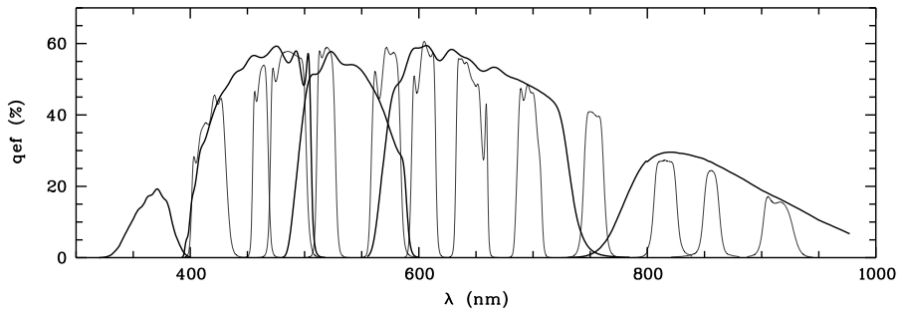


**Figure 1.5:** COMBO-17 filter set: total system efficiencies are shown in the COMBO-17 passbands, including two telescope mirrors, WFI instrument, CCD detector and average La Silla atmosphere (Wolf et al., 2003).

The first is a wide-field imager with 24  $2048 \times 2048$  CCDs on the focal plane with a scale of 0.396 arcsec/pixel that covers the sky in drift-scan mode in five filters in the order r, i, u, z, g. The imaging is done with the telescope tracking great circles at the sidereal rate, allowing to image  $18.75 \text{ deg}^2$  per hour in each of the five filters. The 95% completeness limits of the images are u, g, r, i, z = 22.0, 22.2, 22.2, 21.3, 20.5 respectively.

The photometric catalogs of detected objects are used to identify objects for spectroscopy with the second of the instruments on the telescope: a 640-fibered pair of multi-object double spectrographs, giving coverage from  $3800\text{\AA}$  to  $9200\text{\AA}$  at a resolution of  $\lambda/\Delta\lambda = 2000$ . The latest release (DR7 - Abazajian et al. 2009) includes photometry for more than 350 million objects over an area of  $\approx 12000\text{deg}^2$ , and spectroscopy for  $\approx 1.5$  million objects distributed on an area of  $\approx 10000\text{deg}^2$ .

## ALHAMBRA

The aim of the Advanced Large Homogeneous Area Medium Band Redshift Astronomical (ALHAMBRA) Survey<sup>7</sup> (Moles et al., 2008) is to cover a large-area (4 square degrees) with 20 contiguous, equal width, medium band optical filters from  $3500\text{\AA}$  to  $9700\text{\AA}$ , plus the three standard broad bands, JHKs, in the NIR. The corresponding resolution ( $R \approx 20$ ), the width of the covered field and the limiting

<sup>7</sup><http://alhambra.iaa.es:8080/alhambra/>

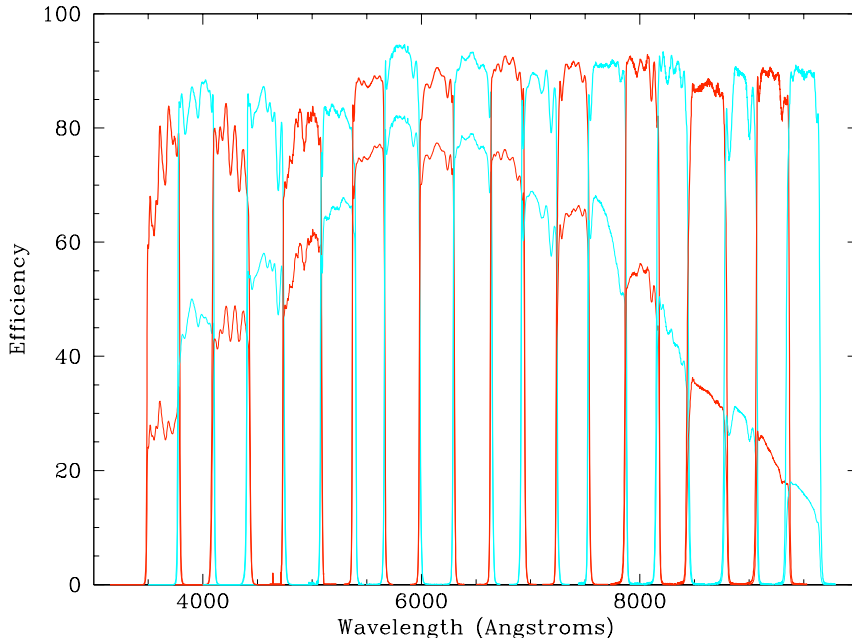


**Figure 1.6:** Transmission curves for one of the optical filter sets for the ALHAMBRA survey as measured in the laboratory. The effective total transmission (lower curve), after taking into account the quantum efficiency of the CCD detector, the atmosphere transmission (at air mass = 1.3), and the reflectivity of the primary mirror of the Calar Alto 3.5 m telescope is also shown (Moles et al., 2008).

magnitude (see Figure 1.3), place the ALHAMBRA Survey halfway in between the traditional imaging and spectroscopic surveys. By design, the ALHAMBRA-Survey will provide precise ( $\Delta z/(1+z) < 0.03$ ) photometric redshifts and spectral energy distribution (SED) classification for  $\geq 6 \times 10^5$  galaxies and AGNs.

**Filter system** The ALHAMBRA optical photometric system was designed to include 20 contiguous, medium-band,  $\text{FWHM} = 310 \text{ \AA}$ , square-like shaped filters with marginal overlapping in  $\lambda$ , covering the complete optical range from 3500 to 9700  $\text{\AA}$ . With this configuration it is possible to accurately determine the SED and  $z$  even for faint objects and to detect rather faint emission lines. The ALHAMBRA  $3\sigma$  rest-frame detection limits for a typical  $\text{AB} \approx 23$  galaxy are

$\text{EW}(H\alpha) > 28 \text{ \AA}$  out to  $z \approx 0.45$ , and  $\text{EW}(OII) > 16 \text{ \AA}$  out to  $z \approx 1.55$ . Furthermore, ALHAMBRA expects to detect  $\approx 50\%$  of the  $H\alpha$  emitters at  $z \approx 0.25$  and  $\approx 80\%$  of the  $OII$  objects at  $z \approx 1.2$  (Benítez et al., 2009).

Figure 1.6 shows the transmission curves of the filters both as measured in the laboratory and after taking into account the CCD quantum efficiency, atmospheric transmission and reflectivity of the telescope main mirror.

**Field selection** Although the Universe is in principle homogeneous and isotropic on large scales, astronomical objects are clustered on the sky on different scales. The clustering signature contains a wealth of information about the structure formation process. A survey wanting to study clustering needs to probe as many scales as possible. In particular, searching contiguous areas is important to cover smoothly the smallest scales where the signal is stronger and obtain an optimally-shaped window function. On the other hand, measuring a population of a certain volume density is a Poissonian process with an associated variance; in order to reduce that variance, it is necessary to sample independent volumes of space. This means that a compromise is necessary between probing contiguous areas, which assure a wide enough field, and independent areas, necessary to reduce the Poisson variance.

The final selection of the fields was based on the following points:

- low extinction;
- no (or few) known bright sources;
- high galactic latitude;
- overlap with other surveys and/or observations in other wavelengths

The selected fields are presented in table 1.2.

**The cameras** The twenty optical filters are onboard the LAICA camera, installed at prime focus of the 3.5m telescope in Calar Alto - Spain.

This camera uses 4 CCDs with  $4096 \times 4096$  pixels each with a pixel size of 15 microns. The arrangement of the four CCDs is shown in Figure 1.7, while Table 1.3 gives the main parameters of this camera. The spacing between the CCDs is

Field	RA (J2000)	Dec (J2000)
ALHAMBRA-1	00 29 46.0	+05 25 28
ALHAMBRA-2	01 30 16.0	+04 15 40
ALHAMBRA-3/SDSS	09 16 20.0	+46 02 20
ALHAMBRA-4/COSMOS	10 00 28.6	+02 12 21
ALHAMBRA-5/HDF-N	12 35 00.0	+61 57 00
ALHAMBRA-6/GROTH	14 16 38.0	+52 25 05
ALHAMBRA-7/ELAIS-N1	16 12 10.0	+54 30 00
ALHAMBRA-8/SDSS	23 45 50.0	+15 34 50

**Table 1.2:** ALHAMBRA Survey selected fields.

Telescope	3.5m Calar Alto
Field	$4 \times 15' \times 15'$
Detector	$4 \times 4096 \times 4096$ CCDs
Scale	0.225 pixel/arcsec

**Table 1.3:** LAICA optical camera main properties.

equal to the size of a single CCD minus an overlap of about 100 arcsecs which can be useful for astrometric and photometric calibration purposes.

The design of the camera with 4 independent CCDs has the advantage of allowing to use 4 small filters instead of a big one, with subsequent cost benefits; however, the use of different optical elements gives raise to an increased optical distortion. This problem needs to be accounted for during the reduction process.

Given the actual LAICA field of view, in order to obtain the desired  $2 \times 1 \text{ deg} \times 0.25 \text{ deg}$ , two contiguous exposures are necessary.

For the NIR images, Omega2000 has been adopted. Similarly to LAICA, also this camera is installed at the prime focus of the 3.5m telescope in Calar Alto.

The Omega2000 camera contains a focal plane array of type HAWAII-2 with  $2048 \times 2048$  pixels, each  $18 \mu\text{m}$  wide (see Table 1.4 for its basic properties). Given that its field of view is the same as LAICA, this means that with one pointing it is possible to cover in the IR the same field of one CCD of the optical frames. It is sensitive from about 850 to 2500 nm.

Considering the main goal of the project, the mean sky conditions of the

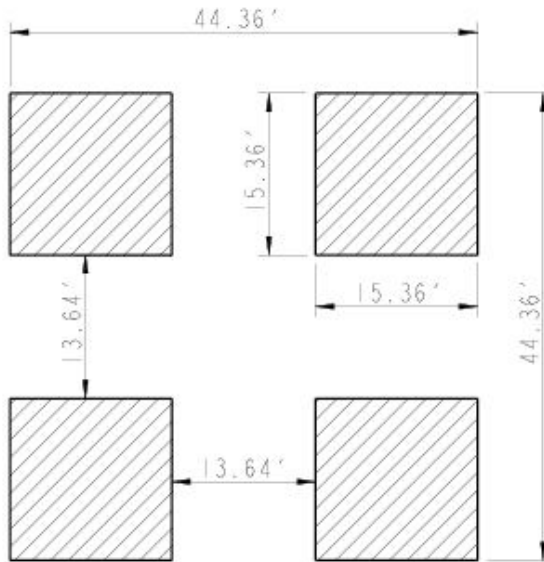


**Figure 1.7:** Layout of the 4 CCDs in LAICA.

Telescope	3.5m Calar Alto
Field	15.4' $\times$ 15.4'
Detector	2048 $\times$ 2048 HAWAII-2 array
Scale	0.45 pixel/arcsec

**Table 1.4:**  $\Omega$ 2000 optical camera main properties.

observing site and the characteristics of the adopted instruments, the requirement for the seeing has been fixed to 1.2 arcsec for LAICA and 1.4 arcsec for the NIR.

## 1.6 Aim of this thesis

In this work we explored the faint end region of a cosmological survey, both on the photometric and on the spectroscopic point of view. On the photometric side, in fact, we implemented two independent methods to estimate the completeness limits of galaxies as a function of intrinsic properties like the absolute magnitude, the spectral energy distribution and the redshift, applying it to the ALHAMBRA

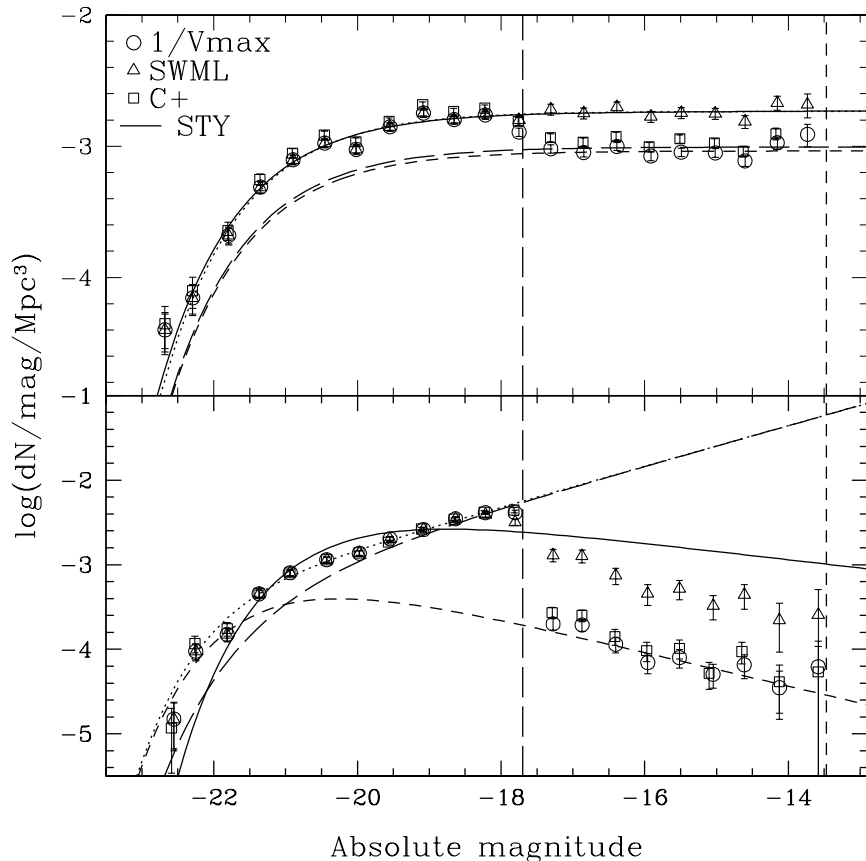


**Figure 1.8:** Estimates of bias due to incompleteness in the computation of the LF using different methods to measure the LF on the mock catalogue represented by the dotted line (Ilbert et al., 2004). In the upper panel the SWML and STYML measurement refer to the case of object classes whose LF have an intrinsic similar slope, while in the lower panel the case for a population from a LF with a flatter slope than the global LF is presented. The dotted line represents the input global LF, result of the contribution of a late-type population LF (long-dashed line) and an early-type population LF (short-dashed line), while the solid line marks the LF recovered using the STY method. Vertical long and short dashed lines mark the input limiting magnitude for the late and early type respectively.

survey.

When dealing with flux limited catalogues one has to face the selection ef-

fect produced by the non uniformity of detection of objects in a given observing band and for a given redshift. This selection is due to two reasons. First, the k-corrections needed to compute the absolute magnitudes depend on the galaxy spectral type, so that at a given redshift and for the same limit in apparent magnitude we will have, in general, different luminosity limits. The second source of selection is the difference in brightness profile and physical size of galaxies as a function of their spectral class. This translates to different apparent limiting magnitudes for different classes of objects on survey frames. A possible approach to overcome this selection problem would be to estimate this bias through simulations (see Ilbert et al. 2004). Another possibility would instead be to derive accurate completeness limits of the different galaxy populations as a function of their morphological type and redshift (acting both on the K-corrections and on the apparent size of the galaxy), and introducing them when computing the LF.

As shown by Ilbert et al. (2004), ignoring the completeness limits of a catalogue introduces a bias at the time of measuring the global LF which depends of the method adopted to compute the LF itself. For example, when using the  $V_{max}$  method, the faint end of the LF will coincide with the LF of those classes whose data is complete in the chosen absolute magnitude and redshift range, leading to an under-estimate of the global LF. When using the methods explicitly based on maximum likelihood (like the SWML or the STYML) the goodness of the recovery depends on the shapes of the LF of each class. When the shapes are similar, then the computed global LF will match the real underlying distribution. Otherwise, the faint end will be either over- or under- estimated, depending on whether the slope of the LF of the types of objects is steeper or flatter than the LF of the incomplete populations (see Figure 1.8).

The large number of filters used to observe the same field and the method adopted by ALHAMBRA to detect objects makes the definition and determination of completeness an even more delicate task.

Our results on the completeness of the LF will finally be applied to a preliminary catalogue from the ALHAMBRA Survey to compute the global and type-dependent LF of field galaxies.

In the spectroscopic branch, we developed a novel technique for the determination of basic intrinsic observables from very low signal-to-noise data, which make

difficult not only the measurement of the value itself, but also to derive a robust estimate of the associated errors. Our method was implemented on the measurement of the redshift, one of the most basic parameters for an extra-galactic object, for the most distant Gamma-Ray Burst (GRB) known at the time of the implementation of the method.

### 1.6.1 Existing methods for the detection completeness measurement

As already discussed in the previous section, cosmological surveys can be classified in a first instance into two main groups, photometric and spectroscopic, depending on whether the main output is a set of photometric points for each object in the set of filters characterizing the survey, or if a spectrum is observed for each object.

This classification reflects also on the methods adopted for measuring the fraction of objects which actually have undergone the measurement procedure. In the following, we will describe them in the context of their parent surveys in which were first developed.

As a general standpoint, spectroscopic surveys being less deep than a photometric surveys with the same amount of exposure time, usually adopt an *indirect* procedure for estimating the completeness. In these cases, in fact, the completeness is computed by comparing the faintest objects whose spectrum has been acquired to the objects in a photometric catalogue covering the same area. The 2 degree Field Galaxy Redshift Survey (2dFGRS - Colless et al. 2001) was designed to obtain a spectrum of all objects brighter than  $b_J = 19.5$ , based on the photometric plates by Maddox et al. (1990). Similarly, its *twin* survey, the Sloan Digital Sky Survey (SDSS), took spectra of objects down to  $r = 17.77$  for the main sample, and  $r = 19.5$  for the Luminous Red Galaxies sample, based on photometric data previously acquired by the same telescope (York et al., 2000). When the spectroscopy is instead deeper than the existing photometric catalogues of the covered region of sky, the solution is to perform deep imaging of the same area (or of a consistent sub-region), as done for the VVDS project (McCracken et al., 2003), so that to fall into the previous case.

Given the usual higher depth, photometric surveys can seldom rely on deeper data (and, in any case, there would always be the problem for the deepest survey), so that a different procedure is needed. Nevertheless, surveys like the SDSS and 2MASS obtain their completeness levels by comparing with the existing photometric surveys COMBO17 (Abazajian et al., 2003) and SDSS itself (McIntosh et al., 2006), respectively. The case for 2MASS is actually more detailed. For extended sources the results from the comparison with SDSS data is complemented by the magnitude limit obtained from number counts. The weak point of this approach is that it is difficult to disentangle the effects of an intrinsic drop of the population from those of the selection effects from the magnitude limited sample. Completeness for point-like sources, instead, was measured from the analysis of the repeated observations of 2MASS calibration fields, linking the percentage of detection of each object to its magnitude (Cutri et al., 2003).

However, comparison with existing catalogues generally does not allow to properly recover the completeness measurement as a function of 2 or more intrinsic parameters (like e.g. luminosity and distance). In fact, the selections on the catalogue implied by such method do not guarantee the existence of a sufficiently populated sample for reliably measuring the limit. The proper way appears then to develop an *auto-consistent* method, based only on the survey images and on the tools adopted for the source detection.

The simplest auto-consistent solution consists in adding to a typical image from the survey a number of artificial stars which are then recovered using the same procedure adopted for the reduction of the whole set of frames (e.g. MUSYC - Quadri et al. 2007). This approach however tends to over-estimate the limiting magnitude in the case of diffuse sources, since their surface brightness will be lower than the surface brightness of stars. A more refined approach is then to simulate objects with representative morphologies and magnitudes, inserting them into the images and allowing the reduction pipeline to recover them, as in the case of COSMOS (Capak et al., 2007) and COMBO17 (Wolf et al., 2003).

An even more realistic approach, studied for the first time in this thesis, would adopt real images of objects to be used as templates. The adoption of real images, in comparison to the simulated objects, would then allow to naturally take into account all the problematics linked to the brightness profile of faint objects, which are very complex when fully reproduced by a purely algorithmic approach (e.g.

GALFIT - Peng et al. 2002 or GIM2D Simard et al. 2002).

A completely different approach has been proposed by Rauzy (2001) and later studied by Johnston, Teodoro, & Hendry (2007). This method is based on the statistical analysis of the count of objects in the absolute magnitude-distance modulus (M-Z) plane. Although it has been shown that this method provides completeness limits in agreement with those already published for SDSS, 2dF-GRS and MGC (Johnston, Teodoro, & Hendry, 2007), it has a couple of issues which may limit its applicability. The first is that the computed magnitude limit may present a dependence on the arbitrary width of the box used to compute the statistics in the M-Z plane, although some work has recently been done in this direction (Teodoro, Johnston, & Hendry, 2010). The second point is that this method does not provide any information on the completeness levels around the limit it provides. This fact denies the possibility of applying statistical corrections which would instead allow to reliably use objects with a deeper magnitude limit, as instead done with the Monte Carlo method developed in this thesis.



# Bibliography

- Abazajian K., et al., 2003, *AJ*, 126, 2081
- Abazajian K. N., et al., 2009, *ApJS*, 182, 543
- Almeida C., Baugh C. M., Lacey C. G., 2007, *MNRAS*, 376, 1711
- Baugh C. M., 2006, *RPPh*, 69, 3101
- Bell E. F., et al., 2004, *ApJ*, 608, 752
- Benítez N., et al., 2009, *ApJ*, 692, L5
- Bennett C. L., et al., 2003, *ApJS*, 148, 1
- Birnboim Y., Dekel A., 2003, *MNRAS*, 345, 349
- Blanton M. R., et al., 2003, *ApJ*, 594, 186
- Blanton M. R., Eisenstein D., Hogg D. W., Schlegel D. J., Brinkmann J., 2005, *ApJ*, 629, 143
- Blumenthal G. R., Faber S. M., Primack J. R., Rees M. J., 1984, *Nature*, 311, 517
- Brammer G. B., et al., 2009, *ApJ*, 706, L173
- Bromm V., Loeb A., 2002, *ApJ*, 575, 111
- Bruzual A. G., Charlot S., 1993, *ApJ*, 405, 538
- Bruzual G., Charlot S., 2003, *MNRAS*, 344, 1000
- Campana S., et al., 2007, *ApJ*, 654, L17
- Capak P., et al., 2007, *ApJS*, 172, 99
- Ciardi B., Loeb A., 2000, *ApJ*, 540, 687
- Cole S., et al., 2005, *MNRAS*, 362, 505
- Colless M., et al., 2001, *MNRAS*, 328, 1039

## BIBLIOGRAPHY

---

- Croton D. J., et al., 2006, MNRAS, 365, 11
- Cucchiara A., et al., 2011, ApJ, 736, 7
- Cutri R. M., et al., 2003, <http://www.ipac.caltech.edu/2mass/releases/allsky/doc/>
- Davis M., Efstathiou G., Frenk C. S., White S. D. M., 1985, ApJ, 292, 371
- Disney M. J., 1976, Natur, 263, 573
- Dressler A., 1980, ApJ, 236, 351
- Eisenstein D. J., et al., 2005, ApJ, 633, 560
- Ellis R. S., Colless M., Broadhurst T., Heyl J., Glazebrook K., 1996, MNRAS, 280, 235
- Faber S. M., et al., 2007, ApJ, 665, 265
- Ferguson H. C., Dickinson M., Williams R., 2000, ARA&A, 38, 667
- Fioc M., Rocca-Volmerange B., 1999, astro, arXiv:astro-ph/9912179
- Franx M., et al., 2003, ApJ, 587, L79
- Freedman W. L., et al., 2001, ApJ, 553, 47
- Freeman K. C., 1970, ApJ, 160, 811
- Fontana A., et al., 2006, A&A, 459, 745
- Gardner J. P., Sharples R. M., Carrasco B. E., Frenk C. S., 1996, MNRAS, 282, L1
- Glazebrook K., Peacock J. A., Collins C. A., Miller L., 1994, MNRAS, 266, 65
- Gou L. J., Mészáros P., Abel T., Zhang B., 2004, ApJ, 604, 508
- Granato G. L., De Zotti G., Silva L., Bressan A., Danese L., 2004, ApJ, 600, 580
- Hjorth J., et al., 2003, Natur, 423, 847
- Hopkins A. M., 2004, ApJ, 615, 209

- Hopkins A. M., Beacom J. F., 2006, *ApJ*, 651, 142
- Hubble E. P., 1926, *ApJ*, 64, 321
- Ilbert O., et al., 2004, *MNRAS*, 351, 541
- Johnston R., Teodoro L., Hendry M., 2007, *MNRAS*, 376, 1757
- Kauffmann G., et al., 2003, *MNRAS*, 341, 54
- Kauffmann G., White S. D. M., Heckman T. M., Ménard B., Brinchmann J., Charlot S., Tremonti C., Brinkmann J., 2004, *MNRAS*, 353, 713
- Komatsu E., et al., 2009, *ApJS*, 180, 330
- Kron R. G., 1980, *ApJS*, 43, 305
- Labbé I., et al., 2005, *ApJ*, 624, L81
- Lamb D. Q., Reichart D. E., 2000, *ApJ*, 536, 1
- Lilly S. J., Le Fevre O., Crampton D., Hammer F., Tresse L., 1995, *ApJ*, 455, 50
- Lin H., Kirshner R. P., Shectman S. A., Landy S. D., Oemler A., Tucker D. L., Schechter P. L., 1996, *ApJ*, 464, 60
- Lin H., Yee H. K. C., Carlberg R. G., Ellingson E., 1997, *ApJ*, 475, 494
- Madau P., Ferguson H. C., Dickinson M. E., Giavalisco M., Steidel C. C., Fruchter A., 1996, *MNRAS*, 283, 1388
- Maddox S. J., Efstathiou G., Sutherland W. J., Loveday J., 1990, *MNRAS*, 243, 692
- Marchesini D., van Dokkum P. G., Förster Schreiber N. M., Franx M., Labbé I., Wuyts S., 2009, *ApJ*, 701, 1765
- Masjedi M., et al., 2006, *ApJ*, 644, 54
- McCracken H. J., et al., 2003, *A&A*, 410, 17
- McIntosh D. H., Bell E. F., Weinberg M. D., Katz N., 2006, *MNRAS*, 373, 1321

## BIBLIOGRAPHY

---

- Mesinger A., Perna R., Haiman Z., 2005, *ApJ*, 623, 1
- Mo H., van den Bosch F. C., White S., 2010, *Galaxy Formation and Evolution* - ISBN: 9780521857932
- Moles M., et al., 2008, *AJ*, 136, 1325
- Moore B., Ghigna S., Governato F., Lake G., Quinn T., Stadel J., Tozzi P., 1999, *ApJ*, 524, L19
- Nagashima M., Lacey C. G., Okamoto T., Baugh C. M., Frenk C. S., Cole S., 2005, *MNRAS*, 363, L31
- Oemler A., Jr., 1974, *ApJ*, 194, 1
- Peebles P. J. E., 1982, *ApJ*, 263, L1
- Peng C. Y., Ho L. C., Impey C. D., Rix H.-W., 2002, *AJ*, 124, 266
- Peng Y.-j., et al., 2010, *ApJ*, 721, 193
- Perlmutter S., et al., 1999, *ApJ*, 517, 565
- Power C., Navarro J. F., Jenkins A., Frenk C. S., White S. D. M., Springel V., Stadel J., Quinn T., 2003, *MNRAS*, 338, 14
- Quadri R., et al., 2007, *AJ*, 134, 1103
- Rauzy S., 2001, *MNRAS*, 324, 51
- Renzini A., 2006, *ARA&A*, 44, 141
- Riess A. G., et al., 1998, *AJ*, 116, 1009
- Sandage A., 1995, *deun.book*, 1
- Simard L., et al., 2002, *ApJS*, 142, 1
- Small T. A., Sargent W. L. W., Hamilton D., 1997, *ApJS*, 111, 1
- Smoot G. F., et al., 1992, *ApJ*, 396, L1
- Somerville R. S., Primack J. R., 1999, *MNRAS*, 310, 1087

- Somerville R. S., Hopkins P. F., Cox T. J., Robertson B. E., Hernquist L., 2008, MNRAS, 391, 481
- Spergel D. N., et al., 2003, ApJS, 148, 175
- Spergel D. N., 2005, ASPC, 344, 29
- Springel V., Frenk C. S., White S. D. M., 2006, Natur, 440, 1137
- Stanek K. Z., et al., 2003, ApJ, 591, L17
- Steidel C. C., Giavalisco M., Pettini M., Dickinson M., Adelberger K. L., 1996, ApJ, 462, L17
- Steidel C. C., Adelberger K. L., Dickinson M., Giavalisco M., Pettini M., 1998, astro, arXiv:astro-ph/9812167
- Stiavelli M., Scarlata C., Panagia N., Treu T., Bertin G., Bertola F., 2001, ApJ, 561, L37
- Strateva I., et al., 2001, AJ, 122, 1861
- Teerikorpi P., 1998, A&A, 339, 647
- Teodoro L., Johnston R., Hendry M., 2010, MNRAS, 405, 1187
- Totani T., 1997, ApJ, 486, L71
- Trenti M., Stiavelli M., Bouwens R. J., Oesch P., Shull J. M., Illingworth G. D., Bradley L. D., Carollo C. M., 2010, ApJ, 714, L202
- van Dokkum P. G., et al., 2004, ApJ, 611, 703
- van Dokkum P. G., 2005, AJ, 130, 2647
- Verde L., Haiman Z., Spergel D. N., 2002, ApJ, 581, 5
- Wang X.-Y., Li Z., Dai Z.-G., Mészáros P., 2009, ApJ, 698, L98
- White S. D. M., Frenk C. S., 1991, ApJ, 379, 52
- Wijers R. A. M. J., Bloom J. S., Bagla J. S., Natarajan P., 1998, MNRAS, 294, L13

## BIBLIOGRAPHY

---

Williams R. E., et al., 1996, *AJ*, 112, 1335

Wolf C., Dye S., Kleinheinrich M., Meisenheimer K., Rix H.-W., Wisotzki L., 2001, *A&A*, 377, 442

Wolf C., Meisenheimer K., Rix H.-W., Borch A., Dye S., Kleinheinrich M., 2003, *A&A*, 401, 73

Wyder T. K., et al., 2007, *ApJS*, 173, 293

Yee H. K. C., Ellingson E., Carlberg R. G., 1996, *ApJS*, 102, 269

York D. G., et al., 2000, *AJ*, 120, 1579

Yoshii Y., 1993, *ApJ*, 403, 552

# 2

## Absolute Magnitudes Measurement

### 2.1 Introduction

---

The distribution of distances to astronomical objects makes the analysis of the quantities directly measured by the telescopes (called *apparent quantities*) of limited interest to understand the physics of the Universe. Nonetheless, number counts of objects (i.e. the number of objects per unit flux and unit area) is not only the predecessor of today's statistical tools like the *Luminosity Function* (Schechter, 1976; Sandage, Tammann, & Yahil, 1979), but it is still often used as a basic tool to test the goodness and the apparent flux limits of survey data. The Hubble test, i. e. the plot of the apparent flux as a function of distance, has been used in the past for  $z < 0.2$  to directly measure the value of the Hubble constant  $H_0$ ; recently the Hubble diagram with type Ia supernovae up to  $z \simeq 1$  (Perlmutter et al., 1999; Schmidt et al., 1998), in conjunction with data from the WMAP satellite, has allowed to assess the acceleration of the expansion of the Universe.

The key parameter which allows to convert apparent quantities (and our two-dimensional perception of the Universe) to intrinsic ones (and to full four-dimensional representation of them) is the distance the object is from the Earth.

In cosmological surveys, the distance measurement of the major fraction of the detected objects can not be done using the methods generally known as the *distance scale ladder*. In fact, these methods rely on the identification of individual

objects which reflect well-defined physical processes of light emission, such as Cepheids or Type Ia Supernovae (SN). This would imply that at least one object per class would need to be identified in each single galaxy whose distance has to be computed, and its flux followed during a sufficiently large amount of time in order to allow reconstructing the light curve. This is unfeasible either because such objects would be too faint to be detected (like Cepheids at distances greater than few tens of Mpc) or because they would need an excessive amount of observation time for their discovery (like SN, if ever) or follow-up, generally not available in *point-and-shoot* surveys, whose aim instead is to cover the largest possible area to the deepest photometric limits (or highest signal to noise ratio).

The only viable alternative is then to directly measure the redshift of the object. This is usually done comparing the measured (or recovered) spectral energy distribution (SED) of the source to templates.

Once the distance to the object is known, it is possible to compute intrinsic observables like the absolute magnitude, which can then be used to make statistical estimates of the galaxy population properties, such as the luminosity function.

In the next section, we will describe the methods we developed and implemented in order to compute the absolute magnitude of an object either using spectra templates approximating the real spectrum of the object or by appropriate recombination of measurements in a set of filters. Section 2 is instead dedicated to the description of three among the most widely adopted methods to compute the Luminosity Function of galaxies.

## 2.2 Absolute magnitudes and K-correction

---

One of the most basic and fundamental observables for celestial objects is the *absolute magnitude*, and it is defined as the magnitude the object would have if it were located at a fixed distance of 10 parsec<sup>1</sup>.

An almost equivalent observable is the *absolute luminosity*, defined as the energy per unit of time and frequency emitted by the source over the full  $4\pi$  solid angle around it. The immediate application of this definition to astronomical objects is clearly unfeasible, so that it is necessary to rely on models for the

---

<sup>1</sup>Parsec is the contraction of parallax of 1 arcsecond, i.e. is the distance from which the Earth major orbital axis is seen under an angle of 1 arcsecond. This corresponds to a distance of 3.26 light years, or  $3.1 \times 10^{16}$ m.

emission of radiation. In the most simple case of isotropic radiation, the relation between absolute magnitude  $M$  and luminosity  $L$  can be written as:

$$L = 10^{-0.4(M-M_0)} \cdot 4\pi D_{10}^2 \quad (2.1)$$

where  $M_0$  is the absolute magnitude of a reference luminosity object, and  $D_{10}$  is the luminosity distance corresponding to 10 parsec.

The apparent magnitude of the source  $m_o$  is related to the spectral energy distribution by:

$$m_o = -2.5 \log \left[ \frac{\int \frac{d\nu_0}{\nu_0} f_\nu(\nu_0) R(\nu_0)}{\int \frac{d\nu_0}{\nu_0} g_\nu(\nu_0) R(\nu_0)} \right] \quad (2.2)$$

with  $f_\nu$  the spectral energy distribution,  $R$  the filter efficiency and  $g_\nu$  the spectral density of flux for the standard source. For the Vega system,  $g_\nu$  is the spectrum of Vega, while for the AB system  $g_\nu$  assumes a constant value, corresponding to a hypothetical constant source with  $g_\nu = 3631$  Jy, i.e. the flux of Vega in the  $V$  band.

When we need to compute the absolute magnitude of extra-galactic objects, we must take into account the effects of the metric describing the Universe geometry: on one side the expansion of the Universe makes the light emitted from a source to displace toward longer (redder) wavelengths, as discussed in the previous section; on the other side, the metric allows to obtain an exact expression for the concept of distance.

In mathematical terms, the absolute magnitude is related to the apparent magnitude by the following relation:

$$M_e = m_o - 5 \log(D_L) - 25 - K_{o \rightarrow e}(z, SED) \quad (2.3)$$

where  $M_e$  is the absolute magnitude in the object rest-frame,  $m_o$  is the apparent magnitude in the observer frame,  $D_L$  is the luminosity distance expressed in Megaparsec and  $K_{o \rightarrow e}$  is the so called K-correction.

The latter term in eq. 2.3 ( $K_{o \rightarrow e}$ ) is responsible for converting a flux measured in a filter at the observer frame to the same quantity, but in the reference frame of the object which emitted it.

An analytic expression for the K-correction was first derived by Oke & Sandage (1968) which allowed to convert from the apparent magnitude in the filter of

observation to the absolute magnitude in the same rest-frame band. At the time that study was published, the horizon available for extra-galactic analysis was mostly limited to the Local Group; the derived expression for the  $K$ -correction, a polynomial form, was then a valid approximation to the real one. This formula was later generalized (Kim, Goobar, & Perlmutter 1996 and Hogg et al. 2002) allowing for different rest-frame and the observer-frame filters. In its more general expression, its exact expression can be written as (Hogg et al., 2002):

$$K_{o \rightarrow e} = -2.5 \log_{10} \left[ (1+z) \frac{\int \frac{d\nu_o}{\nu_o} f_\nu(\nu_o) R(\nu_o) \int \frac{d\nu_e}{\nu_e} g_\nu^Q(\nu_e) Q(\nu_e)}{\int \frac{d\nu_o}{\nu_o} g_\nu^R(\nu_o) R(\nu_o) \int \frac{d\nu_e}{\nu_e} f_\nu \left( \frac{\nu_e}{(1+z)} \right) Q(\nu_e)} \right] \quad (2.4)$$

with  $\nu_e$  and  $\nu_o$  respectively the rest-frame and observer-frame frequency;  $f_\nu$  is the SED in units of energy per unit time per unit area and unit of frequency;  $Q$  and  $R$  represent the filters efficiencies in the rest-frame and observer-frame respectively, while  $g_\nu$  is the spectral density of flux for the standard source.

Expression 2.4 gives the exact correction to apply, but its reliability strongly depends on the accuracy with which the object SED is known. The determination of the SED of an object is in fact a non-trivial process which depends on several factors. The outcome of photometric surveys is the measurement of the apparent flux the selected object has in a set of filters. This translates into a discretized determination of the underlying SED. The width and effective wavelength of the adopted filter system will then determine the *resolution* of the SED. Typical filters adopted in cosmological surveys are broad-band filters, like the Sloan or the Johnson-Cousin systems; however we can also find ad-hoc filters, like those for the Combo-17 (Wolf et al., 2001) and ALHAMBRA (Moles et al., 2008) or NEW-FIRM (van Dokkum et al., 2009) projects. In these latter cases, they are generally medium-band filters, with typical band width of few hundreds of Angstroms for the optical to around half a micron for the NIR. This means that typical resolutions of *photometric* SED lie between few units and  $\approx 30$ . Resolutions of the order of few units are clearly insufficient to allow for the direct recovery of the intrinsic SED using the photometric data alone. For this purpose, the photometric points are usually employed as a base for an analysis via  $\chi^2$  techniques with a proper set of templates. The goodness of the resulting SED then depends both on

the selection of templates and on the algorithm used to perform the fitting. The reliability of the templates depends on the models of star formation and evolution used for their construction. Fitting algorithms can be organized into two classes:

- Single SED fitting
- Multiple SED fitting

The photometric redshift codes falling in the first category rely on the choice from the initial set of SEDs of the template with the best  $\chi^2$  value with the photometric data as a function of redshift, while the second class encompasses linear combination of SEDs and Principal Component Analysis.

The observational errors associated to the photometric points play a critical role in the  $\chi^2$  fitting. In fact, bright galaxies will generally present small photometric errors leading to apparently poor  $\chi^2$  values. On the contrary, faint objects with large photometric errors will more easily show good agreements with templates.

One way (see for example Blanton et al. 2003) for minimizing the effects of the uncertainties is to compute the absolute magnitude in the rest-frame filter which most closely matches the one in which observations were done. The counter-effect is that it is more difficult to compare results at different redshifts, since the effective rest-frame wavelength and FWHM of rest-frame filter are redshift-dependent.

A different possibility arises when the rest-frame wave band is observed by a large number of contiguous non-overlapping filters. In fact, in this case it is possible to adopt the filter set as a geometrical orthogonal base which allows to reconstruct any filter whose wavelength range is covered by the base. This is for example possible for the case of the ALHAMBRA survey and will be presented in section 2.2.2.

In the following section we present the results of our implementation of the computation of absolute magnitudes using the K correction.

Another important aspect to be accounted for when dealing with extra-galactic objects is the absorption effect of the inter-galactic medium (IGM) on the light

Figure 1

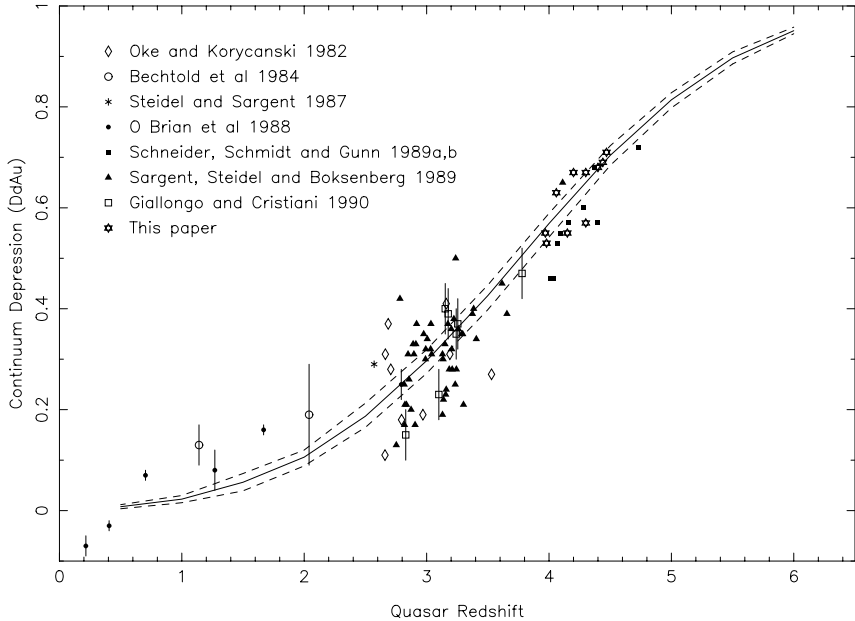


**Figure 2.1:** The distinct points show the flux decrement from Ly $\alpha$  as a function of redshift recovered from different quasar surveys, while the solid line indicates the fitting function adopted throughout our work (J. Webb unpublished).

emitted by galaxies. The IGM is composed by baryonic matter, most of which is the hydrogen ionized after  $z \approx 10 - 20$ , when the first stars appeared and started to emit UV light, during what is known as the *re-ionization Era*.

Even though the bulk of the Hydrogen in the universe is fairly ionized at all redshifts  $z \lesssim 5$ , the residual neutral hydrogen still present in the Ly $\alpha$  forest clouds and Lyman limit systems significantly attenuates the ionizing flux from cosmological distant sources. The quantitative effect of this process can be formalized introducing the concept of an effective continuum optical depth  $\tau_{eff}$  along the line of sight to redshift  $z$ :

$$\langle e^{-\tau} \rangle = e^{-\tau_{eff}} \quad (2.5)$$

where the average  $\langle \dots \rangle$  is taken along all lines of sight.

Any contribution to the far-UV background at observed wavelength  $\lambda_e$  emitted originally at a wavelength below the Lyman limit ( $\lambda_H = 912\text{\AA}$ ), at a redshift  $z_e$  will be subject to photoelectric absorption by neutral hydrogen encountered along at least part of its path.

From an operational point of view, we can then define a *flux decrement*  $D_A$  and  $D_B$  as in Oke & Korycansky (1982):

$$D_A = \int_{Ly\beta}^{Ly\alpha} \frac{f_{cont} - f_{obs}}{f_{cont}} d\lambda \quad (2.6)$$

$$D_B = \int_{Ly_{lim}}^{Ly\beta} \frac{f_{cont} - f_{obs}}{f_{cont}} d\lambda \quad (2.7)$$

where  $Ly\alpha$  and  $Ly\beta$  are respectively the wavelength corresponding to the Lyman  $\alpha$  (1216  $\text{\AA}$ ) and Lyman  $\beta$  (1025  $\text{\AA}$ ),  $Ly_{lim}$  is the Lyman limit (912  $\text{\AA}$ ) and  $f_{cont}$  and  $f_{obs}$  are the rest-frame emitted and observed fluxes respectively.

These effects can be taken into account when computing the K-correction by applying the absorption as a multiplicative factor, corresponding to the redshift and as a function of wavelength. One of the most widely used estimates of the IGM absorption is obtained following the prescription from Madau (1995) as follows:

$$\langle D_A \rangle = 1 - \frac{1}{\Delta\lambda_A} \int_{1050(1+z_{em})}^{1170(1+z_{em})} \exp \left[ -A_2 \left( \frac{\lambda_{obs}}{\lambda_\alpha} \right)^{3.46} \right] d\lambda_{obs} \quad (2.8)$$

$$\langle D_B \rangle = 1 - \frac{1}{\Delta\lambda_B} \int_{920(1+z_{em})}^{1015(1+z_{em})} \exp \left[ -\sum_{j=3}^{11} A_j \left( \frac{\lambda_{obs}}{\lambda_j} \right)^{3.46} \right] d\lambda_{obs} \quad (2.9)$$

where  $\Delta\lambda_A = 120(1+z_{em})\text{\AA}$ ,  $\Delta\lambda_B = 95(1+z_{em})\text{\AA}$ . The term  $A_2$  relative to the  $Ly\alpha$  forest contribution is equal to  $3.6 \times 10^{-3}$ , while the first three coefficients  $A_j$  relative to the  $D_B$  computation are  $A_3 = 1.7 \times 10^{-3}$ ,  $A_4 = 1.3 \times 10^{-3}$  and  $A_5 = 9.4 \times 10^{-4}$ .

In our work, instead, we used a different computation proposed by J. Webb, based on the fitting of an ad-hoc function on data from several quasar surveys. In Figure 2.1 we show a simple mathematical model (John Webb, unpublished) for the average opacity of the Lyman-alpha forest at different redshifts, that has been adopted in our work. The same Figure shows a compilation of opacity values

measured in quasars from different samples, at different redshifts. It is clear (and is a well-known fact in this kind of analysis) that the scatter around the model is larger at intermediate redshifts ( $z \approx 3$ ) because at higher redshift the absorption is almost complete, with very low variance, and at low redshift almost all lines of sight are clean, due to the very low density of Lyman-alpha absorbers.

### 2.2.1 K-correction with SED

As already presented in the previous paragraph, the computation of the absolute magnitude of an extragalactic object is a straightforward operation *once* the exact SED and redshift  $z$  have been determined. In the framework of the ALHAMBRA survey, photometric redshifts are computed using the BPZ (Benítez, 2000) code and adopting six SED templates. These SED templates represent average Elliptical, S0, Sa, Sb types galaxies plus two starburst templates, and showed to produce more reliable photometric redshifts with BPZ. and are shown in Figure 2.2. The templates were constructed extending the Coleman, Wu, & Weedman (1980) stellar evolution library in the UV by means of extrapolation, and in the NIR adding the Bruzual A. & Charlot (1993) templates (CWW hereafter).

It is easy to see from Equation 2.4 that the total  $K$ -correction can be considered as the sum of two distinct terms, a *pure cosmological* (neutral- as it does not depend on the intrinsic properties of the objects nor on the filters selected for the observation, but only on the value of  $z$ ) term, plus a *color* term,  $K_c$ , responsible for relating the observed quantities (SED and filter) to the corresponding rest-frame ones:

$$K_{o \rightarrow e} = -2.5 \log(1 + z) + K_c \quad (2.10)$$

with  $K_c$  given by:

$$K_c = -2.5 \log_{10} \left[ \frac{\int \frac{d\nu_o}{\nu_o} f_\nu(\nu_o) R(\nu_o) \int \frac{d\nu_e}{\nu_e} g_\nu^Q(\nu_e) Q(\nu_e)}{\int \frac{d\nu_o}{\nu_o} g_\nu^R(\nu_o) R(\nu_o) \int \frac{d\nu_e}{\nu_e} f_\nu \left( \frac{\nu_e}{(1+z)} \right) Q(\nu_e)} \right] \quad (2.11)$$

Figure 2.3 shows the  $K$ -correction obtained directly from eq. 2.4, for the six different Spectral Energy Distributions (SED) in the redshift range  $z \in [0.0, 6.0]$ , computed for observations done in the  $K_s$  filter and for the SDSS  $r'$  rest-frame

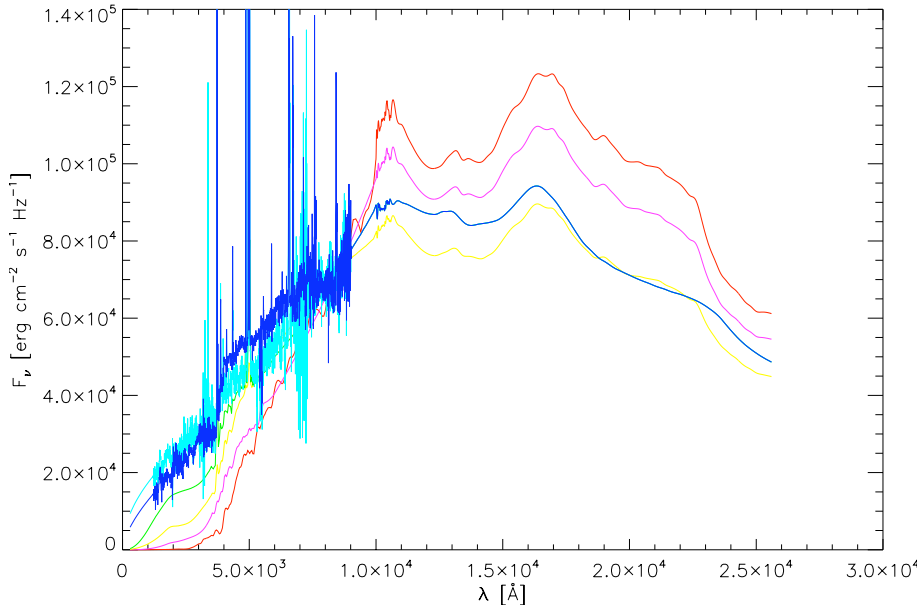


**Figure 2.2:** Spectral Energy Distribution (SED) adopted for the estimation of the photometric redshifts. Red: Elliptical template; Magenta: S0, Green: Sa, Yellow: Sb, Blue: SB1, Cyan: SB2

filter. Superimposed is the *neutral* term given by  $-2.5 \log(1+z)$ .

The high number of contiguous filters together with their medium waveband amplitude in the case of the ALHAMBRA filter system allow us to explore a finer computation of the pure SED-based K-correction.

Suppose that we are interested in computing the absolute magnitude in the rest-frame filter  $F(\lambda)$  whose effective wavelength is  $\lambda_{\text{eff}}$ . Then we can choose from the set of ALHAMBRA filters  $\{b_i(\lambda)\}$  that one whose blue-shifted effective wavelength at the redshift  $z$  of interest best matches the effective wavelength of the rest-frame filter  $F(\lambda)$ , i.e.:

$$\lambda_{\text{eff},F} = \lambda_{\text{eff},b_i} / (1+z) \quad (2.12)$$

In this way we will be computing the K-correction (in the redshift range al-

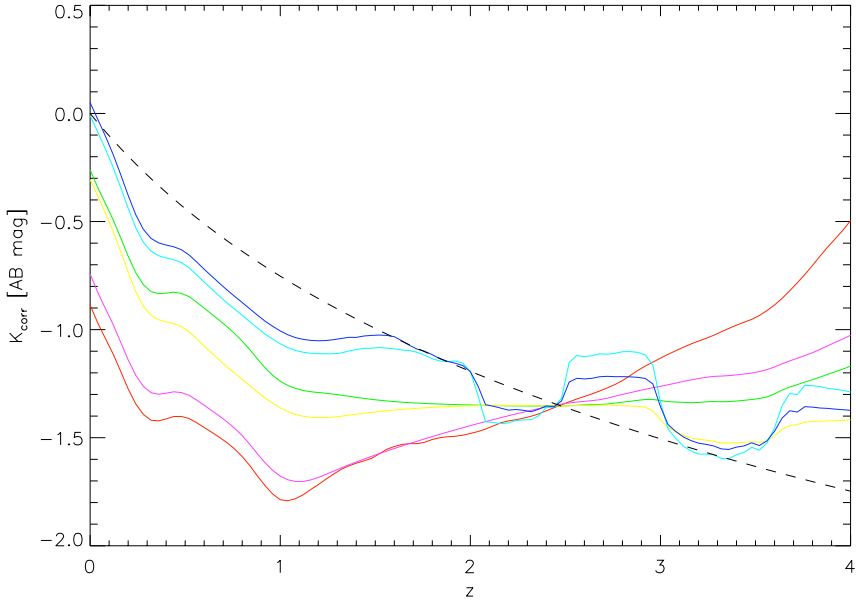


**Figure 2.3:** K-correction relative to the six SED templates adopted for the recovery of ph-z to compute absolute  $r'$  magnitudes from observations in the  $K_s$  band. Elliptical, S0, S1, S2, SB1 and SB2 galaxy types correspond respectively to red, magenta, yellow, green cyan and blue lines. The black dashed line indicates the cosmological term  $K_z = -2.5 \log(1+z)$ .

lowed by the observing filter set) in a more favorable case, i.e. relying more on observational data and minimizing the contribution of the SED template. This translates into values of the K-correction oscillating around zero, as shown in Figure 2.4. The drawback of this method is that it introduces an upper limit to the redshift range where this method can be applied, and given by:

$$z_{max} \approx \lambda_{red}/\lambda_{em} - 1 \quad (2.13)$$

where  $\lambda_{em}$  is the effective wavelength of the rest-frame band in which we want to compute the absolute magnitude and  $\lambda_{red}$  is the effective wavelength of the reddest filter in which observations are available.

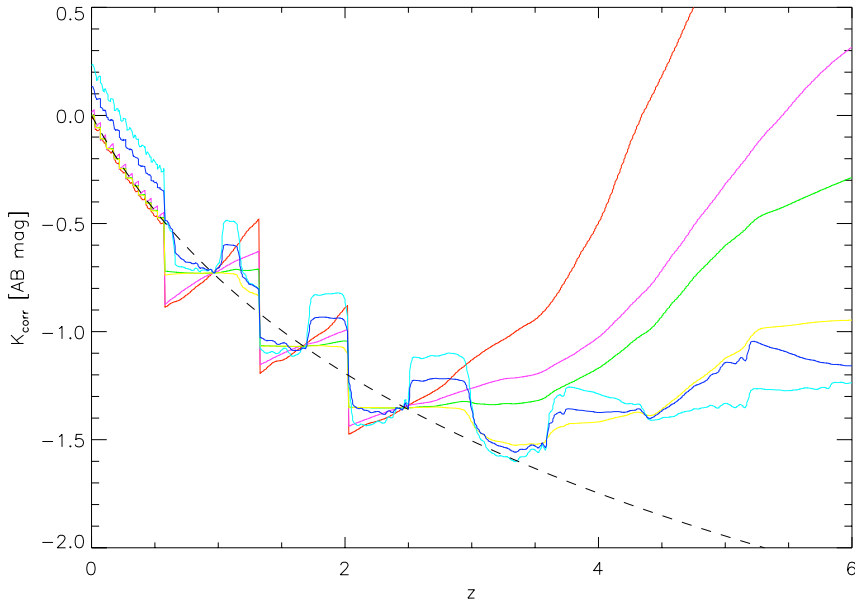


**Figure 2.4:** K-correction computed considering as observation filter the ALHAMBRA filter closest to the red-shifted rest-frame filter Sloan  $r'$ .

## 2.2.2 Linear combination of a base filter set

As already discussed in the previous section, the accuracy of the computation of the absolute magnitude following Eq. 2.4 largely relies on the correct choice of the SED template for the source of interest. A more accurate and reliable result would be obtained if the spectrum of the galaxy for which we want to compute its absolute magnitude were available. In this case, it could be *blue-shifted* by the  $(1+z)$  amount and convolved with the rest-frame filter of interest, obtaining the desired quantity. Unfortunately, this is generally not the case for deep cosmological surveys like ALHAMBRA, which are based on photometric rather than spectroscopic measurements.

However, the observation of a given object in a set of different wavebands can be considered to all practical effects as very low resolution spectroscopy: the higher the number of non-overlapping filters covering a fixed wavelength range, the higher is resolution. To this respect, the ALHAMBRA survey can be seen as

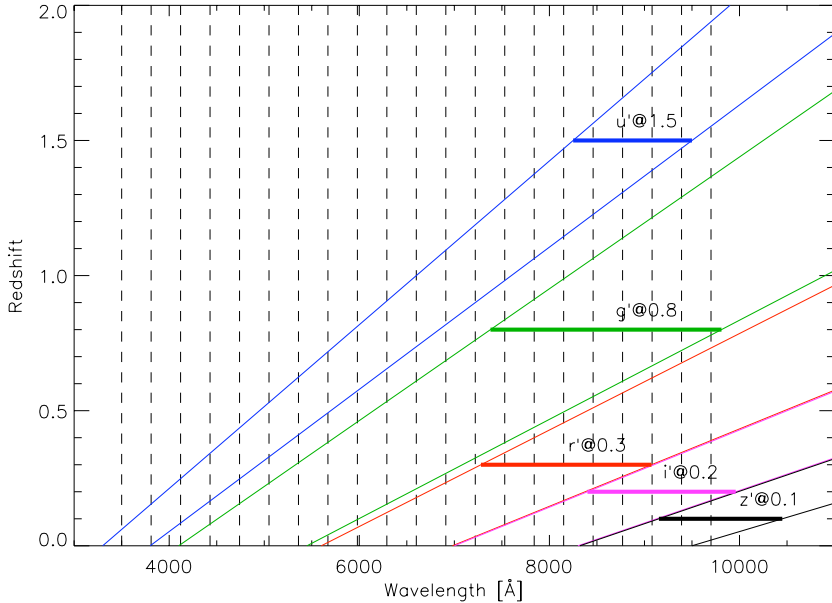


**Figure 2.5:** The vertical dashed line indicate the equivalent width of the 20 ALHAMBRA optical filters; blue, red, green, magenta and black solid transversal lines indicate the rest-frame position of the  $u$ ,  $g$ ,  $r$ ,  $i$ ,  $z$  filters as a function of redshift. The corresponding filter widths at the indicated fiducial limiting redshift are represented by the horizontal colored bars.

the equivalent of a spectroscopic survey with resolution  $R = \lambda/\Delta\lambda \approx 20^\dagger$

We can then think about using the photometric observations in each filter to construct a new filter, obtained as an appropriate linear combination of the available data. In this way we could obtain absolute magnitudes directly from the observed photometry and in a way which does not make any assumption on the SED of the object. As an example, in Figure 2.5 the equivalent width of the 20 ALHAMBRA filters are shown as vertical lines, while the transversal lines indicate the location of the five Sloan filters as a function of redshift. As it can be seen, the  $u'$  rest-frame filter is fully covered by ALHAMBRA observations down to  $z \approx 1.5$ ,  $g'$  to  $z \approx 0.8$ ,  $r'$  to  $z \approx 0.3$ ,  $i'$  to  $z \approx 0.2$  and  $z'$  to  $z \approx 0.1$ .

<sup>†</sup>Typical values for resolution on Amici-prism based spectrographs range from 50 (as for the SPHERE at VLT) to 100 (as for the NICS instrument at TNG or the NIRMOS spectrograph at VLT).

Given a filter  $\phi(\lambda)$  and a set of  $N$  filters  $b_i(\lambda)$  to be used as a base, we can write the relation:

$$\phi(\lambda) = \sum_{i=1}^N a_i b_i(\lambda), \quad 0 \leq a_i \leq 1 \quad (2.14)$$

where  $a_i$  are the coefficient to be computed. In our work, we investigated two different methods to compute these coefficients.

In the first method, the  $N$ -dimensional space of the  $a_i$  is explored through a best fitting algorithm. For each set of  $\tilde{a}_i$ , the following quantity is evaluated:

$$\rho = \int_{\lambda} \left[ F(\lambda) - \sum_{i=1}^N \tilde{a}_i b_i(\lambda) \right]^2 d\lambda \quad (2.15)$$

with  $F(\lambda)$  being the filter efficiency which one wants to reproduce. It should be noted, however, that the ALHAMBRA filters overlap a bit. This generates spikes in the reconstructed filter efficiency with the peak in correspondence of the point of intersection between the two contiguous filters, given the symmetry of the shapes of the efficiencies. The region of superposition is limited to  $\approx 80\text{\AA}$  for each couple of base filters, which however makes the final contribution of minor importance.

The results of this procedure are presented in figure 2.6 for the Bessel B filter. The ALHAMBRA filters are shown as alternating blue/red efficiencies for the sole purpose of clarity. The reference Bessel B filter and its best reconstruction are shown as black solid lines, while the red line shows the difference between the Bessel filter and its reconstruction. The spikes due to the superposition of the efficiencies of contiguous filters are well visible. Figure 2.7 shows the plot corresponding to the SDSS  $g'$  filter.

The second method we implemented is based on a more geometrical approach and, for some aspects, can be considered a natural evolution of the first one.

As already done with the previous method, we consider the set of ALHAMBRA filters  $b_i(\lambda)$  as a base  $\mathcal{B}$ :

$$\mathcal{B} = \bigcup_i b_i(\lambda) \quad (2.16)$$

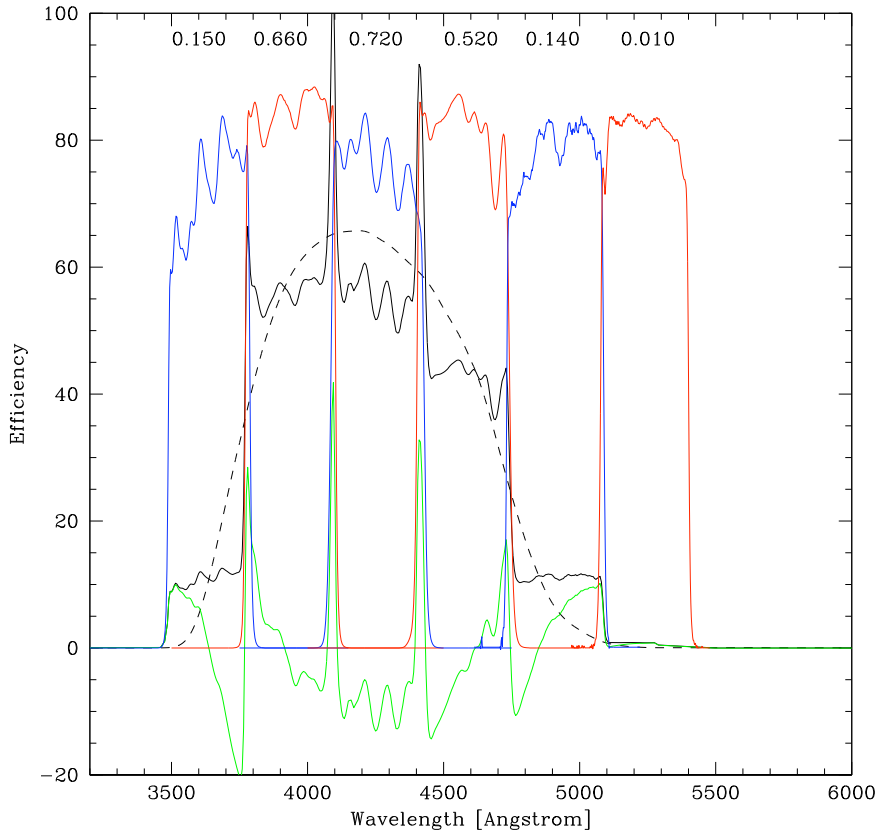


**Figure 2.6:** Result of the filter efficiency reconstruction algorithm presented in this section, for the Bessel  $B$  filter. The alternating blue and red lines mark the efficiency of those ALHAMBRA filters whose wavelength range covers that of the broad band filter, represented by the dotted line. The black solid line indicates the total efficiency of the reconstructed filter, while efficiency residuals are shown by the green solid line.

We now introduce the scalar product between two filters  $f_1(\lambda)$  and  $f_2(\lambda)$  as follows:

$$f_1(\lambda) \cdot f_2(\lambda) \equiv \int_{\lambda} f_1(\lambda) f_2(\lambda) d\lambda \quad (2.17)$$

It is now easy to check whether the ALHAMBRA filter set is actually an

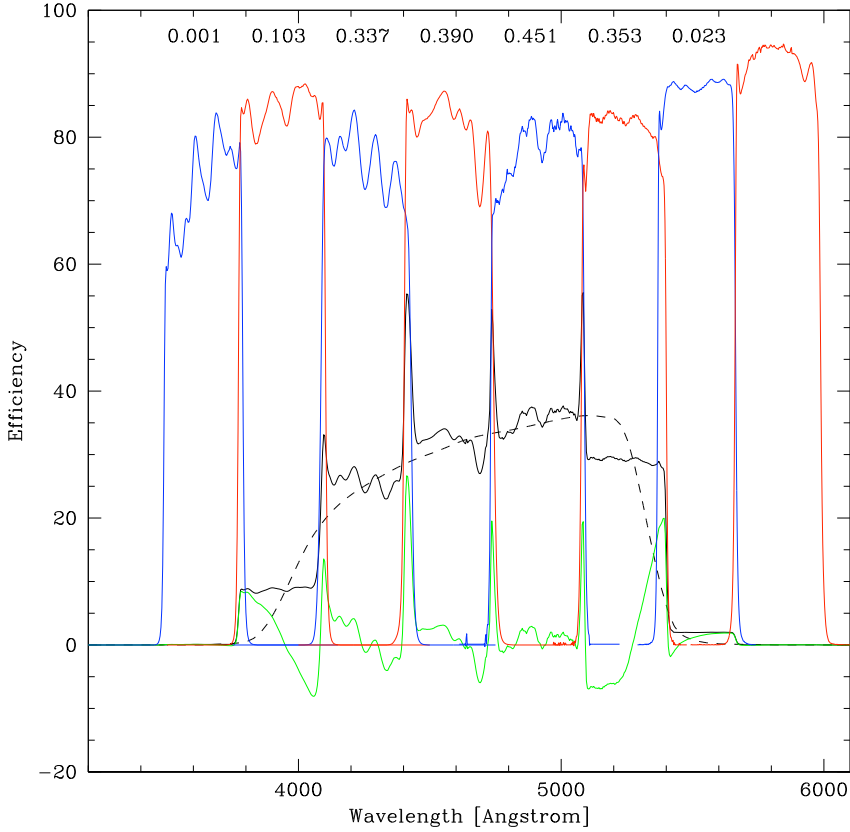


**Figure 2.7:** Similar to figure 2.6, but for the  $g'$  filter.

orthogonal base. In fact, given any two filters  $b_i(\lambda)$  and  $b_j(\lambda)$  belonging to the base, the integrand in Eq. (2.17), for the scalar product between  $b_i(\lambda) \cdot b_j(\lambda)$ , is zero everywhere except for the small region where two adjacent filters overlap. Strictly speaking we could not take the ALHAMBRA filter set as an orthogonal base; however, considering that the scalar product of two non-adjacent filters is zero and that the integral 2.17 for two adjacent filters assumes small values, we will consider the elements in  $\mathcal{B}$  to be a valid orthogonal base.

The coefficients  $a_i$  can now be obtained by just taking the scalar product

---

Filter	Fitting range (mag)	Offset	Slope
u'	[15, 21]	$0.39 \pm 0.34$	$0.001 \pm 0.012$
g'	[13, 22]	$0.15 \pm 0.23$	$-0.002 \pm 0.030$
r'	[12, 21]	$0.18 \pm 0.35$	$-0.005 \pm 0.018$
i'	[14, 20]	$0.01 \pm 0.12$	$-0.008 \pm 0.012$
z'	[14, 20]	$-0.01 \pm 0.08$	$-0.010 \pm 0.010$

**Table 2.1:** Fitting parameters for the magnitude differences in Figure 2.8.

between the base filter set  $b_i(\lambda)$  and the filter  $F(\lambda)$  we want to reconstruct:

$$a_i = b_i \cdot F = \int_{\lambda} b_i(\lambda) F(\lambda) d\lambda \quad (2.18)$$

We tested the goodness of this approach by comparison with both real and synthetic data. At first, we computed the coefficients necessary to obtain the five Sloan filters  $u'$ ,  $g'$ ,  $r'$ ,  $i'$  and  $z'$  from the ALHAMBRA filters. We then transformed the magnitudes of all the objects detected in the ALHAMBRA f08\_p01\_1 field to the magnitudes in the five Sloan bands, using Eq. 2.18, and matched the celestial coordinates of the objects to those contained in the SDSS catalogue of the same region. The plot of the difference between the apparent magnitudes reconstructed from ALHAMBRA observations and the magnitudes originally measured by the SDSS pipeline is shown in Figure 2.8. They show a similar behavior in all the filters with the exception of the  $u'$  filter, which shows both a larger scatter and a larger offset. This could be due to the non complete coverage of the ALHAMBRA filters to the  $u'$  filter. For the remaining filters, there is very little offset between the two magnitudes. This was also confirmed by both looking at the histogram of the difference between the two magnitudes, shown in Figure 2.9 for the  $r'$  filter, and by performing a best fit of a line on the magnitude difference in a range appropriately selected in order to exclude the faintest objects, higher in number but with higher uncertainties and which could introduce spurious effects. The results of the fitting procedure are summarized in Table 2.1.

As a second test, we generated the full set of apparent magnitudes in the 20 ALHAMBRA filters from the CWW templates, renormalized to  $M_r = -20$ , and in the redshift interval  $z \in [0, 6]$ . The fluxes in the 20 filters were then combined following eq. 2.14 to recover the absolute magnitude in the Sloan filter so that

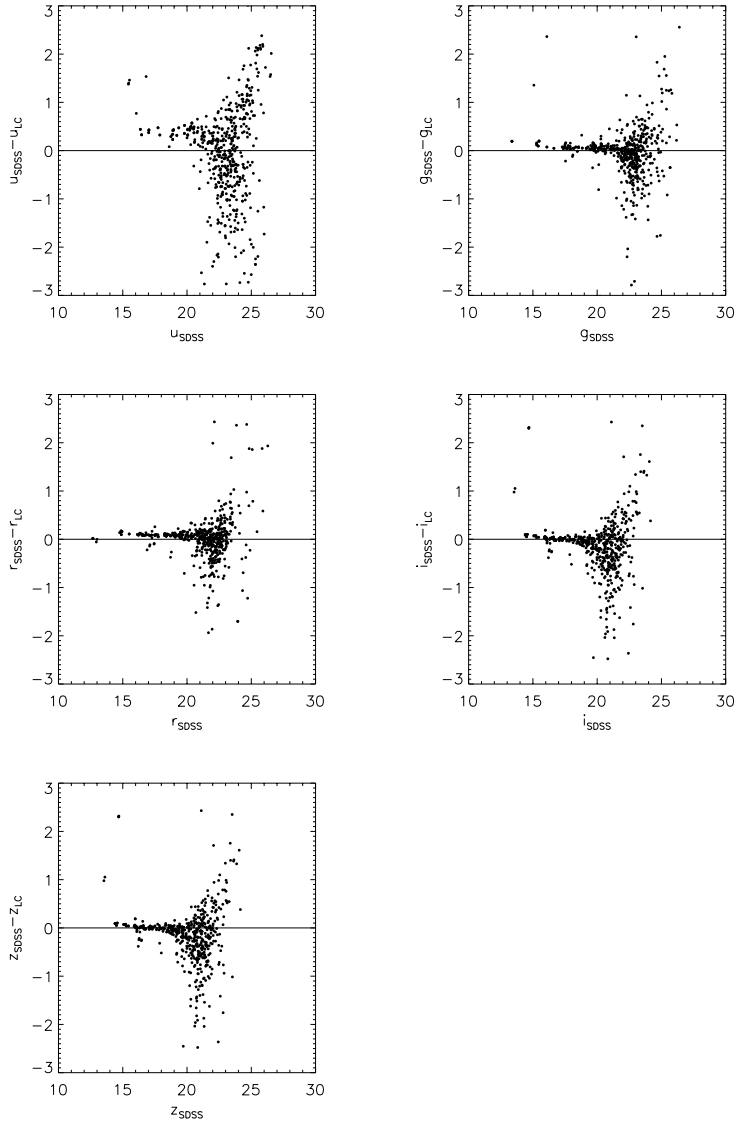


**Figure 2.8:** Difference between direct SDSS photometry and the one reconstructed with our method, in the five Sloan bands.

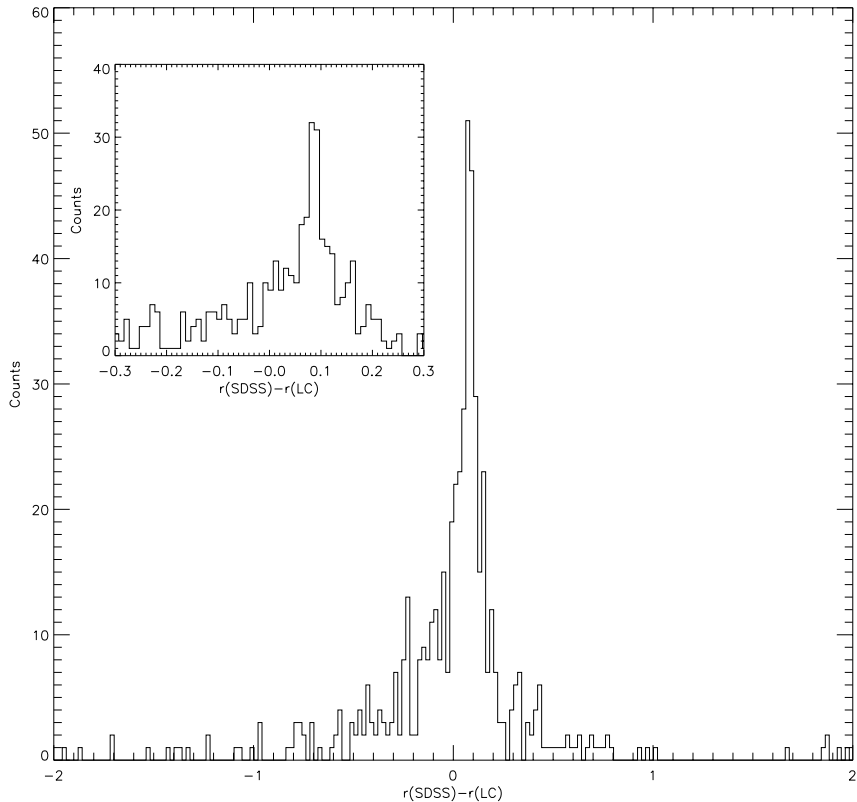


**Figure 2.9:** Histogram of the difference between the magnitudes from the SDSS pipeline and the values recovered by our procedure.

it was possible to compare the input with the reconstructed absolute magnitude. The difference between the input absolute magnitude and the recovered absolute magnitude for the Sloan  $u'$  and  $r'$  as a function of redshift  $z$  and for the six SED templates are shown in figure 2.10 and 2.11.

For the  $u'$  filter, we can see a very high difference at low redshifts. Similarly to the comparison with SDSS magnitudes, also in this case this difference can be due to the fact that the bluest ALHAMBRA filters do not fully cover the blue part of the  $u'$  filter, so that there is a loss of flux in the reconstructed magnitudes at low  $z$  for this filter. With the increase of  $z$ , the observer frame ALHAMBRA filters involved in the reconstruction of the rest-frame filter shift to the red so that the

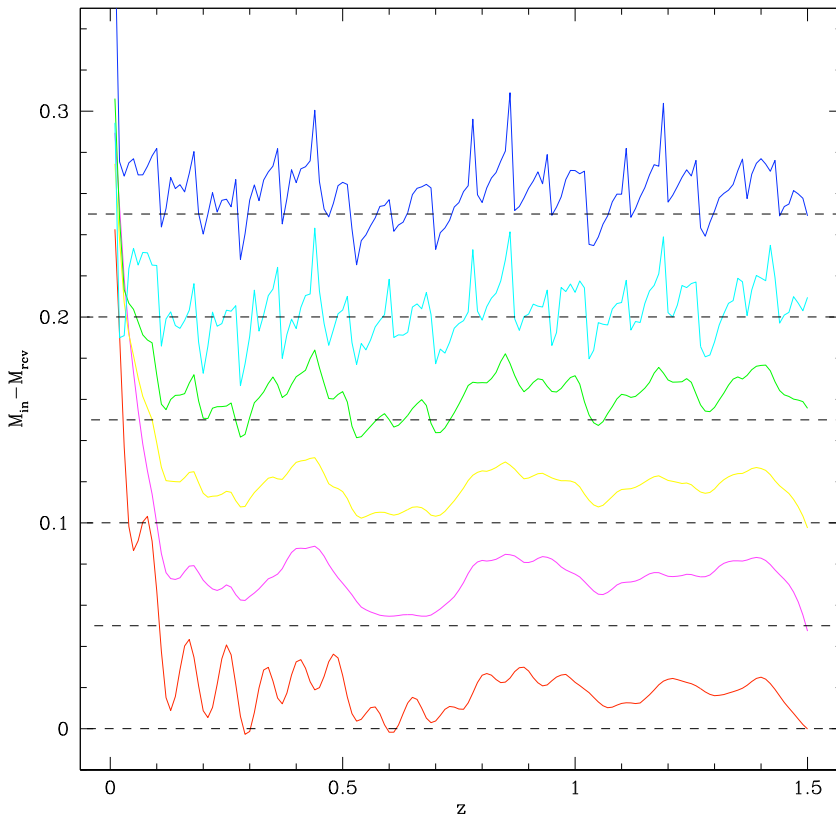


**Figure 2.10:** Difference between absolute  $u'$  magnitudes (bottom-up from Ellipticals to SB2). The differences have been offset by an arbitrary amount of 0.05mag from one to another for clarity. The corresponding zero level is represented as a dashed line.

rest-frame  $u'$  filter is fully covered by ALHAMBRA filters and the difference tends to decrease. In support to this assumption, we can see from the equivalent plot for the  $r'$  filter that this abrupt peak is absent at low redshifts, although the difference ranges between  $\Delta M_r \in [-0.05, 0.05]$ , for  $z < 0.5$ . At higher redshift, the plot for the  $r'$  filter shows the contribution from the NIR filters whose weight passes from 0 to 1 and vice-versa as the red-shifted  $r'$  filter lies at those wavelengths (see also

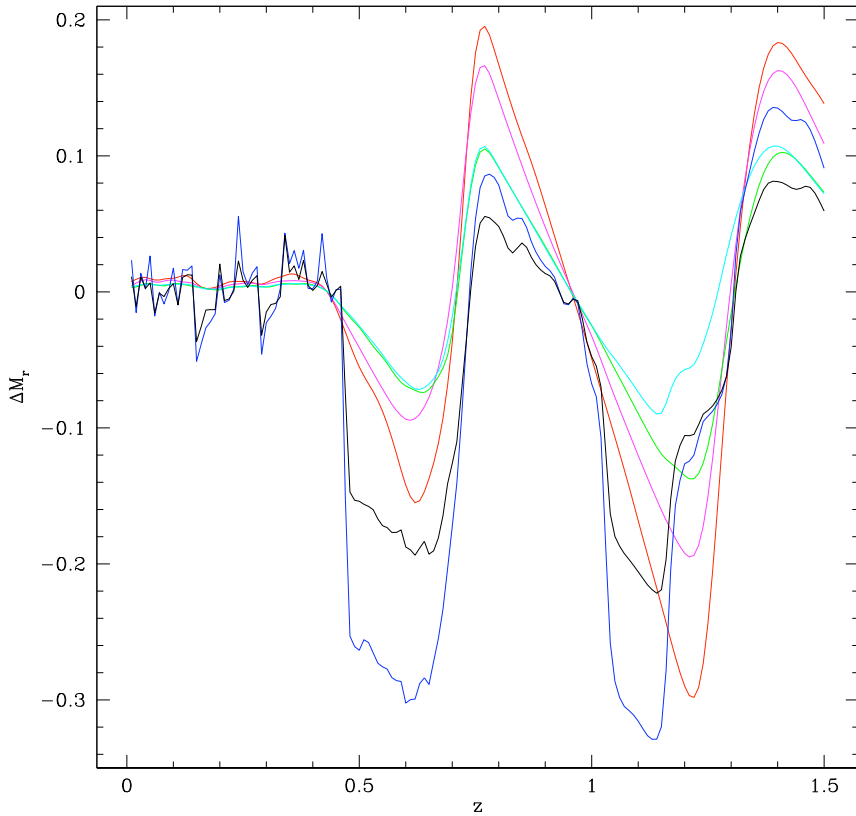


**Figure 2.11:** Difference between absolute  $r'$  magnitudes for the six SED templates. Red: Ellipticals; magenta: S0; green: S1; cyan: S2; blue: SB1; black: SB2.

Figure 2.5).

Another effect visible from figure 2.10 is that while for the reddest SEDs the magnitude difference is always positive, meaning that there is a slight over estimation of the recovered flux with respect to the input one, this offset gradually goes to zero as the templates become bluer, i.e. as we pass from Elliptical to SB galaxy classes. One possible explanation would be that the SED of SB galaxies is flatter than the SED of Ellipticals and spiral galaxies, resulting in a smaller sensitivity to filter position.

The major strength of this method relies on its fully observational base. However, as explained in the previous section, the reconstruction seems to suffer some kind of bias as a function of the intrinsic SED. An attempt that could be done in order to take full profit from this method and, on the other side, to try to minimize the spurious effects, is to join the *reconstruction* and the *K-correction* methods: in a first step, we reconstruct the filter whose effective wavelength best matches the redshifted effective wavelength of the rest-frame filter, as explained in Section 2.2.1. The obtained filter will then be used as the observer frame filter in Eq. 2.4.

### 2.2.3 Discussion

In order to evaluate the impact of the uncertainties introduced by the methods described in the previous sections to the error budget of the estimation of the absolute magnitude, we could compare them to the stochastic errors of redshift determination and to the uncertainties in the SED reconstruction.

For what concerns redshift errors, we should make a distinction between spectroscopic and photometric redshift. For the first class, in fact, errors are usually very small, since the evaluation of the redshift is done comparing the wavelength of known emission or absorption lines to their rest-frame values. In these cases, the uncertainties in the determination of the redshift will directly depend on the error associated to the peak determination of the line, which ultimately depends on the on the signal-to-noise ratio of the data and on resolution of the spectrograph. Typical errors are of the order of  $\Delta z/(1+z) \simeq 10^{-4} - 10^{-3}$ , making the redshift estimated via spectroscopic techniques the reference for the other methods. For completeness, however, and as noted for example by Fernández-Soto et al. (2001), the strength of spectroscopic redshift can also reveal as its weakness point, since the identification of lines can be a subjective process. The mis-identification of lines, especially in low SNR spectra can then lead to completely wrong values of redshift. However, the rate of the misidentifications can nowadays be strongly decreased by applying techniques like Principal Component Analysis.

On the other side, errors associated to photometric redshifts are usually larger than the spectroscopic counterparts. In this case, the most common way of estimating errors is to compare the photometric to the spectroscopic redshift values,

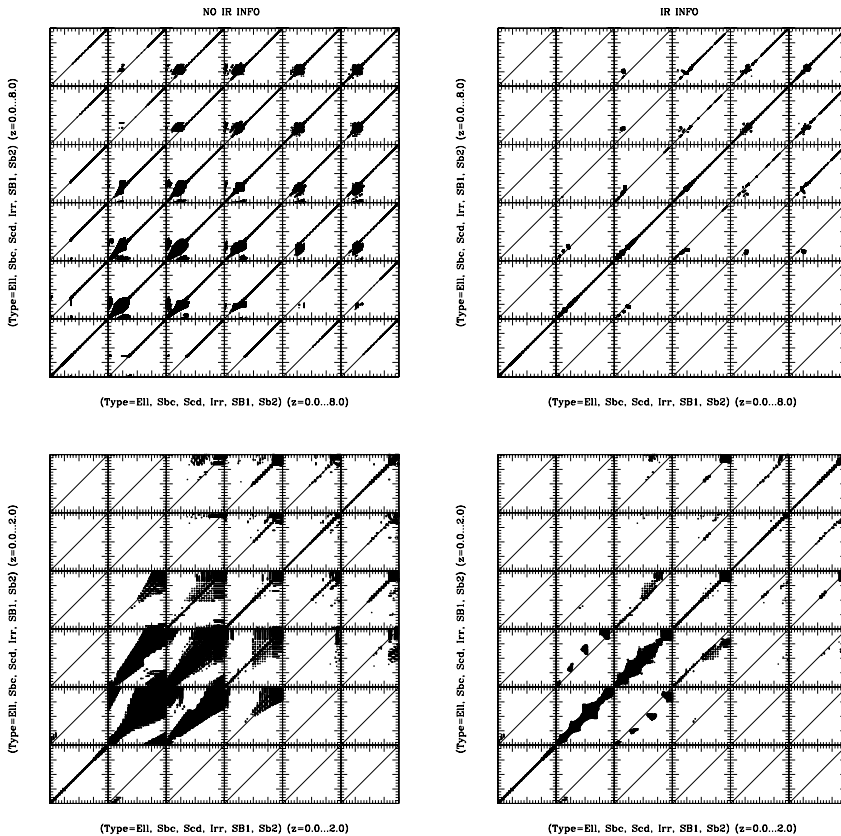


**Figure 2.12:** Preliminary estimates of photometric redshift errors (Moles et al., 2008). The two top panels refer to photometric redshifts computed excluding (left panel) or including (right panel) photometry from the NIR bands. The two bottom panels are a  $z \in [0, 2]$  zoomed version of the corresponding top panels. Inside each panel, each single plot represents a particular combination of input and output SEDs, so that panels in the diagonal are those where the output SED corresponds to the correct one. Inside each panel the usual  $z_{phot}$  vs  $z_{spec}$  diagram is plotted, with redshifts running from  $z = 0$  to  $z = 8$  in both axes. Under perfect circumstances, all the points should fall in the diagonal line ( $z_{phot} = z_{spec}$ ) of the diagonal panels ( $SED_{output} = SED_{input}$ ).

defining the quantity  $\Delta z/(1+z) \equiv (z_{phot} - z_{spec})/(1+z_{spec})$ . On the basis of this parameter, errors are generally divided into two regimes: a Gaussian distribution, characterized by a mean value  $\mu_{\Delta z}$  and a dispersion  $\sigma_z$ , and a *catastrophic error*

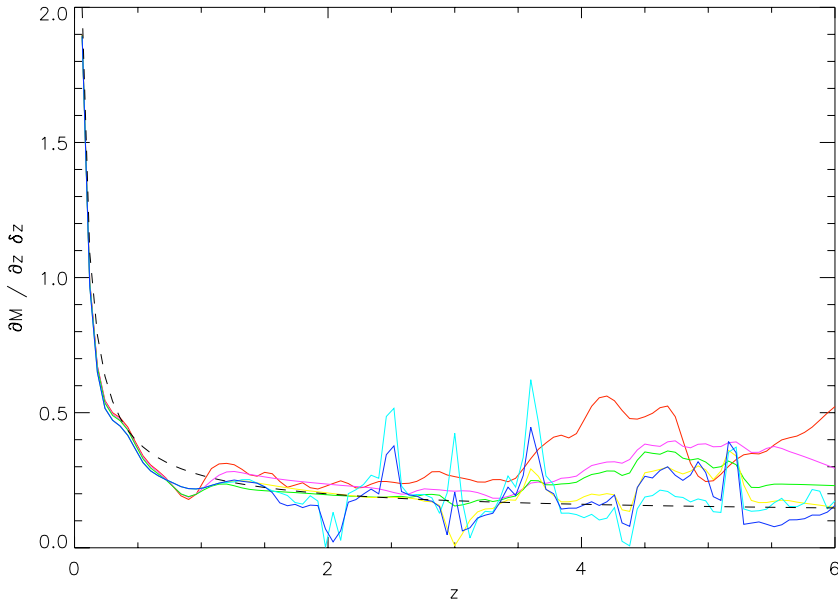


**Figure 2.13:** Effect of the propagation of the error on the photo- $z$  to the absolute magnitude computation, for the cases of E (red line), S0 (magenta), S1 (green), S2 (yellow), SB1 (cyan) and SB2 (blue), in the case of absolute magnitude in the  $r$  rest-frame band and with observations in the  $K_s$  filter. The black dashed line represents the case of suppressing the effects of photo- $z$  errors on the K-correction (K-correction = 0).

region, defined by those points with  $\Delta z / (1 + z) > n\sigma$ , where  $n$  is an appropriate factor allowing for a robust selection, i.e.  $n \simeq 3$ .

Since the ALHAMBRA Survey is a photometric cartography, we will need to take into account uncertainties from the photometric redshifts. Figure 2.12 shows a preliminary distribution of the photometric redshift errors for the ALHAMBRA Survey. Since the fraction of catastrophic error is about 3% and it can in principle be minimized using the odds parameter, we will consider only the normal-distributed errors. In particular, for our comparison, we will take a fixed value for the relative redshift error equal to  $\Delta z / (1 + z) = 0.05$ . This is a conservative value for the photo- $z$  errors for the ALHAMBRA Survey, since its forecasted average error is  $\Delta z / (1 + z) \approx 0.03$  (Moles et al., 2008).

Figure 2.13 shows the effects of propagating the error  $\Delta z/(1+z) = 0.05$  to the computation of the absolute magnitude. The black dashed line represents the contribution from the distance modulus alone, while the solid colored lines show the overall contribution, i.e. taking into account also the effects of the K-correction. For this particular plot, the rest-frame and the observer frame filters are  $K_s$  and  $r$  respectively. The choice of different bands influences to a first order the position of the features along the redshift axis, and, to a second order only, the local differences with the pure contribution of the distance modulus.

An average value of that error, with the exclusion of the lowest region of redshift, where the impact of the error on photo-z is as high as 1-2 magnitudes, is about  $\delta M \simeq 0.2$  mag, meaning that uncertainties from the photo-z errors are of the same order of magnitude of the flux uncertainties (Aparicio Villegas et al., 2010). Moreover, the comparison between Figure 2.13 and Figure 2.10 shows that the errors due to the uncertainties in the filter reconstruction methods are one order of magnitude smaller than uncertainties from photometric redshifts.

In the following paragraphs we compare the uncertainties in absolute magnitude from the filter reconstruction methods with an estimation of those introduced with the SED modelling.

As a conservative reference, we consider for the error of the SED modelling the difference between the K-correction from two *contiguous* SED templates, shown in Figure 2.14. In this way we are trying to mimic the possible effects of incorrect identification of the intrinsic SED of an object.

Form the plot we can see that the systematic error due to the mis-identification of the spectral class of an object can reach about 0.5 mag. If we limit our analysis to the  $0 < z < 1.5$  range, which corresponds to the range where we can apply the methods we developed in the previous sections, we can see that except for the difference between the K-correcion of the two star burst galaxies (blue line), the other differences are at least of 0.1 mag, and generally also assume larger than this value, reaching a maximum of about 0.5 mag. This, compared to the uncertainties discussed for our methods, reveals as a dominant uncertainty, of the same entity as the errors on flux or those due to the photo-z. However, the low frequency with which this occurs, renders this kind of errors negligible.

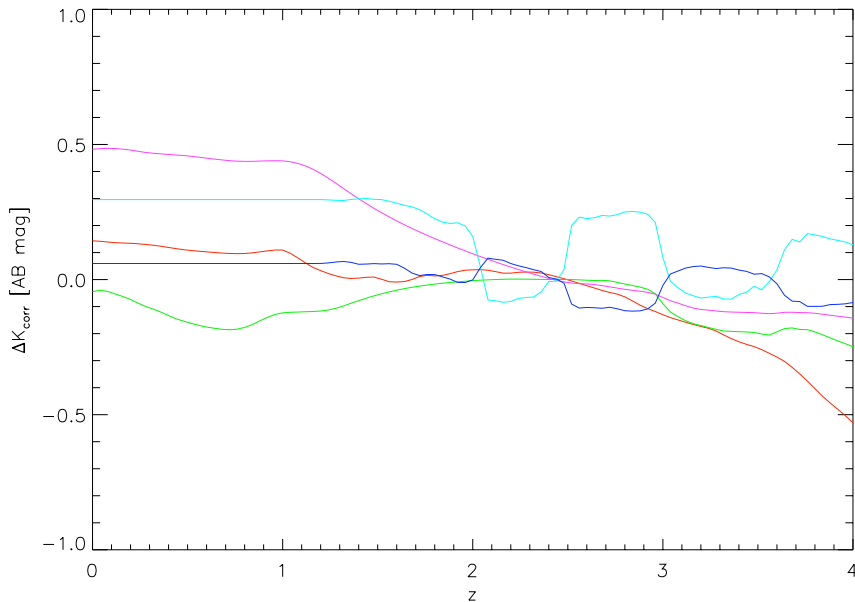


**Figure 2.14:** Difference between the K-correction of E and S0 (red), S0 and S1 (magenta), S1 and S2 (green), S2 and SB1 (cyan) and SB1 and SB2 (blue) galaxy SED, with rest-frame filter  $K_s$  and observed in the  $r$  filter.

### 2.3 Luminosity Function

One of the most direct statistical descriptors of the galaxy population is the number density of galaxies per unit of absolute magnitude (or, equivalently, luminosity), also called the *Luminosity Function* (LF) of galaxies.

When trying to estimate the LF from observational data, one has to deal with the fact that this kind of catalogues are flux limited. This means that the maximum distance for the objects in the catalogue will not be uniform, but will depend as a first instance on the absolute magnitude of the object itself and in a second instance on the class the object belongs to. For example, large and bright elliptical galaxies will be detected down to larger distances than irregular dwarf galaxies. From this example it is clear that when evaluating the LF, it is not sufficient to merely compute the mathematical division of the number of galaxies by the total volume occupied by them.

In order to circumvent this problem, a number of methods have been developed which allow to reliably obtain the LF values.

All the methods developed so far are based on the concept of introducing a weight function, which depends on the range each galaxy can span in the space of intrinsic observables. As an example, taking the redshift  $z$  as parameter for the intrinsic observable space, we can associate the comoving volume defined by the range in  $z$  as the inverse weight, obtaining the core of  $1/V_{max}$  LF method. On the other side, the adoption of the absolute magnitude as the parameter leads to the step-wise maximum likelihood method to compute the LF.

In this work, we implemented three among the most frequently used methods to compute the LF. Their mutual independence allows to obtain three independent estimations of the LF. The three methods are: the  $1/V_{max}$ , Step-Wise Maximum likelihood (SWML) and the Sandage, Tammann and Yahil Maximum Likelihood (STYML). In the following sections we will describe them.

### 2.3.1 $1/V_{max}$

The first description of the  $1/V_{max}$  method was given by Schmidt (1968), and successively by Felten (1976).

The expression for the LF  $\Phi_k(M)$  for the  $k$ -th bin of absolute magnitude  $M$  can be written as:

$$\Phi_k(M)dM = \sum_{i=1}^{N_{gal}} \frac{1}{V_i} \quad (2.19)$$

where  $N_{gal}$  is the number of galaxies in the catalogue and  $V_i$  is the corresponding comoving volume in which the  $i$ -th galaxy can lie while remaining within the observational limits of the catalogue:

$$V_i = \Omega \int_{z_{min}}^{z_{max}} \frac{dV}{dz} dz \quad (2.20)$$

where  $\Omega$  is the apparent area in steradians of the survey,  $dV/dz$  is the comoving volume element,  $z_{min}$  and  $z_{max}$  are respectively the minimum and maximum values of redshift for which the galaxy is still within the observational limits of the catalogue; in particular, for  $z_{max}$  the minimum between the redshift upper limit of the catalogue and the galaxy maximum redshift is taken.

The major advantages of this method are that it directly provides the normalization of the LF, it does not rely on any parameterization and that it does not make any assumption on the spatial distribution of the galaxies. However, this last characteristic can also reveal problematic, in those cases where a clustering is present in the data, affecting the faint end slope of the LF.

Avni & Bahcall (1980) implemented a generalization which allows to evaluate the  $1/V_{max}$  simultaneously on catalogues with different photometric depths (*coherent analysis*). Suppose we have  $n$  catalogues, each one with its limiting apparent magnitude  $m_i$ ,  $i = 1 \dots n$ . We can consider the galaxy as belonging to the catalogue given by the union of the original catalogues; in this case, the volume  $V_i$  in expression 2.20 becomes:

$$V_i = \sum_{j=1}^n \Omega_j \int_{z_{min,j}}^{z_{max,j}} \frac{dV}{dz} dz \quad (2.21)$$

where  $\Omega_j$  is the apparent area corresponding to the  $j$ -th catalogue, and  $z_{min,j}$  and  $z_{max,j}$  the redshift limits that would allow the  $i$ -th galaxy to remain within the  $j$ -th catalogue limits.

The computation of uncertainties is generally based on Poisson statistics. In this case, the uncertainty corresponding to the bin  $k$  is given by:

$$\sigma_k = \sqrt{\sum_i \frac{1}{V_{tot,i}^2}} \quad (2.22)$$

where  $V_{tot,i}$  denotes the total volume given by expression 2.21 and the sum extends to all the galaxies falling in the absolute magnitude bin  $k$ .

### 2.3.2 Step-Wise Maximum Likelihood

This method, first introduced by Efstathiou, Ellis, & Peterson (1988), is based on a discrete, non-parametric representation of the LF.

The LF  $\Phi(M)$  is written as  $N$  independent steps:

$$\Phi(M) = \phi_k, \quad M - \Delta M/2 < M \leq M + \Delta M/2, \quad k = 1 \dots N \quad (2.23)$$

where  $\Delta M$  is the magnitude interval of each step.

The probability that a galaxy with redshift  $z_i$  and absolute magnitude  $M_i$  is seen in a flux limited sample is:

$$p_i \propto \frac{\Phi(M_i)}{\int_{-\infty}^{M_{max}} \Phi(M) dM} \quad (2.24)$$

A likelihood  $\mathcal{L}$  can then be introduced:

$$\mathcal{L} = \prod_i p_i \quad (2.25)$$

which, for the case of eq. 2.23 can be re-written as:

$$\ln \mathcal{L} = \sum_{i=1}^{N_{gal}} W(M_k - M_i) \ln \phi_k - \sum_{i=1}^{N_{gal}} \ln \left\{ \sum_{j=1}^N \phi_j \Delta M H(M_{max}(z_i) - M_j) \right\} + c \quad (2.26)$$

with  $N_{gal}$  the total number of galaxies in the sample,  $c$  a constant,  $W(x)$  a window function given by:

$$W(x) = \begin{cases} 1 & \text{if } -\Delta M/2 < x \leq \Delta M/2 \\ 0 & \text{otherwise} \end{cases} \quad (2.27)$$

and  $H(x)$ :

$$H(x) = \begin{cases} 1 & \text{if } x \leq -\Delta M/2 \\ 1/2 - x/\Delta M & \text{if } -\Delta M/2 < x \leq \Delta M/2 \\ 0 & \text{otherwise} \end{cases} \quad (2.28)$$

Since the likelihood function involves ratios of the  $\phi_k$ , the normalization is lost; a constraint is then necessary. The constraint is then introduced using the Lagrangian multiplier formalism:

$$\ln \mathcal{L}' = \ln \mathcal{L} + \lambda g(\phi_k) \quad (2.29)$$

where the maximization is carried over the multiplier  $\lambda$  and the function  $g(\phi_k)$ .

A convenient choice for the  $g(\phi_k)$  is usually:

$$g = \sum_k \phi_k 10^{-0.4\beta(M_k/M_f)} - 1 = 0 \quad (2.30)$$

where  $M_f$  is a fiducial absolute magnitude and  $\beta$  is a constant, with common values between 1 and 1.5

The likelihood equation then yields:

$$\phi_k \Delta M = \frac{\sum_{i=1}^{N_{gal}} W(M_k - M_i)}{\sum_{i=1}^{N_{gal}} \left[ H(M_k - M_f) / \sum_{j=1}^{N_{gal}} \phi_j \Delta M H(M_j - M_f) \right]} \quad (2.31)$$

The parameters  $\phi_k$  can then be recovered by iteration of eq. 2.31.

The most common (and native) way of estimating the associated errors is based on the assumption that the  $\phi_k$  obtained with the maximum likelihood method are asymptotically normally distributed with covariance matrix:

$$cov(\phi_k) = \mathcal{I}^{-1}(\phi_k) \quad (2.32)$$

with  $\mathcal{I}(\phi_k)$  the information matrix given by:

$$\mathcal{I}(\phi_k) = \left[ \begin{array}{cc} \partial^2 \ln \mathcal{L} / \partial \phi_i \partial \phi_j + (\partial g / \partial \phi_i)(\partial g / \partial \phi_j) & \partial g / \partial \phi_j \\ \partial g / \partial \phi_i & 0 \end{array} \right]_{\phi=\phi_k} \quad (2.33)$$

The dimension of matrix  $\mathcal{I}$  and, as a consequence, also of the covariance matrix, is  $N + 1$ . The effective error estimates are the first  $N$  diagonal elements of the covariance matrix.

So far we have not taken into account the possibility of the union of catalogues with different photometric depth. Expression 2.31 can be easily generalized in this context (see for instance Hill et al. 2010). Suppose we have  $n_{cat}$  different catalogues, each one with its limiting absolute magnitude as a function of redshift. We can then associate to each galaxy the value of the limiting absolute magnitude  $M_{f,k}$  corresponding to the catalogue the galaxy belongs to, obtaining the following

new expression for eq. 2.31:

$$\phi_i \Delta M = \frac{\sum_{k=1}^{N_{gal}} W(M_i - M_k)}{\sum_{k=1}^{N_{gal}} \left[ H(M_i - M_{f,k}) / \sum_{j=1}^{N_{gal}} \phi_j \Delta M H(M_j - M_{f,k}) \right]} \quad (2.34)$$

### 2.3.3 The STY maximum likelihood method

This method is based on a parameterization for the expression of the LF. The expression which is commonly adopted to describe the LF  $\Phi(M)$  is the Schechter (1976) function:

$$\phi(M) dM = 0.4 \ln(10) \phi_* \left[ 10^{-0.4(M-M_*)} \right]^{(1+\alpha)} \exp \left[ -10^{-0.4(M-M_*)} \right] \quad (2.35)$$

where  $\phi_*$  is the normalization of the LF,  $\alpha$  describes the slope of the faint end and  $M_*$  define the position of the knee where the exponential regime is replaced by the power law.

Similarly to the SWML method presented in the previous section, also the STY-ML is based on the computation of the probability  $p_i$  that a galaxy with redshift  $z_i$  and absolute magnitude  $M_i$  is seen in a magnitude limited catalogue:

$$p_i \propto \frac{\Phi(M_i)}{\int_{-\infty}^{M_{max}} \Phi(M) dM} \quad (2.36)$$

Again, we can define the likelihood  $\mathcal{L}$  as:

$$\mathcal{L} = \prod_i p_i \quad (2.37)$$

The free parameters  $\alpha$  and  $M_*$  can then be determined by maximizing the likelihood. Since also in this method the likelihood is constructed as the ratio of quantities proportional to the normalization  $\phi_*$ , this last parameter can not be recovered at the same time of the other two and an independent way of estimating the normalization factor should be applied.

The errors on parameters are generally estimated through the ellipsoid in the

parameter space defined by:

$$\ln \mathcal{L} = \ln \mathcal{L}_{max} - \frac{1}{2} \chi_{\beta}^2(n) \quad (2.38)$$

where  $\chi_{\beta}^2(n)$  is the  $\beta$  point of the  $\chi^2$  distribution with  $n$  degrees of freedom.

The generalization of this method to a set of catalogues with different photometric depth can be reached in a way similar to the one adopted for the SWML method. In fact, the different limiting magnitude appears as an explicit parameter in the definition of probability (see eq. 2.36). There the absolute magnitude  $M_{max}$  can be replaced with the absolute magnitude limit of the catalogue  $k$  the galaxy belongs to, i.e.  $M_{max,k}$ , so that the final expression for the probability 2.36 becomes:

$$p_i \propto \frac{\Phi(M_i)}{\int_{-\infty}^{M_{max,k}} \Phi(M) dM} \quad (2.39)$$

This expression, as the corresponding for the SWML method eq. 2.34, can be used in a more general way. In fact, we can in principle associate a limiting absolute magnitude different for each galaxy, i.e. a limit which would depend not only on the distance of the object but also on its intrinsic properties like its SED or its surface brightness.

### 2.3.4 Comparison among the three methods

The reliability of the above methods in recovering the intrinsic LF has been analyzed by Willmer (1997) and Takeuchi, Yoshikawa, & Ishii (2000) using Monte Carlo simulations. They are somehow complementary, as the work by Willmer (1997) analyzes the ability to recover the LF as a function of the Schechter parameters, while Takeuchi, Yoshikawa, & Ishii (2000) introduced the dependence on the the spatial distribution of galaxies.

Overall, despite being the only method providing the normalization,  $1/V_{max}$  estimator is the one showing the largest bias in  $\alpha$  or  $M_*$ , while the STYML method provides the best results. The SWML algorithm is generally reliable, except when the faint-end region of the LF is under-sampled, in which case the faint-end slope can deviate by more than 25% from the intrinsic value. Despite this, the STYML method tends to be a little biased against flatter faint-end

slopes, effect that becomes more important for steeper slopes and smaller populations. However, these results are not confirmed by Takeuchi, Yoshikawa, & Ishii (2000), who instead found consistent results for all the estimators when galaxies are homogeneously distributed in space.

When galaxies are not homogeneously spread in space, the  $1/V_{max}$  estimator becomes severely affected in measuring the LF, while the SWML is insensitive (as it should be by design) to this effect. In addition, all methods are sensitive to the shot-noise, producing fluctuations at the faint-end, with larger deviations for flatter faint end slopes.

The behaviors of the LF estimators described above thus suggest that the best practice to adopt at the time of measuring a reliable LF would be to adopt more than one method, in order to take advantage of the strengths of each one and to also be able to identify the possible inconsistencies.

### 2.3.5 Normalization of the LF

With the exception of the  $1/V_{max}$ , both the SWML and the STYML methods do not allow to recover the normalization which has to be estimated in some other way.

This quantity is related to the mean density  $\bar{n}$  of the sample through:

$$\phi_* = \frac{\bar{n}}{\int_{M_{bright}}^{M_{faint}} \tilde{\phi}(M) dM} \quad (2.40)$$

where  $M_{bright}$  and  $M_{faint}$  are the brightest and faintest absolute magnitude in the survey and  $\tilde{\phi}(M)$  is the LF whose normalization is set to 1, i.e.  $\phi(M) = \phi_* \tilde{\phi}(M)$ . The problem then shifts to the determination of the mean density.

The probability  $s(z_i)$  that a galaxy at redshift  $z_i$  is included in the sample, or, equivalently, the fraction of objects at distances greater than  $z_i$  falling in the sample, is:

$$s(z_i) = \frac{\int_{M_{bright}}^{M_{faint}} \phi(M) dM}{\int_{M_{bright}}^{\min(M_{faint}, M(z_i))} \phi(M) dM} \quad (2.41)$$

where  $M(z_i)$  is the faintest absolute magnitude visible at redshift  $z_i$ .

The mean density can then be written as the ratio between the number of objects counted in the sample  $N_T$  and the number expected in a homogenous

universe:

$$n = \frac{N_T}{\int s(z) \frac{dV}{dz} dz} \quad (2.42)$$

This expression can be generalized, weighting each galaxy with a function  $w(z_i)$ , leading to:

$$n = \left[ \sum_{i=1}^{N_g} N_i(z_i) w(z_i) \right] / \left[ \int_0^{z_{max}} s(z) w(z) \frac{dV}{dz} dz \right] \quad (2.43)$$

with  $N_i(z_i)$  is the number of galaxies at redshift  $z_i$ . One of the expressions most commonly adopted for the weight  $w(z)$  is the reciprocal of the second moment of the two-point correlation function  $\xi(r)$ , which represents the mean number of galaxies in excess of a random distribution around each galaxy out to a distance  $r$ :

$$w(z_i) = \frac{1}{1 + \bar{n} J_3 s(z)}, \quad J_3 = \int_0^r r^2 \xi(r) dr \quad (2.44)$$

which can be solved by iteration, as the mean density  $\bar{n}$  also appears on the right side. Davis et al. (1980) also proposed for the estimator of the mean density, the ratio between the number of galaxies  $N(z)$  bright enough to be counted in the shell at distance  $z$  and the fraction of objects falling in the sample and with redshifts greater than  $z$ ,  $s(z)$ , in the total survey volume:

$$\bar{n} = \left[ \int_0^{z_{max}} \frac{N(z)}{s(z) dz} \right] / \int_0^{z_{max}} \frac{dV}{dz} dz \quad (2.45)$$

Another estimator, proposed by Efstathiou, Ellis, & Peterson (1988), is the normalization by means of the observed number counts. The expected number of galaxies with apparent magnitude brighter than  $m$  is given by:

$$N(m) = \int_0^\infty dz \frac{dV}{dz} \int_{-\infty}^{M_{max}(z,m)} \phi(M) dM = \phi_* I(m) \quad (2.46)$$

The normalization  $\phi_*$  can then be obtained minimizing with respect to  $\phi_*$  the expression:

$$\chi^2 = \sum_n \frac{[dN(m) - \phi_* dI(m)]^2}{\phi_* dI(m)} \quad (2.47)$$

### 2.3. LUMINOSITY FUNCTION

---

obtaining thus:

$$\phi_* = \left[ \frac{\sum_n dN(m)^2/dI(m)}{\sum_n dI(m)} \right]^{1/2} \quad (2.48)$$

# Bibliography

- Aparicio Villegas T., et al., 2010, *AJ*, 139, 1242
- Avni Y., Bahcall J. N., 1980, *ApJ*, 235, 694
- Benítez N., 2000, *ApJ*, 536, 571
- Blanton M. R., et al., 2003, *ApJ*, 592, 819
- Bruzual A. G., Charlot S., 1993, *ApJ*, 405, 538
- Coleman G. D., Wu C.-C., Weedman D. W., 1980, *ApJS*, 43, 393
- Davis M., Tonry J., Huchra J., Latham D. W., 1980, *ApJ*, 238, L113
- Efstathiou G., Ellis R. S., Peterson B. A., 1988, *MNRAS*, 232, 431
- Felten J. E., 1976, *ApJ*, 207, 700
- Fernández-Soto A., Lanzetta K. M., Chen H.-W., Pascarelle S. M., Yahata N., 2001, *ApJS*, 135, 41
- Hill D. T., Driver S. P., Cameron E., Cross N., Liske J., Robotham A., 2010, *MNRAS*, 404, 1215
- Hogg D. W., Baldry I. K., Blanton M. R., Eisenstein D. J., 2002, *astro*, arXiv:astro-ph/0210394
- Kim A., Goobar A., Perlmutter S., 1996, *PASP*, 108, 190
- Madau P., 1995, *ApJ*, 441, 18
- Moles M., et al., 2008, *AJ*, 136, 1325
- Oke J. B., Sandage A., 1968, *ApJ*, 154, 21
- Oke J. B., Korycansky D. G., 1982, *ApJ*, 255, 11
- Perlmutter S., et al., 1999, *ApJ*, 517, 565
- Sandage A., Tammann G. A., Yahil A., 1979, *ApJ*, 232, 352
- Takeuchi T. T., Yoshikawa K., Ishii T. T., 2000, *ApJS*, 129, 1

## BIBLIOGRAPHY

---

Schechter P., 1976, ApJ, 203, 297

Schmidt B. P., et al., 1998, ApJ, 507, 46

Schmidt M., 1968, ApJ, 151, 393

van Dokkum P. G., et al., 2009, PASP, 121, 2

Willmer C. N. A., 1997, AJ, 114, 898

Wolf C., Dye S., Kleinheinrich M., Meisenheimer K., Rix H.-W., Wisotzki L.,  
2001, A&A, 377, 442

# 3

## Determination of Detection Completeness

### 3.1 Introduction

---

Every time data is collected through a telescope, the observer has to live with the fact that the data will not contain all the information, in the wavelength of interest, of every object that physically exist in that region of the sky. This is the result of many reasons, which we can organize into three categories: practical difficulties of magnitude limits, color dependence and redshift dependence.

The first category includes all those effects related to the way observations are done. Some of the objects will emit too few photons to be collected by the detection system (usually telescope coupled to a camera), effect increased by the general glow of the sky and by the fact that the transmission efficiency of the detection system is generally a fraction of the nominal one. The electronics will also produce its own noise which will further limit the ability to collect useful information. When this is the case, the sampling of objects is usually denoted as *flux-limited*.

Further selection is produced when analysing the data, in particular during the generation of the catalogue of the objects present in each image. In fact, whatever algorithm is used to detect the objects, there will always be a fraction of objects which will not be detected, despite the minimum flux passed as threshold to the algorithm. In addition, when dealing with regions crowded with many objects (as may be the case, for example, of deep extra-galactic images), it is not uncommon

to find overlapping objects, which render even more challenging the detection (and flux measurement) of such objects by the algorithm. A third cause for non-detection is the proximity of the object to the border of the frame (*border-effect*): on one side objects too close (for example up to 3-4 FWHM) are skipped by the detection algorithm because it would not be possible to obtain the integral flux measurement, as the object profile is not entirely contained in the frame. On the other side, the final frames are usually the result of the combination of several frames, each one taken with a small offset with respect to the others (*dithering*). In particular this means that the objects close to the border will not be in all the frames, resulting in a lower signal-to-noise level.

The second class of effects is related to the observed colors of the objects. Usually an object catalogue is built from an image taken in a given band, so that sources with high absolute colors relative to the selection band will most probably be missed. For example, if the detection is made in the  $K_s$  band, very blue objects will be missed.

For extra-galactic objects, there is a third category: the dependence on redshift. Given a rest-frame SED, when observed this will appear as a SED whose wavelengths have been increased by a factor  $(1 + z)$ . The colors of an object will then also depend on the redshift at which the source is. In this case then, the selection operated by the detection image will also depend on the redshift of each object.

The determination of all the physical properties which require a statistical analysis is thus strongly affected by such effects, and more importantly, by the selection effects as a function of the spectral type and distance of the objects. This renders fundamental the estimation of the selection effects acting on a given catalogue.

One of the key features of the ALHAMBRA Survey is the adoption of 20 medium band, contiguous filters covering the range of the optical wavelength, from 3500 Å to 9700 Å plus the three standard  $J$ ,  $H$  and  $K_s$  near-infrared filters, allowing to obtain what can be considered as a low resolution ( $R \approx 15 - 30$ ) spectrum. As a counterpart, this strategy makes the definition of the object detection more complex. The fields characterizing the ALHAMBRA Survey lays all at high galactic latitude, allowing to observe the regions outside our own Galaxy without being strongly affected by the interstellar gas extinction and avoiding an excessive

crowding by stars. However, since the survey has been intended for both galactic and extra-galactic studies, the procedure for the detection of objects must comply to its philosophy. Hence, in terms of detection, any bias against any particular class of object should be avoided. This excludes, for example, making a selection of the reddest filters, which would of course benefit high- $z$  objects, but would cut blue galactic objects.

The strategy defined for the detection of objects was then to build for each CCD a so called *deep image* obtained as the sum of all those frames taken when the atmospheric transparency was better than 50% and with the seeing better than 1.2 arcseconds. This latter constraint is relaxed to 1.3 arcseconds for those cases where there are not enough frames satisfying the original value. In order to avoid any prior-selection on object types, the set of filters used to this aim should then uniformly span the whole range of wavelength. However, given the filter efficiency (see Fig. 1.6), it was decided to discard the low-efficiency ones and to take into account only those covering the filter whose  $\lambda_{eff}$  falls in the range 4585 Å to 8305 Å included. As we will discuss in the following sections, this *deep image* was used to detect objects. An example of the filters used is given in Figure 3.1.

In the following sections we will describe the methods developed to obtain an as much realistic and accurate as possible estimation of the selection effects present in the flux limited ALHAMBRA catalogue, commonly referred to as *completeness*; the results obtained from these methods will be exposed and discussed in Sect. 3.2.7.

## 3.2 Description of the methods

---

The aim of our algorithm was to implement a procedure able to directly estimate the completeness through the data acquisition and object detection phases, as a direct function of the intrinsic physical properties of the different classes of objects. In particular, as the main topic of this thesis is the study of the luminosity function of galaxies, we will concentrate on galaxies.

The intrinsic properties of galaxies we took into account are:

- Redshift

- Spectral/morphological type
- Absolute magnitude in a given rest-frame band

In the following paragraphs we will explain the effects of each property.

The effects of the redshift on the physical properties of an object we are interested in replicating are twofold. On one side, there is a dimming of the object flux related to its distance following the inverse square law. In addition, the observational effects of redshift is to shift by a factor  $(1 + z)$  any restframe wavelength  $\lambda_e$  to  $\lambda_o = (1 + z)\lambda_e$ . These effects are all present in the well known formula for the computation of the absolute magnitude from the apparent one, for extra-galactic objects (see Eq. 2.3), discussed in Sect. 2.2.

This means that, once the observation band has been fixed, the flux falling in it will not just be dimmed by a factor which depends on the comoving distance from the object, but the observation band will be projected on a bluer region of the rest-frame SED. On the other side, the apparent angular dimension of the object is resized as a function of distance. Figure 3.2 shows how the apparent diameter of a typical galaxy changes as a function of redshift. Considering a seeing of 1.2 arcseconds (corresponding to the worst value admitted for the construction of the deep image), it is evident that the observational effects of physical dimensions should be taken into account at least down to  $z \approx 1.0$ .

In our implementation we did not take into account possible evolution in the angular dimension and restframe flux of the object due to merging.

As already mentioned in the previous chapter, spectral types behave differently in the observed band according to the formula 2.3, with respect to a fixed rest-frame flux.

Morphological types can be associated to the surface brightness profile of the object as a function of the distance  $r$  from the center. In the literature, two are the profiles which are commonly used: the *de Vaucouleurs* profile (de Vaucouleurs, 1948) which generally describes well the luminosity profile of elliptical galaxies and the *exponential* profile, generally used for disks of spiral galaxies (whereas the bulge of a spiral galaxy is well approximated by the de Vaucouleurs law). As the name suggests, the de Vaucouleurs profile was first introduced by de Vaucouleurs

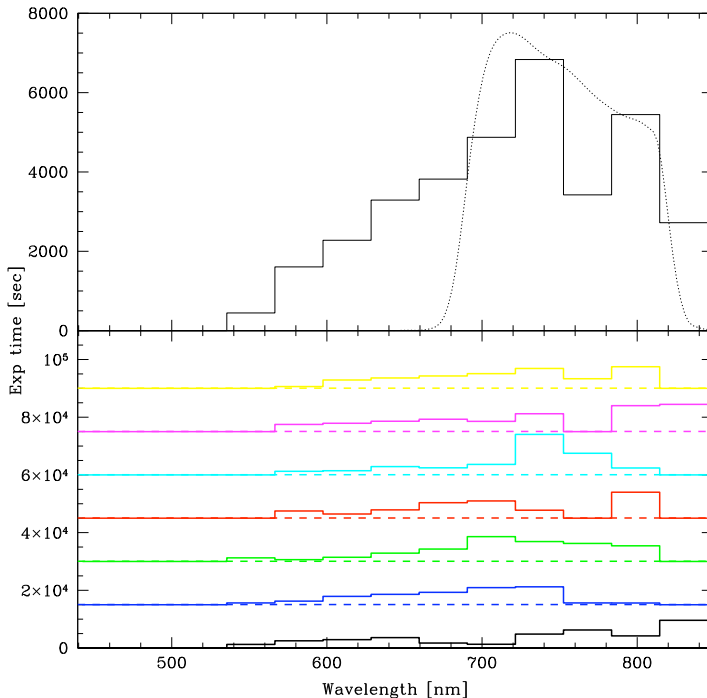


**Figure 3.1:** Bottom panel: total exposure time per filter constituting the deep image. An arbitrary offset of 7000 sec. from one histogram to another has been added for graphical clarity purposes. Colors refer to respectively from top to bottom: f08p02\_1, f08p01\_1, f07p03\_1, f05p01\_1, f04p01\_1, f03p01\_1 and f02p01\_1 ALHAMBRA fields. For clarity, histograms have been offset by an arbitrary value. The reference zero for each histogram is indicated by the dashed line. Top panel shows the average of all the exposure times (solid line), together with the efficiency (with arbitrary normalization) of the SDSS *i* filter (dotted line).

and can be written as:

$$I(r) = I_e e^{-7.67 \left[ \left( \frac{r}{r_e} \right)^{1/4} - 1 \right]} \quad (3.1)$$

$r_e$  is the radius of the isophote containing half of the luminosity and  $I_e$  the surface brightness at  $r_e$ .

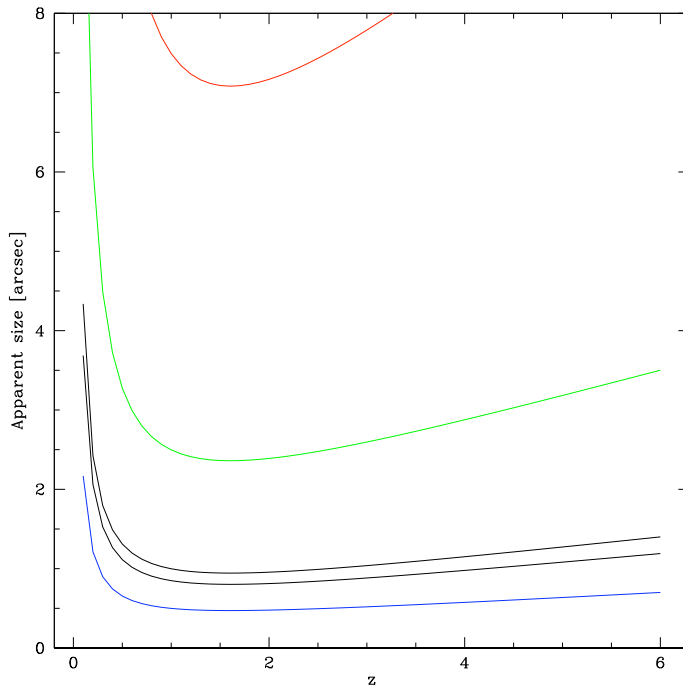


**Figure 3.2:** Apparent dimension in arcseconds of typical galaxies as a function of redshift  $z$ . The red line corresponds to a physical diameter of 60Kpc, the green line to 20Kpc and the blue line to 4Kpc. The two black lines correspond to  $2r_e = 6$ Kpc and 8 Kpc respectively.

The exponential profile is of course of the form:

$$I(r) = I_0 e^{-\frac{r}{r_0}} \quad (3.2)$$

with  $I_0$  the central luminosity and  $r_0$  the characteristic radius.

The evaluation of the completeness is a key point in the determination of physical properties. As such, we were committed to its determination in the most reliable way. For this purpose we developed and implemented two independent ways for determining the completeness: one based on an *analytic* procedure and

the other on *Monte Carlo* simulation with real data.

### 3.2.1 Determination of the weights

As described in the Introduction, the ALHAMBRA source catalog is obtained on the basis of a deep image, resulting from the combination of single exposures selected following criteria involving central wavelength of the filter, seeing and atmospheric transparency during the exposure.

As the conditions under which the images are taken generally change from exposure to exposure, this means that each deep image will be the result of the sum of a different set of frames. In other words, each filter will participate with a different weight to each deep image.

We extracted from the header of the deep images the list of frames used to build it. As the exposure time of the frames is constant through all the involved filters to a good approximation, the weight is just the the number of frames of each filter used to build the deep image. The result of this is shown as histograms in figure 3.1, in which each color corresponds to a deep image.

As our aim is to estimate the completeness not on every deep image, but as an average property, we opted to consider for the weight of the single filter the average value of the weights of each filter for the different deep images, also shown in figure 3.1, as the black solid line. Furthermore, since the variance in the distribution of the weights is small, we did not take into account this effect in our construction of the deep image. As it can be seen, the average deep image resembles the Sloan *i* filter with a pronounced wing into the *r* filter.

### 3.2.2 The analytic method

The reliability of the detection of an object is generally expressed in terms of the number of sigmas above the background of the total flux of the object. The evaluation of the number of sigmas is based on two basic quantities associated to each object: its flux  $f$  and the flux error  $s$ .

In the numerical simulation we developed, the flux  $f$  of an object is a known parameter, which is a function of other input parameters, namely of the absolute magnitude  $M_\phi$  in the rest-frame filter  $\phi$ , of the redshift  $z$ , the spectral type of the galaxy (SED) and of the band  $b$  in which the photons are collected.

For simplicity, in the rest of this section we will omit all these dependencies, and refer to the flux with just the  $f$  symbol, i.e.  $f \equiv f(M_\phi, z, SED, b)$ .

The flux error  $s$  is computed differentiating the definition of apparent magnitude  $m$  as a function of flux  $f$ :

$$s \equiv df = 0.4 \ln(10) f dm \quad (3.3)$$

This relation shifts the problem of evaluating the flux uncertainty to the evaluation of the error on the apparent magnitude  $dm$ .

The magnitude error is generally the result of two components: the Poissonian noise, coupled to the photon statistics, and the propagation of the uncertainties associated to the operations involved in the calibration of the flux in an image. For ALHAMBRA data, the typical errors on the instrumental magnitudes are of the order of 0.01 mag; since the errors associated to the sources for the calibration of the flux are generally smaller than this value by at least one order, we consider this second class of errors negligible, and we will omit them in our estimation of errors, considering only the Poissonian contribution. However, we introduced a threshold for the minimum error equal to  $\Delta m = 0.02$ , allowing a more realistic error estimation for the brightest objects. Although this value was chosen on arbitrary basis, it represents a realistic estimation of systematics and uncertainties from all the calibration steps.

The error on the magnitude can be expressed as a function of the signal-to-noise ratio (SNR) as follows:

$$dm = -2.5 \log \left( 1.0 - \frac{1}{SNR} \right) \quad (3.4)$$

There are at least two ways of computing the SNR which are of our interest, one more direct which only needs the knowledge of magnitude zero-points, and the other more detailed, requiring a precise knowledge of the many parameters characterizing the efficiency of the light path through the telescope, although they are both based on the estimation of the number of photons (or, more precisely, electrons) collected by the detector. Below we briefly present both.

Firstly, and common to both methods, we have to take into account the ab-

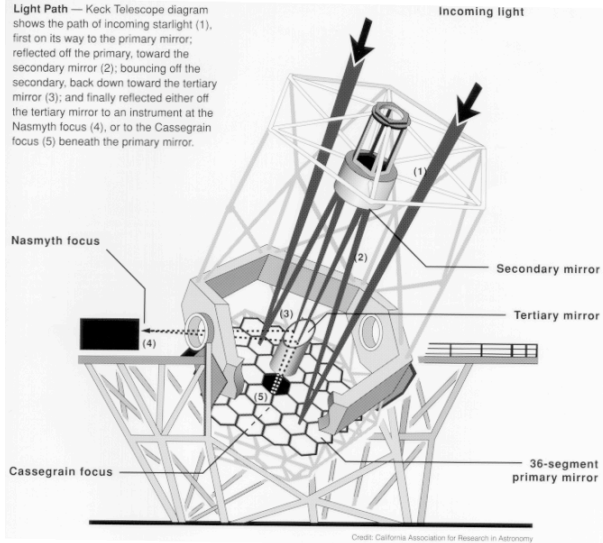


**Figure 3.3:** Schematic view of the optical path through a telescope (image credits: Keck telescope).

sorption of photons due to the atmosphere. This is generally known in units of magnitudes as the *extinction* and depends on the wavelength and on the fraction of water vapour present in the air. The total amount of absorption of the atmosphere given by the extinction depends linearly on another parameter, the *airmass*, which is the length of the optical path through the atmosphere. The loss given to the atmosphere can then be written in terms of magnitude as:

$$\Delta m = X \cdot E \quad (3.5)$$

with  $\Delta m$  the loss in flux expressed in magnitude units,  $X$  the airmass and  $E$  the extinction.

The value of  $E$  is generally recovered from the observation of *standard star fields* and will not be covered here. Instead, we used for it average values. From now on, when we refer to flux or magnitudes, we will be referring to the value of the magnitude after applying the atmosphere absorption correction given in eq. 3.5.

The first method reconstructs the path of the photons starting just after passing through the dome to the photoelectric effect which converts them into electrons in the CCD. Figure 3.3 shows a general schematic of the whole path. As it can be seen, the path involves reflection by at least 2 (although it is also common to find 3) mirrors, each one with its own reflection efficiency, passing through a lens system and a filter. Finally the photons collide on the CCD where they are converted to electrons. Each one of these stages has its own efficiency. The final value for the flux  $\Phi_f$  on the CCD can then be written as:

$$\Phi_f = \Phi_s \cdot Q_{tot} \quad (3.6)$$

with  $\Phi_s$  is the airmass-corrected flux and  $Q_{tot}$  is the convolution of all the efficiencies. The number of photons  $n_\Phi$  collected by the CCD camera is then:

$$n_\Phi = \Phi_f / h \cdot A \cdot t_{exp} \cdot \omega_{filter} \quad (3.7)$$

where  $h$  is the Plank constant,  $A$  is the effective area of the telescope<sup>1</sup>,  $t_{exp}$  is the exposure time and  $\omega_{filter}$  is the width of the pass-band filter. In the case of Poisson noise, then for the  $SNR$  we have:

$$SNR = \frac{n_\Phi}{\sqrt{n_\Phi + n_\Sigma + e^2}} \quad (3.8)$$

where  $n_\Sigma$  is the number of photons coming from the same region of the sky covered by the object and  $e$  is the detector read-out noise.

It is worth to note that the determination of the Poisson noise directly relies on the accuracy with which we know all the contributions to the  $Q_{tot}$  term. It is usually difficult to exactly know for example the percentage of reflectance of a mirror, which may vary (as time passes) between  $\approx 90\%$  to  $\approx 60\%$  in the worst cases.

One way to take into account this problem in an effective way is implemented in the second method. This method is in some sense symmetric to the previous one with respect to the CCD, as the computation of the number of photo-electrons is done starting from the counts (ADU, for Analog to Digital Unit) an object has

---

<sup>1</sup>The effective area is the area of the main mirror, freed by obstructions like secondary mirror and other possible instrumentation.

on the detector.

Continuing to follow the path of the light coming from our source, once the photons have fallen on the detector, the photoelectric effect converts them to electrons. When reading the detector, the electronics will assign a unitary digital value to each fixed bunch of electrons it finds in each pixel. The value of this fixed bunch is called *gain* and is expressed in electron/ADU.

The conversion of the number of ADUs to physical magnitudes  $m$  is given by:

$$m = -2.5 \log(ADU/ADU_0) = -2.5 \log(ADU) + m_{zp} \quad (3.9)$$

where  $ADU_0$  is the number of counts corresponding to an object of with magnitude equal to  $m_{zp}$ .

In this way, the number of electrons of a source given its counts can be directly obtained from the inversion of eq 3.9 and recalling the definition of gain  $g$ :

$$n_{\Phi} = g \cdot 10^{-0.4(m-m_{zp})} \quad (3.10)$$

The zero-point terms  $ADU_0$  and  $m_{zp}$  in eq. 3.9 and 3.10 are the transformation of the  $Q_{tot}$  factor in eq 3.6 to the counts dominion and thus require to be determined somehow. This is done by observing objects whose flux is well known in advance, allowing to recover the values for  $m_{zp}$  as a function of filter, for a given telescope-detector system. At this point, the SNR can then be computed following eq. 3.3 and 3.4.

In our work, we implemented both methods. Since we are going to deal with ALHAMBRA data taken with the LAICA and Omega 2000 instruments at the 3.6m telescope of CAHA Observatory, the  $m_{zp}$  adopted were those corresponding to the respective instruments and filters measured though the ALHAMBRA pipeline.

In the simple case of detecting an object in a single frame, the number of sigmas  $N_{\sigma}$  is then given by:

$$N_{\sigma} = \frac{f}{s} \quad (3.11)$$

When summing up several images with no weight (or a constant one), the

number of sigmas the object will have on the final frame will be given by:

$$N_{\sigma} = \frac{\sum_{i=1}^n f_i}{\left(\sum_{i=1}^n s_i^2\right)^{1/2}} \quad (3.12)$$

where  $n$  is the total number of frames and  $f_i$  and  $s_i$  are the flux and the error of the object in the different frames.

Introducing weights is a quite straightforward step. Indicating with  $w_i$  the weight for the  $i$ -th filter, and applying the normalization condition so that the total weight equals 1, we obtain for the total flux  $F$  and noise  $S$ :

$$F = n \frac{\sum_{i=1}^n w_i f_i}{\sum_{j=1}^n w_j} \quad (3.13)$$

$$S = \left[ \frac{\sum_{i=1}^n (w_i s_i)^2}{\left(\sum_{j=1}^n w_j\right)^2} \right]^{1/2} \quad (3.14)$$

which lead to the following expression for the total number of sigma with weighted images:

$$N_{\sigma_{Tot}} = \frac{F}{S} = \frac{\sum_i w_i f_i}{\left(\sum_i (w_i s_i)^2\right)^{1/2}} \quad (3.15)$$

The number of sigmas  $N_{\sigma_{Tot}}$  was computed following the above procedure as a function of redshift  $z$  and absolute magnitude  $M_r$  in the rest-frame filter  $r$  for an early-type and a spiral SED.

### 3.2.3 Monte Carlo simulation

The implementation of a Monte Carlo method for the determination of the detection completeness was suggested by the idea that simulations done with real data would mimic all the observational effects with improved detail respect to the analytic method. In this section we will describe its implementation.

As explained in section 3.1, our aim was to determine the completeness of the detection of galaxies, as a function spectral type, redshift  $z$  and absolute magnitude in a desired rest-frame band.

The first step was then to choose on one of the fields, an elliptical and a spiral galaxy with average apparent profiles and characteristics, in order to be good representatives of the objects in the fields. As such, the two galaxies were chosen with the following criteria in mind:

1. be among the brightest object ( $m < 18$  in each one of the 20 filters) in the field, with a correspondingly high SNR;
2. be as much isolated from close objects as possible;
3. have a low spectroscopic redshift ( $z = 0.1 - 0.2$ ).

Points 1 and 2 together assure that both the statistical error on the apparent flux is small and the risk of a systematic bias caused by possible contamination from nearby objects is low. The third point shows its reason as we would like to take into account the possible flux losses linked to the light profile of a galaxy seen at different redshift. In fact, the optical resolution on the image is not infinite both because of natural limitation of the detector and because the telescope used to obtain the data is placed on the earth, meaning that the light should have passed through the perturbation of the atmosphere, with a consequent degradation of the details. The choice of spectroscopic redshift (as opposed to the photometric redshift) allows to make sure that the computed corrections are accurate. The appearance in the 20+3 ALHAMBRA filters of the two galaxies chosen as templates is shown in figure 3.4.

Although not necessarily linked in principle, the two morphological types of galaxies chosen as templates were associated each to a *spectral energy distribution* (SED), so that the morphological elliptical galaxy had the SED of an early type

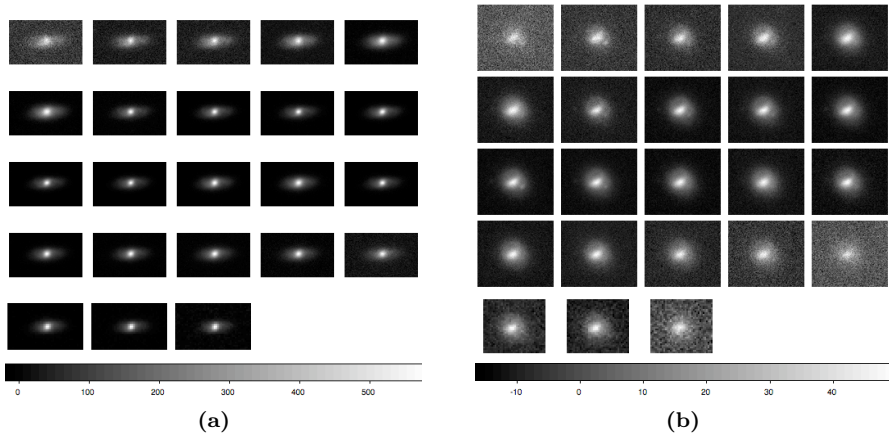


**Figure 3.4:** Raw images of the templates for elliptical (a) and spiral (b) galaxy used for the Monte Carlo procedure, in the 20+3 ALHAMBRA filters (left to right, top to bottom filters are: AL365, AL396, AL427, AL458, AL489, AL520, AL551, AL582, AL613, AL644, AL675, AL706, AL737, AL768, AL799, AL830, AL861, AL892, AL923, AL954, J, H, Ks). ADU values are represented by the grey scale, with black corresponding to -15ADU, and white to 50ADU

galaxy while the morphological spiral galaxy was associated to a late-type SED. In the following, when talking about elliptical (resp. spiral), galaxy template we will be referring to indistinctly its morphological profile or its SED, unless otherwise specified.

The median of the sky value is then computed on two regions (summing to around 200 pixels) close to each template in order to take into account local variations of the background, but nevertheless far enough from the template and from any other object to avoid contamination to its flux. The obtained sky value was then subtracted from the corresponding template.

The actual process starts with the definition of an absolute magnitude-redshift ( $M_i, z_i$ ) grid, the same for each template, although this is not a strict requirement. In our case, the absolute magnitude was chosen to be in the Sloan  $r$  filter, and ranging from -24 to -12; for the redshift, since the median of the redshift of the objects is  $\approx 0.8$ , a range covering  $z_i \in [0.0, 2.0]$  in steps of 0.2 was judged sufficient to cover the great majority of the objects in the ALHAMBRA catalogue.

For each point of the grid, the pixel scale corresponding to the considered redshift  $z_i$  is computed and the original template image is *resized* according to the new pixel scale, under the assumption of conservation of the physical size of the galaxy in the template. In particular this means that we omitted any evolutionary effect from our simulation. Supposing that the original template image refers to a galaxy at  $z = z_0$ , the pixel scale factor corresponding to  $z = z_1$  is:

$$p(z_1) = p(z_0) \frac{da(z_1)}{da(z_0)} \quad (3.16)$$

where  $p(z_i)$  is the pixel scale at redshift  $z_i$  and  $da(z_i)$  is the comoving angular distance at  $z = z_i$ .

The apparent magnitude corresponding to  $(M_i, z_i)$  was computed for each template and in each filter from the matching SED, taking into account K-corrections and IGM absorption following the procedure presented in Section 2.2; the fluxes of the templates were *rescaled* accordingly in each filter.

This last step can be divided into two parts. At first it is necessary to apply the conservation of flux to the *resized* template, so that it will have the same counts as in the original scale. This operation can in principle be done by just multiplying the counts of the rescaled and resized template by the squared ratio of the original pixel scale to the equivalent pixel scale at the given redshift  $z_i$ .

We proceeded to verify the accuracy obtained with this method by extracting with SExtractor the photometry of the template on the original frame and on the rescaled and flux-conserved template image, for the pixel scale range covering the redshift range of our choice. Figure 3.5 shows the difference between the magnitude of the template on the original frame and on the resized frames in the case of the spiral galaxy template. The associated errors are those associated to the photometry, as given by SExtractor. As it can be seen, the peak-to-peak variation is of about 0.06 – 0.07 mag, larger than the intrinsic errors from the photometry. This fact suggested to discard this method for flux conservation and to instead replace it with the empirical way of computing the flux factor directly from the photometry on the resized template.

At this point, the magnitude of the template at the desired redshift  $z_i$  is

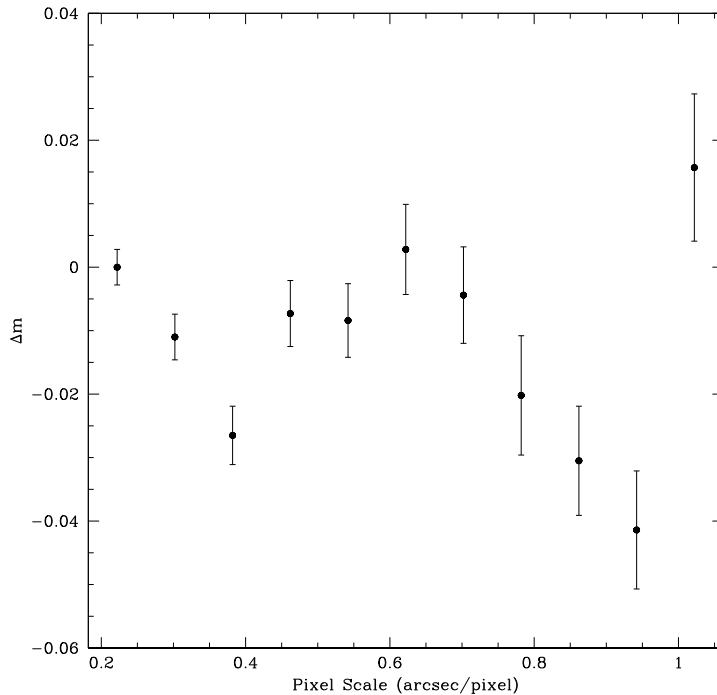


**Figure 3.5:** Magnitude difference as function of pixel scale, for the spiral galaxy template

obtained multiplying the resized template by the factor  $A$  given by:

$$A = 10^{-0.4(m_z - m_0)} \quad (3.17)$$

with  $m_z$  and  $m_0$  the apparent magnitude<sup>2</sup> of the template computed for  $z = z_i$  and on the original frame respectively.

In order to preserve the same image quality of the original image also on the rescaled templates (which would otherwise have had a higher resolution when copied back to the original frames) each template was convolved with a PSF. The

<sup>2</sup>The magnitudes used in eq. 3.17 are instrumental magnitude. In this case, the full photometric calibration is not necessary since the filter, CCD and atmospheric absorption are the same in the two cases.

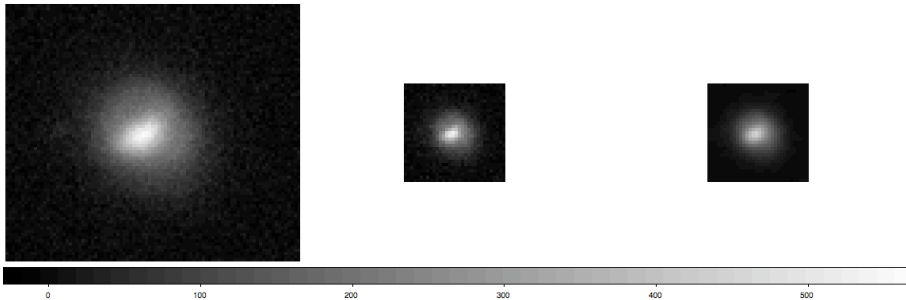


**Figure 3.6:** Construction steps for the spiral galaxy template at  $z = 1.2$  in the 644 nm filter. From left to right: selected template on original frame; template after pixel scale resize corresponding to  $z = 1.2$ ; final template after gauss convolution. Images are displayed with the same cuts levels and magnification factor.

shape of this PSF was chosen to be a gaussian, as it generally describes well the effects of the *seeing*. The FWHM of the convolving gaussian  $f_c$  was then set to:

$$f_c = f_0 - f_r \quad (3.18)$$

where  $f_0$  and  $f_r$  are respectively the FWHM of the PSF on the original frame and on the rescaled frame. Figure 3.6 presents the various stages of the construction of the template for the spiral galaxy at  $z = 0.6$ .

At this point we have one template image for each filter and for each point of the  $(M_i, z_i)$  grid.

The following step was to add each template for the desired point on the  $(M_i, z_i)$  grid to the original frames of each filter in 40 random positions covering the whole frame, extract the photometry and compare the number of recovered templates respect to the number of initially injected templates. The above was repeated 10 times, in order to obtain better statistics. Two distinct routines were run: one for elliptical galaxies and the other for spiral galaxies.

### 3.2.4 Detection completeness on the 20 filters

In the course of our work, the above procedure was implemented in two distinct ways. At first, the set of 40 random positions was generated each time, with different sets for different filters. The template corresponding to the galaxy at

$(M_i, z_i)$  was then added to the original frame in the corresponding filter at the generated positions. SExtractor was then run independently on each filter frame in order to obtain the photometry of the *enriched* image. The obtained catalogue was then compared to the original random positions via IRAF task `tmatch` and the number of detected templates recovered.

The average of the 10 completeness level was the fitted by a Fermi distribution, which approximates the step function in a smooth way. The functional used is of the form:

$$h(m) = \frac{\alpha}{1 + e^{-2\kappa(m-\mu)}} \quad (3.19)$$

where  $\alpha, \kappa$  and  $\mu$  are the free parameters related to the overall normalization, to the slope of the falling region and to the abscissa offset respectively. It is easily recovered that  $h(m = \mu) = \alpha$ , i.e so that we can consider  $\mu$  as the point where the completeness level starts to decrease. Figure 3.7 shows the completeness as a function of absolute  $M_r$  magnitude for the elliptical template at  $z = 1.0$ . The 80% and 50% completeness levels are obtained from the inverse  $j(c)$  of eq: 3.19:

$$j(c) = \mu - \frac{1}{2\kappa} \ln \left( \frac{\alpha}{c} - 1 \right) \quad (3.20)$$

with  $c = 0.8$  and  $0.5$  respectively.

The plot shows that, despite the points at the bright end correspond to a completeness level of 100%, this behavior can not be well reproduced by the Fermi function fit. In order to minimize this effects, the fitting procedure was repeated fixing the value for  $\alpha = 1$ . Figure 3.8 shows the curve corresponding to this new case. As it can be noted, the rapid decline of the completeness level renders the two methods indistinguishable from the completeness point of view.

The absolute magnitudes  $M_r$  corresponding to 80% and 50% completeness level for elliptical and spiral galaxy template as a function of filter and redshift are shown in figure 3.9. As it can be seen from the plots, the value of the absolute magnitude corresponding to the 80 and 50 completeness levels can have peak-to-peak variations of several magnitudes. In order to find a unique value for each redshift, we decided to consider an object as detected when it appears in at least three filters. With this criterion, the absolute magnitude corresponding to the desired completeness level for the redshift value of interest is the third faintest one among the full filter set.

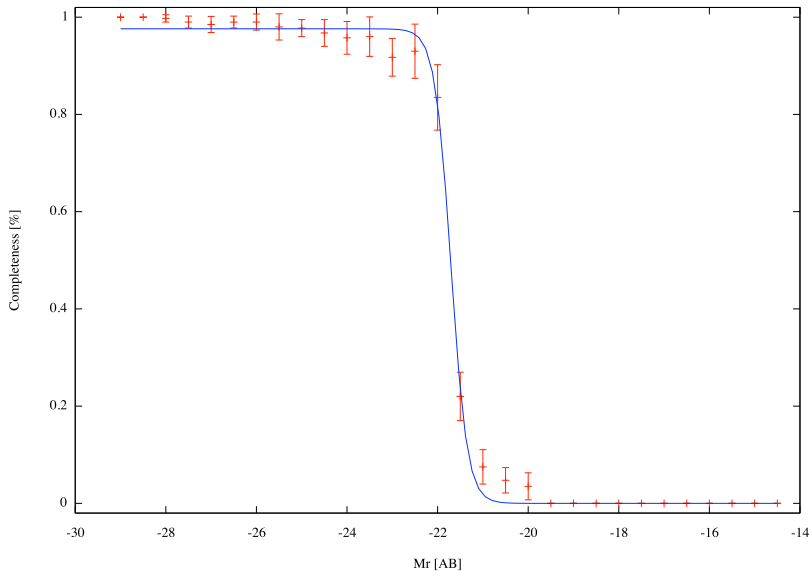


**Figure 3.7:** The points represent the fraction of objects recovered by SExtractor, as a function of absolute  $M_r$  magnitude; error bars are the standard deviation of the average of the 10 samples. The solid line represents the best fitting Fermi distribution.

### 3.2.5 Detection completeness on the deep image

This method however is somehow arbitrary and does not take into account the actual procedure adopted to construct the *deep image*, used by the ALHAMBRA pipeline to determine the catalogue of objects of each field.

The above method was modified so that the same random list of positions was used for all the filters. Each enriched image was then multiplied by the corresponding weight necessary to create the deep image (see section 4.4) and the weighted frames, one per filter, were summed up. In this way we obtained a good approximation of the deep image enriched with synthetic galaxies. The catalogue of all the objects was then created as usual with SExtractor and the actual number of recovered templates obtained via the IRAF tmatch task. In order to keep the simulation as much realistic as possible, SExtractor parameters were synchronized to those actually adopted by the pipeline. Data were then averaged and analyzed as with the previous method, fitting a Fermi distribution

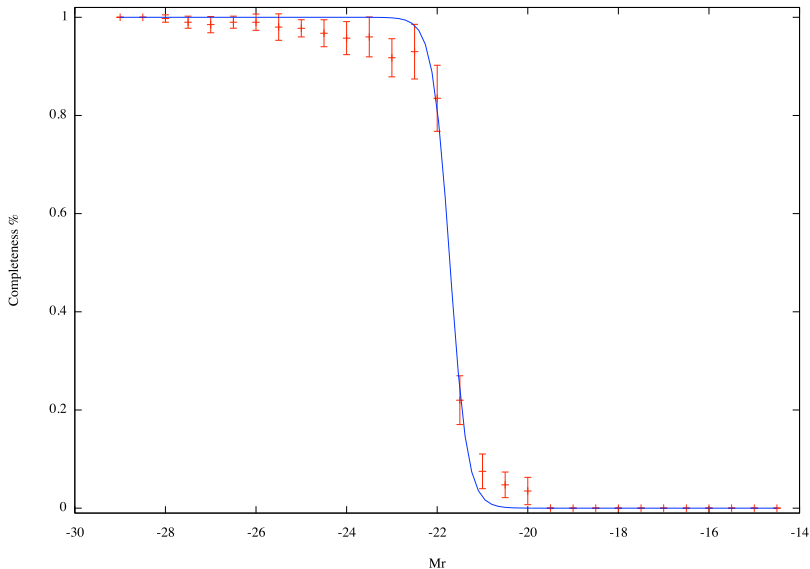


**Figure 3.8:** Same as for Figure 3.7

and computing from the inverse function the absolute magnitude corresponding to the completeness level.

### 3.2.6 Point-source completeness

The fraction of recovered objects was computed also for the case of stellar-like objects. This has a double aim: on one side, we could compare our results with already published data (Cristóbal-Hornillos et al., 2009), while on the other side, we could define a completeness for the limiting case of point-source objects, like very distant and/or small galaxies may appear on the ALHAMBRA frames.

The procedure adopted for this case was slightly different from the one presented in the previous sections. In order to allow for a direct comparison with the literature, the procedure was applied to frames in the  $J$  observational-frame filter. In this case, the image of a star was chosen following the same brightness and isolation criteria adopted for the galaxy templates, as described in the previous section, and the background cleaned from the template. At this point, the flux

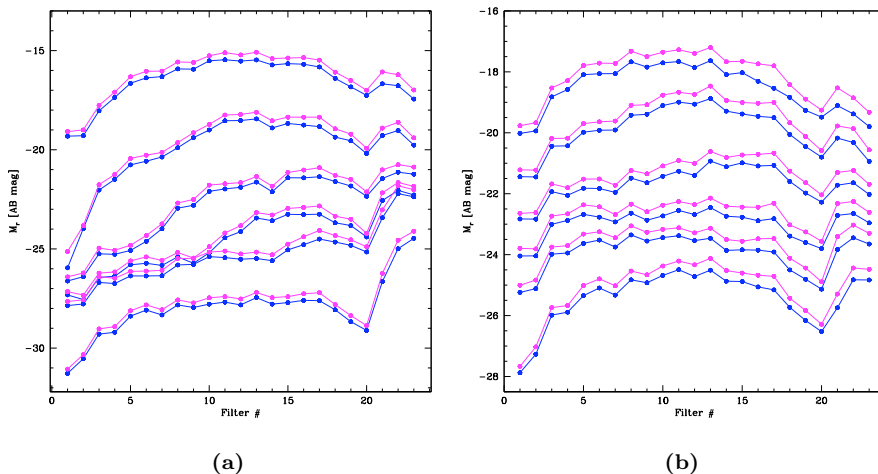


**Figure 3.9:** Left panel: absolute magnitudes corresponding to 80% (blue) and 50% (magenta) completeness levels for elliptical galaxies, as a function of filter. From top to bottom, data refers to  $z = 0.1, 0.5, 1.0, 1.5, 2$  and  $3$ . Right panel shows the equivalent of panel (a), but for spiral galaxies.

of the star was rescaled according to a grid of *apparent* magnitudes. The fraction of detected objects was recovered in the usual way, adding the star template to 40 random positions, extracting the photometry through SExtractor, matching the catalogue with the original random positions, repeating the whole process 10 times, in order to improve the statistics, and analyzing the average of recovered fractions with the Fermi distribution.

The comparison of the completeness curve, visible in figure 3.10, with the similar curve from Cristóbal-Hornillos et al. (2009), also plotted in the same figure, shows a good agreement.

The same routine was finally applied to the whole set of filters. In this case, the apparent magnitude for each filter was computed on the basis of a SED constant in wavelength, so that at each iteration the apparent magnitudes were the same on all the filters. In figure 3.11 we show the 80% and 50% completeness level in terms of apparent magnitude as a function of filter. The shape of the limiting magnitudes as function of filters is more rectangular with respect to the bell-shape of the filter efficiencies, and it is a check that the total exposure time in each filter

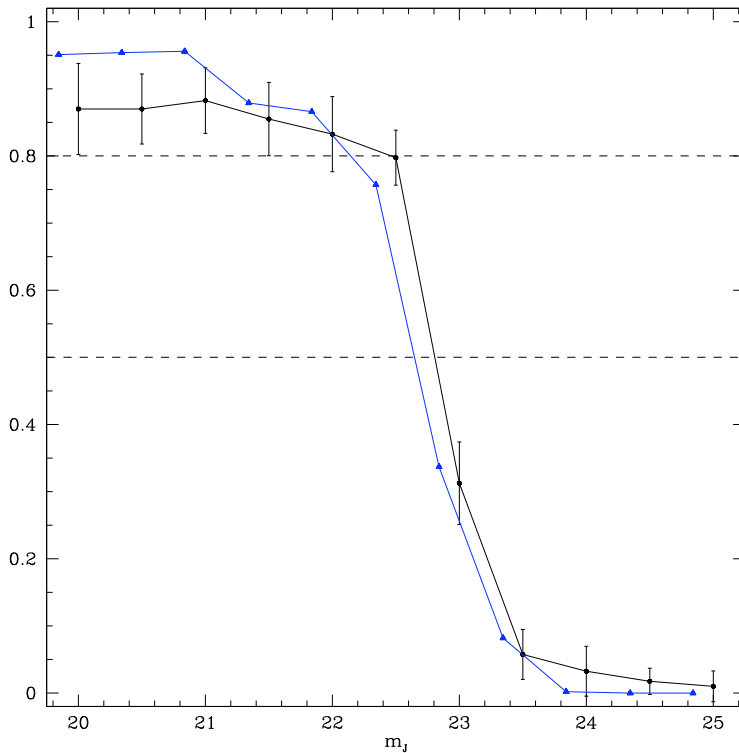


**Figure 3.10:** Black solid line and circles: recovered fraction of point source objects as a function of apparent magnitude, in the J filter. Blue points: completeness in the same band from Cristóbal-Hornillos et al. (2009).

was chosen in order to obtain an as much as possible homogeneous photometric depth.

The apparent magnitude corresponding to the 80% completeness limit was converted to absolute magnitude in the rest-frame filter  $M_r$ , using the same intervals for  $z$  and the same SED used for the galaxy templates completeness. This allowed to obtain a completeness limit for point-like sources which could directly be compared with the completeness limits obtained for the galaxy templates.

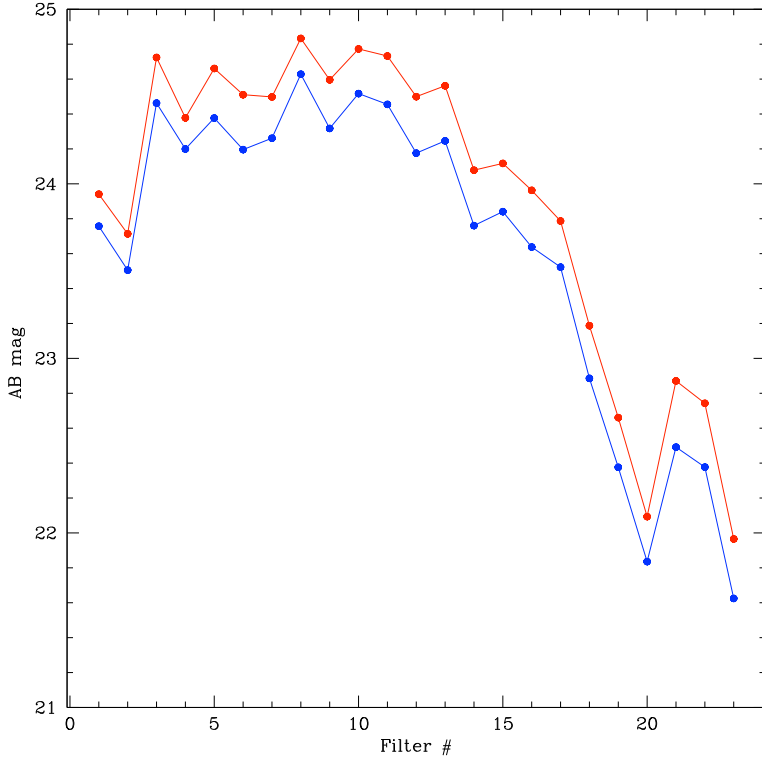


**Figure 3.11:** 80% (blue) and 50% (red) completeness levels for the stellar-like object.

### 3.2.7 Results

The plots in figure 3.12 show the 80% completeness levels obtained with the two different Monte Carlo implementations. The two plots show a substantially similar behaviour from  $z = 0.2$  to  $z \approx 0.7 - 0.8$ . At this value, the two methods show their differences; in particular, the deep image, which is a more realistic representation of the procedure adopted by the pipeline for the object detection, reveals to be more sensitive to the differences in the SED of elliptical and spiral. This suggests that such differences should be fully taken into account at the time of performing statistical analysis, as can be for example the computation of the

luminosity function. The reason for the difference might be found in the way we defined the magnitudes corresponding to the completeness levels for the first case. In fact, as it can be seen from figure 3.9, as far as the redshift increases, the faintest magnitudes move towards the red filters, if not directly to the IR, especially for the case of elliptical galaxies templates.

Figure 3.13 shows the results from both the Monte Carlo and the analytic methods. For this latter case, the line is the contour of the  $N_\sigma \equiv 3$ , which, in our implementation, should correspond to the three sigmas limit imposed by the pipeline to detect objects.

We can identify two major regimes:

1. For  $z < 1.0$  there is not great agreement between the analytic and the Monte Carlo method, with differences that reach  $\approx 1$  magnitude at the lowest redshift bin. The fact that in the analytic method the effect of the luminosity profile is not properly taken into account and the only way the apparent dimension is considered is in a plain way (all the pixels falling inside the shape of the galaxy have the same weight) together with the fact that in this redshift range the effect of apparent dimension is not negligible (see Figure 3.2) could well explain this difference.
2. For  $z > 1.0$  the agreement is quite good, improving as we go to higher redshifts, especially in the case of spiral galaxy. This fact can also be related to what exposed in the previous point.

## 3.3 Conclusions

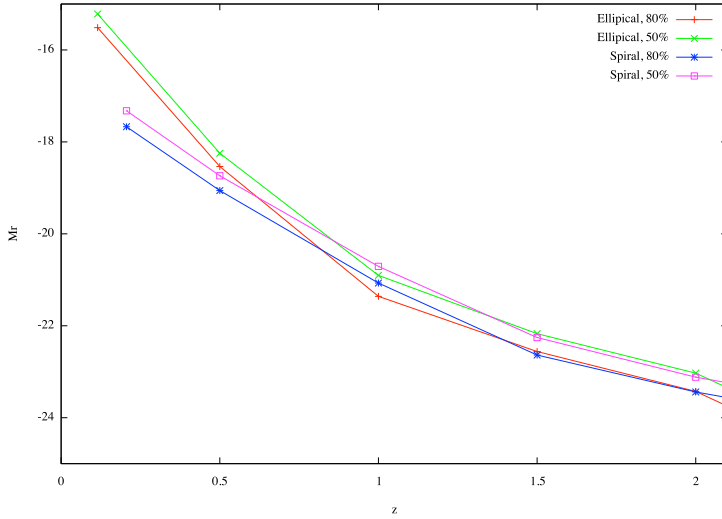
---

The availability of a high number of medium band filters covering the whole optical spectrum makes the definition of detection a critical point. This complication is of course replicated to the definition of completeness.

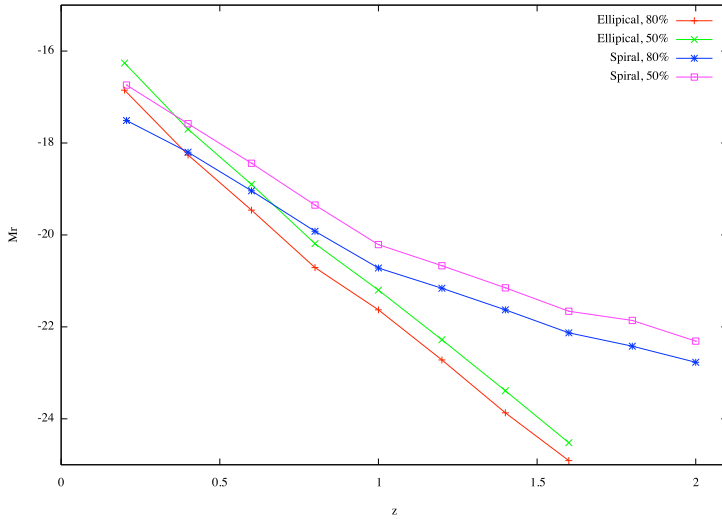
We have shown that the apparent sizes of galaxies are non-negligible to at least  $z \approx 1$ , so that it is important to take into account this effect when determining the completeness.

We have implemented two distinct methods for the determination of the detection completeness, as a function of spectral and morphological type as well as of the effects of the redshift on apparent size and observed SED. One is totally

### 3. DETERMINATION OF DETECTION COMPLETENESS



(a)



(b)

**Figure 3.12:** (a) 80% and 50% completeness levels for elliptical and spiral galaxy, recovered with the first Monte Carlo method presented in the previous section. (b) same as above, but for the second implementation (deep image reconstruction).

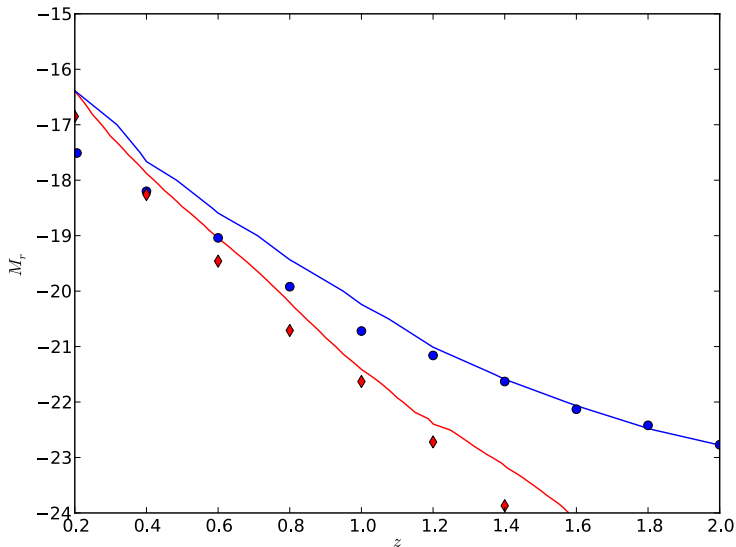


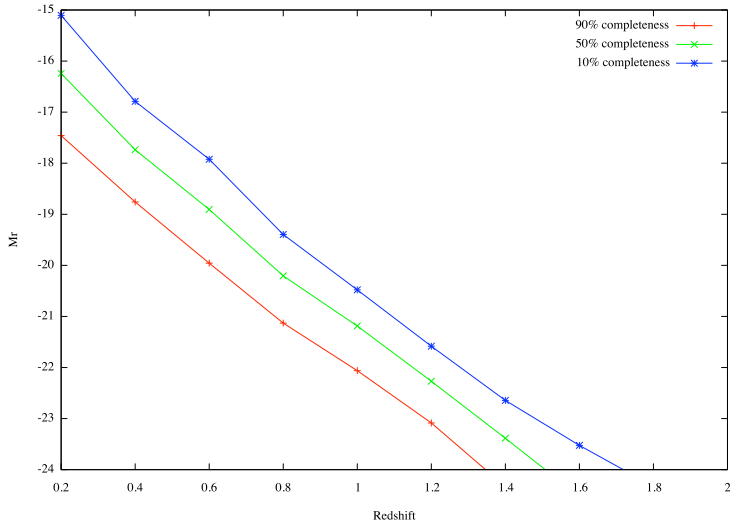
**Figure 3.13:** Solid lines: analytic  $3\sigma$  detection limits for elliptical (red) and spiral (blue) galaxies compared to MC 80 % completeness from the deep image for elliptical (filled diamond) and spiral (filled circles) galaxies.

based on a simulation of the instrumental apparatus (telescope+camera) used for the observations, while the other is a Monte Carlo analysis based on real data.

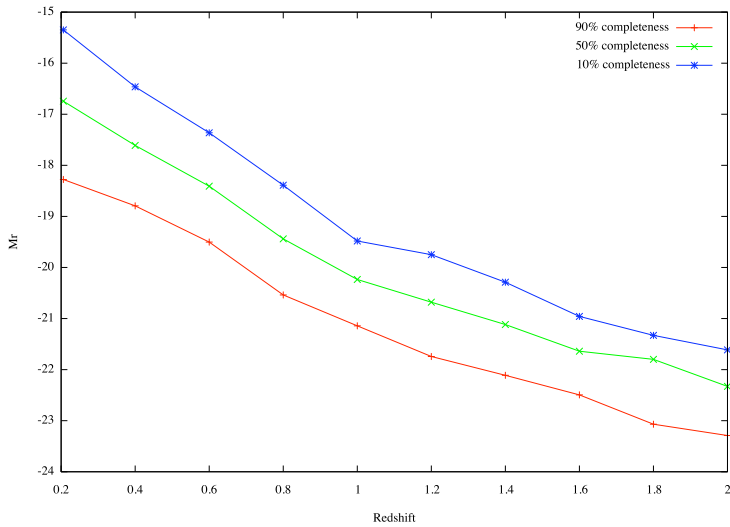
Two different Monte Carlo methods were implemented. The first one allows to derive the completeness from a full filter set basis; the second method, instead, tries to reproduce the way the deep image is created and how the detection is done on it.

The two Monte Carlo implementations showed quite different results in particular starting from  $z \approx 0.7$ . The comparison of the analytic method with the second of the Monte Carlo methods revealed that the analytic way is a fast and quite accurate procedure for determining the completeness. However, the difference with the Monte Carlo method for  $z < 1$  stressed the importance of taking full consideration of the luminosity profiles of objects linked to the apparent sizes and morphological type of objects.

### 3. DETERMINATION OF DETECTION COMPLETENESS



(a)



(b)

**Figure 3.14:** 90%, 50% and 10% completeness levels for elliptical - panel (a) - and spiral galaxy - panel (b) - recovered with the Monte Carlo method on the deep image.

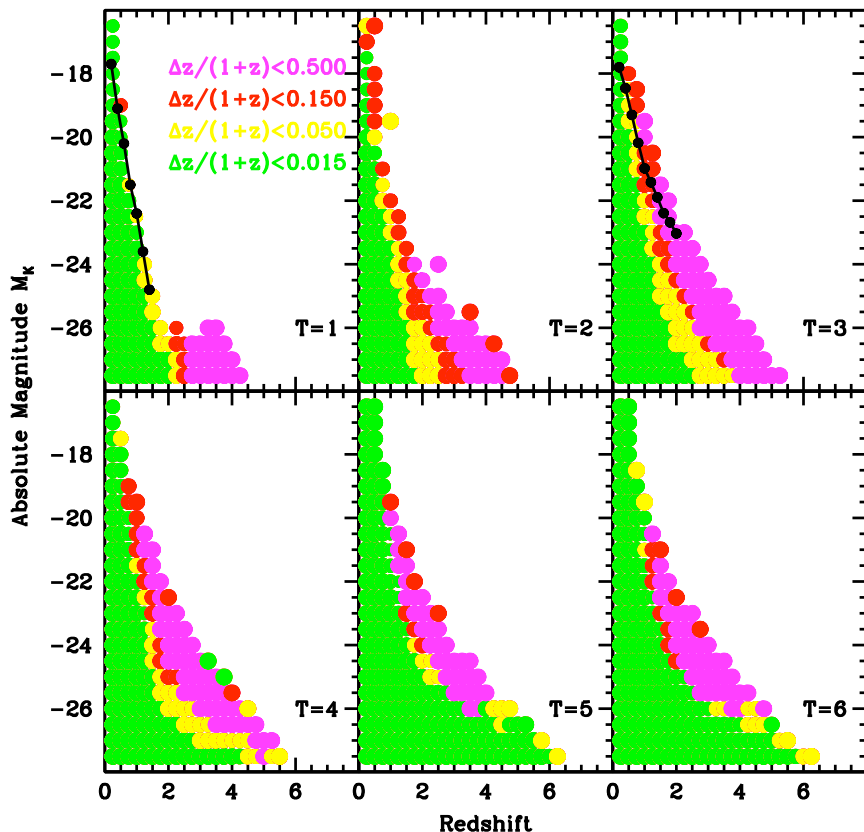


**Figure 3.15:** Photometric redshift uncertainties as a function of spectral type and redshift. The black points mark the completeness detection limits measured via the Monte Carlo method.

We consider the full MC method on the deep image however to be a more realistic reconstruction of the process actually implemented by the ALHAMBRA data reduction pipeline. The results obtained through this method can then be assumed to be a more robust and reliable estimate of the detection completeness levels as a function of redshift and spectral class. The final values for the absolute magnitudes  $M_r$  corresponding to corresponding to the 10%, 50% and 90% of detections is presented in Figure 3.14, for elliptical and spiral galaxies, as a function

of redshift.

So far we were concerned about the completeness in the object detection phase. However, a full determination of the completeness for extra-galactic objects needs to take into account also how well we are able to recover the redshift of each object. This depends in a first instance on the SNR of the photometry which, as we have seen, depends on the absolute magnitude, on the redshift and on the morphological/spectral type of the source. In Figure 3.15 the  $\Delta z/(1+z)$  preliminary uncertainties in photometric redshifts are plotted against redshift, for the six main SEDs adopted by ALHAMBRA. The uncertainties were computed generating a catalogue of synthetic objects. For the elliptical (T=1) and spiral (T=3), the 90% detection completeness levels from the MC on the deep image are also shown. The plot shows that the detection limits for the ellipticals coincide with the boundaries of the  $\Delta z/(1+z) = 0.015$  redshift errors: as far as our objects are brighter than the 90% detection completeness limits, we can reasonably rely on the associated photometric redshift.

The availability of the odds parameter associated to the computation of the photometric redshifts (Benítez, 2000) would allow to estimate in an independent way the completeness in absolute magnitude, for example by applying a threshold to the odds.



# Bibliography

Cristóbal-Hornillos D., et al., 2009, ApJ, 696, 1554

de Vaucouleurs G., 1948, AnAp, 11, 247



# 4

## ALHAMBRA field galaxy Luminosity Function - Preliminary results

### 4.1 Introduction

---

In this chapter we present results for the ALHAMBRA luminosity function (LF), obtained by applying the measurements in object detection completeness to the SWML method for the construction of the LF to preliminary ALHAMBRA catalogues.

The catalogues adopted for this work constitute the *March2011* release. The full data set is composed by 39 fields out of the total of 64 catalogues for the complete list, each one corresponding to a CCD. Each catalogue contains the full photometric information in the 20+3 ALHAMBRA filters together with photometric redshift and best fitting SED template computed with the BPZ code (Benítez, 2000) for  $\approx 13000$  objects, for a total of 501865 sources in the 39 catalogues. The average photometric depth ( $3\sigma$  detection limit) reaches  $AB \approx 24.5$  for the central bulk of optical filters, and  $AB \approx 22$  for the three NIR filters (see Figure 3.11).

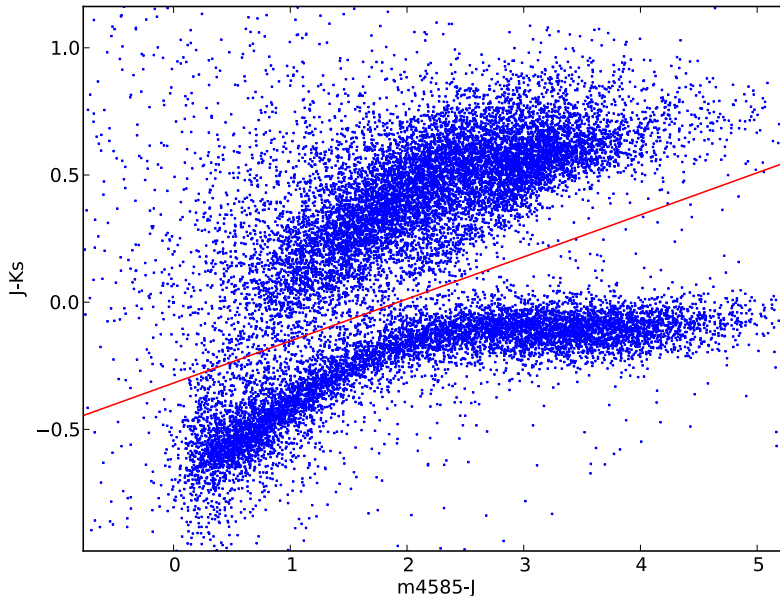


**Figure 4.1:** Two-color diagram used to separate galaxies from stars. For clarity, only objects with a magnitude error smaller than 0.01 are reported. The red line represents Eq. 4.1, used to separate galaxies from stars.

## 4.2 Star-galaxy separation

---

The catalogues of this sample did not include an univocal classification of sources as stars or galaxies, so that, as a first step, we needed to select those objects to be considered as galaxies from the full sample.

The method we applied is the two-color diagram, built using  $(m_{4585} - J)$  vs.  $(J - K_S)$ , very similar to the  $(B - z) - (z - K_S)$  diagram (Daddi et al., 2004) and to that applied in Sect. 5.2.5 on MUSYC data. In particular, in this latter case, the selected stars were checked against an existing catalogue, obtained via SExtractor stellarity parameter and visual inspection on HST images, confirming the validity of the adopted two-color selection. Although the  $U - J$  would have offered a more clear separation between the two classes of objects, we preferred to adopt for the selection a filter with a higher transmission (see. Figure 1.6).

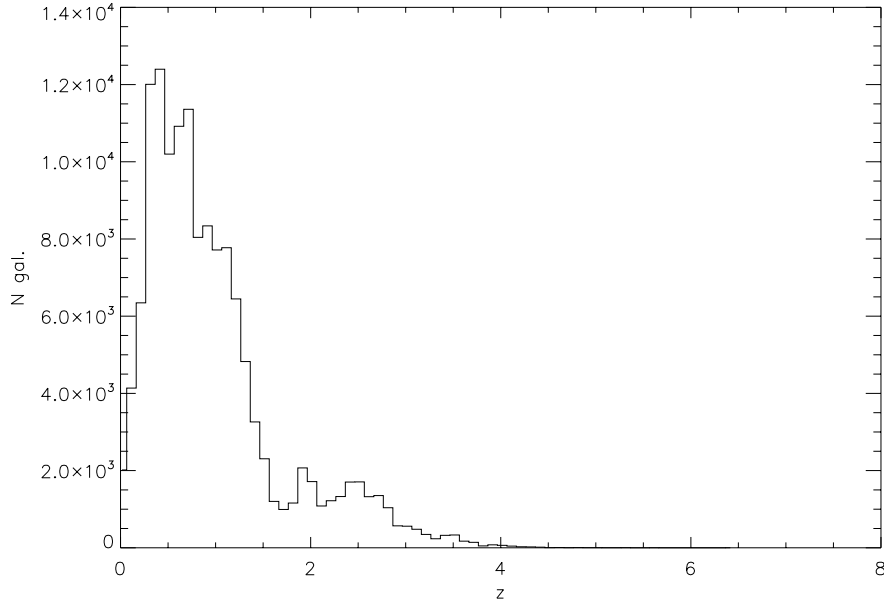


**Figure 4.2:** Histogram of redshift distribution of the sample of objects selected as galaxy through the two-color diagram and satisfying the odds and weight selection criteria.

The two-color diagram is shown in Figure 4.1. We adopted the following limit to split stars from galaxies:

$$(J - K_S) = 0.16 \cdot (m_{4585} - J) - 0.32 \quad (4.1)$$

Very red objects, i.e. those which were not detected in the *AL4585* band were also included in our sample. The fraction of objects selected in this way corresponds to 62% of the whole sample.

In order to consolidate the sample of galaxies and the values of the associated redshift, we applied a selection on the odds parameter<sup>1</sup>, selecting those objects with odds > 0.90. This is the most substantial cut, halving the fraction of selected galaxies.

<sup>1</sup>An estimate given by the photometric redshift code BPZ (Benítez, 2000) of the quality of every calculated redshift.

Since the pointings of each field for each filter do not exactly overlap, the total exposure time across the final image is not uniform, with regions at lower SNR. A further selection was then applied to purge the sample from objects with lower signal-to-noise ratio. A *PixelWeight* parameter, available in the catalogue and defined for each object from its total exposure time and the associated noise map, was then adopted for the selection. The main result of this procedure was the removal of objects falling close to the borders, as expected.

The sample of galaxies selected through this method is composed by 139460 objects (corresponding to the 28% of the total number of objects in the full sample), with redshift between 0.0106 and 7.0 and median  $z_{med} = 0.82$ . Galaxies in the range  $0.3 < z < 1.5$  represent 74% of the total selection, while for  $1.5 < z < 4$  this fraction reduces to 17%; for  $z > 4$  the fraction is totally negligible. Figure 4.2 shows the final distribution of the objects with redshift after applying the selections above described.

The photometric redshifts in the ALHAMBRA catalogue were compared to those available from the COSMOS survey (Scoville et al., 2007). The equatorial coordinates of the galaxies in the catalogue obtained with the previous steps was matched with those in the publicly available COSMOS redshift catalogue (Ilbert et al., 2009). This allowed to compute the difference of photometric redshifts for each object from the two surveys. The result of this comparison is shown in Figure 4.3. In the left panel, the  $\Delta z/(1+z) = z_{COSMOS} - z_{ALHAMBRA}/(1+z_{ALHAMBRA})$  as a function of apparent  $I$  magnitude for the full set of matched galaxies is plotted as black dots, while green circles identify those galaxies whose *ODDS* parameter from the ALHAMBRA catalogue exceeds 0.85. The vertical dash-dotted line indicates the apparent magnitude limit from the COSMOS catalogue obtained from  $\sigma_{\Delta z_{COSMOS}/(1+z)} < 0.012$  (Ilbert et al., 2009). The plot shows that, apart from a small number of outliers and for objects brighter than the limiting magnitude, the photometric redshifts in the ALHAMBRA catalogue agree well with those of COSMOS. This applies to both the full ALHAMBRA sample and to the odds-selected one. The right panel of Figure 4.3 shows the histogram of the distribution of  $\Delta z/(1+z)$  for the odds-selected sample. Fitting a gaussian to the distribution (green line) gives a standard deviation  $\sigma = 0.022$ . Considering that  $\sigma_{\Delta z,cosmos} = 0.012$  and  $\sigma_{\Delta z,alhambra} = 0.015$ , this would give a total standard

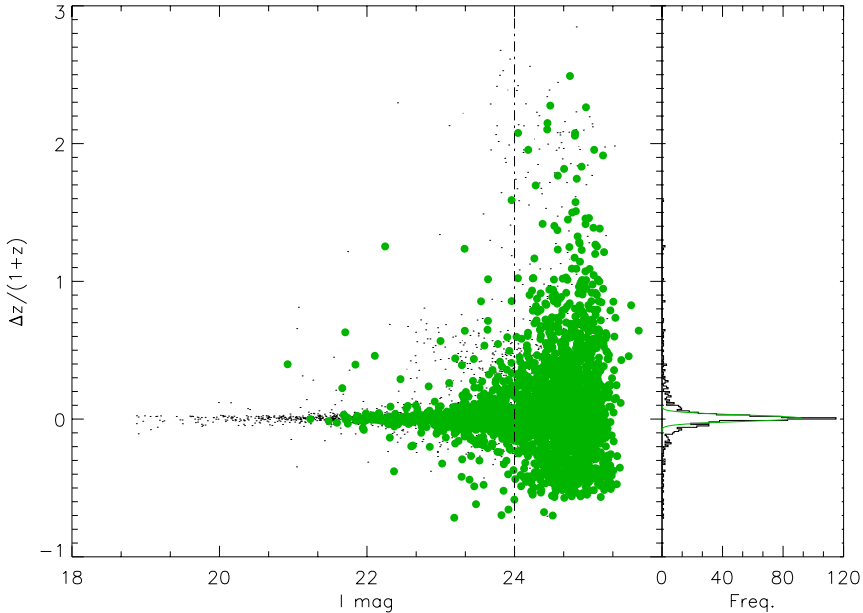


**Figure 4.3:** Left panel: difference between ALHAMBRA photometric redshifts and COSMOS photometric redshifts for a matched sample of galaxies (black points) as a function of apparent magnitude  $I$ . The vertical dash-dotted line marks the apparent magnitude limit of *good* photometric redshifts in the COSMOS catalogue. The green points mark those objects in the ALHAMBRA catalogue with ODDS parameter higher than 0.85. Right panel: histogram of the distribution of the odds-selected sample, with apparent magnitude brighter than  $I = 24AB$ . The green line indicates the result from a gaussian fit.

deviation  $\sigma_{\Delta z, tot} = 0.019$ , in rough agreement with the value obtained from the fit. The above comparison of ALHAMBRA photometric redshifts with those from a deeper survey like COSMOS allows then to rely on the values of photometric redshifts even for the faintest objects in the ALHAMBRA catalogue.

### 4.3 Absolute magnitudes

Given the availability of SED template for each object in the catalogue, absolute magnitudes were computed applying the method described in Sec. 2.2.1, i.e. absolute magnitudes were measured starting from the apparent magnitude in the

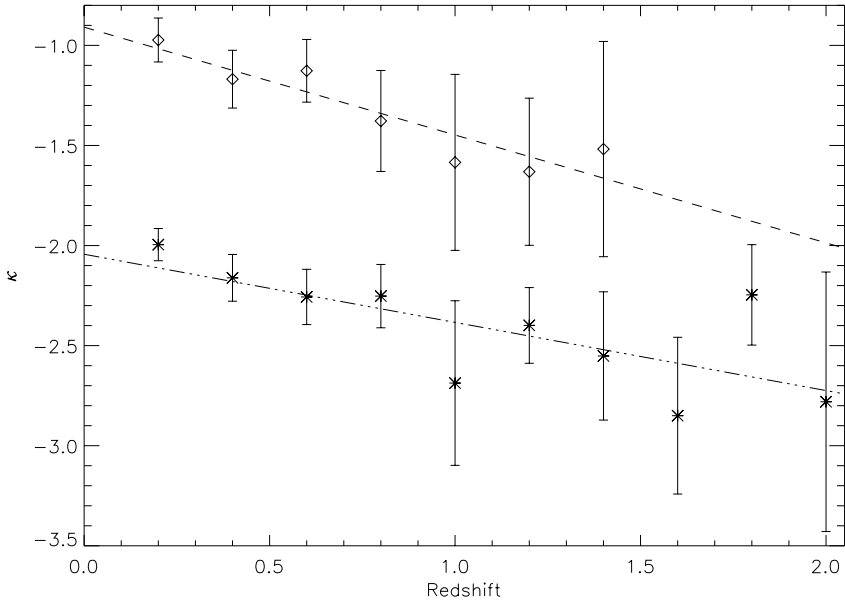


**Figure 4.4:** Evolution with redshift of the  $\kappa$  parameter of the Fermi function used to describe the detection completeness, for the Elliptical (diamonds) and Spiral (asterisks) spectral types. The dashed and dotted-dashed lines indicate the results of the fitting procedure for Ellipticals and Spirals respectively. To improve plot readability, the points and the corresponding fitting line for the spiral galaxies have been arbitrarily lowered by 1.2 units.

filter best matching the redshifted chosen rest frame filter. In our case, the rest-frame magnitudes were computed in the rest-frame SDSS  $r'$  and  $u'$  filters.

The spectral type information available in the catalogues is in the form of a fractional value, meaning that the best-fitting SED template is a linear combination of two consecutive SED templates, the first SED being that one corresponding to the integer part of the spectral classification parameter. This was taken into account at the time of computing absolute magnitude, as this same procedure was replicated. However, since the original templates were not normalized to a common filter, and since a normalization is necessary when summing different templates, we established to normalize each SED template to have the same  $r'$ -band AB magnitude.

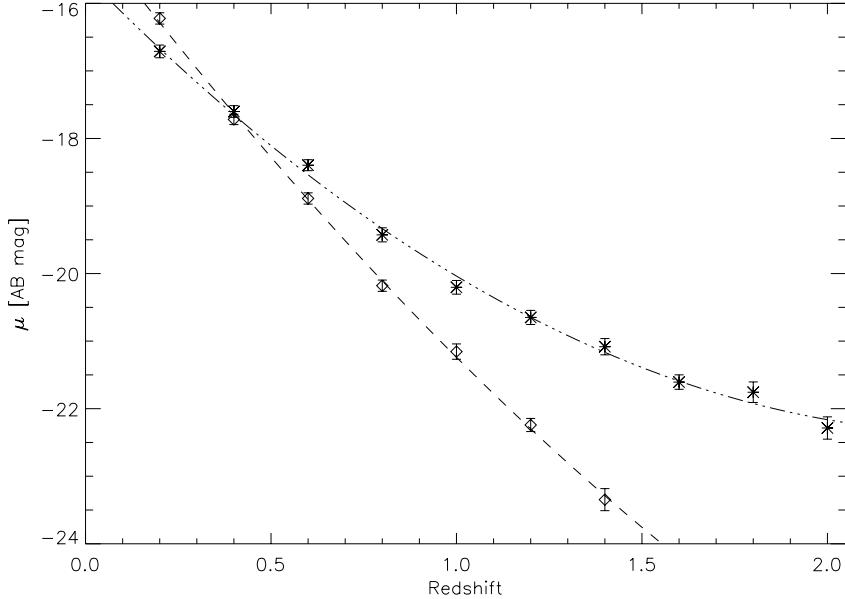


**Figure 4.5:** Evolution with redshift of the  $\mu$  parameter of the Fermi function used to describe the detection completeness, for the Elliptical (diamonds) and Spiral (asterisks) spectral types. The dashed and dotted-dashed lines indicate the results of the fitting procedure for Ellipticals and Spirals respectively.

## 4.4 Detection completeness

In order to take full advantage of the information contained in the plots relative to the detection completeness (Figure 3.14) presented in Sect. 3.3 in the computation of the LF, we parameterized the behavior of the two coefficients ( $\kappa$  and  $\mu$ )<sup>2</sup> defining the Fermi function (Eq. 3.19) as a function of redshift for each of the two used spectral types, i.e. elliptical and spiral template.

The  $\kappa$  parameter was fitted by a straight line, while for the  $\mu$  a parabola was adopted. Data together with the results of the fits are presented in Figure 4.4 and Figure 4.5.

The described procedure allowed to associate to each redshift value (i.e. to

<sup>2</sup>We omitted to fit the  $\alpha$  parameter, related to the normalization of the Fermi function, as in our work this was kept fixed to a constant value of  $\alpha \equiv 1.0$ .

z range	z median	Age (Gyr)	Comoving Volume (Mpc <sup>3</sup> )	Num. objects
0.004-0.08 <sup>a</sup>	0.04	12.919	$9.3 \times 10^6$	66846
0.3-0.6	0.45	8.789	$2.3 \times 10^6$	33743
0.6-1.0	0.78	6.735	$6.4 \times 10^6$	39250
1.0-1.5	1.19	5.065	$11.9 \times 10^6$	30851

<sup>a</sup> Baldry et al. (2004) SDSS data set.

**Table 4.1:** Synoptic table with the main physical parameters corresponding to the redshift intervals chosen for our analysis. The age corresponds to the median redshift, while the co-moving volume was computed for the 2.5 square degrees covered by the current data release. For comparison, in the first line of the table we report the corresponding parameters from the SDSS local sample analyzed by Baldry et al. (2004).

each galaxy) a reasonably consistent weight given by the inverse of the completeness fraction of the corresponding spectral type at the given redshift (Zucca, Pozzetti, & Zamorani, 1994; Lin et al., 1996). This weight was directly used in the procedure computing the LF.

## 4.5 Color-Magnitude diagram

In Figure 4.6 we show the galaxy color-magnitude (CM) plot, for three redshift ranges:  $0.3 < z < 0.6$ ,  $0.6 < z < 1.0$  and  $1.0 < z < 1.5$ , built using absolute magnitudes in the Sloan  $u'$  and  $r'$  filters, plotted as contour density, with the 80% completeness level marked by the red dashed line. The redshift intervals were chosen such that each one would approximately contain the same number of galaxies, which in our case corresponds to  $n_{gal} \approx 35000$ . In Table 4.1 we report the median redshift, the age of the Universe corresponding to the median redshift, the comoving volume and the number of galaxies for each redshift bin.

This kind of diagram is a useful tool for a first estimate of the evolution of the galaxy populations. The color distribution suggests to split the full sample into two classes of objects, red and blue galaxies, coinciding with early and late types (see for instance Baldry et al. 2004 for the local CM diagram; in the first line of Table 4.1 we outline the main parameters associated to that data set). In our

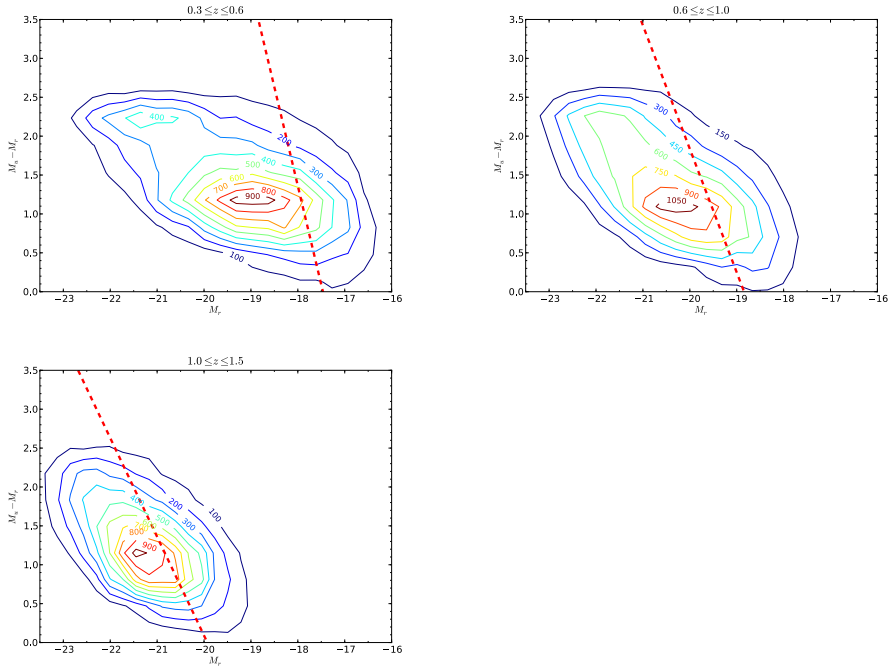


**Figure 4.6:** Absolute color-magnitude diagram for the three redshift bins  $0.3 < z < 0.6$ ,  $0.6 < z < 1.0$  and  $1.0 < z < 1.5$ . The thick red dashed line indicates the 80% completeness limit for our sample.

sample, the dual population can be roughly separated by  $u - r \simeq 1.7$ , value which remains almost the same also for the second redshift bin, while in the last bin this separation is difficult to determine, although the elongation of the contour profile towards redder colors doesn't allow to exclude its presence.

The comparison of the position of the cloud through the different redshift values shows evolution, mainly in luminosity. In fact, the position of the highest value contour for the blue population at  $z \simeq 0.45$  lays at  $M_r \simeq -19$ , moving to  $M_r \simeq -20.2$  at  $z \simeq 0.8$  and brightening even more at  $z \simeq 1.25$ , with  $M_r \simeq -21.2$ .

In order to probe this behaviour to fainter limits, we applied the weights obtained from the completeness correction to the color-magnitude diagram. The result is presented in Figure 4.7. In this case, with the red dashed line we indicate the region corresponding to an original completeness of 10%, which we assumed

## 4.5. COLOR-MAGNITUDE DIAGRAM

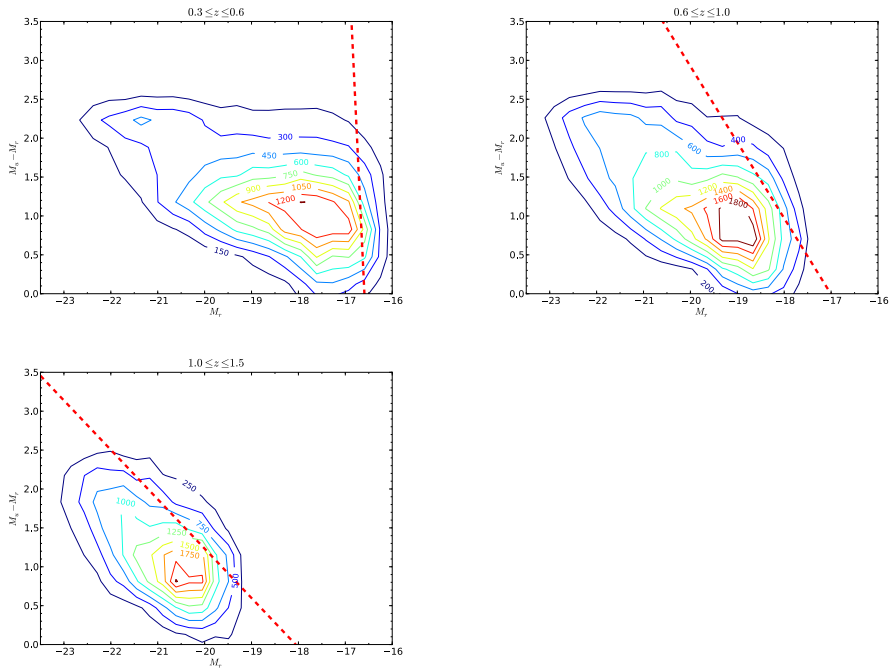


**Figure 4.7:** Absolute color-magnitude diagram after applying the completeness correction, for the three redshift bins  $0.3 < z \leq 0.6$ ,  $0.6 < z \leq 1.0$  and  $1.0 < z \leq 1.5$ . The thick red dashed line indicates the 10% completeness limit for our sample.

as the limiting case for a reliable determination of the weights.

We confirm the bimodality of the galaxy population as described by Baldry et al. (2004) at 0.04, and that this bimodality holds at least out to redshift  $z = 1$ , and probably to  $z = 1.5$ . The red population hardly evolves at all in that redshift range, either in terms of colour or luminosity, as could be expected from those models that explain their formation as the result of single star formation bursts happening at very high redshifts and passive evolution ever since. The blue population, on the other hand, has evolved from being dominated by more luminous and bluer objects in the past to the population we see today. Once again, this can be understood in terms of popular galaxy evolution models and a constantly decaying (but detectable) average star formation rate in this type of objects. All these qualitative ideas can be checked in more detail via an analysis

of the LF, that will be the object of the next Section.

## 4.6 Luminosity Functions

In this section we present our measurements of the LF in the three redshift bins  $0.3 < z < 0.6$ ,  $0.6 < z < 1.0$  and  $1.0 < z < 1.5$ , and as a function of the spectral type. Galaxies were grouped into three classes, according to their SED, as measured by the BPZ code. The first class contains objects with a red SED, typical of quiescent galaxies like elliptical and S0. The second class includes galaxies with a bluer SED, resulting from star formation activity, as in spiral galaxies. In the third class we considered objects with a very blue SED, corresponding to starburst galaxies.

The LF were computed by introducing to the SWML method a correction for the detection completeness. Since the SWML method does not provide a normalization, this was obtained by applying the conservation of the total number density of galaxies given by the *Vmax* method in an absolute magnitude range of confidence. The range was chosen such that the sample was  $\approx 100\%$  complete so that it varied according to both the redshift range and the population of galaxies under analysis. In the lowest redshift range we adopted an absolute magnitude upper limit equal to  $M_r = -19.5$  for the normalization of the global LF and  $M_r = -20.0, -19.5, -19.5$  for elliptical, spiral and SB LF; at  $z_{med} = 0.8$ , the adopted limits were  $M_r = -21.0, -21.5, -20.5, -20.$  respectively, while at  $z_{med} = 1.25$  these were  $M_r = -22.5, -23.0, -21.5, -21.5$ . The rest-frame *r*-band was chosen as a compromise between the the redshift range available when computing rest-frame magnitudes without need to exclusively rely on the SED models (see Fig 2.4) and the adequateness of the rest-frame band to describe the underlying mass distribution.

The completeness weights were introduced in a way analogous to what was done by (Lin et al., 1996), obtaining for the recursive expression of the SWML  $k$ -th LF bin (Eq. 2.31) the following form:

$$\phi_k \Delta M = \frac{\sum_{i=1}^{N_{gal}} w_i \cdot W(M_k - M_i)}{\sum_{i=1}^{N_{gal}} \left[ w_i \cdot H(M_k - M_f) / \sum_{j=1}^{N_{gal}} \phi_j \Delta M H(M_j - M_f) \right]} \quad (4.2)$$

#### 4.6. LUMINOSITY FUNCTIONS

---

z range	Type range	$\alpha$	$M_r^*$ [AB mag]	$\phi^*$ [mag <sup>-1</sup> Mpc <sup>-3</sup> ]
0.30-0.60	all	$-1.27 \pm 0.01$	$-22.03 \pm 0.08$	$1.74 \pm 0.11 \times 10^{-3}$
	Ell	$-0.59 \pm 0.02$	$-21.70 \pm 0.04$	$2.07 \pm 0.06 \times 10^{-3}$
	Spi	$-1.26 \pm 0.03$	$-20.98 \pm 0.09$	$2.11 \pm 0.19 \times 10^{-3}$
	SB	$-1.63 \pm 0.08$	$-20.28 \pm 0.15$	$0.80 \pm 0.17 \times 10^{-3}$
0.60-1.00	all	$-1.23 \pm 0.06$	$-22.11 \pm 0.11$	$2.15 \pm 0.12 \times 10^{-3}$
	Ell	$-0.60 \pm 0.10$	$-21.91 \pm 0.13$	$1.99 \pm 1.10 \times 10^{-3}$
	Spi	$-1.11 \pm 0.05$	$-21.86 \pm 0.16$	$1.12 \pm 0.16 \times 10^{-3}$
	SB	$-1.89 \pm 0.05$	$-20.93 \pm 0.17$	$0.51 \pm 0.21 \times 10^{-3}$
1.00-1.50	all	$-1.21 \pm 0.04$	$-22.01 \pm 0.09$	$3.84 \pm 0.36 \times 10^{-3}$
	Ell	$-1.06 \pm 0.07$	$-21.90 \pm 0.14$	$2.59 \pm 0.35 \times 10^{-3}$
	Spi	$-0.70 \pm 0.18$	$-21.61 \pm 0.13$	$2.79 \pm 0.15 \times 10^{-3}$
	SB	$-1.13 \pm 0.12$	$-20.74 \pm 0.14$	$2.36 \pm 0.36 \times 10^{-3}$

**Table 4.2:** LF parameters obtained from fitting a Schechter function to the SWML measurements.

where the  $w_i$  are the weights from the completeness correction, defined in Sect. 4.4.

In order to allow a first check on the goodness of the applied correction, we also re-computed all the LFs without applying any weighting coefficient (i.e. the adopted weights were  $w_i \equiv 1, i = 1..N_g$ ). We computed the LF for four galaxy population sets: a *global* LF, considering all the spectral types, a *red population* LF, which considers only the redder types (E and S0), an *intermediate population*, obtained by selecting normal spiral galaxies (types S1 and S2) and a *blue population*, where we considered only starburst galaxies (types SB1 and SB2).

The computed LF are presented in Figure 4.8, Figure 4.9 and Figure 4.10 for the redshift ranges  $0.3 < z < 0.6$ ,  $0.6 < z < 1.0$  and  $1.0 < z < 1.5$  respectively. In the left panel we plot the global LF. Asterisks refer to the computation of the LF without taking into account completeness correction, while the open diamonds refer to the LF obtained applying our measurement of the detection completeness. The vertical dash-dotted line indicates our estimated completeness limit. The right panel shows the LF for the three selected populations. Red marks indicate the LF for the early types (E and S0), green marks for average spiral galaxies (S1 and S2), while blue marks refer to starburst galaxies (SB1 and SB2). Open triangles refer to the LF computed without the completeness correction, while filled squares represent the completeness-corrected LFs. Schechter fit to the LF

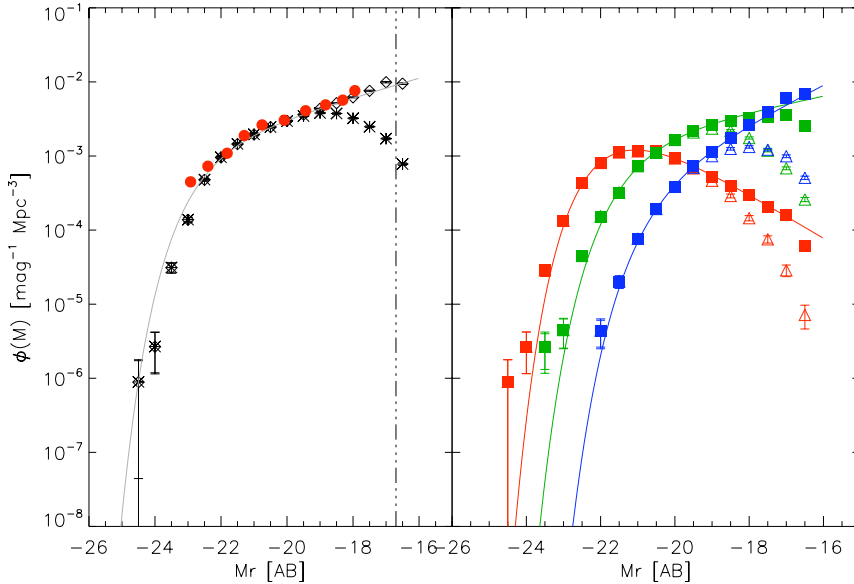


**Figure 4.8:** Luminosity function at  $z \approx 0.45$ . In the left panel the global LF is shown. Asterisks refer to the computation of the LF without taking into account completeness correction, while the open diamonds refer to the LF obtained applying our measurement of the detection completeness. The vertical dash-dotted line indicates our estimated completeness limit. The LF measurement from Ilbert et al. (2005) for a similar redshift range is plotted as filled red circles. The right panel shows the LF for three spectral types. Open triangles refer to the LF computed without the completeness correction, while filled squares represent the completeness-corrected LF. Red marks indicate the LF for the early types (E and S0), green marks for average spiral galaxies (S1 and S2), while blue marks refer to starburst galaxies (SB1 and SB2). The Schechter fit to the LF of each type is marked by the solid line of the corresponding color.

of each type is marked by the solid line of the corresponding color; the fitted Schechter parameters are summarized in Table 4.2.

When compared with the corresponding un-weighted LF, the weight-corrected LFs show the same value up to the absolute magnitude corresponding to the  $\approx 85\%$  completeness level, as one would expect, since in this range the weight factor should be close to 1. Starting from this absolute magnitude, the corrected LFs assume higher values, due to the weights greater than unity in this magnitude

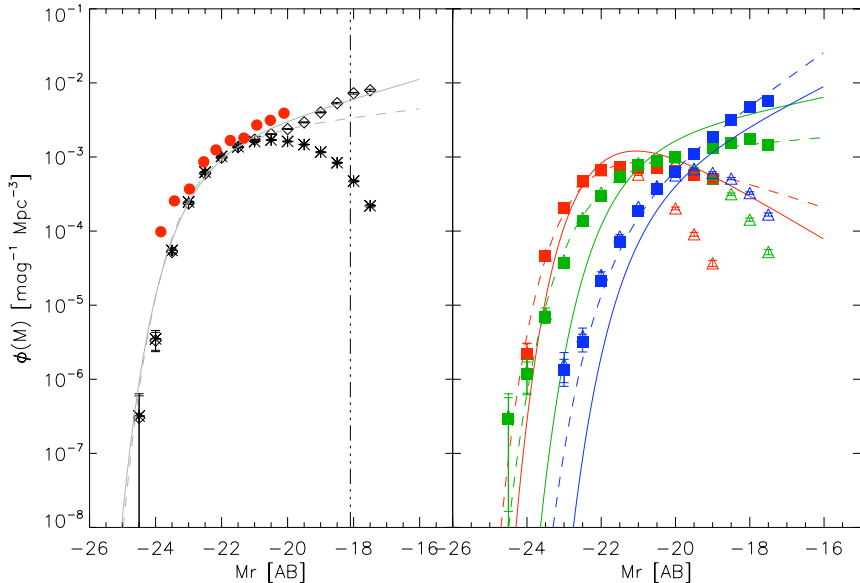


**Figure 4.9:** Luminosity function at  $z \approx 0.8$ . See caption to Figure 4.8 for details. Schechter fit to the LF of each type is marked by the dashed line of the corresponding color. Solid lines indicate the Schechter fits for the  $z \simeq 0.45$  LFs and presented in Figure 4.8.

region.

As a further check, we compared our global LF with the LF from the VVDS project (Le Fèvre et al., 2004, 2005), presented in Ilbert et al. (2005). The VVDS LFs of the redshift bin closest to ours are marked in the left panels as filled red circles. Our global LF show good agreement with the LFs from the VVDS survey in all the three redshift ranges, with our absolute magnitude limits fainter than the VVDS one by 1 – 1.5 mag in the first two redshift bins. The agreement between the LFs from the two different data sets allows us to increase our confidence for the fainter region of the LF. Despite this fact, the photometric depth reached by the ALHAMBRA Survey is still not sufficient to allow for a solid determination of the faint-end slopes of the three global LFs.

By looking at the right panel of Fig. 4.8, we see that elliptical galaxies dominate the bright end of the global LF, spiral galaxies reside in the central absolute

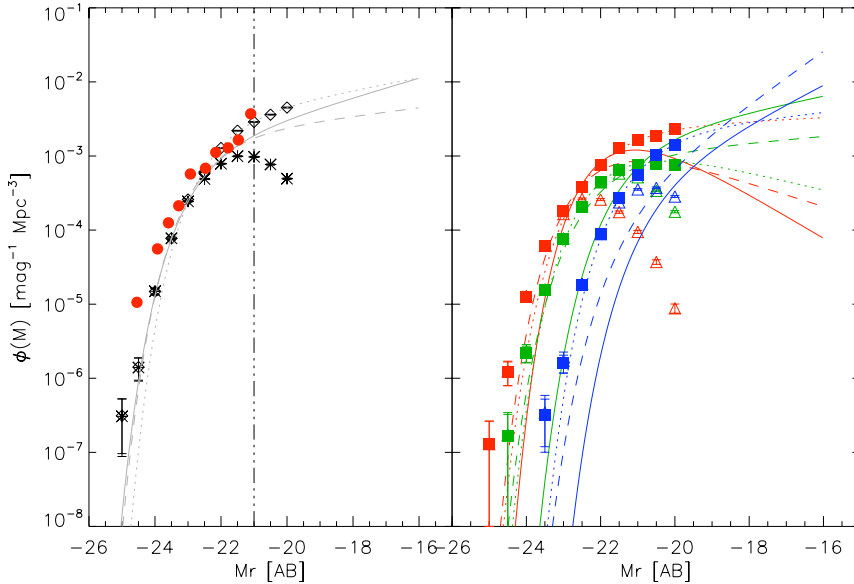


**Figure 4.10:** Luminosity function at  $z \approx 1.25$ . See caption to Figure 4.8 for details. Schechter fit to the LF of each type is marked by the dotted line of the corresponding color. Solid lines indicate the Schechter fits presented in Figure 4.8, while dashed lines show the Schechter fit of the  $z \simeq 0.8$  LFs.

magnitude range, while the faint-end slope is determined by starburst galaxies. The faint-end slopes increase going from the red population to the blue one.

This behaviour is well replicated also for the redshift bin centered at  $z \simeq 0.8$ , shown in Fig. 4.9, and, even though to a less degree, also in the highest redshift range (see Fig. 4.10).

As a qualitative way to determine if some kind of evolution has occurred since  $z \simeq 1.25$ , we plotted the Schechter fits to the global and to the single population LFs of the  $z \simeq 0.45$  bin in the corresponding panels of Fig. 4.9 and Fig. 4.10 (solid lines), and the Schechter fits to the  $z \simeq 0.8$  LFs as dashed lines in Fig. 4.10. This allows us to see that:

- The bright-end of the global LF shows little to no evolution from  $z \simeq 0.45$  to  $z \simeq 1.25$ . As discussed before, the analysis of the faint end would require deeper data, especially for the higher redshift bin;

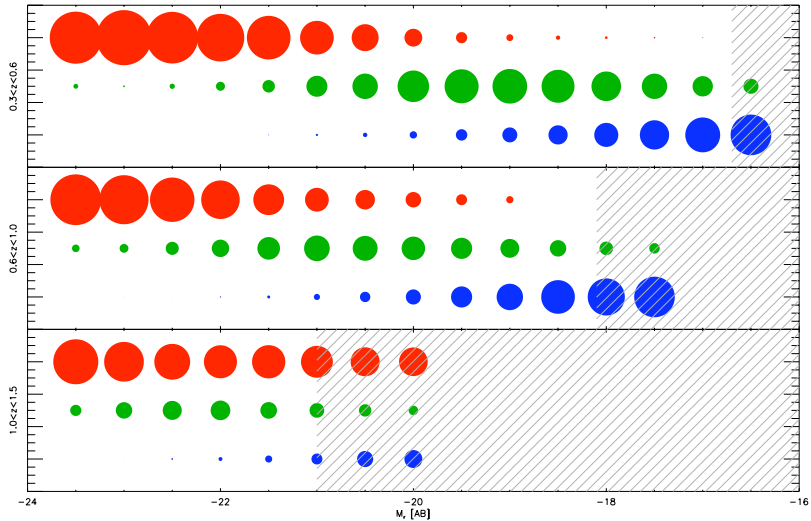


**Figure 4.11:** Relative fraction of galaxy population in LFs. Each panel refers to a redshift bin ( $0.3 < z < 0.6$ ,  $0.6 < z < 1.0$  and  $1.0 < z < 1.5$  from top to bottom respectively); each color corresponds to a galaxy population: red for ellipticals, green for spirals and blue for starburst galaxies. The radius of the points is proportional to the ratio of the corresponding LF to the global LF at that redshift.

- As for the global LF, also the LF of elliptical galaxies does not show any significant evolution, in agreement with the fact that the bright-end of the global LF is populated by red objects;
- The LF of spiral galaxies shows evident evolution, possibly in the luminosity domain, from  $z \simeq 0.45$  to  $z \simeq 0.8$ , with the LF shifting towards brighter magnitudes with  $z$ , while in the two highest redshift ranges the two LFs look similar;
- The population of starburst galaxies is the one presenting clear evolution in all the three redshift ranges, although determining if it is luminosity or number density evolution would require additional analysis.

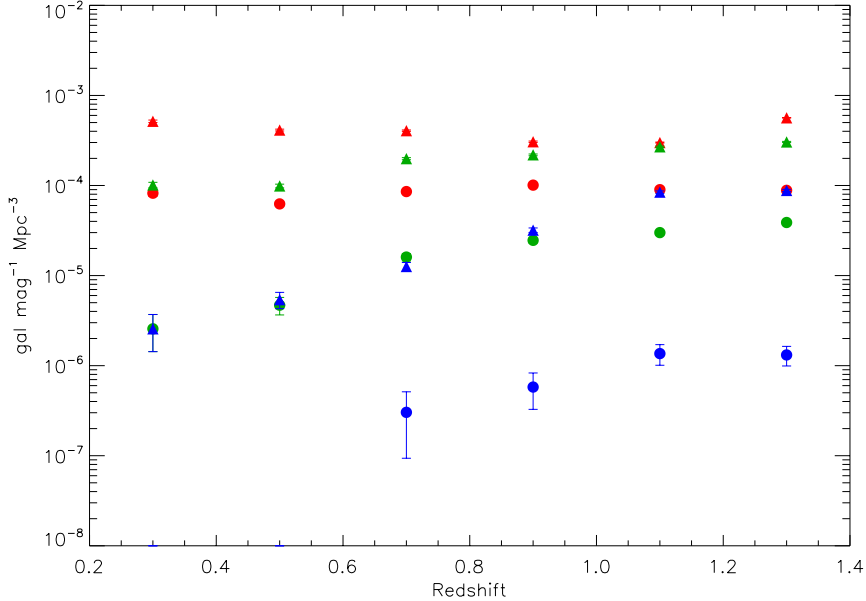


**Figure 4.12:** Evolution of the number density for  $M_r < -22.5$  (filled circles) and  $-22.5 < M_r < -20$  (filled triangle), for elliptical (red), spiral (green) and star-burst (blue) classes.

An attempt to graphically represent the above points is shown in Fig. 4.11. Each panel refers to a redshift bin ( $0.3 < z < 0.6$ ,  $0.6 < z < 1.0$  and  $1.0 < z < 1.5$  from top to bottom respectively); each color corresponds to a galaxy population: red for ellipticals, green for spirals and blue for starburst galaxies. The radius of the points is proportional to the ratio of the corresponding LF to the global LF at that redshift. The area shaded by the grey lines indicates the magnitude range where our completeness correction is no more reliable (i.e. the original completeness level is below 10%).

We finally investigated the evolution with redshift of the number density of galaxies as a function of the spectral type. The whole redshift range was divided into six equal-size bins ( $\Delta z = 0.2$ ), from  $z = 0.2$  to  $z = 1.4$ . At each bin, galaxies were separated into three classes (elliptical, spiral and SB) according to their spectral type. The resulting population was further divided into two

sub-populations: *massive* galaxies, defined by  $-22.5 < M_r < -20$ . and *high-massive* galaxies, satisfying  $M_r < -22.5$ . The resulting number density per unit magnitude is presented in Figure 4.12. The density of elliptical galaxies remains roughly constant throughout the whole redshift range, for both the mass ranges. Spiral galaxies, instead, show a differential evolution: while the less massive have little to no evolution, the most massive galaxies present a significant evolution, increasing by one order of magnitude from  $z = 0.3$  to  $z = 1.3$ , with  $\approx 80\%$  of this increase already in place by  $z \simeq 0.9$ . For SB galaxies this behavior is even more clear, considering that for  $z < 0.6$  in our catalogues there are no galaxies with  $M_r < -22.5$ . The above results should however be taken with care: the  $r$ -band may in fact be not red enough to conduct such analysis, mixing star-formation with total mass effects.

## 4.7 Conclusions

---

In this chapter we present global colour-magnitude diagrams for the galaxy population in three different epochs, global and type-dependent luminosity functions and their evolution in those same three epochs, and compare them to previous results from SDSS and VVDS, using a preliminary catalogue from the ALHAMBRA Survey.

We made full use of the detection completeness evaluations, previously determined in this work, to apply a correction for the completeness to both the color-magnitude diagram and the LF computation.

The comparison of the position of the cloud in the CM diagram through the different redshift values shows evolution, mainly in luminosity. The position of the highest value contour for the blue population at  $z \simeq 0.45$  lays at  $M_r \simeq -19$ , moving to  $M_r \simeq -20.2$  at  $z \simeq 0.8$  and brightening even more at  $z \simeq 1.25$ , with  $M_r \simeq -21.2$ . We also confirm the bimodality of the galaxy population as described by Baldry et al. (2004) at 0.04; this bimodality holds at least out to redshift  $z = 1$ , and probably to  $z = 1.5$ . The red population hardly evolves at all in that redshift range, either in terms of color or luminosity, supporting those models that explain their formation as the result of single star formation bursts happening at very high redshifts and passive evolution ever since. On the other hand, for the blue population we see an evolution from being dominated by more

luminous and bluer objects in the past to the population we see today. This fact can also be understood in terms of galaxy evolution models and a constantly decaying (but detectable) average star formation rate in this type of objects.

The LF was computed for 4 distinct populations (full sample, ellipticals only, spirals only and starburst only), for three redshift bins ( $0.3 < z < 0.6$ ,  $0.6 < z < 1.0$  and  $1.0 < z < 1.5$ ).

The agreement of the global LF with the LF from published data, obtained from samples whose photometric depth is comparable to that in ALHAMBRA catalogues, allowed to increase the confidence on the estimated completeness corrections. The comparison of ALHAMBRA LFs at the three redshift ranges confirmed the conclusions we derived from the analysis of the CM diagram. The bright-end of the global LF shows little to no evolution from  $z \simeq 0.45$  to  $z \simeq 1.25$ , although a more solid analysis of the faint end would require deeper data, especially for the higher redshift bin. Similarly to the global LF, also the LF of elliptical galaxies does not show any significant evolution, in agreement with the fact that the bright-end of the global LF is populated by red objects. The LF of spiral galaxies shows marked evolution, possibly in the luminosity domain, from  $z \simeq 0.45$  to  $z \simeq 0.8$ , with the LF shifting towards brighter magnitudes with  $z$ , while in the two highest redshift ranges the two LFs look similar. Starburst galaxies present the clearest signs of evolution in all the three redshift ranges, although determining if it is luminosity or number density evolution would require additional analysis.



# Bibliography

- Baldry I. K., Glazebrook K., Brinkmann J., Ivezić Ž., Lupton R. H., Nichol R. C., Szalay A. S., 2004, *ApJ*, 600, 681
- Benítez N., 2000, *ApJ*, 536, 571
- Daddi E., Cimatti A., Renzini A., Fontana A., Mignoli M., Pozzetti L., Tozzi P., Zamorani G., 2004, *ApJ*, 617, 746
- Ilbert O., et al., 2005, *A&A*, 439, 863
- Ilbert O., et al., 2009, *ApJ*, 690, 1236
- Le Fèvre O., et al., 2004, *A&A*, 417, 839
- Le Fèvre O., et al., 2005, *A&A*, 439, 845
- Lin H., Kirshner R. P., Shectman S. A., Landy S. D., Oemler A., Tucker D. L., Schechter P. L., 1996, *ApJ*, 464, 60
- Scoville N., et al., 2007, *ApJS*, 172, 1
- Zucca E., Pozzetti L., Zamorani G., 1994, *MNRAS*, 269, 953



# 5

## The evolution of the rest-frame J and H luminosity function from $z=1.5$ to $z=3.5$ <sup>1</sup>

### 5.1 Introduction

---

In the current concordance model, galaxies are the result of continuous mergers of dark matter halos driving baryonic matter assembly. In the last decades, simulations on halo occupation models have been able to quite accurately plot the formation of dark matter clusters. However, there still remain big uncertainties at the time of translating dark matter haloes to what can actually be detected with our telescopes.

To this respect, the luminosity function (LF) of galaxies, i.e. the number density of galaxies per unit flux, is an extremely powerful tool to study the galaxy population and its evolution with cosmic time.

Specifically, the analysis of the LF at different rest-frame wavelengths can give us information on different aspects of our present view of the Universe. The UV-optical LF allows for the study of the content and the evolution of the star formation rates with cosmic time. On the other hand the near infra-red (NIR) LF, being less sensitive to the absorption by dust and dominated by the light of older stars, is a better estimator of the overall mass assembly of galaxies and of its rate of growth with time, revealing itself as a good test-bench for halo models.

---

<sup>1</sup>This work was published in Stefanon, M. and Marchesini, D., 2011 MNRAS accepted

The local NIR LF is still not yet well determined. Although a number of measurements have been derived so far, there seems to be uncertainties especially for the faint end slope  $\alpha$ . Estimates of the slope  $\alpha$  range from  $\approx -0.8$  (Bell et al. 2003; Eke et al. 2005), to  $\alpha \approx -1.2$  (Jones et al. 2006), with a median value around -1 (Mobasher, Sharples, & Ellis 1993; ?; Cowie et al. 1996; Gardner et al. 1997 and Szokoly et al. 1998; Kochanek et al. 2001; Cole et al. 2001 and Hill et al. 2010). In particular, Hill et al. (2010) found also an increase of the number density compared to previous determinations, likely due to the high photometric depth of the adopted UKIDSS LAS sample.

At even larger redshift, the LF determinations (most of which are done in the rest-frame  $K_S$  band) still suffer from significant uncertainties (Saracco et al. 2006). The faint-end slope seems to be always compatible with  $\alpha = -1$  (Drory et al. 2003; Pozzetti et al. 2003; Dahlen et al. 2005; Saracco et al. 2006; Cirasuolo et al. 2010) although these measurements suffer from the large uncertainties given by the limits in the depth of the photometric catalogues available so far. There seems to be a general consensus however that the NIR LF does not significantly evolve to  $z \approx 1$  with respect to the local LF (Cowie et al. 1996; Pozzetti et al. 2003; Drory et al. 2003; Feulner et al. 2003; Dahlen et al. 2005). A brightening is instead found around  $z \approx 1.2 - 1.5$  together with a decrease of the normalization (Saracco et al. 2006; Cirasuolo et al. 2010), decrease that is seen up to  $z = 3$ . even if to a lesser degree.

In this chapter we present the rest-frame  $J$  and  $H$  bands LFs and luminosity density (LD) of field galaxies, obtained from three deep photometric redshift surveys, namely MUSYC, FIRES and FIREWORKS, complemented by deep *Spitzer* 3.6, 4.5, 5.8, and 8  $\mu\text{m}$  data. As discussed in e. g. Berta et al. (2007), the combination of the Planck spectral peak from low-mass stars, the minimum in the  $H^-$  opacity in stellar atmospheres and the molecular absorptions in the spectra of cold stars produce a maximum for the emission in the rest-frame NIR portion of galaxy spectra located at 1.6 $\mu\text{m}$  (the so called 1.6 $\mu\text{m}$  *bump*). Furthermore, the AGN light can contribute significantly to the rest-frame K-band. Specifically, the contribution from the dust torus of the AGN can be in the rest-frame K-band a factor of 10 larger than in the rest-frame J-band, and a factor of 4 larger than in the rest-frame H-band (e.g., Polletta et al. 2008). The adoption of the rest-frame  $J-$  and  $H-$  bands makes thus the measurement of the LFs and LDs less sensi-

tive to potential dust-obscured AGN contamination compared to measurements of the LFs in the rest-frame  $K_s$ , yet allowing us to sample a wavelength range dominated by stellar emission and very little affected by obscuration by dust. The combination of depth and wavelength coverage in the mid-IR out to  $8\mu\text{m}$  allows us to directly probe the rest-frame  $J-$  and  $H-$  bands out to  $z \simeq 3.5$ , relying more on observational data rather than on stellar population models, which are still significantly uncertain in the rest-frame NIR, due to different implementations of the TP-AGB phase (Maraston, 2005; Conroy, Gunn, & White, 2009). The total surveyed area sums to  $450 \text{ arcmin}^2$  with complete U-to- $8\mu\text{m}$  coverage, reducing thus the effects of cosmic variance, which we estimate to give on average a 15-20% contribution.

This chapter is organized as follows: in section 5.2 we present the data set used for this work, how we recover photometric redshifts and how we select galaxies from the full sample. Section 5.3 presents the three methods adopted to estimate the LF and its associated uncertainties. In section 5.4 we present our results and compare them with the current models. Our conclusions are summarized in section 5.5.

Throughout this work, the adopted cosmology is  $\Omega_\Lambda = 0.7$ ,  $\Omega_m = 0.3$  and  $H_0 = 70 \text{ Km/s/Mpc}$ . All magnitudes are expressed in the AB system.

## 5.2 Description of the sample

---

For this work we used a total of seven public  $K_s$ -selected catalogues coming from three different deep multi-wavelength galaxy surveys covering the range from the optical to the Spitzer IRAC  $8 \mu\text{m}$  waveband: the MUlti-wavelength Survey by Yale-Chile (MUSYC - Marcesini et al. 2009), the Faint InfraRed Extragalactic Survey (FIRES - Labbè et al. 2003, Forster Schreiber et al. 2006) and the GOODS Chandra Deep Field-South (FIREWORKS - Wuyts et al. 2008). Although they have all been presented in Marcesini et al. (2009), for readers' sake these surveys will be briefly described in the following sections.

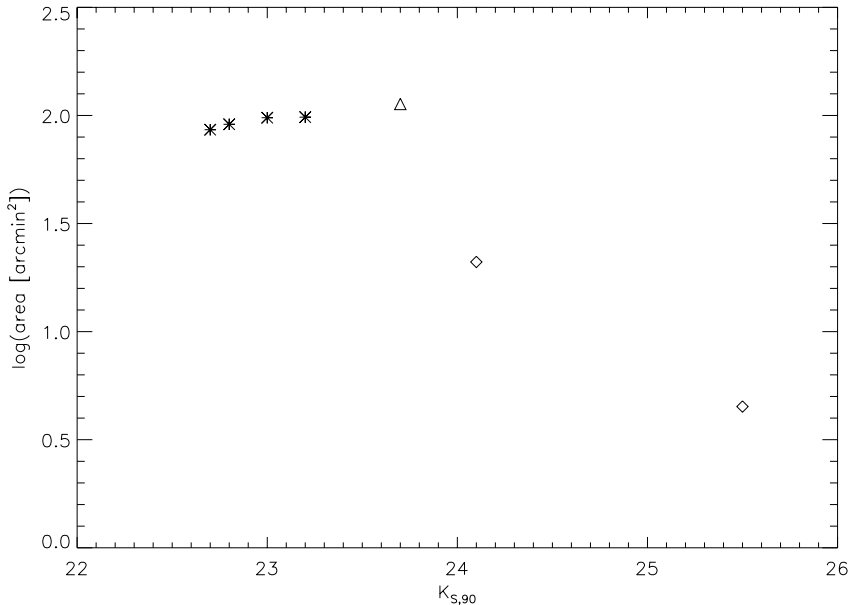


**Figure 5.1:** Field area plotted against the 90% completeness magnitude. Asterisks refer to the MUSYC fields, diamonds to the FIRES fields, while the triangle refers to the FIREWORKS CDF-S data.

### 5.2.1 MUSYC

The deep NIR MUSYC survey consists of four  $10' \times 10'$  fields, namely, Hubble Deep Field-South 1 and 2 (HDFS-1, HDFS-2, hereafter), the SDSS-1030 field, and the CW-1255 field, observed with the Infrared Side Port Imager (ISPI) camera at the Cerro Tololo Inter-American Observatory (CTIO) Blanco 4 m telescope, for a total surveyed area of  $430 \text{ arcmin}^2$ . A complete description of the deep NIR MUSYC observations, reduction procedures, and the construction of the  $K$ -selected catalog with  $U$ -to- $K$  photometry is presented in Quadri et al. (2007). Deep Spitzer-IRAC  $3.6\text{-}8.0 \mu\text{m}$  imaging is also available for the four fields. The average total limiting magnitudes of the IRAC images are 24.5, 24.2, 22.4, and 22.3 ( $3\sigma$ , AB magnitude) in the 3.6, 4.5, 5.8, and  $8.0 \mu\text{m}$  bands, respectively. The  $K$ -selected catalogs with IRAC photometry included is publicly available at <http://www.astro.yale.edu/musyc>. The SDSS-1030, CW-1255, HDFS-1, and

HDFS-2 catalogs are  $K_S$  band-limited multicolor source catalogs down to  $K_{S,tot} = 23.6, 23.4, 23.7,$  and  $23.2,$  for a total of 3273, 2445, 2996, and 2118 sources, over fields of 109, 105, 109, 106 arcmin<sup>2</sup> respectively. All four fields were exposed in 13 different bands, U, B, V, R, I, z, J, H, K, and the four IRAC channels. The SDSS-1030, CW-1255, HDFS-1, and HDFS-2 K-selected catalogs have 90% completeness levels at  $K_{S,90}=23.2, 22.8, 23.0,$  and  $22.7,$  respectively. The final catalogs used in the construction of the composite sample have 2825, 2197, 2266, and 1749 objects brighter than the 90% completeness in the  $K_S$  band, over an effective area of 98.2, 91.0, 97.6, and 85.9 arcmin<sup>2</sup>, respectively, for a total of 9037 sources over 372.7 arcmin<sup>2</sup>.

### 5.2.2 FIRES

FIRES consists of two fields, namely, the Hubble Deep Field-South proper (HDF-S) and the field around MS 1054-03, a foreground cluster at  $z = 0.83$ . A complete description of the FIRES observations, reduction procedures, and the construction of photometric catalogs is presented in detail in Labbè et al. (2003) and Forster Schreiber et al. (2006) for HDF-S and MS 1054-03 (hereafter HDFS and MS-1054, respectively). Both  $K_S$ -selected catalogs were later augmented with Spitzer-IRAC data (Wuyts et al., 2007; Toft et al., 2007)). The HDFS catalog has 833 sources down to  $K_{S,tot}=26.0$  over an area of  $2.5 \times 2.5$  arcmin<sup>2</sup>. The MS-1054 catalog has 1858 sources down to  $K_{S,tot}=25.0$  over an area of  $5.5 \times 5.3$  arcmin<sup>2</sup>. The HDFS field was exposed in the WFPC2 U300, B450, V606, I814 passbands, the ISAAC JS, H, and KS bands, and the four IRAC channels. The MS-1054  $K_S$ -selected catalog comprises FORS1 U, B, V, WFPC2 V606 and I814, ISAAC J, H, and KS, and IRAC 3.6-8.0  $\mu\text{m}$  photometry. The HDFS and MS-1054 catalogs have 90% completeness levels at  $K_{S,90}=25.5$  and 24.1, respectively. The final HDFS and MS-1054 catalogs used in the construction of the composite sample have 715 and 1547 objects brighter than the 90% completeness in the  $K_S$  band, over an effective area of 4.5 and 21.0 arcmin<sup>2</sup>, respectively.

### 5.2.3 FIREWORKS

In this work, we adopted the  $K_S$ -selected catalog (dubbed FIREWORKS) of the CDFS field constructed based on the publicly available GOODS-CDFS data by

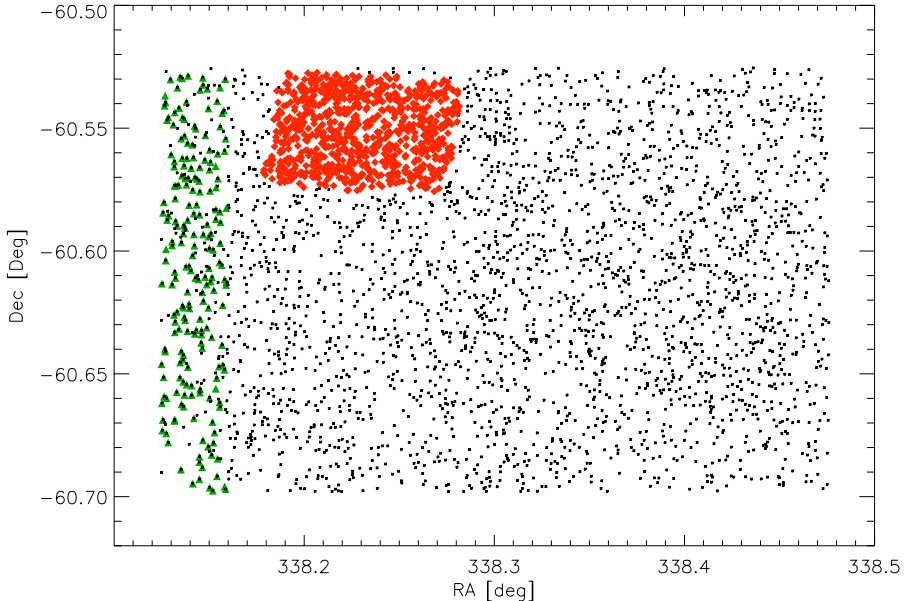


**Figure 5.2:** Overlapping regions in the three HDF5 pointings. Black points represent MUSYC HDF51 data, green triangles MUSYC HDF52 sources, while red filled diamonds are the the objects from FIRES HDF5.

Wuyts et al. (2008). The photometry was performed in an identical way to that of the FIRES fields, and the included passbands are the ACS B435, V606, i775, and z850 bands, the WFI U38, B, V, R, and I bands, the ISAAC J, H, and  $K_S$  bands, and the four IRAC channels. The KS-selected catalog comprises 6308 objects down to  $K_{S,tot}=24.6$  over a total surveyed area of 138 arcmin<sup>2</sup>; the variation in exposure time and observing conditions between the different ISAAC pointings lead to an inhomogeneous depth over the whole GOODS-CDFS field (hereafter CDFS). The final CDFS catalog used in the construction of the composite sample comprises 3559 objects brighter than the 90% completeness level ( $K_{S,90} = 23.7$ ), over an effective area of 113 arcmin<sup>2</sup> with coverage in all bands.

In Figure 5.1 we plot the field area as a function of the  $K_S$  magnitude corresponding to the 90% completeness level.

### 5.2.4 Sample selection

The MUSYC HDFS1, HDFS2 and FIRES HDFS fields partly overlap. Figure 5.2 shows the distribution of the objects centered on the HDFS1. The black points represent all the objects from the HDFS1 catalogue; red filled diamonds correspond to the 833 sources in the FIRES catalogue, while the green triangles represent the sources in the HDFS2 catalogue whose positions overlap with the field covered by the HDFS1 pointing.

In order to avoid duplicate counts, we selected objects according to the photometric depth of the three involved catalogues. Since the FIRES object list is the deepest catalogue of our sample, the corresponding region in the MUSYC HDFS1 catalogue was discarded. Analogously, since the HDFS1 is deeper than the HDFS2 catalogue, the corresponding objects were removed from the HDFS2 catalogue.

Spitzer IRAC pointings do not fully cover MUSYC, FIRES and FIREWORKS fields. Since one of the major aims of our work was to derive absolute magnitudes with the highest reliability, we decided to select only those sources with full Spitzer IRAC photometry. The selection was based on a weighting factor, previously defined in the catalogue, constructed as the exposure time normalized to the median of the weights. This definition allows to easily select objects on the expected signal-to-noise ratio. In particular this method allows to discard those sources falling too close to the edges of each field.

Figure 5.3 shows the corresponding plot for the MUSYC HDFS2 field. The black points represent the whole object list, while the color-coded asterisks represent the object whose weight is above a given value. From the image, we can see two broad behaviours: on one side, given the partial coverage of Spitzer pointing, we are going to lose a fraction of objects. In our cases, this loss can be quantified between 5% and 20% (as for the case of the HDFS2). Secondly, as long as we increase the weight threshold, we will be losing objects which also reside in the center of the image. Since the IRAC detector has a four-channel converter, the most notable effect would be that one quadrant would be suddenly almost discarded, so that an accurate determination of the weighting threshold is fundamental.

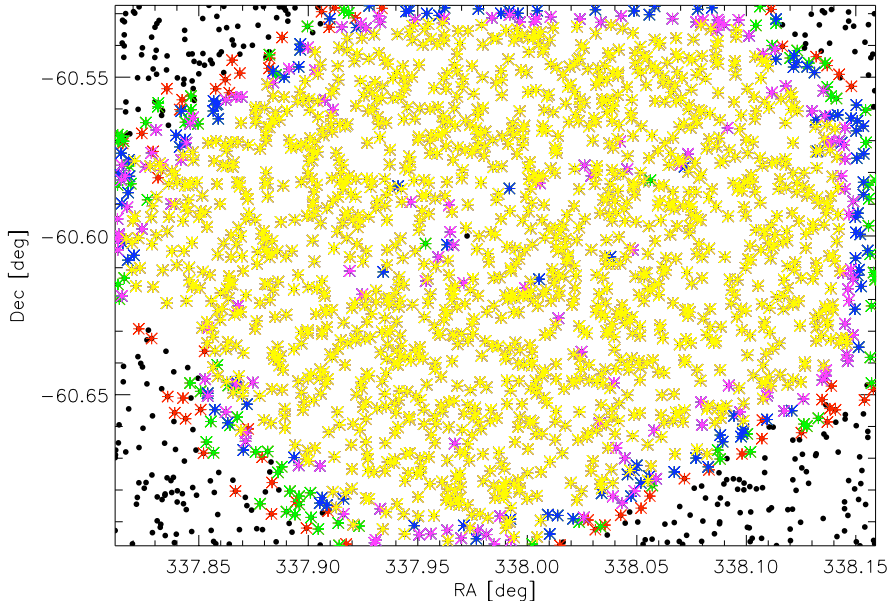


**Figure 5.3:** Selection of IRAC sources on the HDF52 field. Different colors refer to different weight thresholds  $\omega$ . Red:  $\omega = 0.2$ , green:  $\omega = 0.3$ , blue:  $\omega = 0.4$ ; magenta:  $\omega = 0.5$ ; yellow:  $\omega = 0.6$

### 5.2.5 Photometric redshift and star/galaxy separation

The downloaded catalogues all come with photometric redshift information; spectroscopic redshifts are also available for a small fraction (around 10% of the whole sample) of galaxies. However, we re-computed photometric redshifts, using the publicly available EAZY code (Brammer et al. 2008), and adopting four different sets of Spectral Energy Distribution (SED) templates and are presented in Figures 5.4 through 5.7. The first SED set (Figure 5.4) is the EAZY default template set; it consists of 5 SED templates built on the base of PEGASE models (Fioc & Rocca-Volmerange 2006), reproducing the colors of galaxies in the semi-analytic models by De Lucia & Blaizot (2007), plus a template representing a 50 My galaxy with heavy dust obscuration. The second set (Figure 5.5) is composed by a modified version of the standard EAZY templates, with the addition of  $H\alpha$  ( $\lambda_{H\alpha} = 6562.8\text{\AA}$ ),  $H\beta$  ( $\lambda_{H\beta} = 4861.3\text{\AA}$ ), [OII] (this is actually a doublet:

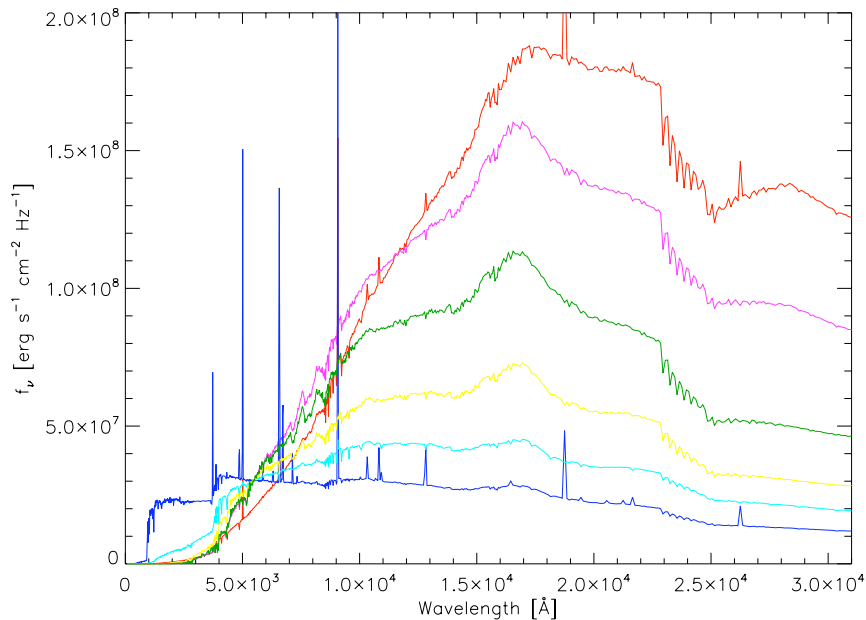


**Figure 5.4:** EAZY default template set; the 5 SED templates built on the base of PEGASE models range from elliptical (magenta line) to starburst (blue line) galaxies. The 50 My galaxy with heavy dust obscuration is represented by the red line.

$\lambda_{[OII]} = 3726.1\text{\AA}$  and  $\lambda_{[OII]} = 3728.8\text{\AA}$ ) and [OIII] (doublet:  $\lambda_{[OIII]} = 5007\text{\AA}$  and  $\lambda_{[OIII]} = 4959\text{\AA}$ ) emission lines. The third (Figure 5.6) is a set of six templates based on Coleman, Wu, & Weedman (1980) colors, included in the Bayesian Photometric Redshift code (BPZ - Benítez 2000). The last set we used is an extension of the standard EAZY template set with the inclusion of a 1Gyr galaxy template, with  $\tau = 100$  Myr and  $A_V = 3$  mag, similar to the reddest template used in Blanton & Roweis (2007). This template is shown in Figure 5.7.

For all the four cases, the same default template error function and  $K$  band prior was adopted.

Figure 5.8 shows the  $z_{spec}$  vs.  $z_{phot}$  plot for the four SED template sets used. The average  $\Delta z/(1+z)$  are respectively -0.01, -0.01, -0.01 and -0.02 for the EAZY, EAZY+lines, CWW and EAZY+dust template sets when considering the full sample, and -0.05, -0.04, -0.02 and -0.07 when computed on the redshift range

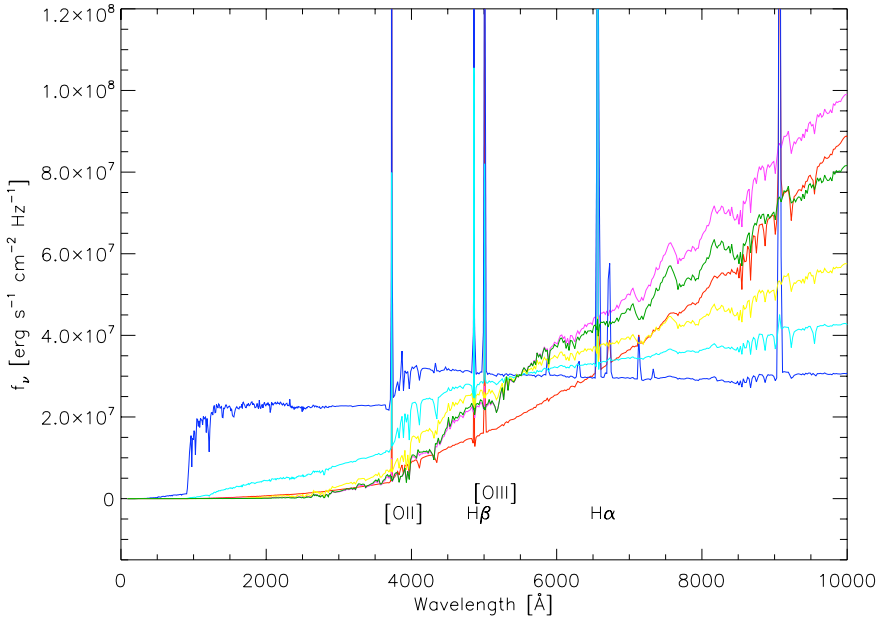


**Figure 5.5:** EAZY SEDs with emission lines. Indicated are the lines added to the templates.

$1.5 < z < 4.0$ . The standard deviations  $\sigma_{\Delta z/(1+z)}$  are 0.12, 0.12, 0.12 and 0.13 respectively for the full sample and 0.17, 0.17, 0.17 and 0.19 for the  $z$ -selected sample. The fraction of catastrophic photometric redshift ( $n(\frac{\Delta z}{1+z}) > 5\sigma$ ) is 0.007, 0.008, 0.008 and 0.01 respectively.

We finally chose to adopt the standard EAZY template set, which is the one presenting the smallest deviation between spectroscopic and photometric redshifts in the redshift range of our interest.

The separation between stars and galaxy was done with the colour-colour diagram ( $U - J$ ) vs. ( $J - K_s$ ) (see figure 5.9). The same colours were also computed from the Pickles (1998) stellar atmosphere models, in order to improve the boundaries between stars and galaxy, especially for the reddest stars which fall out of the main sequence (see figure 5.9 for full details).

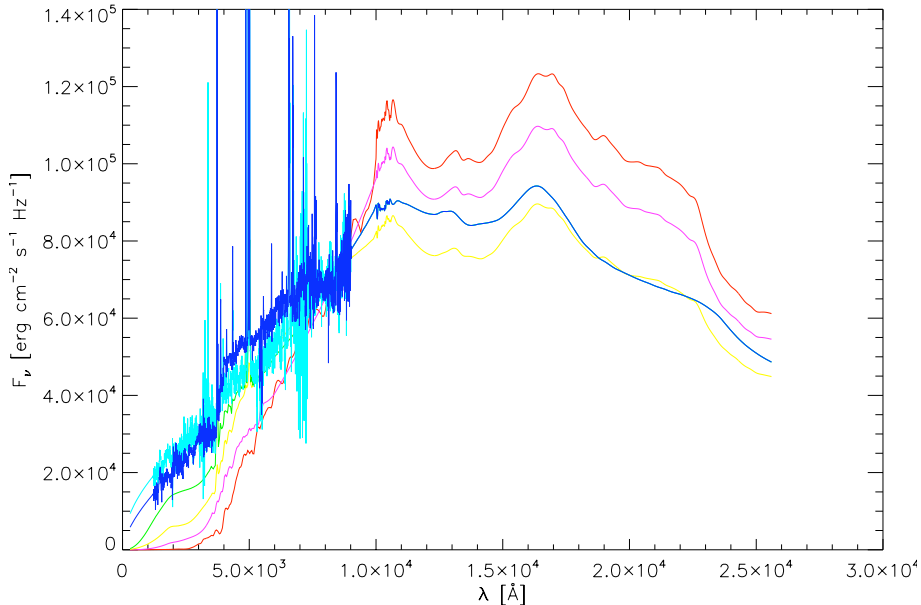


**Figure 5.6:** Spectral energy distribution from the Coleman, Wu and Weedman library (Coleman, Wu, & Weedman, 1980), and included in the BPZ photometric redshift code (Benítez, 2000).

Galaxies were selected among the object satisfying the relation:

$$(J - K_s) \geq 0.145 \cdot (U - J) - 0.45 \quad (5.1)$$

As a cross-check, we run the EAZY code with the Pickles (1998) model stellar atmosphere and checked that the objects identified as galaxies via the two-colour diagram had a  $\chi^2$  greater than the  $\chi^2$  obtained on the same object with the EAZY galaxy template set. The result of this process are presented in figure 5.10. This criteria was satisfied by all objects previously selected as galaxies with only around 6.5% of the objects selected as stars showing a discordant value for the  $\chi^2$ , giving confidence in our method to separate stars from galaxies.

A star-galaxy separation was also available in the original FIRES and FIREWORKS public catalogues. This selection was based on spectroscopy, SED-fitting with stellar templates and visual inspection of the object morphology (Rudnick

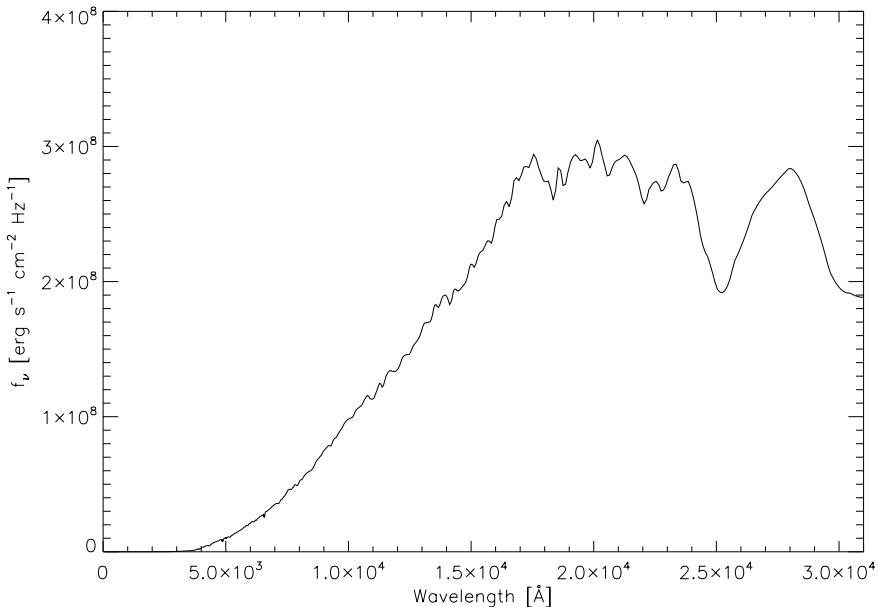


**Figure 5.7:** The 1Gyr galaxy template, with  $\tau = 100$  Myr and  $A_V = 3$  mag.

et al., 2006, 2003). We verified that those objects selected as stars in the FIRES catalogue were actually falling in the correct region of our two-color plot.

The availability of *Spitzer* IRAC data for all our sample allows us to compute absolute magnitudes in the rest-frame  $J$ - and  $H$ - bands with little dependence on the SED templates; in fact, as an extreme case, the rest-frame  $H$  band at  $z = 3.5$  is shifted to the range  $6.7 - 7.9\mu\text{m}$ , well bracketed by the *IRAC* channels 3 and 4, centered at  $5.8$  and  $8\mu\text{m}$ .

Our final catalogue, after selecting only those sources with full *Spitzer* IRAC information, is composed by a total of 14295 galaxies, with redshift determinations to  $z = 6.2$  and median redshift  $z_{med} \simeq 1$ , distributed over an effective area of  $450$  arcmin<sup>2</sup>. The redshift range of interest, result of the trade-off between number of objects in the sample and covered comoving volume, is  $1.5 < z < 3.5$  with a total of 3496 objects, of which  $\approx 6\%$  have also a spectroscopic redshift.

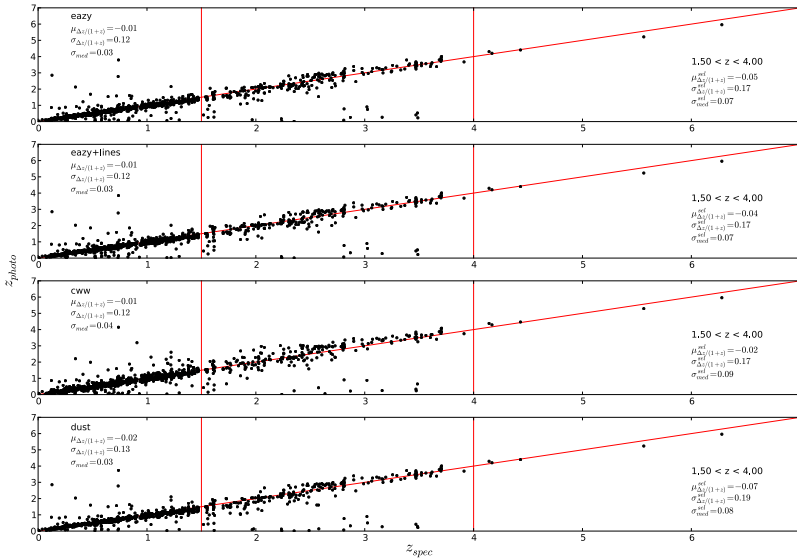


**Figure 5.8:** Photometric redshifts compared to spectroscopic redshifts, for the four different SED sets. From top to bottom: EAZY default template set; EAZY default template set with the addition of Ly $\alpha$ , H $\alpha$ , H $\beta$ , [OII] and [OIII] emission lines; Coleman, Wu and Weedman template set and EAZY SED set with dusty galaxy template (see text for details). The red line represents the ideal case where  $z_{phot} = z_{spec}$ .

### 5.3 Methodology

For the measurement of the LF, we adopted three among the most widely used methods, namely the  $1/V_{max}$  (Schmidt, 1968), the STY maximum likelihood (Sandage, Tammann, & Yahil, 1979) and the Step-Wise Maximum Likelihood (Efsthathiou, Ellis, & Peterson, 1988).

The need to analyze composite samples with different photometric depth was overcome by applying standard techniques available for each chosen method. These methods were described in Section 2.3

Confidence levels for  $\alpha$  and  $M^*$  corresponding to 68%, 95% and 99% were

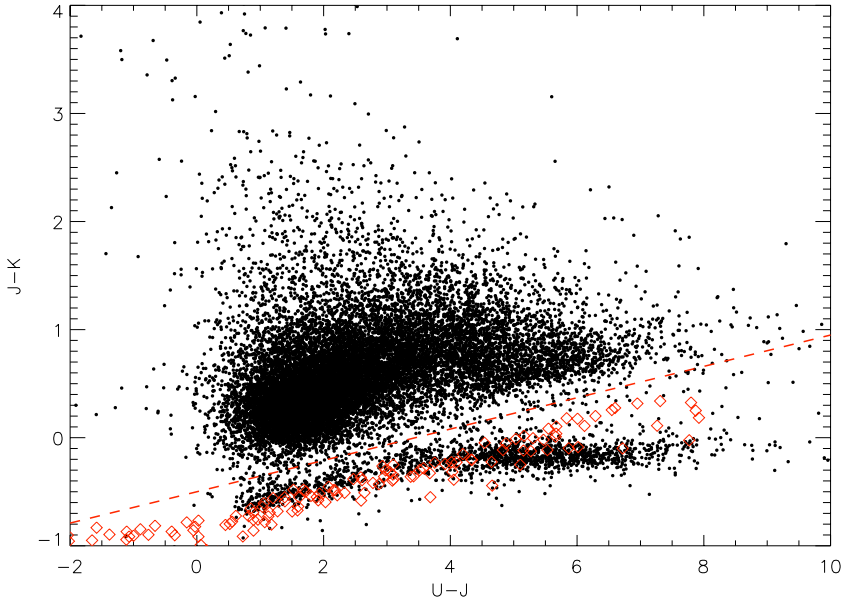


**Figure 5.9:** Two colours diagram for all the sources in the composite catalogues. Colours from Pickles (1998) stellar atmosphere models are shown as red diamonds. The red dashed line represents Eq. 5.1, which we adopted to separate stars from galaxies

computed from the ellipsoid of parameters defined by:

$$\ln \mathcal{L} = \ln \mathcal{L}_{max} - 0.5\chi_{\beta}^2(N) \quad (5.2)$$

where  $\mathcal{L}$  is the maximum likelihood function and  $\mathcal{L}_{max}$  its value at maximum, while  $\chi_{\beta}^2(N)$  is the  $\beta$ -point of the  $\chi^2$  distribution with  $N$  degrees of freedom (Efstathiou, Ellis, & Peterson 1988). Uncertainties on the normalization factor  $\phi^*$  were computed from the range of values compatible with the  $1\sigma$  uncertainties in the  $\alpha$  and  $M^*$  parameters.

### 5.3.1 Cosmic variance and photometric redshift uncertainties

The data set used for our measurement of the LF is the combination of seven catalogues, each one related to a different region of the sky. This allows to keep

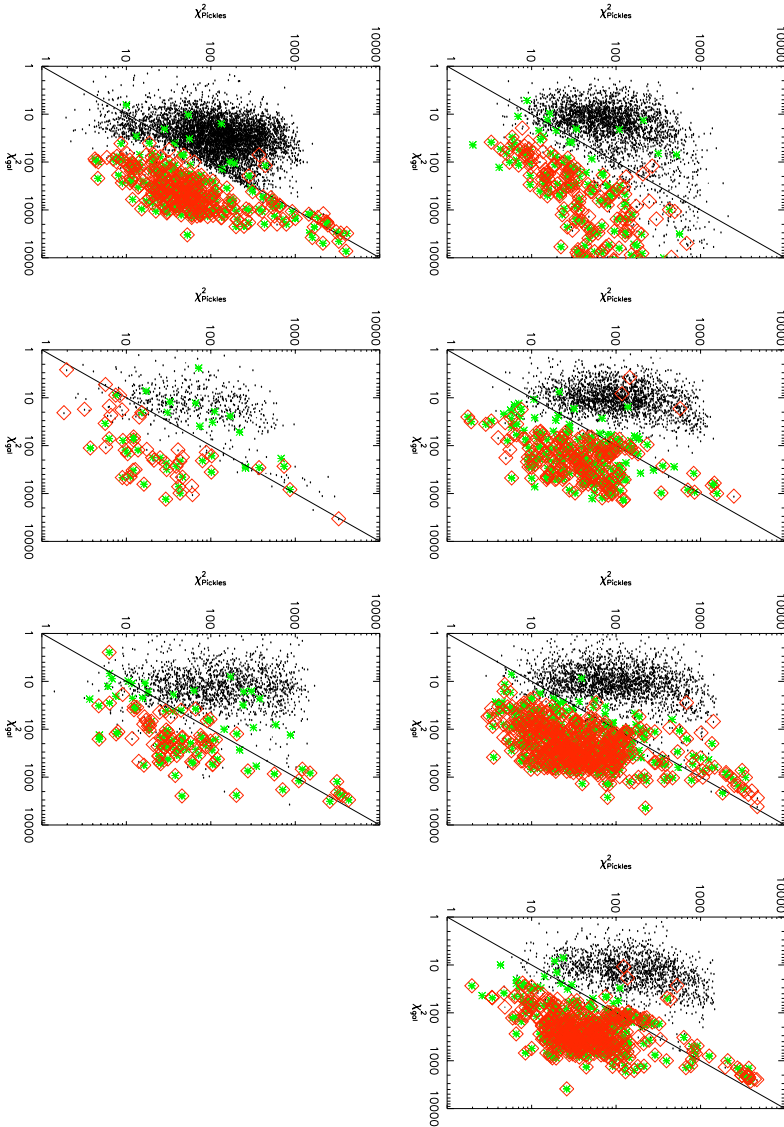


**Figure 5.10:** Comparison between the  $\chi^2$  obtained for the fitting with the EAZY galaxy templates and the  $\chi^2$  obtained with the Pickles (1998) models, for the 7 catalogues composing our sample. The green points represent the stars selected via the two-color diagram, while red diamonds refer to objects flagged as star in the downloaded catalogue.

in principle the effects of cosmic variance to low levels.

In this work, we included a more refined estimate of cosmic variance following the recipe by Moster et al. (2010). A halo distribution model is used to relate the stellar mass to the dark matter halo as a function of redshift; the galaxy bias is then estimated via dissipation-less N-body simulations. The cosmic variance is first computed on dark matter haloes, and then converted to galaxy cosmic variance by applying the galaxy bias. This estimate was cross-checked with the different evaluation of cosmic variance by Driver & Robotham (2010). Their work is based on direct computation of the cosmic variance using  $M^*$  galaxies from the SDSS catalogue. The expression found is then generalized to any redshift bin amplitude and mean value and to any geometry of the survey. We find that the two estimates, in the case of  $M^*$  galaxies, are consistent within 70% in the lowest redshift bin, but differ up to a factor of 2.5 in the higher redshift ranges. As discussed in Driver & Robotham (2010), this discrepancy can be explained as the change in  $M^*$  stellar mass value with redshift.

The computation of the luminosity as a function of mass (or, more frequently, the computation of mass from the luminosity), necessary to obtain the values for cosmic variance is generally a non trivial task, involving the generation of synthetic SEDs based on different initial mass functions, which are then fitted on a per-galaxy basis. For our purposes of cosmic variance estimate in the final LF, we performed the conversion between galaxy baryonic mass  $M$  and luminosity  $L_{J_{AB}}$  and  $L_{H_{AB}}$  a-posteriori on the LF, under the work hypothesis that the mass-to-light ratio can be considered constant over all the involved luminosity range and equal to its average value. We adopted the mean value  $\langle M/L \rangle = 1.0^{+0.32}_{-0.27} M_{\odot}/L_{\odot}$  from Cole et al. (2001) for both the  $J$  and  $H$  bands. In our estimation of the cosmic variance we did not take into account any variation in the  $M/L$  ratio as these would be a second order correction, being our primary goal the measurement of the variance related to the cosmic distribution of galaxies. In addition, while a uniform  $M/L$  ratio would be incompatible with observations at UV-to-optical wavelength (see e.g. González et al. (2010)), the rest-frame NIR wavelength range is better related to the stellar mass of a galaxy, suggesting a roughly constant  $M/L$  ratio at these wavelengths.

Figure 5.11 shows as a contour plot the values of the cosmic variance for our data as a function of redshift and galaxy mass, as computed using the Moster

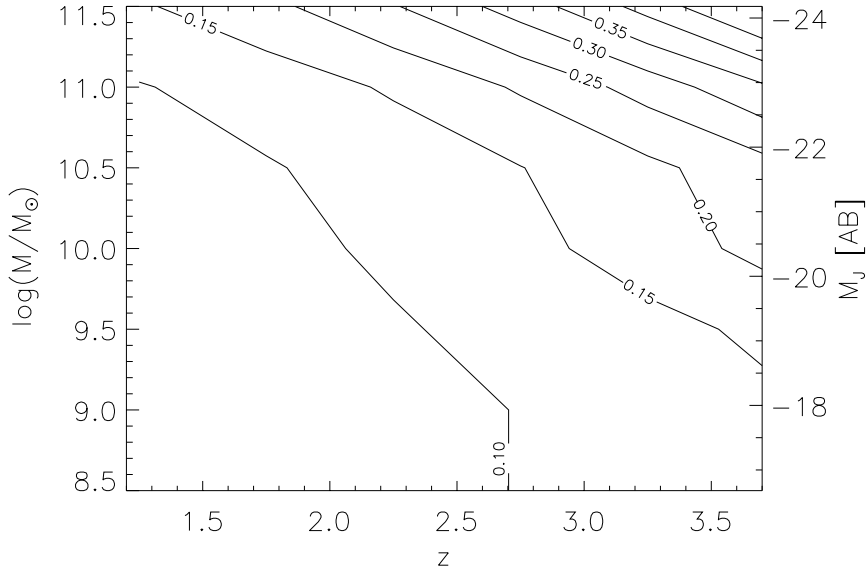


**Figure 5.11:** Cosmic variance estimate for our survey geometry following Moster et al. (2010), as a function of redshift and mass (left vertical axis) and absolute magnitude (right vertical axis).

et al. cookbook. The values of cosmic variance range from 0.07 to 0.19 in the lowest redshift bin, from 0.09 to 0.24 in the  $2.0 < z < 2.5$  bin, from 0.10 to 0.32 in the  $2.5 < z < 3.0$  bin and from 0.12 to 0.42 in the  $3.0 < z < 3.5$  redshift bin. The recovered uncertainties have been added in quadrature to the standard errors computed in the  $1/V_{max}$  and SWML methods, while the cosmic variance corresponding to  $M^*$  has been added in quadrature to the error on  $\phi^*$ .

The effects of photometric redshift errors have been studied via Monte Carlo simulations. Five hundred realizations of the LF in each redshift bin were computed. The redshift of each source in the original catalogue was randomly modified according to the gaussian standard deviation recovered from figure 5.8; the absolute magnitude of each object was then modified accordingly. The distribution of parameters of the recovered LF did not show any systematic effect and the spread of the parameters was compatible with the photometric errors. The distribution of the differences in the Schechter parameters for each redshift bin is presented in Figure 5.12.

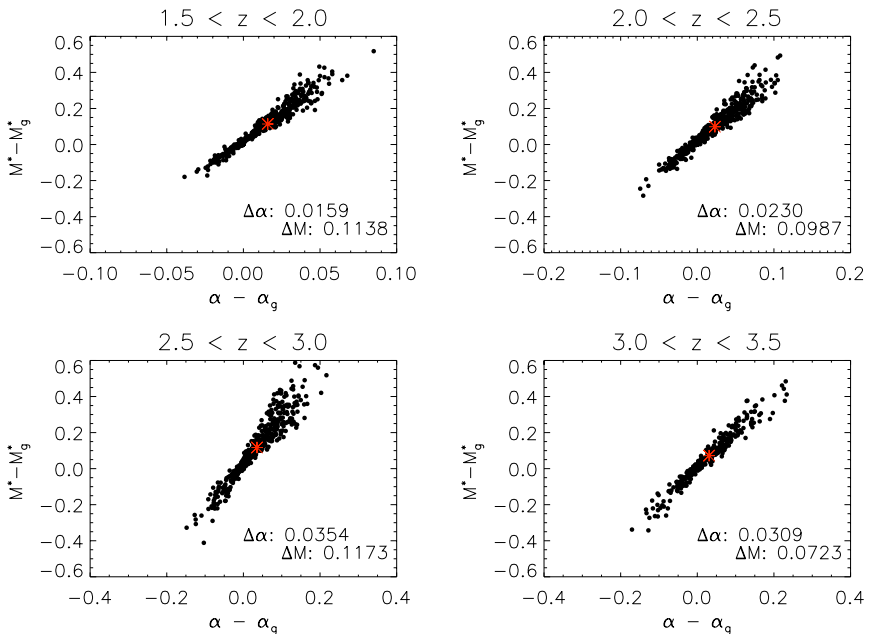


**Figure 5.12:** Effects of the error on the photometric redshifts on the recovery of the LF  $\alpha$  and  $M^*$  Schechter parameters. The black filled dots correspond to the difference between the input LF and the LF recovered after applying a gaussian spread to the redshift values, while the red asterisk indicates the mean displacement.

## 5.4 J and H Luminosity Functions

Both rest-frame J and H luminosity function were estimated in the redshift intervals  $1.5 < z < 2.0$ ,  $2.0 < z < 2.5$ ,  $2.5 < z < 3.0$  and  $3.0 < z < 3.5$  with the three methods described in Sec 5.3. In Table 5.3 and Table 5.4 we present our measurements obtained with the SWML and  $1/V_{max}$  method, while the derived Schechter parameters in each filter and redshift range are summarized in Table 5.1 and Table 5.2.

Figure 5.13 shows the LF for the rest-frame J filter in the four redshift bins. The number of objects used to construct the LF in each redshift bin are respectively 996, 419, 298 and 103. The three methods return consistent measurements of the LFs.

In Figure 5.14 we show our measurement of the LF obtained in the H filter,

z range	$\alpha$	$M^*$	$\phi^*$ ( $10^{-4}$ Mag $^{-1}$ Mpc $^{-3}$ )
1.5-2.0	$-1.24^{+0.03}_{-0.03}$	$-23.72^{+0.09}_{-0.06}$	$11.31^{+0.28}_{-0.10}$
2.0-2.5	$-1.12^{+0.11}_{-0.13}$	$-23.60^{+0.14}_{-0.17}$	$7.45^{+0.53}_{-0.38}$
2.5-3.0	$-1.17^{+0.18}_{-0.22}$	$-23.42^{+0.22}_{-0.23}$	$9.73^{+5.37}_{-2.33}$
3.0-3.5	$-0.92^{+0.42}_{-0.48}$	$-23.28^{+0.33}_{-0.39}$	$4.36^{+8.61}_{-1.93}$

**Table 5.1:** Schechter parameters for the J LF from the maximum likelihood analysis with one  $\sigma$  errors.

z range	$\alpha$	$M^*$	$\phi^*$ ( $10^{-4}$ Mag $^{-1}$ Mpc $^{-3}$ )
1.5-2.0	$-1.30^{+0.04}_{-0.03}$	$-24.03^{+0.06}_{-0.05}$	$8.79^{+0.50}_{-0.20}$
2.0-2.5	$-1.23^{+0.12}_{-0.07}$	$-23.94^{+0.13}_{-0.12}$	$4.35^{+0.68}_{-0.45}$
2.5-3.0	$-1.11^{+0.19}_{-0.18}$	$-23.74^{+0.21}_{-0.23}$	$6.32^{+4.52}_{-1.36}$
3.0-3.5	$-1.30^{+0.40}_{-0.49}$	$-23.89^{+0.36}_{-0.42}$	$2.03^{+8.50}_{-2.04}$

**Table 5.2:** Schechter parameters for the H LF from the maximum likelihood analysis with one  $\sigma$  errors.

for the same four redshift bins as for the J LF. The number of objects used to compute the LF is 996, 419, 298 and 103 respectively for the  $1.5 < z < 2.0$ ,  $2.0 < z < 2.5$ ,  $2.5 < z < 3.0$  and  $3.0 < z < 3.5$  intervals. To date, this is the first measurement of the rest-frame H LF in the interval  $z \in [1.5, 3.5]$ .

### 5.4.1 Discussion

The work by Saracco et al. (2006) is the only measurement of the LF in the rest-frame  $J$  band in redshift ranges comparable with those in our work available so far. In that paper, they estimate the J LF in three redshift ranges, namely  $z < 0.8$ ,  $0.8 < z < 1.9$  and  $1.9 < z < 4.0$ , based on observations of 101, 100 and 84 galaxies respectively, collected from HDF-S data and complemented by VLT-ISAAC J,H and K imaging.

At  $z \approx 1.5$ , the absolute magnitude ranges of the two determinations are quite different: their lack of points at the bright end, presumably due to the very small field of the HDF-S compared to ours, is compensated by a deeper limit at the faint end. Their Schechter representation of the LF is flatter ( $\alpha = -0.94$ ) than our lowest redshift LF and presents a dimmer characteristic magnitude, with a difference of about 1 magnitude. However, when directly comparing the  $1/V_{max}$

## 5.4. J AND H LUMINOSITY FUNCTIONS

$z$ range	$M_J[AB]$	$SWML[h_{70}^3 mag^{-1} Mpc^{-3}]$	$V_{max}[h_{70}^3 mag^{-1} Mpc^{-3}]$
$1.5 < z < 2.0$	-25.51	$4.78 (\pm 3.30) \pm 3.42 \times 10^{-6}$	$5.65 (\pm 3.99) \pm 4.13 \times 10^{-6}$
	-25.01	$2.87 (\pm 0.77) \pm 0.94 \times 10^{-5}$	$3.39 (\pm 0.98) \pm 1.16 \times 10^{-5}$
	-24.51	$1.08 (\pm 0.14) \pm 0.25 \times 10^{-4}$	$1.27 (\pm 0.19) \pm 0.30 \times 10^{-4}$
	-24.01	$2.90 (\pm 0.25) \pm 0.59 \times 10^{-4}$	$3.42 (\pm 0.31) \pm 0.71 \times 10^{-4}$
	-23.51	$4.44 (\pm 0.35) \pm 0.90 \times 10^{-4}$	$5.03 (\pm 0.38) \pm 1.01 \times 10^{-4}$
	-23.01	$5.90 (\pm 0.49) \pm 1.20 \times 10^{-4}$	$5.82 (\pm 0.43) \pm 1.17 \times 10^{-4}$
	-22.51	$9.09 (\pm 0.84) \pm 1.38 \times 10^{-4}$	$7.80 (\pm 0.62) \pm 1.13 \times 10^{-4}$
	-22.01	$1.26 (\pm 0.14) \pm 0.20 \times 10^{-3}$	$9.39 (\pm 0.84) \pm 1.41 \times 10^{-4}$
	-21.51	$1.61 (\pm 0.20) \pm 0.25 \times 10^{-3}$	-
	-21.01	$2.08 (\pm 0.36) \pm 0.41 \times 10^{-3}$	-
-20.51	$2.29 (\pm 0.66) \pm 0.69 \times 10^{-3}$	-	
$2.0 < z < 2.5$	-25.17	$1.36 (\pm 0.52) \pm 0.61 \times 10^{-5}$	$1.61 (\pm 0.66) \pm 0.77 \times 10^{-5}$
	-24.67	$4.52 (\pm 0.91) \pm 1.44 \times 10^{-5}$	$5.36 (\pm 1.20) \pm 1.78 \times 10^{-5}$
	-24.17	$1.15 (\pm 0.15) \pm 0.32 \times 10^{-4}$	$1.38 (\pm 0.19) \pm 0.39 \times 10^{-4}$
	-23.67	$2.24 (\pm 0.25) \pm 0.61 \times 10^{-4}$	$2.65 (\pm 0.29) \pm 0.71 \times 10^{-4}$
	-23.17	$4.08 (\pm 0.47) \pm 1.11 \times 10^{-4}$	$4.48 (\pm 0.48) \pm 1.20 \times 10^{-4}$
	-22.67	$4.22 (\pm 0.64) \pm 0.92 \times 10^{-4}$	$4.36 (\pm 0.58) \pm 0.89 \times 10^{-4}$
	-22.17	$5.52 (\pm 0.93) \pm 1.27 \times 10^{-4}$	$4.24 (\pm 0.59) \pm 0.89 \times 10^{-4}$
	-21.67	$6.51 (\pm 1.28) \pm 1.50 \times 10^{-4}$	$7.48 (\pm 1.41) \pm 1.67 \times 10^{-4}$
	-21.17	$7.58 (\pm 2.12) \pm 2.31 \times 10^{-4}$	-
$2.5 < z < 3.0$	-25.19	$8.41 (\pm 3.73) \pm 4.62 \times 10^{-6}$	$1.61 (\pm 0.66) \pm 0.84 \times 10^{-5}$
	-24.69	$2.82 (\pm 0.76) \pm 1.19 \times 10^{-5}$	$4.43 (\pm 1.11) \pm 1.81 \times 10^{-5}$
	-24.19	$8.45 (\pm 1.54) \pm 3.14 \times 10^{-5}$	$1.21 (\pm 0.21) \pm 0.44 \times 10^{-4}$
	-23.69	$1.68 (\pm 0.27) \pm 0.60 \times 10^{-4}$	$2.19 (\pm 0.36) \pm 0.79 \times 10^{-4}$
	-23.19	$3.78 (\pm 0.53) \pm 1.33 \times 10^{-4}$	$4.35 (\pm 0.58) \pm 1.52 \times 10^{-4}$
	-22.69	$7.48 (\pm 1.07) \pm 1.88 \times 10^{-4}$	$5.80 (\pm 0.73) \pm 1.40 \times 10^{-4}$
	-22.19	$1.03 (\pm 0.17) \pm 0.27 \times 10^{-3}$	-
	-21.69	$1.14 (\pm 0.29) \pm 0.38 \times 10^{-3}$	-
	-	-	-
$3.0 < z < 3.5$	-24.93	$2.64 (\pm 1.25) \pm 1.67 \times 10^{-5}$	$1.83 (\pm 0.75) \pm 1.07 \times 10^{-5}$
	-24.43	$3.81 (\pm 1.42) \pm 2.13 \times 10^{-5}$	$2.51 (\pm 1.13) \pm 1.54 \times 10^{-5}$
	-23.93	$9.80 (\pm 1.67) \pm 4.43 \times 10^{-5}$	$7.45 (\pm 2.23) \pm 3.83 \times 10^{-5}$
	-23.43	$1.68 (\pm 0.14) \pm 0.72 \times 10^{-4}$	$1.54 (\pm 0.38) \pm 0.75 \times 10^{-4}$
	-22.93	$2.19 (\pm 0.25) \pm 0.95 \times 10^{-4}$	$2.82 (\pm 1.35) \pm 1.79 \times 10^{-4}$
	-22.43	$2.55 (\pm 0.47) \pm 0.83 \times 10^{-4}$	-

**Table 5.3:** Luminosity function values obtained with the SWML and  $V_{max}$  methods in the four redshift bins for the  $J$  filter. The first error value refers to the error estimated via the information matrix for the SWML method and to the Poisson error for the  $V_{max}$  method, while the second term is the cumulative error taking into account also cosmic variance uncertainties.

$z$ range	$M_H[AB]$	$SWML[h_{70}^3 mag^{-1} Mpc^{-3}]$	$V_{max}[h_{70}^3 mag^{-1} Mpc^{-3}]$
$1.5 < z < 2.0$	-25.63	$4.12 (\pm 2.85 \pm 2.95 \times 10^{-6})$	$5.69 (\pm 4.02) \pm 4.16 \times 10^{-6}$
	-25.13	$3.71 (\pm 0.79) \pm 1.05 \times 10^{-5}$	$5.08 (\pm 1.20) \pm 1.53 \times 10^{-5}$
	-24.63	$1.24 (\pm 0.14) \pm 0.27 \times 10^{-4}$	$1.69 (\pm 0.22) \pm 0.38 \times 10^{-4}$
	-24.13	$2.74 (\pm 0.23) \pm 0.56 \times 10^{-4}$	$3.73 (\pm 0.33) \pm 0.77 \times 10^{-4}$
	-23.63	$3.92 (\pm 0.32) \pm 0.80 \times 10^{-4}$	$4.91 (\pm 0.37) \pm 0.99 \times 10^{-4}$
	-23.13	$5.04 (\pm 0.44) \pm 1.04 \times 10^{-4}$	$4.86 (\pm 0.38) \pm 0.98 \times 10^{-4}$
	-22.63	$8.61 (\pm 0.81) \pm 1.32 \times 10^{-4}$	$6.19 (\pm 0.50) \pm 0.90 \times 10^{-4}$
	-22.13	$1.04 (\pm 0.12) \pm 0.17 \times 10^{-3}$	$7.49 (\pm 0.73) \pm 1.16 \times 10^{-4}$
	-21.63	$1.53 (\pm 0.19) \pm 0.27 \times 10^{-3}$	-
	-21.13	$2.03 (\pm 0.34) \pm 0.39 \times 10^{-3}$	-
-20.63	$2.26 (\pm 0.61) \pm 0.64 \times 10^{-3}$	-	
$2.0 < z < 2.5$	-25.29	$2.04 (\pm 0.55) \pm 0.74 \times 10^{-5}$	$2.95 (\pm 0.89) \pm 1.15 \times 10^{-5}$
	-24.79	$4.06 (\pm 0.80) \pm 1.28 \times 10^{-5}$	$5.89 (\pm 1.26) \pm 1.92 \times 10^{-5}$
	-24.29	$1.23 (\pm 0.15) \pm 0.34 \times 10^{-4}$	$1.74 (\pm 0.22) \pm 0.48 \times 10^{-4}$
	-23.79	$1.76 (\pm 0.21) \pm 0.48 \times 10^{-4}$	$2.02 (\pm 0.23) \pm 0.55 \times 10^{-4}$
	-23.29	$3.46 (\pm 0.44) \pm 0.96 \times 10^{-4}$	$2.97 (\pm 0.34) \pm 0.81 \times 10^{-4}$
	-22.79	$3.62 (\pm 0.57) \pm 1.06 \times 10^{-4}$	$3.75 (\pm 0.51) \pm 1.05 \times 10^{-4}$
	-22.29	$5.04 (\pm 0.88) \pm 1.18 \times 10^{-4}$	$4.36 (\pm 0.71) \pm 0.99 \times 10^{-4}$
	-21.79	$5.56 (\pm 1.14) \pm 1.44 \times 10^{-4}$	$5.05 (\pm 0.94) \pm 1.23 \times 10^{-4}$
-21.29	$6.27 (\pm 1.69) \pm 1.84 \times 10^{-4}$	-	
$2.5 < z < 3.0$	-25.60	$5.69 (\pm 2.93) \pm 3.46 \times 10^{-6}$	$1.34 (\pm 0.60) \pm 0.74 \times 10^{-5}$
	-25.10	$1.91 (\pm 0.58) \pm 0.84 \times 10^{-5}$	$3.49 (\pm 0.97) \pm 1.49 \times 10^{-5}$
	-24.60	$5.21 (\pm 1.06) \pm 1.99 \times 10^{-5}$	$6.98 (\pm 1.37) \pm 2.64 \times 10^{-5}$
	-24.10	$1.05 (\pm 0.18) \pm 0.39 \times 10^{-4}$	$9.98 (\pm 1.72) \pm 3.65 \times 10^{-5}$
	-23.60	$2.20 (\pm 0.35) \pm 0.79 \times 10^{-4}$	$2.67 (\pm 0.39) \pm 0.95 \times 10^{-4}$
	-23.10	$3.93 (\pm 0.65) \pm 1.43 \times 10^{-4}$	$4.40 (\pm 0.59) \pm 1.54 \times 10^{-4}$
	-22.60	$5.56 (\pm 1.03) \pm 1.54 \times 10^{-4}$	$4.25 (\pm 0.60) \pm 1.06 \times 10^{-4}$
	-22.10	$7.23 (\pm 1.51) \pm 2.12 \times 10^{-4}$	-
$3.0 < z < 3.5$	-25.25	$1.40 (\pm 1.02) \pm 1.17 \times 10^{-5}$	$1.10 (\pm 0.55) \pm 0.72 \times 10^{-5}$
	-24.75	$3.32 (\pm 1.13) \pm 1.79 \times 10^{-5}$	$1.93 (\pm 0.73) \pm 1.09 \times 10^{-5}$
	-24.25	$6.10 (\pm 1.98) \pm 3.23 \times 10^{-5}$	$4.11 (\pm 1.19) \pm 2.10 \times 10^{-5}$
	-23.75	$4.69 (\pm 2.10) \pm 2.87 \times 10^{-5}$	$5.38 (\pm 1.94) \pm 2.97 \times 10^{-5}$
	-23.25	$1.47 (\pm 0.62) \pm 0.87 \times 10^{-4}$	$1.77 (\pm 0.39) \pm 0.84 \times 10^{-4}$
	-22.75	$1.35 (\pm 0.54) \pm 0.65 \times 10^{-4}$	$1.88 (\pm 0.45) \pm 0.68 \times 10^{-4}$

**Table 5.4:** Luminosity function values obtained with the SWML and  $V_{max}$  methods in the four redshift bins for the  $H$  filter. The first error value refers to the error estimated via the information matrix for the SWML method and to the Poisson error for the  $V_{max}$  method, while the second term is the cumulative error taking into account also cosmic variance uncertainties.

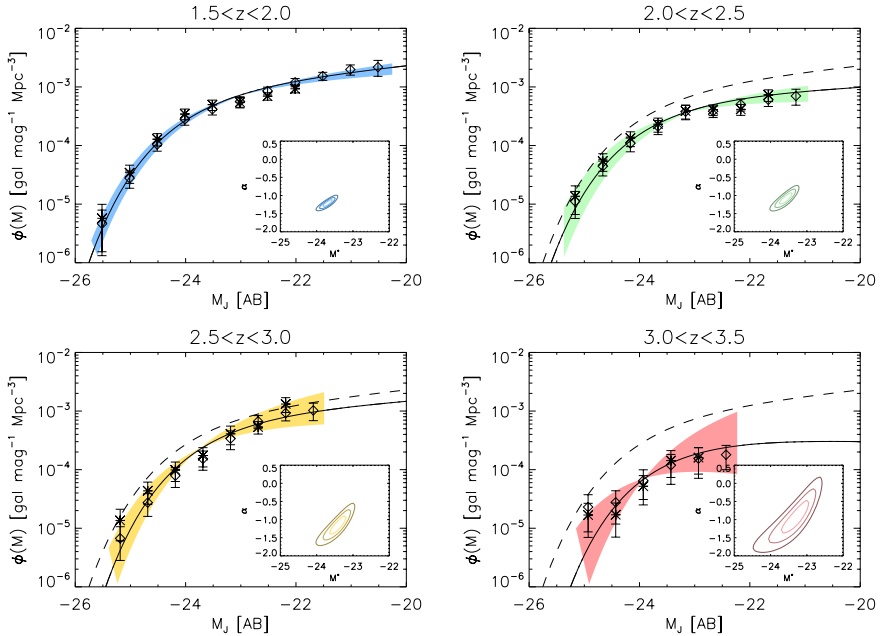


**Figure 5.13:** Luminosity function for the J rest frame band, in the four redshift bins. Asterisks represent the  $1/V_{max}$  measurement, diamonds are from the SWML. The Schechter function obtained via the maximum likelihood is shown as the solid black line. The coloured area in each plot indicates the  $1\sigma$  (68% confidence level) from the parametric maximum likelihood. The inset shows the 1, 2 and 3  $\sigma$  contours (corresponding to 68%, 95% and 98% confidence region) for the joint  $\alpha$ - $M^*$  parameters from the ML analysis. As a reference, the  $z=1.75$  LF is reported as a dashed line in the panels corresponding to higher redshift bins.

estimate from Saracco et al. (2006) with our non parametric  $1.5 < z < 2.0$  LFs, we find similar LFs (see Figure 5.15, left panel) with points lying within the 1 sigma error bars. Despite these differences, our Schechter parameterization is substantially compatible also with their points. We would like to note that our composite catalogue provides an improved sampling of the bright end, resulting in overall better constrained Schechter parameters.

In the highest redshift bin, the differences in the Schechter parameters are still present, with the faint-end slope  $\alpha$  being the parameter showing the larger dispersion. Also in this case, when comparing our non parametric estimate with their points, we find a good agreement (see the right panel in Figure 5.15).

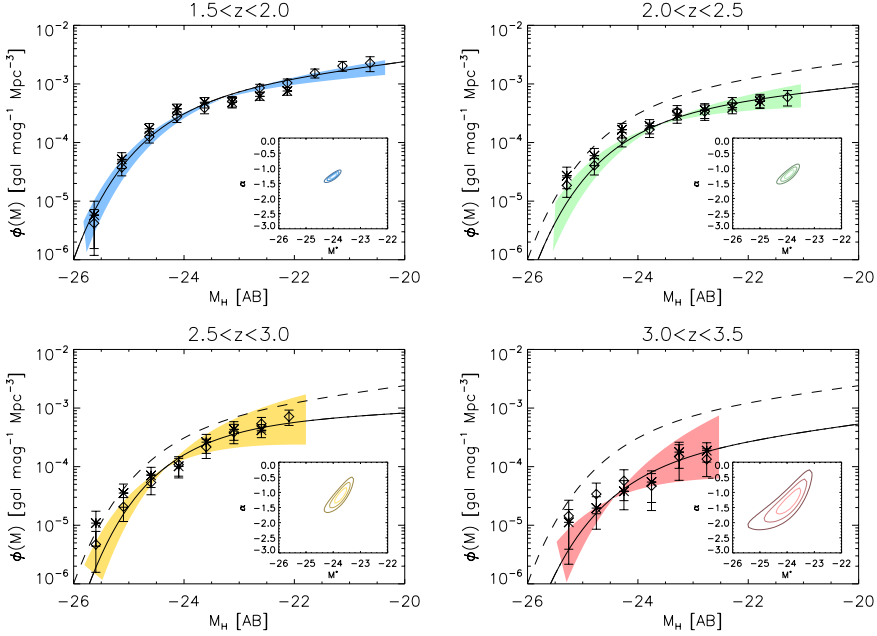


**Figure 5.14:** Luminosity function in the H rest frame filter. Plot conventions are the same as for Figure 5.13.

In Figure 5.16 we compare the Schechter parameters for the rest-frame  $J$ -band obtained in this work with those available in the literature as a function of redshift.

The upper panel shows the evolution of  $\phi^*$  as a function of redshift.  $\phi^*$  is monotonically decreasing with increasing  $z$ . By  $z \simeq 2$ ,  $\phi^*$  has decreased by a full order of magnitude compared to the local values. The following parameterization was adopted to model the observed evolution of  $\phi^*$  with  $z$ :

$$\phi^*(z) = \theta \exp \left[ \gamma / (1+z)^\beta \right] \quad (5.3)$$

where  $\theta$ ,  $\gamma$  and  $\beta$  are the free parameters. The best-fit values obtained for the parameters of the J rest-frame band are  $\theta_J = 2.9 \pm 0.9 \times 10^{-5} \text{ mag}^{-1} \text{ Mpc}^{-3}$ ,  $\gamma_J = 6.5 \pm 0.3$ ,  $\beta_J = 0.56$ . The  $\beta$  parameter was estimated together with the other two in the first instance of the best fitting procedure, and kept fix in a second iteration. The quoted errors refer to the second iteration. Equation 5.3 appears

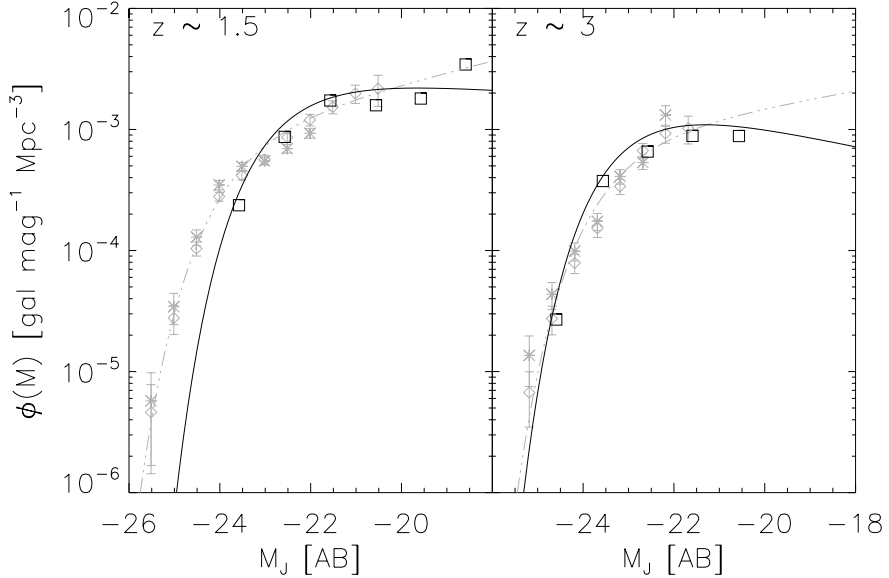


**Figure 5.15:** Comparison of Saracco et al. (2006) LFs (black squares and black solid line) with our measurements (grey symbols: asterisks for  $1/V_{max}$ , diamonds for the SWML, dash-dotted line for the Schechter parameterization). The left panel refers to  $z \approx 1.5$  LF, while the right panel to the  $z \approx 3$  LF.

as a dashed line in the upper panel of Figure 5.16.

In the middle panel we present the evolution of  $M^*$  as a function of redshift. Data show a brightening of  $M^*$  from the local universe to  $z \simeq 2$ , followed by a slow dimming. In analogy to the LF shape by Schechter (1976), it is then possible to introduce the following ad-hoc representation for  $M^*(z)$ :

$$M^*(z) = \mu [(1+z)/(1+z^*)]^\eta \exp[-(1+z)/(1+z^*)] \quad (5.4)$$

with  $\mu$ ,  $z^*$  and  $\eta$  free parameters to be determined. By performing a least-square fit to the available data set we obtain the following values:  $\mu_J = -44.6 \pm 0.2$  mag,  $z_J^* = 9.5 \pm 0.5$ ,  $\eta_J = 0.28 \pm 0.15$ . The resulting curve is plotted as a dashed line in the middle panel of Figure 5.16.

The lower panel illustrates the behavior of  $\alpha$  as a function of redshift. The error bars are here generally large and do not allow to properly evaluate the

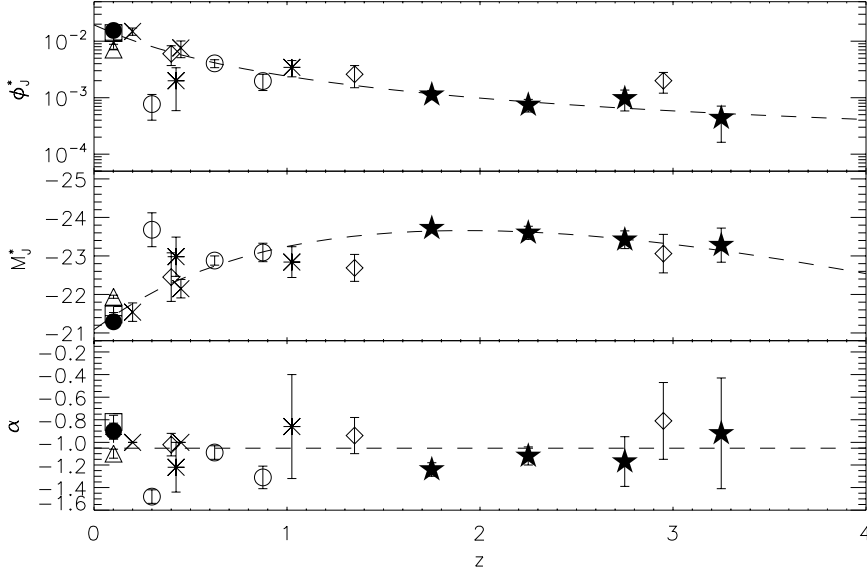


**Figure 5.16:** Evolution of the Schechter parameters of the J LF as a function of redshift. Estimates from this work are shown as filled black stars. Measurements from the literature are also plotted (vertical crosses: Cole et al. 2001; asterisks: Pozzetti et al. 2003; crosses: Feulner et al. 2003; open squares: Eke et al. 2005; open circles: Dahlen et al. 2005; open diamonds: Saracco et al. 2006; open triangles: Jones et al. 2006; filled circle: Hill et al. 2010). Top panel shows the data for  $\phi^*$ . The dashed line represents Eq. 5.3 (see text for details); the middle panel presents the measurements for  $M^*$ , with the dashed line representing Eq. 5.4; in the lower panel the faint end slopes  $\alpha$  together with the average value (dashed line) are shown.

presence of evolution as a function of  $z$ . Therefore we limit ourselves to compute an average value, resulting in  $\bar{\alpha} = -1.05 \pm 0.03$ .

Figure 5.17 shows the plots of the Schechter parameters as a function of redshift corresponding to the rest-frame  $H$ -band. For this band, there are only two determinations of the LF from the literature, so that it is more challenging trying to deduce any evolution. Despite this, we applied the same analysis done for the rest-frame  $J$ -band, obtaining  $\theta_H = 9.1 \pm 3.9 \times 10^{-6} \text{ mag}^{-1} \text{ Mpc}^{-3}$ ,  $\gamma_H = 7.8 \pm 0.5$ ,  $\beta_H = 0.56$  for the parameters of Eq. 5.3;  $\mu_H = -46.5 \pm 4.3$ ,  $z_H^* = 9.0 \pm 3.9$ ,  $\eta_H = 0.30 \pm 0.08$  for Eq. 5.4 and  $\bar{\alpha} = -1.15 \pm 0.02$ . The resulting curves are shown as dashed lines in Figure 5.17.

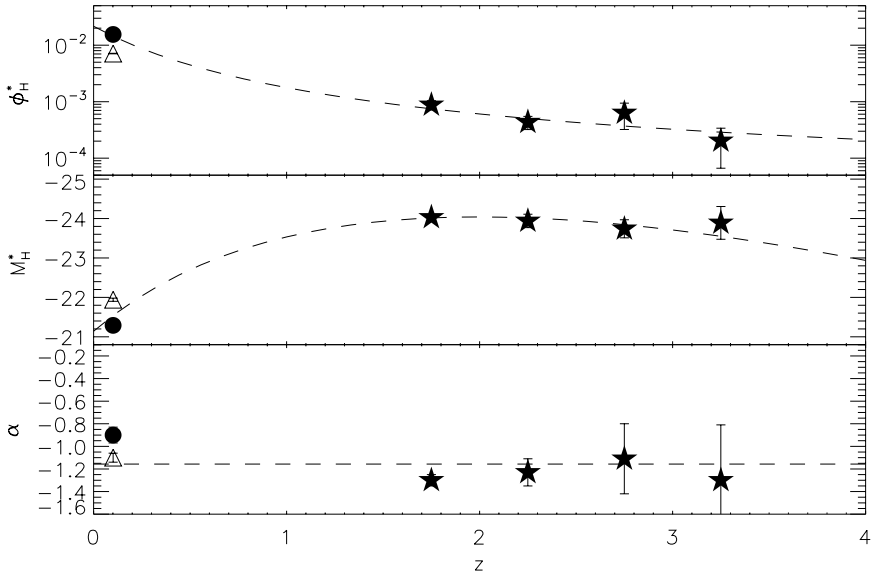


**Figure 5.17:** Evolution of the Schechter  $\phi^*$ ,  $M^*$  and  $\alpha$  parameters from the H LF as a function of redshift. See caption to Figure 5.16 for details.

## 5.4.2 Luminosity densities

Here we present our measurements of the luminosity density, obtained in the standard way, i.e. as:

$$\rho_J = \int_0^{+\infty} L\Phi(L)dL = \Gamma(2 + \alpha)L^*\phi^* \quad (5.5)$$

where the last equality holds when assuming a Schechter parametrization for the  $\Phi(L)$ . This means that we are assuming that the Schechter distribution is a good representation of the underlying luminosity function. Figure 5.18 shows the evolution of the luminosity density in the  $J$  filter, while Figure 5.19 displays the corresponding plot for the rest-frame  $H$ -band. Values of the luminosity density at each redshift and for each filter are presented in Table 5.5.

In order to be less sensitive to the derived faint end slope of the LF, we also computed the luminosity density assuming a limiting absolute magnitude equal to the limit of our survey, i.e.  $M_{lim} = -20.0$ . These results are presented in the

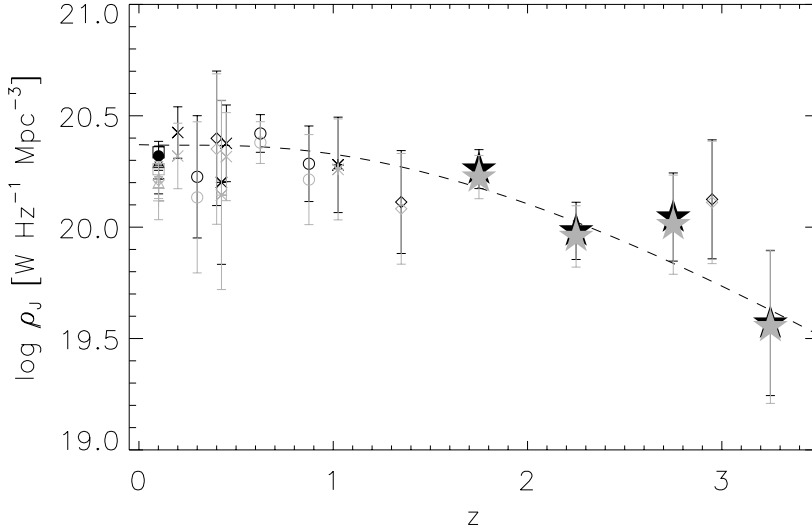


**Figure 5.18:** Luminosity density  $\rho_J$  as computed from our Schechter parameters (filled black stars) and compared with the available data in the redshift range  $[0,3.0]$ . Greyed symbols indicate the luminosity density computed assuming an absolute magnitude limit of  $M_J = -20.0$ . The dashed line represents the LD obtained directly from Eq. 5.5 in terms of Eq. 5.3 and 5.4. Plotting symbols same as for Fig. 5.16.

plots as greyed symbols.

The overall plot of the J luminosity density shows a constant or slightly increasing value for  $z \lesssim 0.8 - 1.0$ . At  $z \approx 0.8 - 1.0$  the luminosity density starts to decrease down to  $z \approx 3.5$ , although the points at  $2.0 \lesssim z \lesssim 3.0$  suggest a possible plateau at this epoch. This can be better visualized by comparing this plot with the top and middle panels of Figure 5.16. Here we see in fact that for  $z \lesssim 1$  the decrease in number of galaxies is balanced by a brightening of the characteristic magnitude. After this point both quantities decrease, making the luminosity density also decrease.

Using the expression of Eq. 5.3 and Eq. 5.4 in Eq. 5.5, it is possible to obtain a functional representation of the luminosity density. The dashed line in Figure 5.18 represents the luminosity density for the rest-frame J-band obtained with

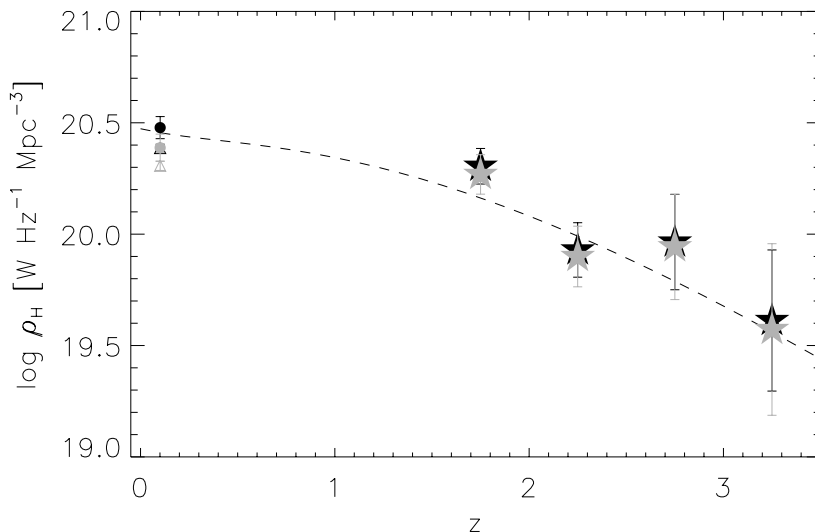


**Figure 5.19:** Luminosity density  $\rho_H$  as computed from our Schechter parameters (filled black stars) and compared with the available data. See caption to Fig. 5.18 for details.

this method and adopting the values of the parameters previously recovered via best-fit. The agreement with the points is good in the entire redshift range. We would like to stress that no best fit has been done using the data of the luminosity density, as we only used the parametric expressions for the evolution of  $\phi_*$  and  $M_*$ .

Similarly to the case of the LF, the luminosity density in the  $H$  filter has been poorly studied, so that it is more difficult to trace the path of its evolution. Our data however indicate a decline with redshift of the LD, similar in shape to the one found also in the  $J$  band, with a faster evolution from  $z = 3.5$  to  $z = 1.5$ , followed by a much smaller evolution. An exercise similar to what done for computing the  $J$  luminosity density, introducing our parameterizations, is shown as a dashed line in Figure 5.19. The agreement seems to be quite good in the whole redshift range, although more measurements are necessary at  $z < 1.5$ .

Filter	$z$ range	$\log \rho$	$\log \rho(M_{lim} = -20)$
<i>J</i>	1.5-2.0	$20.26 \pm 0.08$	$20.22 \pm 0.09$
	2.0-2.5	$19.98 \pm 0.12$	$19.96 \pm 0.13$
	2.5-3.0	$20.05 \pm 0.18$	$20.01 \pm 0.20$
	3.0-3.5	$19.57 \pm 0.30$	$19.55 \pm 0.32$
<i>H</i>	1.5-2.0	$20.30 \pm 0.08$	$20.27 \pm 0.09$
	2.0-2.5	$19.93 \pm 0.12$	$19.90 \pm 0.14$
	2.5-3.0	$19.96 \pm 0.21$	$19.94 \pm 0.24$
	3.0-3.5	$19.61 \pm 0.32$	$19.57 \pm 0.38$

**Table 5.5:** Luminosity density in logarithmic scale and expressed in units of  $\log[\text{W Hz}^{-1} \text{Mpc}^{-3}]$ , in the rest-frame *J*- and *H*- bands. Quoted errors include the effects of cosmic variance. In the third column we report the luminosity density computed using Eq. 5.5 and corresponding to the black stars in Figures 5.18 and 5.19; the values of the luminosity density in the fourth column reflect the upper limit in absolute magnitude corresponding to  $M_{lim} = -20$ , which we imposed in order to limit the effect of the uncertainties in the determination of  $\alpha$  (grey stars in the same figures).

### 5.4.3 Star Formation Rate

As a last exercise, we computed the star formation rate (SFR) by differentiating with respect to cosmic time the parametric formula obtained for the luminosity density from Eqq. 5.3 and 5.4, and adopting a mass-to-light ration  $M_{\odot}/L_{J,\odot} = 1$ . (Cole et al., 2001) The result is shown in Figure 5.20 by the solid line, while data points and corresponding errors have been taken from Bouwens et al. (2005).

The line approximates quite well the data points to  $z \simeq 2$ . However, in the region between  $z \simeq 2.5$  and  $z \simeq 8$  our measurement disagrees with the SFR from Bouwens et al. (2005) by a factor  $\approx 0.4 - 0.5$ , appearing also lower compared with other measurements (Bouwens et al. 2011 and references therein). However, we must recall that our parameterization has been fitted on data up to  $z = 3.5$ , so that the comparison is done on an extrapolation. Another factor could be the different wavebands the SFR are extracted from. Our SFR, in fact, is based on rest-frame J band, while the measurements presented by Bouwens et al. (2005) are all based on UV data.

Whereas our measurement is simpler, in the sense that it directly estimates stellar mass as it is formed, theirs can be seen a more straightforward as they

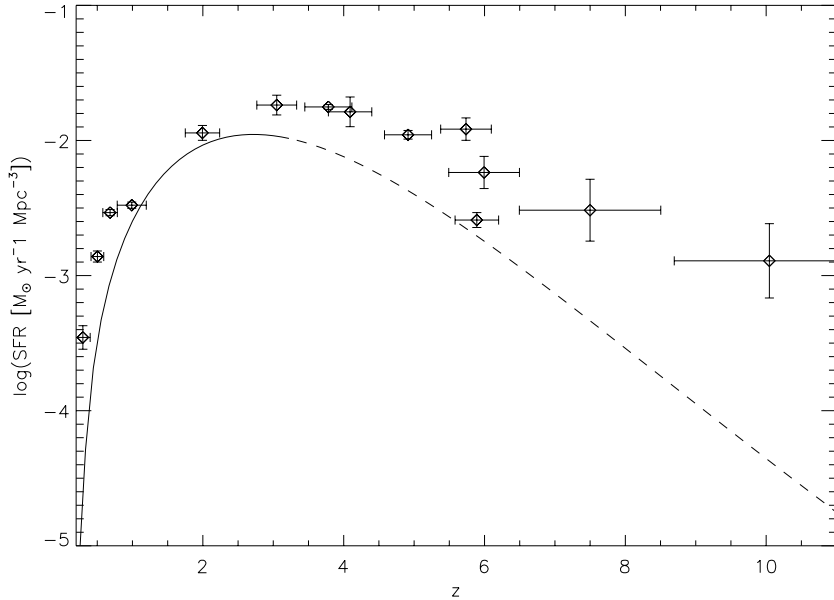


**Figure 5.20:** Star formation rate as computed from our parameterization of the luminosity density (solid line). Diamonds refer to the measurements collected in Bouwens et al. (2005).

measure UV flux from young stars directly, but depend upon modelling to estimate the total stellar mass that it is created.

## 5.5 Conclusions

In the present work, we used a composite sample constructed from deep multi-wavelength publicly available photometric catalogues from the MUSYC, FIRES and FIREWORKS projects. The availability of *Spitzer* data in the 3.6, 4.5, 5.8 and 8 $\mu$ m channels allows us to robustly estimate the LF and LD in the rest-frame *J*– and *H*– bands with a minimum dependence on the SED templates up to  $z = 3.5$ .

Uncertainties introduced by the cosmic variance were estimated using two distinct methods, one by Moster et al. (2010) and the other by Driver & Robotham

(2010). We find that for our data the two approaches agree to within a factor of 2.5, which can be due to the change for the  $M^*$  stellar mass value with redshift (Driver & Robotham, 2010).

We determined the LF with three independent methods, namely the  $1/V_{max}$ , the SWML and the STYML methods. We find that they do agree well with each other.

Our rest-frame  $J$ -band LF is consistent with previous determination by Saracco et al. (2006), although the recovered Schechter parameters  $M^*$  and  $\alpha$  are consistent only at the  $2\sigma$  level. This might be due to the limited range in rest-frame magnitudes probed by the sample in Saracco et al. (2006). Our determination of the rest-frame  $J$ -band improves the coverage of the bright end measurement by 1 full magnitude.

We determined for the first time the LF in the rest-frame  $H$ -band up to  $z = 3.5$ . Given that this band is less contaminated from AGN dust emission than the rest-frame  $K$ -band, it suggests itself as a more direct and solid measurement of the mass assembly across cosmic time, simplifying the task of comparison with the current models.

We analyzed the evolution of the Schechter function parameters as a function of redshift, making full use of the data available from the literature. We found that the faint end slope  $\alpha$  of the LF is nearly constant over the whole redshift range and that  $\phi^*$  decreases by a factor of  $\approx 10$  from  $z = 0$  to  $z = 1.75$ , and by a factor of  $\approx 3$  to  $z = 3.25$ . We introduced a parameterization based on an exponential form for the evolution of  $\phi^*$  as a function of  $z$ . The fit of this function to the available data shows good agreement, especially for the rest-frame  $J$ -band, where more data from the literature are available in the redshift range  $z \in [0, 1]$ , complementing our measurements at  $z > 1.5$ .

The behavior of  $M^*$  as a function of  $z$  shows an increase from  $z = 0$  to  $z \simeq 2$ , followed by a smoother decrease. We adopted a Schechter (1976)-like expression for its description, resulting in a good representation of the observed evolution.

We finally computed the LD in the rest-frame  $J$ - and  $H$ - bands, using the Schechter parameters previously determined. The LD is nearly constant up to  $z \approx 1$  and decreases as a power-law by a factor of  $\approx 6$  from  $z \approx 1$  to  $z = 3.25$ .

## 5.5. CONCLUSIONS

---

In order to obtain a more solid constraint of the LF, a larger area is needed to better probe the bright end and reduce the impact of field-to-field variations and low number statistics. To this aim, projects with data publicly available like the NEWFIRM Medium Band Surveys (van Dokkum et al., 2009) or the Cosmic Assembly Near-IR Deep Extragalactic Legacy Survey (CANDELS - Koekemoer et al. 2011) will be of invaluable help, paving the way to the results from the surveys of the next decades with new telescopes like the JWST and E-ELT.

# Bibliography

- Avni Y., Bahcall J. N., 1980, *ApJ*, 235, 694
- Bell E. F., McIntosh D. H., Katz N., Weinberg M. D., 2003, *ApJS*, 149, 289
- Benítez N., 2000, *ApJ*, 536, 571
- Berta S., et al., 2007, *A&A*, 476, 151
- Blanton M. R., Roweis S., 2007, *AJ*, 133, 734
- Bolzonella M., Pelló R., Maccagni D., 2002, *A&A*, 395, 443
- Bouwens R. J., Illingworth G. D., Thompson R. I., Franx M., 2005, *ApJ*, 624, L5
- Bouwens R. J., et al., 2011, *ApJ*, 737, 90
- Brammer, G. B., van Dokkum, P. G., and Coppi, P. 2008, *ApJ*, 686, 1503
- Caputi K. I., McLure R. J., Dunlop J. S., Cirasuolo M., Schael A. M., 2006, *MNRAS*, 366, 609
- Cimatti A., et al., 2002, *A&A*, 392, 395
- Cirasuolo M., et al., 2007, *MNRAS*, 380, 585
- Cirasuolo M., McLure R. J., Dunlop J. S., Almaini O., Foucaud S., Simpson C., 2010, *MNRAS*, 401, 1166
- Cole S., et al., 2001, *MNRAS*, 326, 255
- Coleman G. D., Wu C.-C., Weedman D. W., 1980, *ApJS*, 43, 393
- Conroy C., Gunn J. E., White M., 2009, *ApJ*, 699, 486
- Cowie L. L., Songaila A., Hu E. M., Cohen J. G., 1996, *AJ*, 112, 839
- Dahlen T., Mobasher B., Somerville R. S., Moustakas L. A., Dickinson M., Ferguson H. C., Giavalisco M., 2005, *ApJ*, 631, 126
- De Lucia G., Blaizot J., 2007, *MNRAS*, 375, 2
- Driver S. P., Robotham A. S. G., 2010, *MNRAS*, 407, 2131

## BIBLIOGRAPHY

---

- Drory N., Bender R., Feulner G., Hopp U., Maraston C., Snigula J., Hill G. J., 2003, *ApJ*, 595, 698
- Efstathiou G., Ellis R. S., Peterson B. A., 1988, *MNRAS*, 232, 431
- Eke V. R., Baugh C. M., Cole S., Frenk C. S., King H. M., Peacock J. A., 2005, *MNRAS*, 362, 1233
- Feulner G., Bender R., Drory N., Hopp U., Snigula J., Hill G. J., 2003, *MNRAS*, 342, 605
- Fioc, M., & Rocca-Volmerange, B. 1997, *A&A*, 326, 950
- Forster Schreiber N. et al., 2006, *AJ* 131, 1891
- Gardner J. P., Sharples R. M., Frenk C. S., Carrasco B. E., 1997, *ApJ*, 480, L99
- Gawiser, E. et al., 2006, *ApJSS*, 162, 1
- Glazebrook K., Peacock J. A., Miller L., Collins C. A., 1995, *MNRAS*, 275, 169
- González V., Labbé I., Bouwens R. J., Illingworth G., Franx M., Kriek M., Brammer G. B., 2010, *ApJ*, 713, 115
- Goto T., et al., 2010, *A&A*, 514, A6
- Hill D. T., Driver S. P., Cameron E., Cross N., Liske J., Robotham A., 2010, *MNRAS*, 404, 1215
- Huang J.-S., Glazebrook K., Cowie L. L., Tinney C., 2003, *ApJ*, 584, 203
- Ilbert O., et al., 2006, *A&A*, 442, 423
- Jones D. H., Peterson B. A., Colless M., Saunders W., 2006, *MNRAS*, 369, 25
- Kashikawa N., et al., 2003, *AJ*, 125, 53
- Kochanek C. S., et al., 2001, *ApJ*, 560, 566
- Koekemoer, A. M., et al., 2011, *ApJS* submitted [arXiv:1105.375]
- Labbé I. et al., 2003, *AJ* 125, 1107

- Loveday J., 2000, MNRAS, 312, 557
- Maraston C., 2005, MNRAS, 362, 799
- Marchesini D., et al., 2007, ApJ, 656, 42
- Marchesini D. et al., 2009, ApJ 701, 1765
- Mobasher B., Sharples R. M., Ellis R. S., 1993, MNRAS, 263, 560
- Moster B. P., Somerville R. S., Newman J. A., Rix H.-W., 2010, arXiv, arXiv:1001.1737
- Pickles A. J., 1998, PASP, 110, 863
- Polletta M., et al., 2008, A&A, 492, 81
- Pozzetti L., et al., 2003, A&A, 402, 837
- Quadri R., et al., 2007, AJ, 134, 1103
- Rudnick G., et al., 2003, ApJ, 599, 847
- Rudnick G., et al., 2006, ApJ, 650, 624
- Sandage A., Tammann G. A., Yahil A., 1979, ApJ, 232, 352
- Saracco P., et al., 2006, MNRAS, 367, 349
- Schechter P., 1976, ApJ, 203, 297
- Schmidt M., 1968, ApJ, 151, 393
- Skrutskie M. F., et al., 2006, AJ, 131, 1163
- Szokoly G. P., Subbarao M. U., Connolly A. J., Mobasher B., 1998, ApJ, 492, 452
- Toft, S., et al. 2007, ApJ, 671, 285
- Whitaker K. E., et al., 2011, ApJ, 735, 86
- Wuyts, S., et al. 2007, ApJ, 655, 51
- Wuyts S. et al., 2008, ApJ, 682, 985



# 6

## Spectrophotometric redshifts: a new approach to the reduction of noisy spectra and its application to GRB090423<sup>1</sup>

### 6.1 Introduction

---

Measuring redshifts is one of the most important techniques in astronomy; however, it is also one that depends critically on the quality of the available data. Because of its nature it is sometimes difficult to attest the quality of the results, since no quantitative error estimates are obtained. In the optical range, the standard approach is to reduce all the available data to a one-dimensional array, which is flux- and wavelength-calibrated with the help of auxiliary data. In most cases, detection of emission and/or absorption lines is necessary for a valid measurement, although in some instances, only the continuum and some basic spectral features (e.g. breaks) are needed. Even the latter is sometimes difficult because of the paucity of photons. Ideally, in cases of low signal-to-noise data, one would bin the spectrum in the wavelength direction, but even this is sometimes useless. Moreover, information is often lost in the process of extracting the spectrum.

A different approach from the informational point of view would be to choose a model that represents the best possible fit to the available two-dimensional spec-

---

<sup>1</sup>This work was published in Stefanon, M., Fernandez-Soto, A. and Fugazza, D. 2011 *A&A*, 525, 75

tral data. This is actually the approach used by photometric redshift techniques, when a series of spectral energy distributions are considered at different redshifts and converted into photometric data that can be compared with the available photometry. It is also the method that has become standard in high-energy (X and gamma-ray) spectroscopy, where the models are convolved with the instrumental response and compared to the data, instead of the data being extracted and calibrated. In order for this kind of approach to work, at least three conditions need to be fulfilled:

- The real spectrum must be included in the family of models under analysis. This would be relatively difficult, for instance, in the case of quasars or galaxies at moderate resolution, because the intrinsic scatter amongst different models or types is very large. However, GRB afterglows make for an excellent example, as their intrinsic optical spectrum can usually be approximated very well with a single power law (van Paradijs, Kouveliotou, & Wijers, 2000), where the effects of the GRB host gas and dust, the intergalactic medium, and our local extinction can be superimposed.
- The technical characteristics of the instrument must be well known, in order to model their effect into the simulated data. This includes the total wavelength-dependent efficiency, any possible geometric distortions in the spectral direction, and of course the exact position of the target in the slit image.
- The characteristics of the noise in the CCD must also be modelled accurately, so that the statistical analysis will accurately estimate the model parameters and also the uncertainties associated to them.

Even though we have not mentioned it explicitly, it is of course necessary to ensure an accurate first reduction of the data, going from the raw individual images to the combined two-dimensional spectrum, which constitutes the input data for our analysis.

## 6.2 Gamma-Ray Bursts

---

Gamma-ray bursts (GRB) are brief events occurring at an average rate of a few per day throughout the universe: for a very short time, typically of the order of tens of seconds, their luminosity converts them into the brightest gamma-ray objects in the whole sky. Their energy flow during the burst is comparable to that of the Sun over  $\text{few} \times 10^{10}$  years or to that of our entire Milky Way over a few years. In fact, they are the most concentrated and brightest electromagnetic explosions in the Universe. Being originated by the death of massive stars (whose lifetimes are much shorter than the expansion time-scale at the redshifts of interest), they propose as tracer of the star-formation history of the universe, as discussed by many authors (see Salvaterra & Chincarini 2007; Porciani & Madau 2001 and references therein)

GRBs remained undetected at any wavelengths but gamma-rays until 1997, when the BEPPO-SAX satellite was launched. The detection through its X-ray camera allowed to decrease the positional errors so that it became possible to identify the source with optical telescopes; these observations confirmed that the GRB were originated at cosmological distances.

The current model of the central engine able to produce such a high energy is the occurrence of a cataclysmic stellar event like the collapse of the core of a massive star or the subsequent merger of two remnant compact cores, involving a very limited fraction ( $\approx 10^{-6}$ ) of stars toward the end of their evolutionary phases. These phenomena would be bound in a very small region (of the order of ten kilometers) and would release a high amount of gravitational energy (equivalent approximately to a rest solar mass) in an extremely short time (up to few seconds). Most of the energy would be emitted in the first seconds as thermal neutrinos, while a major fraction of the remaining energy could be emitted in the form of gravitational waves.

The result of this rapid energy liberation would be the formation of a very high temperature fireball expanding at a relativistic speed. The dissipation processes inside the fireball would then be at the origin of the observed gamma rays; at later times, this fireball would convert into a blast wave as it decelerates against the external medium and produce an afterglow, which would dim with time (see Figure 6.1).

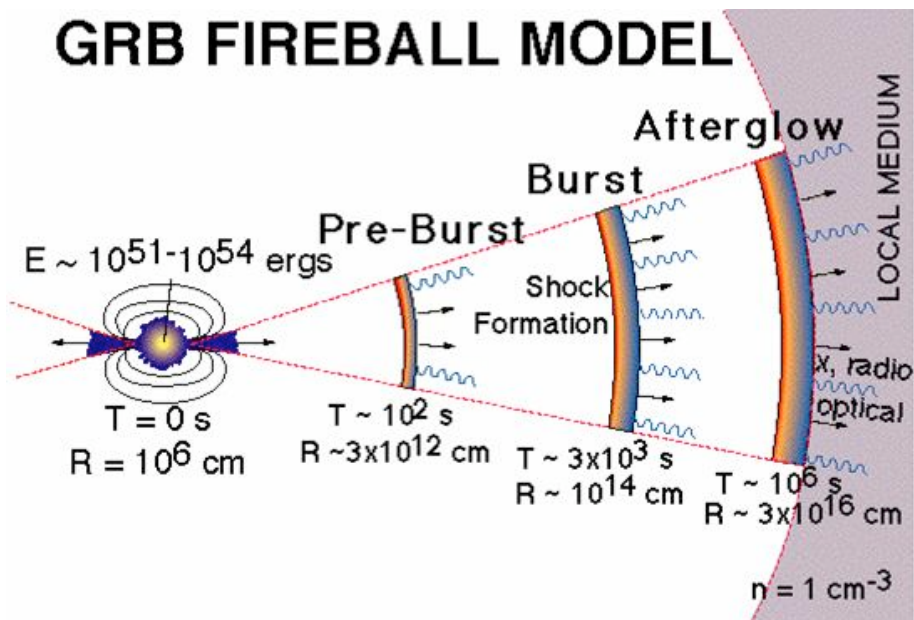


**Figure 6.1:** Schematic representation of the GRB fireball model (Credits: Swift team)

Depending primarily on the duration of the observed afterglow, GRBs can be divided into two distinct classes: long and short GRB.

The class of long GRBs is populated by massive stars whose core collapses to a black-hole, either directly or after a short accretion phase. This scenario is often called as the *hypernova* or *collapsar* and has been supported by several spectroscopic observations of associated supernovae (e.g. Galama et al. 1998; Stanek et al. 2003).

Short GRBs are thought to be originated by the merging of binary stars formed by two neutron stars or a neutron star and a black-hole (Eichler et al., 1989; Meszaros & Rees, 1992). These binary systems would lose orbital angular momentum by gravitational wave radiation, causing the merger.

For both of these progenitors, the current models foresee the final formation of a black-hole of a few solar mass, surrounded by a debris disk.

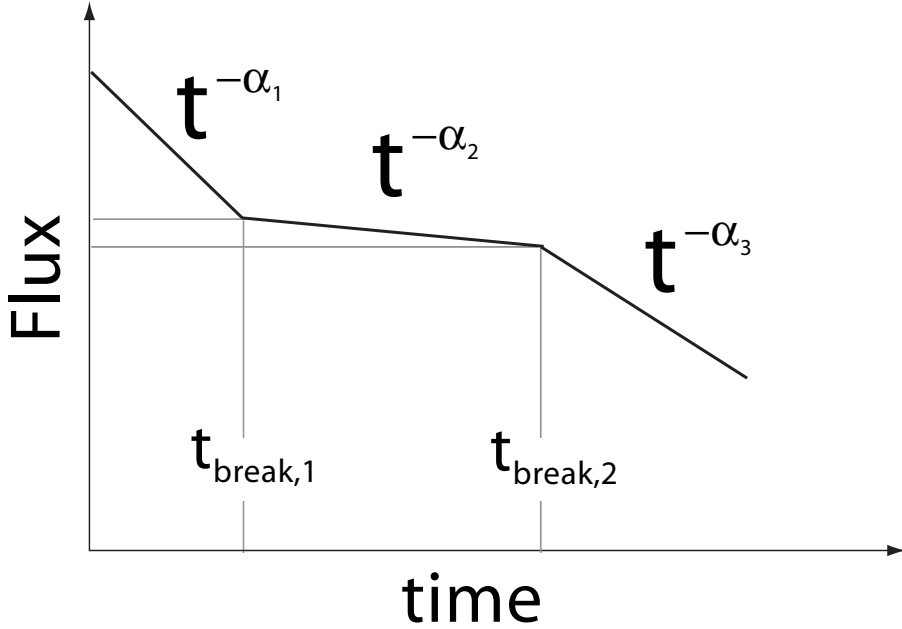


**Figure 6.2:** Schematic features seen in early x-ray afterglows detected with the Swift XRT instrument (Nousek et al., 2006).

The analysis of photometric and spectroscopic data from the X-Ray Telescope (XRT) and Burst Alert Telescope (BAT) onboard the Swift satellite has allowed to draw a canonical X-ray afterglow picture (Nousek et al., 2006), schematized also in Figure 6.2, which includes one or more of the following: (1) an initial steep decay  $F_X \propto t^{-\alpha_1}$  with a temporal index  $3 \lesssim \alpha_1 \lesssim 5$  and an energy spectrum  $F_\nu \propto \nu^{-\beta}$  with energy spectral index  $1 \lesssim \beta_1 \lesssim 2$ , extending up to a time  $300s \lesssim t_1 \lesssim 500s$ , (2) a flatter decay portion  $F_X \propto t^{-\alpha_2}$  with temporal index  $0.2 \lesssim \alpha_2 \lesssim 0.8$  and energy index  $0.7 \lesssim \beta_2 \lesssim 1.2$ , at times  $10^3s \lesssim t_1 \lesssim 10^4s$ , (3) a *normal* decay  $F_X \propto t^{-\alpha_3}$  with  $1.1 \lesssim \alpha_3 \lesssim 1.7$  and  $0.7 \lesssim \beta_2 \lesssim 1.2$ , up to a time  $t_3 \approx 10^5s$  which in some cases can be longer.

## 6.3 Description of the data

---

To describe our work in detail, we concentrate on the particular case for which we developed our original idea, thus we start by describing those data.

### 6.3.1 GRB090423 afterglow data

GRB090423 was a gamma-ray burst detected by the *Swift* satellite on April 23, 2009 (Krimm et al 2009). Early observations in the optical and near infrared distinctly pointed towards the possibility of it being a high-redshift object, when it went undetected for all observers using visible bands, but showed as a relatively bright near-infrared source (Tanvir et al 2009a, Cucchiara et al 2009a). Photometric data alone indicated a very high-redshift nature, with basically zero dust absorption (Cucchiara et al 2009b, Olivares et al 2009). Our group used the Italian 3.6m Telescopio Nazionale Galileo on the island of La Palma, to obtain a low-resolution spectrum using the Amici prism with the spectrograph NICS (Oliva 2003), and measured its redshift to be  $z = 8.1_{-0.3}^{+0.1}$  (Thoene et al 2009, Fernandez-Soto et al 2009, Salvaterra et al 2009). A compatible result ( $z = 8.23_{-0.07}^{+0.06}$ ) was reached independently by Tanvir et al (2009b, 2009c) using two sets of higher-quality data obtained with the VLT in Chile.

The Amici spectrum covers in a single exposure the wavelength range  $0.8 - 2.5\mu\text{m}$  with very low resolution ( $R \approx 50$ ) but very high efficiency, and thus became the ideal choice for this kind of analysis. We obtained a total of 128 minutes of on-target exposure time. The exposures were dithered following the usual NIR technique, and combined into a single two-dimensional frame, which is showed in Fig. 6.3. The slit was positioned with the help of a nearby star, whose extracted spectrum will be one of the keys in our analysis.

The position of the star along the slit (measured at the reference position  $X=600$  in the CCD frame) is  $Y=765$ . The angular distance between the reference star and the afterglow was  $\approx 30$  arcseconds, which corresponds to 120 pixels along the slit. To avoid possible issues caused by misalignments or the effect of distortions in the focal plane, we use this distance only as a reference, and perform a careful recentering, as described in the next section.

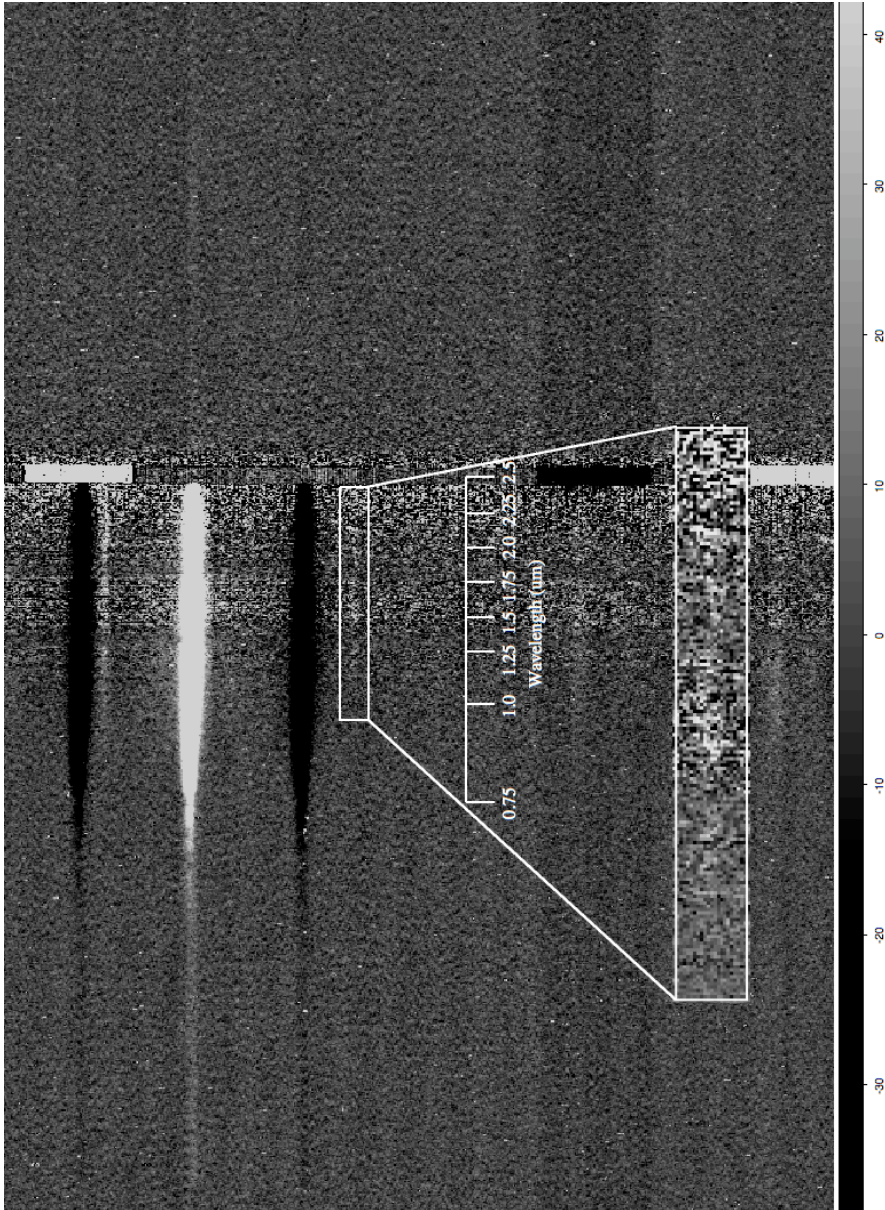


**Figure 6.3:** The combined two-dimensional spectrum used as input data. The white rectangle identifies the region of the GRB afterglow spectrum that was used for the analysis. The box height is equal to  $4 \times fwhm$ , corresponding to 21 pixels which ensures that we completely include both wings of the Gaussian. The inset shows a magnification of the same region.

## 6.4 Description of the method

---

Our aim is to reproduce the spectrum of the afterglow of GRB090423 as perfectly as possible, and to reconstruct the spectral equivalent of the wavelength-dependent *point spread function* as generated when the light passes through the atmosphere, telescope, and instrument optics, and reaches the detector. We present in this section the different steps to reach this objective.

### 6.4.1 Model spectra

We have created a library of model spectra, where there are three basic input parameters: the redshift  $z$ , the slope  $\alpha$  in the power-law spectral model  $f_\nu \propto \lambda^\alpha$ , and the total neutral hydrogen column density in the host interstellar medium  $N(\text{HI})$ , which produces a strong damped Lyman alpha (DLA) profile at the host redshift. It is important to include this profile in the analysis, because a dense ( $N(\text{HI}) \gtrsim 10^{21} \text{cm}^{-2}$ ) DLA profile would displace the position of the break, thus mimicking a higher redshift. A fourth parameter, the apparent magnitude normalisation in the observed  $K$  band (at the epoch of our observations)  $m_K$ , will be left as an uninteresting parameter, and it is directly fitted to the data during the process.

The effect of the Inter-Galactic Medium (IGM) at the redshifts of interest ( $z \gtrsim 6$ ) is very simple to include. At such a high redshift, the HI absorption is complete—within our observational capabilities—below the Lyman- $\alpha$  line, and as such we include it in the models (Yoshii & Peterson 1994). The putative effects of a significantly different neutral fraction in the IGM were deliberately neglected for two reasons. on one hand, the literature on GRB090423 points to a normal environment (i.e. neutral, see Tanvir et al. 2009c); on the other, some authors have shown that those effects are difficult to model and are challenging to observe even with better quality data (e.g. Patel et al. 2010).

In other cases one would of course need different parameters. It could be necessary to add dust extinction either at the host or by the Milky Way (or both), with the amount of extinction and even its grain type left as free parameters. We do not consider it here, because the available afterglow photometry indicates a blue object with an almost complete lack of intrinsic extinction (Fernandez-Soto et al 2009 and Tanvir et al 2009c, in particular their Fig. 2 which shows how the

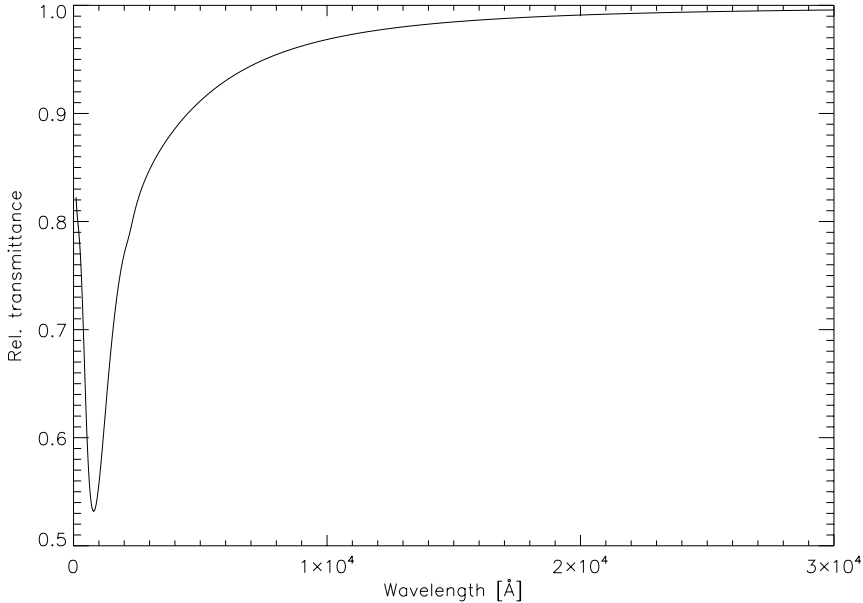


**Figure 6.4:** Relative transmittance for the  $E(B - V)=0.03$  extinction curve.

spectral slope is represented by a pure power law). Moreover, given the narrow rest-frame wavelength range that we are observing ( $\lambda \approx 1200 - 2200 \text{ \AA}$ ), as well as the resolution and signal-to-noise ratio of our data, there is an almost perfect degeneracy between the amount of dust extinction and a change in spectral slope. We used the Schlegel et al (1998) maps to include in the templates the effect of Milky Way dust at the level of  $E(B - V)=0.03$ ; the corresponding relative transmittance is plotted in Fig. 6.4.

Figure 6.5 shows a selection of spectral templates that sample part of the parameter space. The full range covered by our templates is  $\alpha \in [-1, 3]$ ,  $z \in [5, 10]$ , and  $N(\text{HI}) \in [10^{20}, 10^{24}] \text{ cm}^{-2}$ . All three ranges safely include the expected values of each variable. All models are normalised to have  $AB_K = 21.3$ , a value measured by GROND (Tanvir et al 2009c) at almost exactly the same time our observations were performed. It must be pointed out, however, that, because of the possibility of slit losses affecting the detected flux, we leave the normalisation factor for the flux as a free parameter, as explained in the next section.

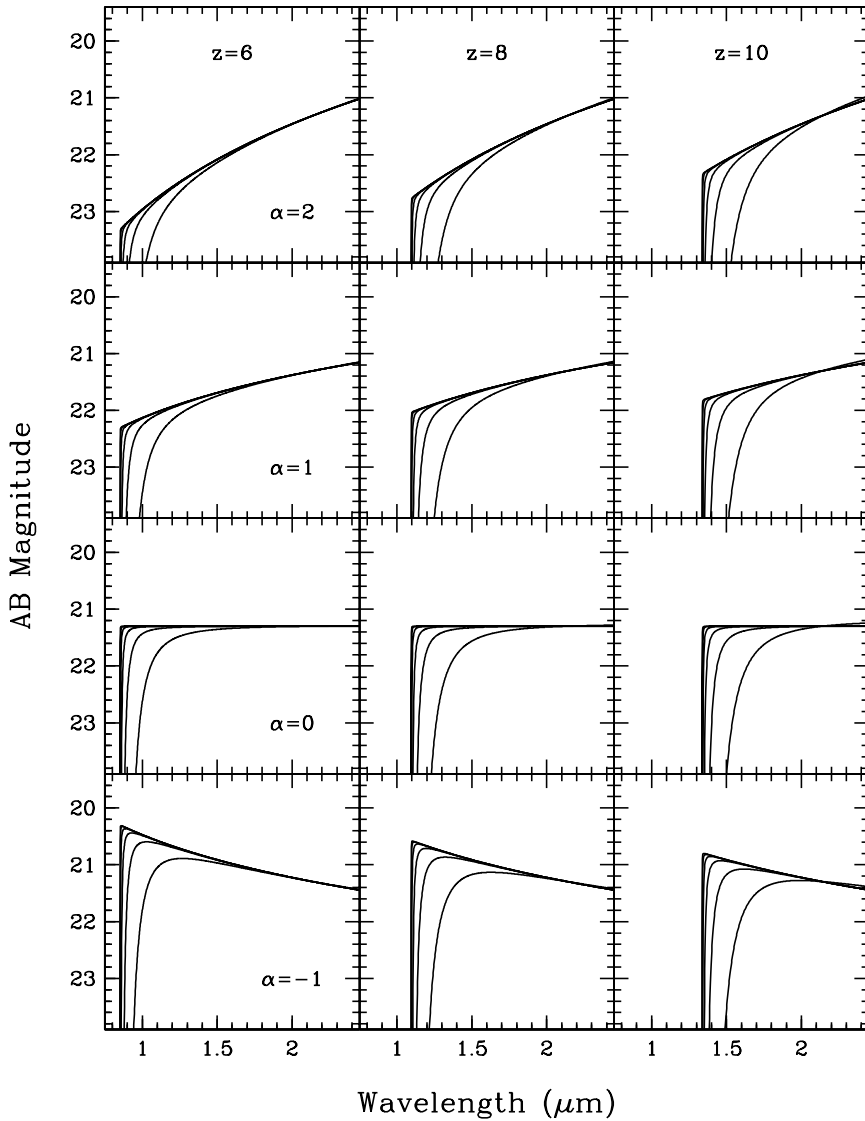


**Figure 6.5:** Some of the templates used for the analysis. Each column corresponds to a different redshift as labelled in the top panels, and each line to a different spectral slope, as labelled on the leftmost column. Within each panel, the different curves correspond to values of  $\log[N(\text{HI})]$  varying from 19 to 24 in steps of one.

**Table 6.1:** Stellar data. SDSS and 2MASS photometry taken from their respective catalogues, expressed in their usual reference-AB magnitudes for SDSS, Vega-based for 2MASS.

Parameter	<i>Value</i>
SDSS name	$J095535.28 + 180903.8$
R.A. (J2000)	09:55:35.286
Dec (J2000)	+18:09:03.88
Spectral Type	<i>M4V</i>
$u_{\text{SDSS}}$	$22.17 \pm 0.21$
$g_{\text{SDSS}}$	$19.27 \pm 0.01$
$r_{\text{SDSS}}$	$17.78 \pm 0.01$
$i_{\text{SDSS}}$	$16.54 \pm 0.01$
$z_{\text{SDSS}}$	$15.91 \pm 0.01$
$J_{2\text{MASS}}$	$14.52 \pm 0.03$
$H_{2\text{MASS}}$	$13.97 \pm 0.04$
$K_{2\text{MASS}}$	$13.77 \pm 0.05$

### 6.4.2 CCD and instrumental characteristics

Once satisfied with the set of spectral templates, we need to characterise the observations in terms of spectral resolution, efficiency of the instrument at different wavelengths, noise characteristics of the detector, and position of the spectrum along both the spectral and spatial directions.

#### Instrumental Characteristics

We used an archival solution to calibrate the Amici spectrum in wavelength. As described in Fernandez-Soto et al (2009) we needed to add an offset of 5 pixels, determined via comparison with the observed sky absorption features.

As we mentioned in the previous section, there is a nearby star that falls within the slit—it was in fact used to position the slit, as the afterglow was too dim to be pointed at directly. Its spectral type is M4V, as determined via available SDSS and 2MASS photometry (Adelman-McCarthy et al 2008, Skrutskie et al 2006, see Table 6.1 for the complete data). We used the corresponding spectrum from the Bruzual-Persson-Gunn-Stryker library (Bruzual et al 1996) to determine the

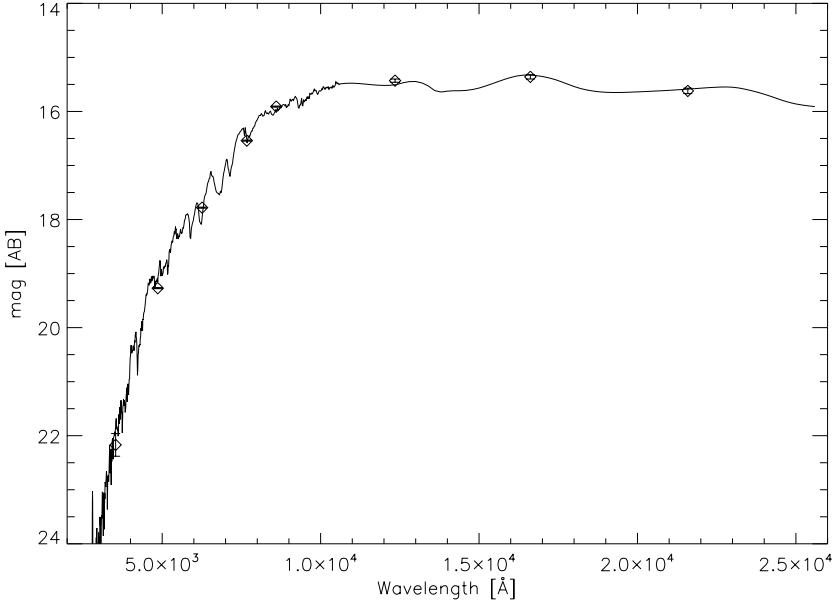


**Figure 6.6:** Comparison between the photometric data of the reference star (diamonds) with the Bruzual-Persson-Gunn-Stryker library (solid line -Bruzual et al 1996) M4V spectral energy distribution template.

total efficiency of the instrument as a function of wavelength. In the  $0.95 - 1.1\mu\text{m}$  region, corresponding to the Lyman break of a  $z \approx 8$  source — the most prominent feature in our GRB spectrum — the spectrum of an M4V star is free of strong spectral features. This, considered together with the low resolution of the spectra and the fact that the M4V star shows even less features at higher wavelengths, allows us to rely on the total instrumental efficiency we derived. Figure 6.6 shows the photometric points from table 6.1 overplotted to the model spectra of the M4V class star.

It must be noted that there is a free factor involved in the calculations, as we cannot ensure that the slit losses in the stellar spectrum are the same in the one corresponding to the afterglow. However, as long as the pointing was reasonably accurate—and we can assume it was from the comparison of the fluxes—at least to first order, it will be a single number (i.e., not wavelength-dependent) since the slit angle is obviously the same for both objects.

The seeing at the time of the observations was  $\approx 1.4$  arcseconds in the J band, as measured in the acquisition images. The slit width was 1.0 arcsecond, so we expect some slit losses, and no degradation in resolution induced by the slit width. We show in Fig. 6.7 the measured total efficiency, obtained as the (arbitrarily normalised) ratio of the counts to the model spectrum of the star.

As is usually done when reducing spectroscopic data of very faint sources, we assume that the shape of the afterglow spectrum in the CCD follows the trace left by the much brighter star (plotted in Fig. 6.7, second panel from the top), which can easily be traced at all wavelengths from 0.8 to 2.5 microns. We determined the distortions along the dispersion axis of the stellar spectrum, fitted it via Legendre polynomials, and used it to define the template spectrum position. We determined the vertical offset by using a zero-order solution (an  $f_\nu$ -flat spectrum at  $z = 8.4$  with HI absorption of  $10^{20} \text{ cm}^{-2}$ ) and displacing it vertically, evaluating its likelihood at different positions when compared to the CCD data. We measured an offset of 115.4 pixels (equivalent to 28.8 arcseconds).

The FWHM in the spatial direction of the stellar spectrum varies with wavelength from  $\approx 1.2$  arcseconds at  $2.2 \mu\text{m}$  to  $\approx 1.5$  arcseconds at  $\approx 0.8 \mu\text{m}$  (corresponding to  $\approx 5.8$  to  $\approx 4.9$  pixels on our plate scale). We used a smoothed fit to those values (also shown in Fig. 6.7) to reproduce the afterglow spectrum.

### CCD characteristics

Observations in the IR are more complex than the corresponding in the optical range. The differences are mainly due to a higher and more variable sky, by stronger atmospheric absorption and by telluric emission throughout the 1-2.5  $\mu\text{m}$  wavelength range.

For wavelengths bluer than 2.3  $\mu\text{m}$ , the background is dominated by non-thermal emission, such as that produced by OH and O<sub>2</sub> emission lines. The vibrational excited OH lines are highly variable in time, with scales of few minutes. These lines are stronger just after sunset and weaker around midnight.

For wavelength values higher than 2.3  $\mu\text{m}$ , the background is instead dominated by thermal emission from both the telescope and from the sky. The sky background in the  $K_S$  band can vary by a factor of two from winter to summer, although it is more stable than the  $J$  and  $H$  bands on the short time scales.

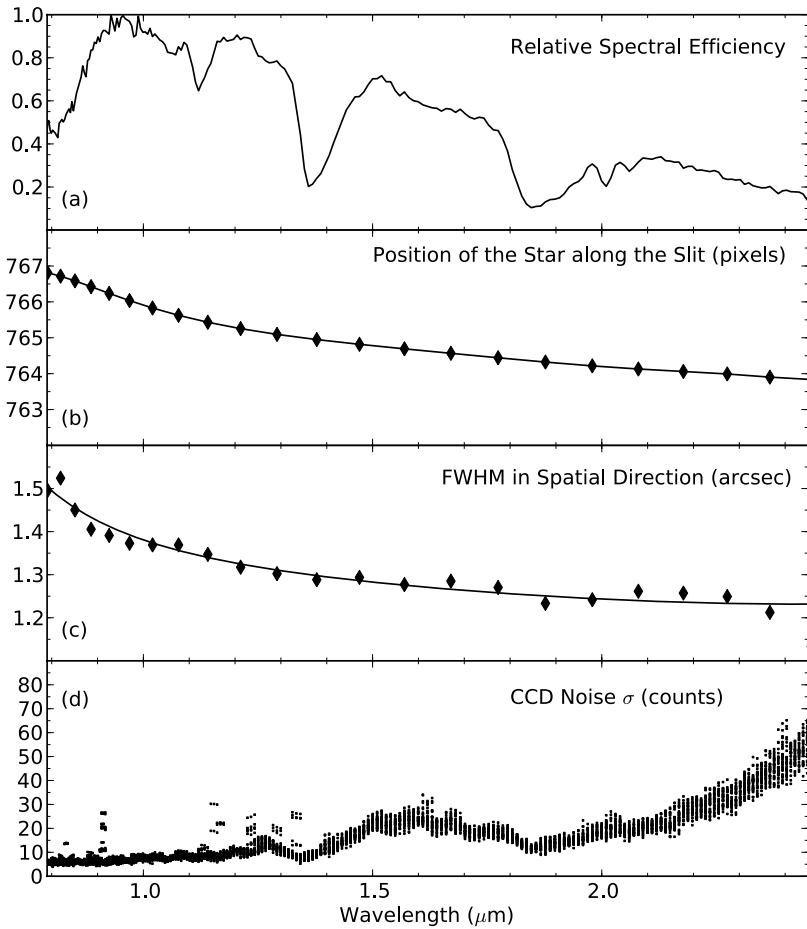


**Figure 6.7:** Total efficiency of the atmosphere, telescope, and instrument combination (a). Changes in the spectral position (b) and width (c) with wavelength, and projection of the measured CCD noise (rms counts per pixel) as a function of wavelength (d).

All these difficulties have led to the development of specific observing techniques for the IR.

It is not unusual for the objects of interest to be hundreds or even thousands of times fainter than the sky. Under these conditions it has become standard procedure to observe the source (together with the sky) and subtract from it an estimate of the sky. Since the sky emission is variable, the only way to obtain good sky measurement is to frequently repeat this kind of observation. The frequency depends on the wavelength of observation, on the nature of the emission of the sky background and on meteorological conditions; as a general guideline, the measurement of the sky should be taken at least as frequently as the sky varies. With modern arrays this is usually done with frequencies of the order of once per minute. The observations consist in slightly displacing the telescope by random values between consecutive exposures. Although this observing technique introduces large amounts of overheads, it has the advantage that it automatically removes the counts offsets generated by the electronics such as the bias and the dark current.

The CCD image we are working with is the result of a careful reduction procedure following the usual steps for NIR spectroscopy.

We did, however, perform one extra check: we measured the background in detail, to ensure that it is flat in both the spectral and spatial directions.

Since the final image contains the trace of the sky subtraction in form of negative spectra, we needed a way to *clean* it. The background was then reconstructed following the below steps:

1. We run SExtractor on the reduced image; the output image was chosen to be the subraster of the (positive) detected sources, which, in our case, were the spectra of the GRB and of the star.
2. We subtracted the output image previously obtained from the reduced image and inverted the result, so that the *negative* spectra would now appear as positive features
3. We repeated step 1 on the inverted image. The output was the result of source subtraction.

4. We now have an image clean from sources (both positive and negative). This image was then multiplied by -1 in order to re-convert it to its original scale.
5. The clean image was then given as input to SExtractor which this time was set to produce as output the frame corresponding to the background.

The result of this procedure is shown in Figure 6.8. As it can be seen, there appears no significant trend either in the spatial or in the dispersion direction, with the background flat to a fraction of the CCD noise.

We also estimated the CCD noise using different methods. This is a very important step, because we want not only to determine the basic parameters of the GRB afterglow (redshift, spectral slope, and neutral hydrogen column density), but also to measure confidence limits on all of them. We decided that the best method consists in using 7 rectangular areas of equal size in the CCD, each one covering the interval  $X \in [480, 650]$  and 21 pixels in the Y direction. Those boxes were chosen in areas that are free of any (positive or negative) feature. Their location on the frame is presented in Figure 6.9. With them we estimated the noise as a function of X position (that is, wavelength) by using a 3x3 grid around each pixel and all 7 independent images. In this way we obtained a  $170 \times 21$  mini-CCD noise frame, which we will use for the subsequent chi-square analysis. The projection of this noise array on the Y direction is also shown at the bottom in Fig. 6.7.

We finally computed the noise expected from an ideal  $\chi^2 \equiv 1$  relation when comparing each one of the noise regions to an empty (zero counts) one. The average of the obtained noise values differs from the RMS of our noise array by  $\approx 0.3\%$ .

### 6.4.3 Application of the method

We used all the knowledge about the instrument gathered in the previous subsection to create replicas of the GRB afterglow spectrum, for each one of the templates described in Sect. 3.1.

In brief, we choose a spectrum template combination (i.e., values of  $z$ ,  $\alpha$ , and  $N(\text{HI})$ ) and generate a one-dimensional spectrum using them. We redden this spectrum using the measured Galactic value  $E(B - V) = 0.03$ . Then this spectrum

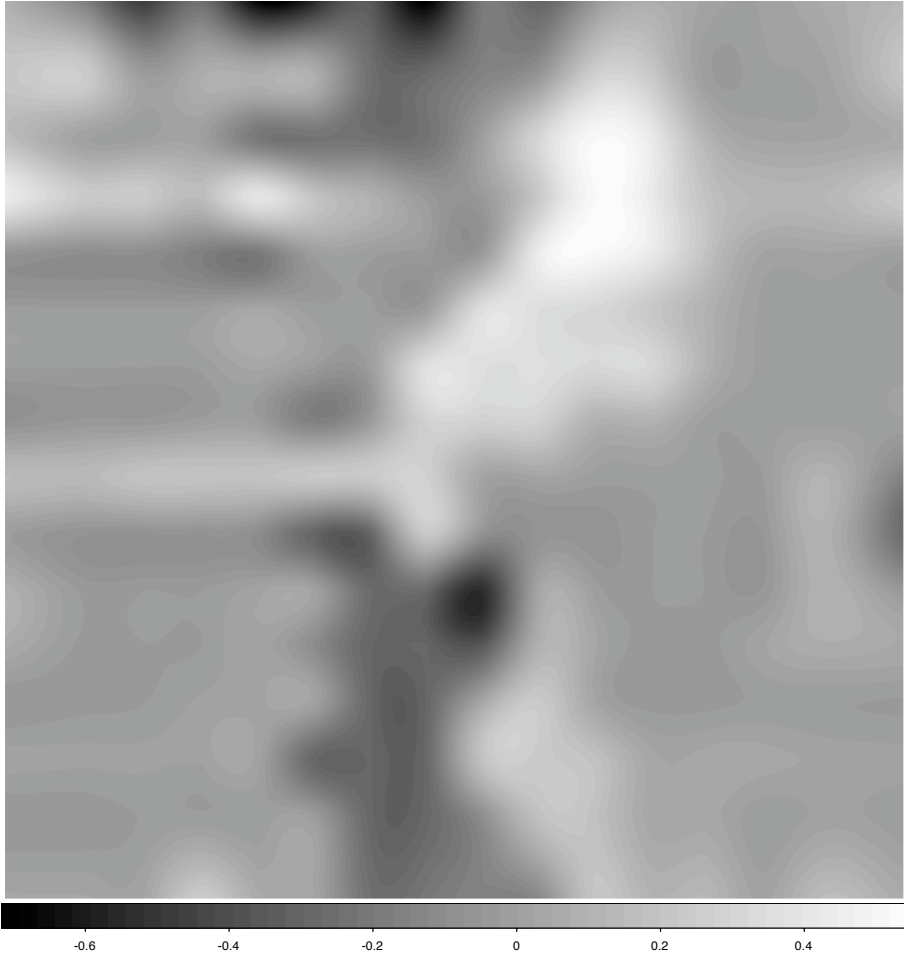


**Figure 6.8:** Background measurement obtained from the original reduced frame, following the steps described in section 6.4.2. Note the reduced spread of values.

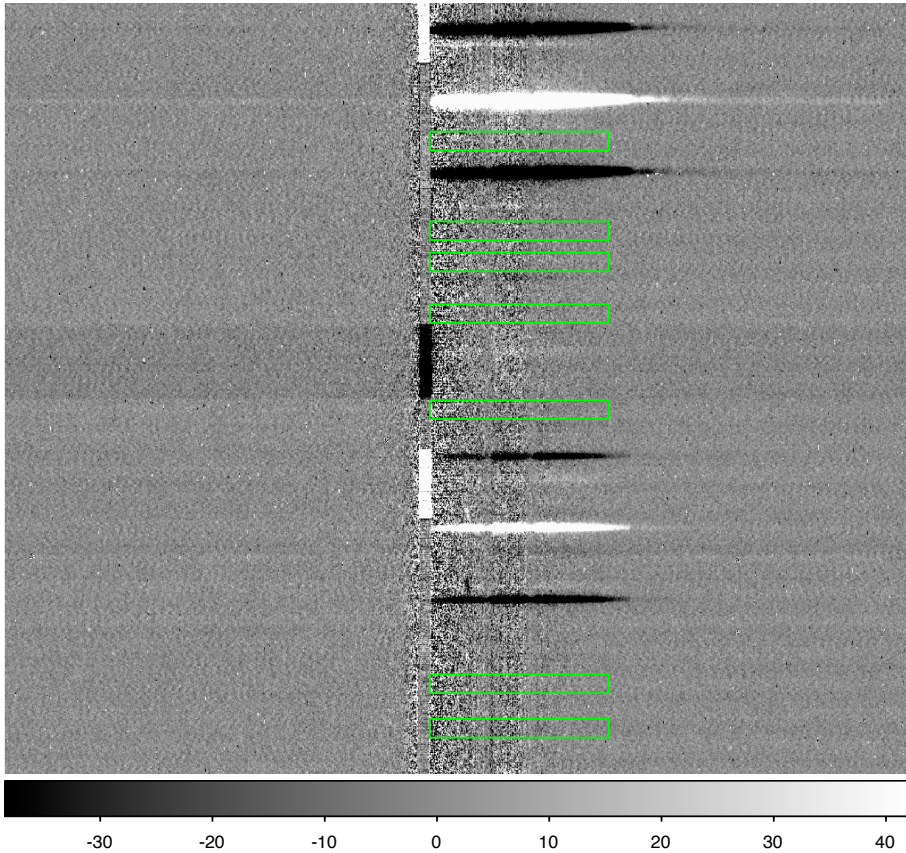


**Figure 6.9:** The green rectangles represent the 7 boxes we used to measure the CCD noise.

is converted to a two-dimensional image, using the measured efficiency, adjusting and block-averaging the wavelength axis to the known dispersion solution of the Amici prism, and convolving it in the spectral direction with a Gaussian function of the measured FWHM at each wavelength. This two-dimensional spectrum is forced to follow the trace that was measured with the stellar spectrum, and is set on a mini-CCD matrix measuring  $170 \times 21$  pixels, as was described above for the noise image. Figure 6.10 shows some of the same spectra that were presented in Fig. 6.5, now converted to two-dimensional images with this process.

Each of them is then compared to the real data, using the section of the

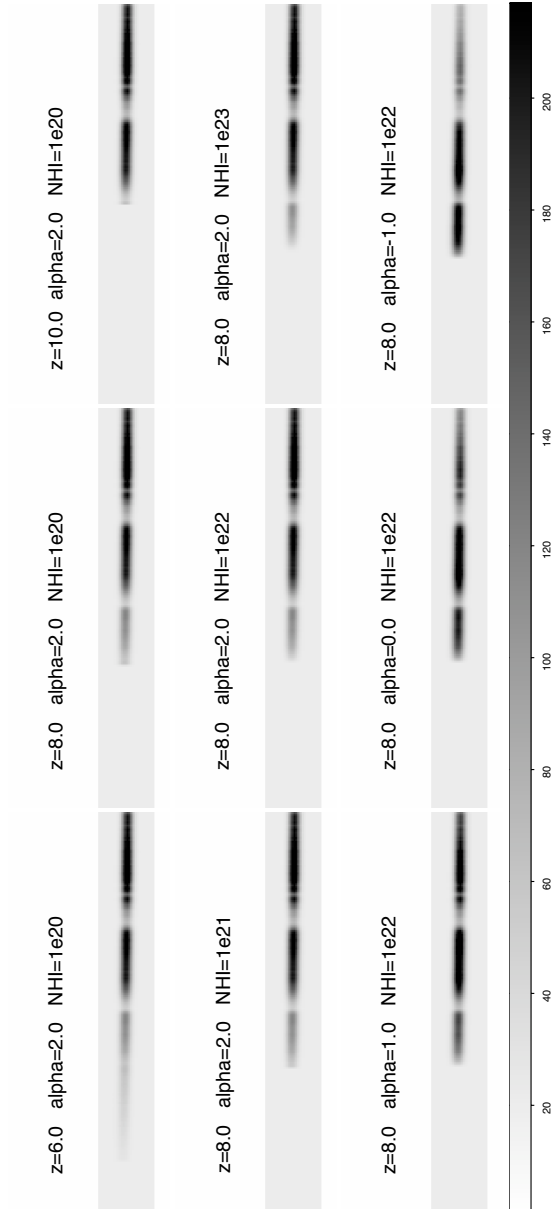


**Figure 6.10:** Some of the templates that were shown in Fig. ?? are shown here as two-dimensional arrays, after applying the procedures described in Sect. 6.4.

CCD that contains the GRB afterglow spectrum, centred to the same position of each of the template frames. We do this comparison using a  $\chi^2$  fit, where the noise array corresponds to the one that was obtained in the previous section. Calling the template  $\mathcal{T}(z, \alpha, N(\text{HI}))$ , the CCD data  $\mathcal{D}$ , and the noise matrix  $\mathcal{S}$ , and remembering each one of them represents a  $170 \times 21$  matrix, one obtains

$$\chi^2[z, \alpha, N(\text{HI})] = \sum_{i=1}^{170} \sum_{j=1}^{21} \frac{[A\mathcal{T}(z, \alpha, N(\text{HI}))_{ij} - \mathcal{D}_{ij}]^2}{\mathcal{S}_{ij}^2}, \quad (6.1)$$

where  $A$  represents a normalisation parameter for the flux. This is actually fixed for each template by minimising  $\chi^2$ , which renders

$$A = \frac{\sum_{i=1}^{170} \sum_{j=1}^{21} \mathcal{D}_{ij} \mathcal{T}(z, \alpha, N(\text{HI}))_{ij} / \mathcal{S}_{ij}^2}{\sum_{i=1}^{170} \sum_{j=1}^{21} \mathcal{T}(z, \alpha, N(\text{HI}))_{ij}^2 / \mathcal{S}_{ij}^2}. \quad (6.2)$$

Thus, once the normalisation  $A$  is fixed, the calculation of  $\chi^2$  is straightforward for each template.

## 6.5 Results

In Fig. 6.11 we present the result of the calculation above, projected on the different planes of parameter space. Throughout our analysis, we associated the 68.3% confidence level to  $1\sigma$  and 95.4% to  $2\sigma$ . As can be seen, the best fit corresponds to  $z = 8.40$ ,  $\alpha = 1.2$ ,  $N(\text{HI}) = 10^{20.0} \text{cm}^{-2}$ . We calculated the confidence regions corresponding to the best fit on each of the individual parameters, reaching the results presented in Table 6.2. We must point out that the best-fit solution represents a value of  $\chi^2 = 4019$ . This value indicates a good fit for our problem, which has  $\approx 3600$  degrees of freedom, albeit obviously most of them void in terms of information content.

As can be observed, there is no lower limit to the neutral hydrogen column density. This is a natural observational consequence of the fact that below  $N(\text{HI}) \approx 2 \times 10^{20} \text{cm}^{-2}$  there is no damped profile, and the absorption is not significant at our resolution and signal-to-noise level. On the other end of the column density scale, we stop our analysis at  $N(\text{HI}) = 10^{24} \text{cm}^{-2}$ , a value high enough to include even the densest absorbers ever observed. At  $2\sigma$  level, even higher values could be

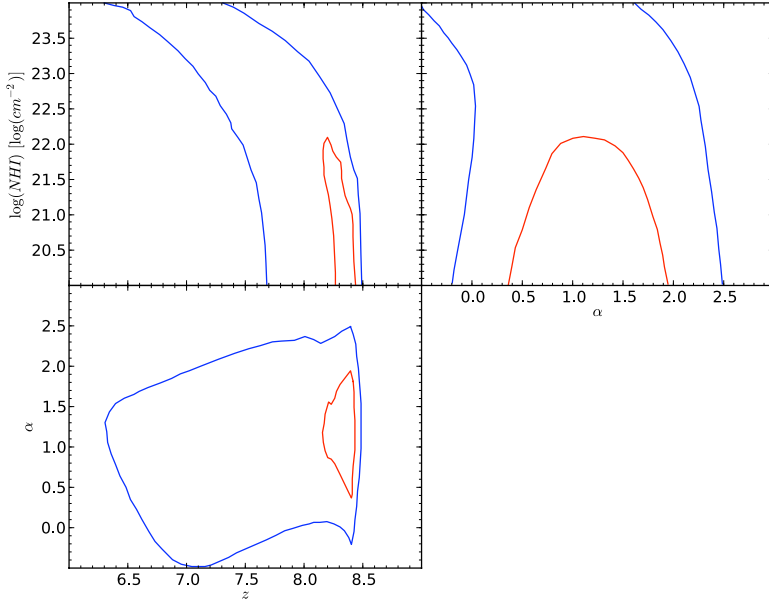


**Figure 6.11:** Results of the fitting procedure, projected on each of the two-dimensional planes of parameter space. Red (blue) contours correspond to  $1\sigma$  ( $2\sigma$ ) confidence levels.

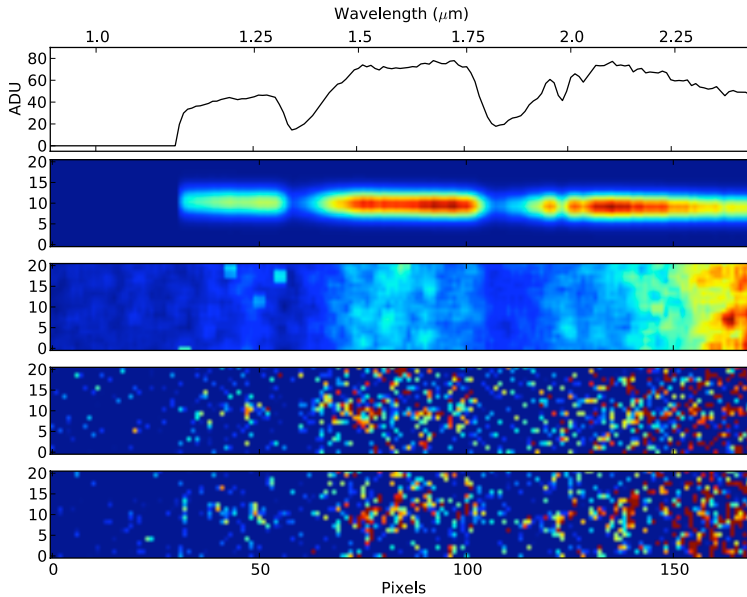
accommodated, paired to lower redshifts  $z < 6.5$  and flatter spectral slopes  $\alpha < 0.5$ .

Figure 6.12 shows the best-fit spectrum, seen in the two top panels both as a one-dimensional plot and as a clean two-dimensional model, and compared to the real data in the two lower panels.

We may also use the spectral slope of the GRB afterglow spectrum, as measured from broad-band NIR photometry, as a prior condition in our analysis. In this way, using the 1-sigma limit presented in Salvaterra et al (2009) for the spectral slope measured from availability of higher S/N photometry ( $\alpha = -0.4_{-0.2}^{+1.4}$ ), one would obtain a more stringent limit on the redshift, approximately  $z > 7.5$  at the 2-sigma confidence level.

**Table 6.2:** Results of the fitting procedure.

Parameter	Value	$1\sigma$	$2\sigma$
Redshift	8.40	(8.38, 8.45)	(6.67, 8.49)
Spectral Slope	1.2	(0.7, 1.8)	(0.1, 2.2)
$\log[N(\text{HI})]$	20.0	(< 20.7)	—



**Figure 6.12:** The best-fit spectrum, convolved with the instrument response. It is shown in the top panel as a one-dimensional spectrum and as a clean two-dimensional array in the second one. The third panel shows a  $1\sigma$  noise two-dimensional array in the CCD area corresponding to the afterglow spectrum, as described in Sect. 6.4.2. The fourth panel shows one realisation of the CCD noise *plus* the best-fit spectrum, which can be directly compared to the real data at the bottom panel. The contrast scale is the same in the two last panels, but not in the previous ones.

## 6.6 Conclusions

We have presented a different method for the analysis of spectroscopic data, akin in spirit to the one used in X-ray astronomy and also in photometric redshift

techniques. This method does not attempt to extract a one-dimensional spectrum from the CCD data. On the other hand, we generate simulated two-dimensional spectra from template spectra of known characteristics, and decide which one fits the real data best, choosing the best-fit parameters as the solutions to the problem.

We used this method to carefully analyse a very low signal-to-noise spectrum of the afterglow of the very distant GRB090423, showing that it is possible to extract information from this kind of data, more than is usually assumed. Our best result at  $1\sigma$  level ( $z = 8.40_{-0.02}^{+0.05}$ ) is slightly higher than previous results using the same data (Salvaterra et al 2009) or data from other sources (Tanvir et al 2009c), although still compatible well within the  $2\sigma$  confidence level. We consider our confidence intervals to be reliable, given the full analysis of the noise characteristics performed in this work.

The same method can be applied to other cases where the source belongs to a well-defined spectral class of objects, and there is a need to extract the maximum possible information from low-quality data. This is usually the case for faint, rapidly fading GRB afterglows, and we expect this method to be used in future measurements.



# Bibliography

- Adelman-McCarthy J. K., et al., 2008, ApJS, 175, 297
- Band D., et al., 1993, ApJ, 413, 281
- Bruzual, G., Persson, E., Gunn, J. & Stryker, L. 1996, Bruzual-Persson-Gunn-Stryker Spectrophotometry Atlas, [http://www.stsci.edu/instruments/observatory/cdbs/astronomical\\_catalogs.html](http://www.stsci.edu/instruments/observatory/cdbs/astronomical_catalogs.html)
- Cucchiara A., Fox D. B., Berger E., 2009, GCN, 9209, 1
- Cucchiara A., Fox D. B., Berger E., 2009, GCN, 9213, 1
- Eichler D., Livio M., Piran T., Schramm D. N., 1989, Natur, 340, 126
- Fernandez-Soto A., et al., 2009, GCN, 9222, 1
- Galama T. J., et al., 1998, Natur, 395, 670
- Krimm H. A., de Pasquale M., Perri M., Stratta G., Ukwatta T. N., 2009, GCNR, 211, 1
- Meszáros P., Rees M. J., 1992, ApJ, 397, 570
- Nousek J. A., et al., 2006, ApJ, 642, 389
- Oliva E., 2003, MmSAI, 74, 118
- Olivares F., Kruehler T., Greiner J., Filgas R., 2009, GCN, 9215, 1
- Patel M., Warren S. J., Mortlock D. J., Fynbo J. P. U., 2010, A&A, 512, L3
- Porciani C., Madau P., 2001, ApJ, 548, 522
- Salvaterra R., Chincarini G., 2007, ApJ, 656, L49
- Salvaterra R., et al., 2009, Natur, 461, 1258
- Schlegel D. J., Finkbeiner D. P., Davis M., 1998, ApJ, 500, 525
- Skrutskie M. F., et al., 2006, AJ, 131, 1163
- Stanek K. Z., et al., 2003, ApJ, 591, L17

## BIBLIOGRAPHY

---

Tanvir N., Levan A., Kerr T., Wold T., 2009, GCN, 9202, 1

Tanvir N., Levan A., Wiersema K., Fynbo J., Hjorth J., Jakobsson P., 2009, GCN, 9219, 1

Tanvir N. R., et al., 2009, Natur, 461, 1254

Thoene C., et al., 2009, GCN, 9216, 1

van Paradijs J., Kouveliotou C., Wijers R. A. M. J., 2000, ARA&A, 38, 379

Yoshii Y., Peterson B. A., 1994, ApJ, 436, 551

# 7

## Conclusions

In this thesis we explored the faint end region of a cosmological survey, both from the photometric and from the spectroscopic point of view.

In the framework of the ALHAMBRA photometric survey, we implemented two distinct methods for the determination of the detection completeness, as a function of spectral and morphological type as well as of the effects of the redshift on apparent size and observed SED. In particular, we showed that the apparent sizes of galaxies are non-negligible to at least  $z \approx 1$ , so that it is important to take into account this effect when determining the completeness.

The high number of filters adopted by the ALHAMBRA Survey makes the definition of detection (and consequently of completeness) a challenging topic. The adopted strategy consists in detecting objects on the image (called the *deep image*) resulting from the sum of single frames (of the same field) among a wide range of filters, satisfying constraints about seeing and transparency conditions during observations.

The first method we developed is totally based on a simulation of the instrumental apparatus (telescope+camera+detector) used for the observations. In order to grant a higher level of detail in the estimation of the signal-to-noise ratio for the simulated extended objects, we implemented a statistical correction to the measure of the flux related to the apparent area covered by the extended source.

The second novel method is a Monte Carlo analysis based on real data. Our approach tries to reproduce the way the deep image is created and how the detection is performed on it. The completeness is computed on the basis of the

---

recovery fraction of copies of real objects adopted as templates, whose flux and apparent size have been rescaled in order to match a grid of realistic values as a function of redshift.

The comparison between the analytic and the Monte Carlo methods revealed that the analytic way is a fast and quite accurate procedure for determining the completeness. However, the difference with the Monte Carlo method for  $z < 1$  stressed the importance of taking full consideration of the luminosity profiles of objects linked to the apparent sizes and morphological type of objects.

The Monte Carlo method, making full use of real data, as opposed to the methods used so far in surveys like COMBO-17 or COSMOS which instead adopts at most a set of artificial luminosity profiles for the extended objects, is able to produce more reliable limits to the source detection completeness measurement. In addition, the full information about the completeness levels as a function of intrinsic parameters allows to easily apply corrections to statistical estimators of the galaxy population like the Luminosity Function (LF), thus allowing to reliably deal with intrinsically fainter objects. Part of the above conclusions were presented with a poster at the conference *Harvesting the desert : the universe between redshift 1 and 3*, held in Marseille, 2009.

The above results were tested using a preliminary catalogue from the ALHAMBRA survey. The luminosity function was computed in three different redshift bins and for the three main classes of galaxies, i.e. elliptical, spiral and starburst. The application of completeness corrections allowed us to measure the LF one magnitude deeper than the VVDS survey - a spectroscopic survey with similar apparent magnitude limits.

The bright-end of the global LF shows little to no evolution from  $z \simeq 0.45$  to  $z \simeq 1.25$ , although a more solid analysis of the faint end would require deeper data, especially for the higher redshift bin. Similarly to the global LF, also the LF of elliptical galaxies does not show any significant evolution, in agreement with the fact that the bright-end of the global LF is populated by red objects. The LF of spiral galaxies shows marked evolution, possibly in the luminosity domain, from  $z \simeq 0.45$  to  $z \simeq 0.8$ , with the LF shifting towards brighter magnitudes with  $z$ , while in the two highest redshift ranges the two LFs look similar. Starburst galaxies present the clearest signs of evolution in all the three redshift ranges, although determining whether it is luminosity or number density evolution would

require additional analysis. The above conclusions were also supported by rest-frame color-magnitude diagrams on the same sample.

The study of the evolution of the LF was extended to the rest-frame J and H bands up to  $z = 3.5$ . This was the result of the analysis of three publicly available catalogues from the MUSYC, FIRES and FIREWORKS projects. The analysis allowed for the first time to measure the rest-frame H-band LF of field galaxies in the redshift interval  $z \in [1.5, 3.5]$ ; at the same time, the larger volume allowed to improve the measurement of the bright end of the LF significantly in one of the highest redshift bin.

We analyzed the evolution of the Schechter function parameters as a function of redshift, making full use of the data available from the literature. We found that the faint end slope  $\alpha$  of the LF is nearly constant over the whole redshift range and that  $\phi^*$  decreases by a factor of  $\approx 10$  from  $z = 0$  to  $z = 1.75$ , and by a factor of  $\approx 3$  to  $z = 3.25$ . We introduced a parameterization based on an exponential form for the evolution of  $\phi^*$  as a function of  $z$ . The fit of this function to the available data shows good agreement, especially for the rest-frame  $J$ -band, where more data from the literature are available in the redshift range  $z \in [0, 1]$ , complementing our measurements at  $z > 1.5$ . The results of this work have been accepted for publication in Monthly Notices of the Royal Astronomical Society (Stefanon and Marchesini, 2011).

On the spectroscopic side, we developed a different method for the analysis of spectroscopic data, akin in spirit to the one used in X-ray astronomy and also in photometric redshift techniques. This method consists in generating simulated two-dimensional spectra from template spectra of known characteristics, and deciding which one fits the real data best, choosing the best-fit parameters as the solutions to the problem. This method was used to analyze a very low signal-to-noise spectrum of the afterglow of the very distant GRB090423, showing that it is possible to extract information from this kind of data, more than is usually assumed. Our best result at  $1\sigma$  level ( $z = 8.40_{-0.02}^{+0.05}$ ) is slightly higher than previous results using the same data or data from other sources, although still compatible well within the  $2\sigma$  confidence level. We consider our confidence intervals to be reliable, given the full analysis of the noise characteristics performed in this work. This method was published in Astronomy and Astrophysics (Stefanon, Fernandez-Soto and Fugazza, 2011).

---

## Future work

---

We have started a spectroscopic campaign to study the high redshift ( $z > 3$ ) population of massive galaxies ( $M_* \gtrsim 3 \times 10^{11} M_\odot$ ). In particular we will analyze the spectra of C1-23152, a very massive galaxy at  $z = 3.3$ , whose observations are already queued for the end of 2011-beginning of 2012 at the Gran Telescopio Canarias (GTC) with the OSIRIS instrument. The resulting rest-frame UV spectra will allow us to study the Lyman  $\alpha$  emission, to determine the presence of an AGN, and to measure superwind outflows through the comparison of UV absorption lines and Lyman  $\alpha$  emission line.

We will also make use of a composite NIR-selected sample of galaxies built from several multi-wavelength surveys, all having very high-quality UV to mid-infrared photometry, to improve the rest-frame optical and NIR measurement of the evolution of the LF and LD for  $1 < z < 4$ . The catalogue is composed by the ultra-deep Faint InfraRed Extragalactic Survey (FIRES), the Great Observatories Origins Deep Survey (GOODS), the NEWFIRM Medium-Band Survey (NMBS), the ultra-deep NICMOS observations over the HDF-North (HDFN) GOODS field, the ultra-deep WFC3/IR observations taken as part of the HUDF09 program over the Hubble Ultra-Deep Field (HUDF), and the wide-area WFC3 Early Release Science (ERS) observations over the CDF-South GOODS field, and provides redshift information for over 20000 galaxies distributed on an area of 1600 arcmin<sup>2</sup>.

The forthcoming official release of the ALHAMBRA catalogue will allow to complement the above measurements with rest-frame optical LF and LD measurements up to  $z = 1.5$ . Spitzer IRAC images are already available for half the total area covered by the ALHAMBRA survey. The addition of the IRAC photometry will also allow us to improve the photometric redshifts for the objects in the overlapping regions and to extend the study of the LF to the rest-frame NIR bands, with minimal dependence on the spectral energy distribution models.



# Resumen del trabajo de tesis

## A.1 [Cap. 1] Introducción

---

El estudio de las propiedades físicas del Universo como un todo requiere observaciones de una región de cielo de tamaño significativo, que generalmente se define con el término *cartografiado*. El paso sucesivo es extraer, desde las imágenes obtenidas a través de los telescopios, cuanta mas información posible, y con el mayor grado de confianza posible.

### A.1.1 Límites de detección

Cuando se analizan imágenes astronómicas, tenemos que ponernos delante del hecho que la razón señal-ruido (RSN) de cada objeto depende del flujo total que podamos recuperar de él. Este hecho lleva a la determinación de un *límite de detección*. Aunque podamos pensar en primera partida que ese valor dependa unicamente del tiempo total de exposición, de hecho existe un tiempo límite de exposición (que depende del conjunto telescopio-instrumentación) pasado el cual no hay conveniencia en extender el tiempo de exposición, ya que la RSN sólo tendrá un pequeño aumento. La RSN depende, además del tiempo de exposición, de la intensidad de la fuente y del fondo. La razón entre estas dos intensidades determina dos regimenes: cuando la fuente es más luminosa que el fondo se habla de *regimen limitado por los fotones*, mientras que si el fondo es mas luminoso que la fuente se habla de *regimen limitado por el fondo*.

### **A.1.2 Efectos observacionales de selección**

El estudio del Universo a través de imágenes muy profundas puede llevar a resultados discordantes sobre la naturaleza de la población de galaxias y de su evolución con el tiempo cósmico si no se tienen en debida cuenta los *efectos de selección*.

El principal efecto de selección es el que depende directamente del flujo. Debido a este efecto, solo podemos tener información sobre los objetos más luminosos con el aumento del desplazamiento al rojo, reduciendo el número total de objetos detectados en un campo. Este efecto depende de tres factores principales: condiciones de observación, propiedades intrínsecas del objeto y parámetros cosmológicos. Cuando desperfectos físicos de la CCD u objetos brillantes impiden la detección de objetos se habla de selección espacial.

### **A.1.3 Cartografiados multi-banda**

Los cartografiados multi-banda consisten en la observación de una región de cielo extensa en un conjunto de filtros fotométricos. En estudios de cosmología este tipo de cartografiado lleva la ventaja sobre su equivalente espectroscópico de que, gracias a las técnicas de recuperación para desplazamientos al rojo, se puede obtener información sobre objetos más débiles.

En este marco, entre los varios proyectos, destacan el *Hubble Deep Field*, el cartografiado que dio origen a una serie de los cartografiados más profundos jamás observados, el proyecto COMBO-17, un cartografiado de un grado cuadrado de cielo, observado en 17 filtros de banda media, el SDSS, un cartografiado en 5 filtros que cubre más de 8000 grados cuadrados de cielo, y ALHAMBRA, un cartografiado que cubre 4 grados cuadrados de cielo, en 20 filtros ópticos contiguos más los 3 estándares del infrarrojo cercano.

### **A.1.4 Finalidades de esta tesis**

La finalidad principal de esta tesis es la exploración del rango de fuentes débiles, tanto desde el punto de vista fotométrico, como espectroscópico. En el marco fotométrico, determinaremos los límites fotométricos en la observación de galaxias, en función del tipo espectral, de su magnitud absoluta y de su distancia. La determinación de este límite es importante para estudios de tipo estadístico de

poblaciones estelares. Aplicaremos nuestros resultados al calculo de la función de luminosidad de poblaciones de galaxias observadas por ALHAMBRA y MUSYC. En el marco espectroscópico, desarrollaremos un método para la determinación de parámetros intrínsecos y de sus incertidumbres en imágenes con muy baja RSN, aplicando este procedimiento al destello de rayos gamma más lejano observado a la fecha de hoy.

---

## A.2 [Cap. 2] Medida de magnitudes absolutas

---

La distribución de las distancias de los objetos astronómicos hace que el análisis de los parámetros directamente observados a través de los telescopios sea de interés limitado para comprender la física del Universo. El parámetro clave que permite obtener observables intrínsecos es la distancia del objeto desde la Tierra, o, de manera equivalente, su desplazamiento al rojo  $z$ .

### A.2.1 Magnitudes absolutas y correcciones K

La *magnitud aparente* de un objeto con distribución espectral de energía (DEE)  $f_\nu(\nu_0)$ , recibida a través de un filtro  $R(\nu_0)$  se puede escribir como:

$$m_o = -2.5 \log \left[ \frac{\int \frac{d\nu_0}{\nu_0} f_\nu(\nu_0) R(\nu_0)}{\int \frac{d\nu_0}{\nu_0} g_\nu(\nu_0) R(\nu_0)} \right] \quad (\text{A.1})$$

donde  $g$  es una función que depende del sistema fotométrico adoptado.

La magnitud absoluta se define como la magnitud que tendría un objeto si estuviera a una distancia fija de 10 parsec. Su expresión es:

$$M_e = m_o - 5 \log(D_L) - 25 - K_{o \rightarrow e}(z, DEE) \quad (\text{A.2})$$

dónde  $D_L$  es la distancia de luminosidad y  $K_{o \rightarrow e}(z, DEE)$  la corrección K, que usando las informaciones de desplazamiento al rojo  $z$  del objeto y de su DEE permite reconstruir el flujo en un filtro elegido  $e$  a partir desde observaciones hechas en un filtro  $o$ . A partir de las relaciones entre el flujo y la magnitud absoluta es posible obtener una expresión exacta para la corrección K.

Otro aspecto fundamental en el cálculo de magnitudes absolutas para objetos

extra-galácticos es la absorción por el medio intergaláctico. Los valores de absorción utilizados en nuestro trabajo son el resultados de un ajuste a absorciones medidas desde observaciones de cuásares, recopiladas por J. Webb.

### **Correcciones K con DEE**

El cálculo de la magnitud absoluta con el método de las correcciones K depende fuertemente de las DEE utilizadas. La disponibilidad en el cartografiado de ALHAMBRA de una consistente cantidad de filtros en banda media permite también implementar otros métodos. El primero consiste en utilizar como filtro de observación  $o$  el filtro de ALHAMBRA que más se acerque a la longitud de onda central del filtro en el que queremos la magnitud absoluta desplazado por el factor que corresponde a la distancia del objeto, permitiendo reducir el peso de la DEE, que depende de modelos de formación estelar.

### **Combinación lineal de una base de filtros**

El hecho que los filtros de ALHAMBRA son de banda media y, en general, las magnitudes absolutas usadas están referidas a filtros de banda ancha, permite calcular las magnitudes absolutas como suma pesada de los flujos que el objeto tiene en los filtros de ALHAMBRA que cubren el filtro en banda ancha correspondiente a la distancia al objeto. El calculo de los pesos fue implementado en dos maneras distintas. La primera consiste en un procedimiento de  $\chi^2$  entre el perfil del filtro de referencia y la suma pesada de las eficiencias de los filtros de ALHAMBRA. El segundo método, que se puede considerar como una evolución geométrica del primero, considera al conjunto de los filtros de ALHAMBRA como una base ortogonal. El cálculo de los coeficientes de los filtros, entonces, se reduce a calcular el producto escalar entre el filtro de referencia y cada elemento de la base.

Comprobamos la calidad de reconstrucción de filtros en dos maneras: primero confrontamos las magnitudes aparentes reconstruidas en los 5 filtros Sloan para objetos en un campo de ALHAMBRA que también tiene cobertura en el SDSS. Las diferencias entre los dos valores muestran pequeños desplazamientos, menores en los filtros más rojos. Otra prueba se hizo generando magnitudes aparentes sintéticas a partir de magnitudes absolutas y analizando las diferencias entre las

dos magnitudes absolutas. Los resultados muestran que hay offsets del orden de 0.03 mag para los tipos más rojos, mientras que el offset es cerca de 0 para los tipos más azules.

## Discusión

Confrontamos los errores en magnitud absoluta, calculados con el método anterior, con estimaciones de errores en magnitudes absolutas procedentes de los errores en el cálculo de los desplazamiento al rojo con medidas fotométricas. Las incertidumbres en ese valor son del orden de  $\Delta z/(1+z) \simeq 0.05$ , uno o dos órdenes de magnitud más altos que los errores en  $z$  por medidas espectroscópicas, se propagan al calculo de la magnitud absolutas produciendo errores de entre medio y un orden de magnitud más altos respecto a los errores por reconstrucción de filtros. Una comparación analoga se hizo suponiendo que el programa de cálculo de los  $z$  cogiera una DEE cercana a la original. En este caso los errores en magnitud absoluta son de hasta 0.5 mag, aunque hay que notar que este caso es de frecuencia muy baja.

## A.2.2 Cálculo de la función de luminosidad

Uno de los descriptores estadísticos de la población de galaxias es la densidad numérica de galaxias por unidad de magnitud, llamada *función de luminosidad* (FL). A lo largo de los años se han desarrollado varios métodos para su cálculo. En este trabajo, implementamos tres de los métodos más usados.

El primer método es el  $V_{max}$ , basado en el cálculo, para cada galaxia, del máximo volumen comóvil en que la galaxia puede estar sin salir de los límites fotométricos y de distancia que caracterizan el catálogo de datos usado. El segundo y tercer métodos se basan en la maximización de la probabilidad de que cada galaxia se encuentre efectivamente en el catálogo. Esta probabilidad se puede calcular asumiendo una expresión paramétrica para la distribución de galaxias con la magnitud absoluta (método de Schechter) o considerando una distribución discretizada para la función de luminosidad (método SWML).

Estos últimos dos métodos no permiten determinar la normalización de la FL a la vez que su forma. Por tanto hay que determinar este valor con métodos distintos, disponibles en la literatura.

## A.3 [Cap. 3] Determinación de la completitud en la detección de objetos

---

### A.3.1 Introducción

Las imágenes tomadas por telescopios nunca contienen toda la información sobre todos los objetos que físicamente se encuentran en esa región de cielo. Eso depende de varios factores que se pueden organizar dentro de tres categorías: dificultades prácticas de los límites de magnitud, dependencia del color de los objetos y dependencia del desplazamiento al rojo. La primera categoría comprende efectos como la agitación de la atmósfera, toda la electrónica de los dispositivos usados en la toma de los datos y de los algoritmos usados en su reducción. Objetos con colores muy extremos respecto al filtro en que se hizo la detección de las fuentes serán incluidos en el catálogo final con muy poca probabilidad. Este hecho constituye la segunda clase de factores. En la tercera caen los efectos de cambio de color observado causados por el desplazamiento al rojo de las fuentes extra-galácticas.

En la determinación de las propiedades físicas de los objetos, entonces, un rol importante juega la medida de estos efectos de selección sobre la muestra completa. El método empleado por ALHAMBRA para la detección de las fuentes, basado en la construcción de una imagen profunda resultado de la suma de las mejores imágenes en varios filtros, hace que la detección sea muy sensible a las tres categorías de selección, y entonces la determinación de la completitud requiere una atención particular.

### A.3.2 Descripción de los métodos

La finalidad principal de este trabajo ha sido la de definir e implementar un procedimiento automatizado para la medida de la completitud en la detección de fuentes en función de  $z$ , del tipo espectro-morfológico y de la magnitud absoluta de cada galaxia. Para que el procedimiento fuera lo más parecido a lo que efectivamente está implementado por la pipeline de ALHAMBRA con la imagen profunda, estimamos un valor de peso medio por cada filtro, que utilizamos luego para la creación de una imagen profunda media.

## El método analítico

El primer método que implementamos se basa en la implementación del camino de un fotón desde que entra en la atmósfera hasta la producción de electrones por efecto fotoeléctrico en la CCD. El número de foto-electrones recolectados por la CCD es usado para calcular tanto el flujo total en electrones como el error poissoniano asociado. De manera analoga a los algoritmos de detección de objetos en imágenes astronómicas, definimos como método de detección el cálculo del número de desviaciones estándares asociadas al objeto. De esta manera una fuente se puede considerar detectada si el número de desviaciones estándares supera un dado umbral. En nuestra implementación utilizamos como umbral una detección a nivel de  $3\sigma$ , la misma adoptada por el proceso oficial de reducción de datos de ALHAMBRA.

Para que la simulación considerara también los efectos debidos a la extensión de los objetos (y consecuentes efectos de selección por brillo superficial), en el cálculo del ruido poissoniano incluimos un término proporcional a la raíz cuadrada del número de píxeles cubiertos por el objeto de interés.

## La simulación Monte Carlo

El segundo método que implementamos para la determinación de la completitud se basa en una simulación de tipo Monte Carlo, utilizando imágenes reales.

A partir de las 20 imágenes en los filtros ópticos, elegimos una galaxia espiral y una elíptica, suficientemente grandes y aisladas que utilizamos como modelo, quitando la mediana del nivel de fondo desde los modelos. Luego se definió un conjunto de  $z$  en el que correr la simulación. Las imágenes de las galaxias se re-escalaron para que el tamaño aparente fuera similar al de las correspondientes galaxias al dado  $z$ . El flujo de cada imagen de galaxia se ajustó a partir del valor de magnitud absoluta  $M$  elegido y según la DEE correspondiente a la galaxia.

El modelo renormalizado y re-escalado se copió en 40 posiciones aleatorias distintas (aunque las mismas para todos los filtros), en la imagen de cada filtro. Las imágenes así obtenidas se multiplicaron por el correspondiente factor de peso y sumaron, obteniendo una buena aproximación de una imagen de detección profunda, con las 40 galaxias añadidas. Sobre esta imagen se corrió el programa SExtractor, con los mismos parámetros usados por la pipeline estándar, para re-

cuperar todas las fuentes. La comparación entre los objetos recuperados y los añadidos nos proporciona el valor de completitud en función de la magnitud absoluta. Estos datos fueron ajustados por una función de Fermi, obteniendo así una parametrización de la completitud para un dado punto en el plano ( $z$ ,  $M$ , DEE). Este procedimiento se repitió para un conjunto de valores de  $0.2 < z < 2.0$  y  $-24 < M < -15$ , por cada uno de los dos modelos.

El algoritmo de arriba se aplicó también a dos casos más. En el primero, en lugar de la imagen de una galaxia, se ha usado como modelo la de una estrella. Esto nos ha permitido obtener una medida de los límites de completitud en magnitud aparente, para objetos puntuales. Ejecutar este mismo proceso sobre imágenes en el filtro  $J$  nos permitió comparar nuestros resultados con una medida publicada con datos similares, encontrando buen acuerdo. En la segunda implementación, en lugar de generar la imagen profunda, se corrió SExtractor en cada una de las imágenes en cada filtro.

### A.3.3 Conclusiones

Comparando el método analítico con la simulación Monte Carlo encontramos un buen acuerdo para  $z > 1$ , donde las diferencias entre las magnitudes correspondientes al nivel de completitud no superan las 0.3-0.4 mag. En el caso  $z < 1$ , los dos métodos muestran diferencias más marcadas, con el método analítico proporcionando magnitudes absolutas más débiles que el método Monte Carlo. Esta diferencia se puede imputar a la simple implementación del tamaño angular de los objetos en el método analítico, resultando en una posible sobre-estimación de la profundidad alcanzada.

Consideramos el método Monte Carlo en la imagen profunda un mejor proceso de reconstrucción del procedimiento efectivamente implementado por la pipeline de ALHAMBRA. Los resultados obtenidos con este método se pueden considerar una determinación de la completitud en detección más robusta y fiable.

Sin embargo, una completa determinación de la completitud no puede prescindir de la capacidad que tenemos de recuperar los desplazamientos al rojo fotométricos. Estos dependen en primer lugar de la calidad fotométrica de los datos, que depende de  $z$ , del tipo morfológico y de la magnitud absoluta de la fuente.

## A.4 [Cap. 4] Función de luminosidad con datos ALHAMBRA

---

### A.4.1 Introducción

Utilizamos los catálogos de ALHAMBRA para testear los resultados de la determinación de la completitud en detección en el cálculo de la función de luminosidad.

Los catálogos usados son la versión de marzo2011 e incluyen información fotométrica en los 20+3 filtros y medidas de desplazamiento al rojo para 39 de los 64 catálogos totales, cada uno correspondiente a una CCD, para un total de 501865 fuentes. La profundidad fotométrica media alcanza  $AB \approx 24.5$

### A.4.2 Separación estrellas-galaxias

La separación entre estrellas y galaxias se basó en un diagrama color-color, construido utilizando el filtro centrado a  $4585\text{\AA}$  (similar a un B), J y K. Para que la muestra fuera más solida, incluimos una selección con el parámetro odds, proporcionado por el programa da calculo de los  $z$ . También utilizamos la información sobre el tiempo de exposición total para cada objeto para excluir de nuestra muestra los objetos que, quedando en los bordes de las imágenes, tienen un menor tiempo de exposición, degradando la razón señal-ruido. Al final del proceso de selección, la muestra está formada por 139460 objetos con redshift entre 0.01 y 7, y  $z_{med} = 0.9$ .

### A.4.3 Magnitudes absolutas

Las informaciones incluidas en los catálogos contienen también una medida del tipo espectral de cada objeto, de manera que podemos utilizar esa información para calcular las correcciones  $K$  necesarias. Para mejorar el proceso, en el cálculo de las magnitudes absolutas utilizamos como magnitud aparente de inicio la relativa al filtro que más se acerca a la banda en reposo desplazada al redshift de la fuente. Las magnitudes absolutas fueron calculadas para las bandas Sloan  $r$  y  $u$ .

### A.4.4 Completitud en detección

Por cada uno de los parametros que describen la función de Fermi utilizada para calcular la completitud, se introdujo un ajuste con una función. Esto nos permite una determinación más precisa de la completitud en función de  $z$ .

El inverso del valor de completitud relativo al desplazamiento al rojo de cada galaxia fue usado como peso tanto en el cálculo de los diagramas color-magnitud, como en la medida de la función de luminosidad.

### A.4.5 Diagrama color-magnitud

Construimos los diagramas color-magnitud usando las magnitudes absolutas  $M_r$  y  $M_u$ , para tres intervalos de redshift:  $0.3 < z < 0.6$ ,  $0.6 < z < 1.0$  y  $1.0 < z < 1.5$  usando primero el conjunto de datos sin corrección por completitud y luego añadiendo la corrección. La comparación de los diagramas muestra una neta evolución en luminosidad de la población de galaxias más azules en el sentido de hacerse más luminosas con  $z$ , mientras que las galaxias más rojas parecen no desplazarse, aunque la identificación de esta población es más difícil en el rango de redshift más alto.

### A.4.6 Funciones de luminosidad

Las funciones de luminosidad se calcularon en los mismos rangos de redshift adoptados para los diagramas color-magnitud, aplicando la corrección por completitud. En cada rango se midió la FL global y la relativa a las tres poblaciones principales: elípticas, espirales y starburst.

Nuestra FL global en los 3 rangos está en buen acuerdo con FL publicadas en la literatura, lo que nos hace confiar también en las correcciones por completitud, permitiendo alcanzar magnitudes absolutas más débiles en hasta 1.5 mag.

La comparación de las FL en los rangos de redshift nos permite decir que:

- El extremo luminosa de la FL global muestra muy poca evolución entre  $z \simeq 0.45$  y  $z \simeq 1.25$ . Un análisis más detallado de la cola débil requiere datos más profundos, en particular para el intervalo de redshift más alto;
- La FL para las galaxias elípticas, como para la FL global, no muestra signos

evidentes de evolución, en acuerdo con el hecho de que la cola luminosa de la FL está poblada por objetos muy rojos;

- La FL para las galaxias espirales muestra una evolución evidente, probablemente en el dominio de luminosidad, desde  $z \simeq 0.45$  hasta  $z \simeq 0.8$ , con la FL que se desplaza hacia magnitudes mas luminosas con  $z$ , mientras que en los dos rangos de redshift mas altos las FL aparecen similares;
- La población de galaxias *starburst* es la que presenta mayor evolución en los tres rangos de redshift, aunque un análisis mas detallado es necesario para definir si la evolución es sobre todo en luminosidad o en densidad.

## A.5 [Cap. 5] Evolución de la FL en bandas J y H desde $z = 1.5$ hasta $z = 3.5$

---

### A.5.1 Introducción

En el actual modelo cosmológico de concordancia, las galaxias son el resultado de agrupamientos continuos de halos de materia oscura, que guían el ensamblaje de materia barionica. La función de luminosidad (FL) de las galaxias es entonces una herramienta muy útil para el estudio de las poblaciones de galaxias y de su evolución en el tiempo. En particular la FL en bandas infrarrojas, siendo menos sensible a los efectos de absorción por el polvo interestelar y siendo dominada por la luz de estrellas más viejas, proporciona una estimación mejor de la tasa de formación de las galaxias, presentándose como una mejor tabla de prueba para los modelos de formación de halos.

### A.5.2 Descripción de los datos

Para este trabajo hemos utilizado un conjunto de siete catálogos de datos disponibles publicamente y procedentes de tres distintos cartografiados: el MUlti-wavelength Survey by Yale-Chile (MUSYC), el Faint InfraRed Extragalactic Survey (FIRES) y el GOODS Chandra Deep Field-South (FIREWORKS).

El cartografiado MUSYC consiste en cuatro campos de  $10' \times 10'$  arcmin<sup>2</sup> (el Hubble Deep Field South 1 y 2 y los campos alrededor de SDSS-1030 y CW1255), observados en bandas ópticas (UBVRIZ), en el infrarrojo cercano (J, H, y  $K_S$ ) y por el telescopio Spitzer (bandas a 3.6, 4.5, 5.8 y  $8.0\mu\text{m}$ ). Los límites al 90% de detección de fuentes puntuales se encuentran en  $K_S \simeq 23$  AB. El catálogo final contiene 9037 fuentes sobre un área de 372.7 arcmin<sup>2</sup>.

FIRES se compone de dos campos, el Hubble Deep Field South y el campo alrededor de un cúmulo de galaxias a  $z = 0.83$ . La fotometría existe en las bandas ópticas U,B,V,WFPC2 V606 y I814, en el infrarrojo cercano J, H y  $K_s$  y complementada por datos Spitzer en los 4 canales de IRAC centrados en 3.6, 4.5, 5.8 y  $8.0\mu\text{m}$ . Estos son los catálogos más profundos utilizados en nuestro trabajo, llegando a una profundidad de  $K_S \simeq 25$ AB para el HDF-S. En total los dos catálogos proporcionan informaciones sobre 715+1547 fuentes, en un área de 4.5 y 21 arcmin<sup>2</sup> respectivamente.

El catálogo FIREWORKS se compone de datos disponibles públicamente del GOODS-CDFS. La información fotométrica es disponible en las bandas U38,B,V, R, I, J, H,K y los 4 canales Spitzer. La profundidad llega a  $K_S \simeq 24$  AB. El catálogo se compone de 3559 objetos sobre un área de 113 arcmin<sup>2</sup>.

Los campos MUSYC HDFS-1, HDFS-2 y FIRES HDFS tienen una parte que se sobrepone, así que tuvimos que excluir los objetos repetidos desde los catálogos menos profundos. Además, seleccionamos solo las fuentes que presentaran fotometría en todas las bandas infrarrojas, de manera que nuestras magnitudes absolutas se apoyaran en la menor parte posible en el conjunto de DEE.

Calculamos los desplazamientos al rojo fotométricos utilizando el programa EAZY y probando cuatro conjuntos distintos de DEE: el conjunto que viene por defecto con EAZY, el mismo, pero con líneas de emisión añadidas, un conjunto basado en los modelos de Coleman., Wu y Weedman, y el conjunto EAZY al que se añadió el modelo de una galaxia joven muy enrojecida. La comparación con los  $z$  espectroscópicos disponibles para el 6% de las fuentes nos sugirió utilizar los  $z$  obtenidos con los modelos EAZY.

La separación entre estrellas y galaxias se basó en el diagrama color-color (U-J)-(J-K), acompañado por un chequeo de los  $\chi^2$  con modelos de DEE estelares y

de EAZY.

### A.5.3 Metodología

Las FL se calcularon con los tres métodos más comúnmente usados:  $V_{max}$ , SWML y STYML. Debido al relativo pequeño tamaño del campo total, la determinación de las incertidumbres debidas a la varianza cósmica tienen un rol importante. Estas se midieron según una receta publicada por Moster, basada en simulaciones semi-analíticas.

### A.5.4 Funciones de luminosidad en J y H

Calculamos las FL en las banda de reposo J y H, y en 4 intervalos de desplazamiento al rojo:  $1.5 < z < 2.0$ ,  $2.0 < z < 2.5$ ,  $2.5 < z < 3.0$  y  $3.0 < z < 3.5$ . El número total de objetos utilizados es de 996, 419, 298 y 103. Comparamos la FL en la banda J y para  $1.5 < z < 2.0$  y  $2.5 < z < 3.0$  con FL publicadas en la literatura. Nuestras medidas discretizadas están en buen acuerdo con las publicadas en los dos rangos de redshift, aunque las parametrizaciones de Schechter muestran diferentes faint-end slopes, sobre todo a redshift más alto. Nuestra determinaciones de la FL en H son la primeras en este intervalo de  $z$ .

Para estudiar la evolución de las FL, hicimos un ajuste con funciones establecidas ad-hoc sobre los parámetros de Schechter  $\alpha$ ,  $M_*$ ,  $\phi_*$  en función de  $z$ , incluyendo también todas las determinaciones encontradas en la literatura. Encontramos que  $\phi_*$  decrece en un factor 10 desde  $z = 0.1$  a  $z = 2$ ;  $M_*$  después de hacerse más brillante hasta  $z = 2$ , disminuye de luminosidad, aunque de forma menos acentuada. La determinación de una tendencia para  $\alpha$  es más difícil, debido a las grandes incertidumbres, así que decidimos considerarlo constante.

Utilizando tanto los parámetros de Schechter como nuestras parametrizaciones también calculamos la densidad de luminosidad. El cálculo obtenido simplemente desde la parametrización está de acuerdo con las estimaciones obtenidas a partir de los puntos medidos. La evolución de la densidad de luminosidad muestra que este observable se mantiene constante en el rango  $0 < z < 1$ , seguido por una caída constante, tanto en J como en H.

Como último ejercicio, derivando nuestra expresión paramétrica de la densidad de luminosidad obtenida desde los parámetros de Schechter, calculamos la tasa de formación estelar. Comparando con las estimaciones disponibles en la literatura, obtenidas desde la densidad de luminosidad en UV, nuestras medidas son un factor 0.4-0.5 más bajas, sobre todo a  $z > 3$ , donde estaríamos extrapolando nuestros datos. Aunque nuestra medida es más sencilla, estimando la tasa de formación directamente como masa que se forma, las obtenidas por UV son más directas porque se relacionan a las estrellas más jóvenes, aunque necesitan modelos para estimar la masa total que se va formando.

### **A.5.5 Conclusiones**

Analizamos la evolución de las FL en las bandas de reposo J y H, obtenidas a partir de catálogos públicos profundos. Las en banda H son las primeras medidas hechas hasta redshift 3.5. Dada la menor sensibilidad de esta banda a los efectos del polvo, la FL en banda H se propone como herramienta muy útil en el estudio del ensamblaje de masa a lo largo del tiempo. Encontramos que la faint-end slope se puede considerar constante en un rango  $0 < z < 4$ ;  $M_*$  crece en función de  $z$  para  $0 < z = 2$  y luego disminuye más suavemente;  $\phi_*$  decrece en todo el rango. Introducimos una parametrización que nos ha permitido calcular la densidad de luminosidad y la tasa de formación estelar, con un buen y razonable acuerdo respectivamente con otras determinaciones desde la literatura. Nuestras medidas de FL mejoraron considerablemente también la estadística en la medida del extremo brillante de la FL.

## **A.6 [Cap. 6] Redshift espectrofotométricos: un nuevo enfoque para la reducción de espectros a bajo RSN y su aplicación a GRB090423**

---

### **A.6.1 Introducción**

La medición de los desplazamiento al rojo para objetos extra-galácticos es una de las técnicas más importantes en astronomía. Sin embargo, también depende

de manera crítica de la calidad de los datos. Por su naturaleza, a veces es difícil evaluar la calidad de los resultados, porque ha sido difícil medir cuantitativamente los errores.

La manera estandar de reducir los datos prevee la extracción de los espectros y su calibración en flujo y longitud de onda. Un enfoque diferente sería el de escoger un modelo que represente el mejor ajuste en dos dimensiones. Este procedimiento necesita unas condiciones:

- El espectro intrínscico de la fuente tiene que estar incluido en la familia de modelos usados. Este proceso tendría bastantes dificultades para cuásares o galaxias observadas a media resolución, por la dispersión intrínscica entre los tipos diferentes;
- Se tienen que conocer bien las características del instrumento. Éstas incluyen la eficiencia total en función de la longitud de onda, todas las distorsiones geométricas en la dirección espectral y, claramente, la posición exacta del objeto en la imagen.
- El ruido necesita una modelización adecuada, indispensable para medir de la manera mas precisa posible no solo los valores de los parámetros, sino también las incertidumbres asociadas.

### **A.6.2 Estallidos de rayos gamma**

Los estallidos de rayos gamma (ERG) son eventos muy breves que ocurren con una frecuencia de unos pocos al día. En un tiempo muy breve, del orden de unas décimas de segundos, su brillo los convierte en las fuentes de rayos gamma más brillantes de todo el cielo.

El modelo más comunmente aceptado para un similar motor central, capaz de producir tan alta energía, prevé el acontecimiento de un evento estelar catclísmico, como puede ser el colapso del núcleo de una estrella masiva.

Dependiendo de la duración de la post-luminiscencia, los ERG se pueden dividir en dos poblaciones: largos y cortos. Los ERG largos son generados por estrellas masivas cuyo nucleo colapsa en un agujero negro. En cambio, los ERG cortos son originados por la fusión de dos estrellas de neutrones o de una estrella de neutrones y un agujero negro.

### A.6.3 Descripción de los datos

Para desarrollar nuestro método, utilizamos los datos relativos al estallido de rayos gamma GRB090423. Éste fue un ERG detectado por el satélite Swift el 23 de abril 2009. Ya desde las primeras observaciones se comprendió que debía ser un objeto a muy alto  $z$ , con muy poca absorción por el polvo. Los datos que utilizamos fueron tomados por el Telescopio Nazionale Galileo (TNG), utilizando el espectrógrafo NICS en combinación con un prisma de Amici. El espectro cubre el rango  $0.8 - 2.5\mu\text{m}$ , con una resolución de  $R \approx 80$ . Cerca del espectro del ERG hay también el espectro de una estrella, que ha sido utilizada como referencia en la caracterización instrumental.

### A.6.4 Descripción del método

Nuestro objetivo es el de reproducir el espectro de la post-luminiscencia del GRB090423 de la manera más precisa posible y de reconstruir el equivalente espectral de la función de ajuste de perfil como es generada cuando la luz atraviesa la atmósfera, el telescopio, el instrumento, la óptica y llega al detector.

Creamos una librería de espectros modelos, basados en tres parámetros fundamentales: el desplazamiento al rojo, el exponente  $\alpha$  del modelo espectral  $f_\nu \propto \lambda^\alpha$  y la columna de densidad total de hidrógeno neutro (NHI), que produce un marcado perfil de línea Lyman  $\alpha$  saturada.

Utilizamos el espectro de una estrella brillante en la misma imagen para determinar la eficiencia total del sistema, confrontando el espectro extraído con el modelo de la librería de Bruzual-Persson-Gunn-Stryker. El espectro de la estrella, en el rango de longitudes de ondas observadas, es libre de características espectrales dominantes. El espectro observado de la estrella fue utilizado también para determinar las distorsiones a lo largo del eje de dispersión y la FWHM en función de la longitud de onda.

Estimamos el ruido de la CCD analizando 7 regiones rectangulares con el mismo tamaño, y cubriendo el mismo rango en la dirección de dispersión. Estimamos el ruido en función de la longitud de onda utilizando cajas de  $3 \times 3$  píxeles

alrededor de cada uno de los píxeles en cada una de las cajas. El resultado de este procedimiento fue la creación de una mini-imagen de ruido.

Se definió una rejilla de valores  $z, \alpha$  y NHI y se creó un espectro sintético por cada punto del espacio definido. El espectro uni-dimensional se convirtió a imagen 2D utilizando las propiedades obtenidas anteriormente. Finalmente, se procedió a una evaluación del  $\chi^2$  entre el espectro 2D sintético y el espectro real, usando la imagen de ruido como medida de la incertidumbre.

### A.6.5 Resultados y conclusiones

Utilizamos la caracterización del instrumento obtenida en los pasos descritos en el párrafo anterior para crear réplicas del espectro observado del ERG, para cada uno de los modelos escogidos. En breve, escogimos un conjunto de valores de  $z, \alpha$  y N(HI) y los utilizamos para generar un espectro uni-dimensional. En fin, enrojecemos el espectro utilizando el valor de extinción galáctica que le corresponde,  $E(B-V)=0.03$ . Luego este espectro es convertido a una imagen bi-dimensional, usando la eficiencia medida, ajustando el eje de longitud de onda a la solución de dispersión del prisma de Amici y convolucionándola en la dirección espectral con una función gaussiana, según la FWHM medida a cada longitud de onda. Al final se fuerza el espectro a que siguiera en la dirección espacial la traza medida por el espectro de la estrella.

Cada realización se compara luego con la sección de la imagen que contiene el espectro del ERG, a través un ajuste de  $\chi^2$ , donde la imagen de ruido se corresponde a la que medimos.

El mejor ajuste encontrado a nivel de  $1\sigma$  corresponde a  $z = 8.4_{-0.2}^{+0.5}$ ,  $\alpha = 1.2_{-0.3}^{+0.8}$  y  $N(\text{HI}) = 10^{20.0} \text{ cm}^{-2}$ , calculamos las regiones de confianza en cada uno de los parámetros. El valor de NHI no tiene límite inferior; esta es una consecuencia natural ya que para  $N\text{HI} \approx 10^{20} \text{ cm}^{-2}$  no existe el perfil saturado de la línea de  $\text{Ly}\alpha$ .

También se podría utilizar el valor de la pendiente del espectro medida a partir de la fotometría infrarroja, como una condición a-priori de nuestro análisis. De esta manera, utilizando el límite a  $1\sigma$  presentado en Salvaterra et al. (2009), se obtendría un límite más restringido para el redshift, aproximadamente  $z > 7.5$  a

un nivel de confianza de  $2 - \sigma$ .

Nuestros resultados aparecen ligeramente más elevados de los que se han presentados en la literatura tanto con los mismos datos como con otros conjuntos de datos, aunque siempre compatible a nivel de  $2\sigma$ . Consideramos fiables nuestros intervalos de error, dado el análisis de las características del ruido evaluadas en este trabajo.

Este mismo procedimiento se puede aplicar a otros casos, donde la fuente pertenece a una clase espectral de objetos bien definida, necesitando la extracción de la máxima cantidad posible de información desde espectros con muy baja calidad, como es el caso de ERG a alto  $z$ .

## A.7 [Cap. 7] Conclusiones

---

En esta tesis exploramos el rango débil de un cartografiado cosmológico, tanto desde el punto de vista fotométrico como espectroscópico.

En el marco del proyecto ALHAMBRA, implementamos dos distintos métodos para la medida del nivel de completitud en la detección de objetos, en función del tipo espectro-morfológico y del redshift.

El primer método está totalmente basado en la simulación del aparato instrumental (telescopio, cámara y detector) empleado para las observaciones.

El segundo método consiste en una simulación Monte Carlo basada en datos reales. Nuestro enfoque intenta reproducir la manera en que se crea la imagen profunda y como se hace la detección de los objetos en dicha imagen. Se obtiene la completitud a partir de la fracción de objetos detectados cuyo flujo y tamaño aparente se han previamente re-escalado para que representen los de galaxias típicas a esos redshifts.

Los resultados obtenidos con los dos métodos anteriores se aplicaron a un catálogo preliminar del cartografiado ALHAMBRA, para la medida de la función de luminosidad en tres diferentes rangos de redshift y para las tres clases principales de galaxias. La aplicación de las correcciones en completitud nos permitió medir la función de luminosidad llegando a una profundidad mayor de una magnitud respecto al cartografiado VVDS, un cartografiado espectroscópico con límites en magnitud aparente parecidos.

El estudio de la evolución de la FL se extendió al rango infrarrojo, en las bandas en reposo J y H, hasta redshift 3.5. Este fue el resultado del análisis de tres catálogos públicos desde los proyectos MUSYC, FIRES y FIREWORKS. El análisis nos permitió medir por primera vez la FL en la banda H de reposo de galaxias de campo en el rango de redshift  $z \in [1.5, 3.5]$ ; al mismo tiempo, el mayor volumen nos permitió mejorar de manera significativa la medida del extremo brillante de la FL.

Desde el punto de vista espectroscópico, desarrollamos un método novedoso para el análisis de espectros con baja razón señal-ruido, parecido a los utilizados en el análisis de datos de rayos X. El método consiste en generar espectros bi-dimensionales a partir de espectros modelos, seleccionando el que mejor reproduce los datos observados a través de minimización de  $\chi^2$ . El método se aplicó en concreto al caso del GRB090423, el GRB más lejano observado hasta el momento, demostrando que se puede extraer más información de lo que generalmente se asume desde este tipo de datos.

**Trabajos futuros:** Hemos empezado una campaña espectroscópica para estudiar la población de galaxias masivas a alto redshift. En particular analizaremos el espectro del objeto masivo C1-23152, una galaxia con masa  $M = 3 \times 10^{11} M_{\odot}$  a redshift  $z = 3.3$ , cuya observaciones ya están programadas para finales de este año-principio de 2012, con el Gran Telescopio Canarias, con el instrumento OSIRIS. Los espectros medidos en el ultravioleta nos permitirán estudiar la emisión Lyman  $\alpha$  para determinar la presencia de un AGN y medir los vientos interestelares comparando las líneas de absorción en UV con la de Lyman  $\alpha$ .

Utilizaremos también las muestras de galaxias seleccionada en las bandas NIR, obtenidas a partir de varios cartografiados multi-banda, para mejorar la medida de la evolución de la FL y DL en el óptico y NIR de reposo para redshift entre 1 y 4. En total emplearemos datos de más de 20000 galaxias dentro de un área de 1600 arcmin<sup>2</sup>.

El catálogo final de ALHAMBRA, que será disponible en los próximos meses, nos permitirá completar las medidas de la FL en el rango óptico hasta  $z = 1.5$ . Además, se analizarán las imágenes tomadas por el instrumento IRAC del satélite Spitzer disponibles para mitad del area cubierta por ALHAMBRA, para obtener la fotometría en bandas hasta  $8\mu\text{m}$ . Esto nos permitirá por un lado mejorar las medidas de redshift fotométricos para los objetos en los campos comunes, y por

otro lado estudiar la evolución de la FL en el rango infrarrojo de reposo con una dependencia mínima en los modelos de distribución espectral.